Geometric Nonlinear Analysis of Steel Members with Imperfections

by
Mohammed Bhiri

Supervised by
Dr. Magdi Mohareb

Dissertation submitted to the University of Ottawa
in partial fulfillment of the requirements for the degree of

Doctor of Philosophy
in Civil Engineering

Department of Civil Engineering
Faculty of Engineering
University of Ottawa

Abstract

Steel members inherently possess Initial Out-of-Straightness (IOS) and residual stresses, both of which are known to reduce their lateral-torsional buckling (LTB) resistance. Despite this, current Canadian and American design standards evaluate the LTB resistance of long-span, laterally unbraced members (expected to fail by elastic LTB) based on the critical moment of perfectly straight members, thereby neglecting the adverse effects of IOS. This approach stands in contrast to Eurocode and Australian standards, which explicitly account for IOS in their design provisions. Within this context, the present study investigates the impact of imperfections on LTB capacity of long-span, laterally unbraced steel members and advances the existing body of knowledge through three key contributions.

In the first contribution, a novel finite element formulation is developed for the geometrically nonlinear analysis of doubly symmetric I-shaped steel members. The formulation is grounded in the kinematics of thin-walled beam theory, thus capturing warping effects, and incorporates an algorithm to account for initial out-of-straightness (IOS) in the form of sweep, camber, twist, or combinations thereof. The model's ability to predict displacements and stresses is validated through comparisons with benchmark problems based on shell models and other thin-walled beam solutions. The model is subsequently employed in conjunction with a first-yield criterion to evaluate the buckling resistance of flexural members associated with various IOS patterns.

In the second contribution, the developed finite element is employed to conduct a parametric study involving 504 simulations of long-span, laterally unbraced flexural members with hot-rolled wide-flange cross-sections. The investigation focuses on members whose capacities are governed by elastic LTB, aiming to quantify the influence of IOS on their buckling resistance. The analyses account for geometric nonlinearity, IOS, and residual stress effects. The study investigates the

influence of various IOS characteristics, including pattern (symmetric vs. asymmetric), type (lateral, twist, and lateral-torsional), amplitude, member span, cross-sectional geometry, and loading conditions, on the LTB resistance of long-span steel members. Based on the parametric results, regression equations are developed to characterize the LTB resistance for members with different IOS types and amplitudes. The practical application of these equations is demonstrated through a design example.

The third contribution builds upon the capabilities of the finite element formulation developed in the first contribution by introducing three key enhancements: (a) incorporation of cross-sectional monosymmetric, thus enabling the analysis of I beams with a reduced flange; (b) inclusion of the destabilizing effect associated with load height; and (c) integration of residual stresses into the constitutive model as initial stresses. The enhanced model's capabilities are demonstrated through illustrative examples, and its accuracy is validated through comparisons with shell finite element models.

Acknowledgment

First and foremost, I thank Allah Almighty for granting me the strength, patience, and perseverance to complete this research. Without His blessings and guidance, this achievement would not have been possible.

I would like to express my deepest gratitude to my supervisor, Professor Magdi Mohareb, for his continuous guidance, patience, valuable advice, and unwavering support throughout this research. His mentorship and encouragement have been a constant source of inspiration and have played a vital role in the successful completion of this work.

I also extend my sincere appreciation to Dr. Saher Attia at Cairo University for his valuable contributions and insightful discussions, which greatly enriched this study.

I am profoundly grateful to my beloved parents for their endless love, prayers, and sacrifices. Their encouragement and faith have been the foundation of my perseverance and success.

I would like to express my sincere appreciation to my family, colleagues and friends for their continuous support, and understanding throughout my studies. Their presence and encouragement have been my greatest source of motivation.

My heartfelt thanks go to the Libyan Ministry of Education for providing the scholarship and financial assistance that made this academic journey possible.

Table of Contents

List of Figures

List of Tables

Chapter 1: Introduction and Scope

1.1 Introduction

Lateral-torsional buckling (LTB) is a critical failure mode that often governs the resistance of long-span laterally unbraced steel beams that bent about their major axis. In the idealized case of a perfectly straight wide-flange section, LTB occurs at a well-defined bifurcation point at which the beam suddenly undergoes coupled lateral displacement and twist. The corresponding critical load is obtained through an eigenvalue analysis. In practice, however, beams are never perfectly straight. Manufacturing, handling, and erection processes inevitably introduce initial out-of-straightness (IOS), which causes beams to gradually deform in a lateral torsional mode. Under such conditions, LTB is no longer associated with a distinct bifurcation point, and the eigenvalue solution approach becomes unsuitable for defining the precise elastic buckling strength. Instead, a geometrically nonlinear analysis is required to capture the progressive instability response of imperfect beams. In this context, the elastic buckling resistance is not distinctly defined but may be assessed by the attainment of the onset of yielding within the cross-section or by the attainment of a serviceability-based displacement threshold.

The presence of IOS is widely recognized to have a detrimental influence on the stability of members. While some structural steel design standards, such as Eurocode 3 [1.1], explicitly incorporate IOS effects in their LTB provisions, others, including the Canadian standard [1.2] and American specifications [1.3], characterize the strength of long-span unbraced members on the basis of elastic lateral-torsional buckling analysis for a perfectly straight beam. Within this context, the present study aims to quantify the effect of initial out-of-straightness on the elastic lateral–torsional buckling resistance of steel beams and evaluate the adequacy of current design provisions in capturing this influence.

1.2 Elastic Lateral Torsional Buckling Failure Mechanism of Steel Beams

1.2.1 Perfectly Straight Beam

When a transverse load V is applied to a perfectly straight beam, it initially deflects vertically by a displacement v, moving from its undeformed configuration (Configuration 1) to Configuration 2. As the loading increases by a factor λ, the beam reaches Configuration 3, which represents the bifurcation point. At this stage, the vertical displacement reaches λV, and the beam suddenly becomes unstable. Beyond this point, the equilibrium path shifts abruptly to Configuration 4, characterized by lateral displacement u_b and twist θ_b. The corresponding load-displacement relationship is illustrated in Fig. 1.1 between Configurations 1 and 3, the deformation is purely vertical, with no lateral movement. At the bifurcation point, the beam experiences a sudden transition into combined lateral displacement and twist. The associated buckling load λV is determined through eigenvalue analysis, and it represents the theoretical maximum resistance of the ideal, perfectly straight beam.

1.2.2 Initially Imperfect Beam

For a beam with initial out-of-straightness (IOS), whether lateral u_0, torsional θ_0, or combined lateral–torsional IOS, the load-displacement behaviour differs fundamentally from that of the perfectly straight case. Such imperfections are often assumed to be affine to the first buckling mode shape scaled by a specified amplitude. At Configuration 1, the imperfect beam already possesses geometric deviations from the perfectly straight hypothesis. As the load increases, the beam develops additional lateral displacement and twist progressively, as shown in Configurations 2 through 4. Unlike perfectly straight beams, there is no distinct bifurcation point. Instead, the

response follows a smooth nonlinear path towards the ultimate load V. This results in a gradual loss of stability rather than a sudden transition.

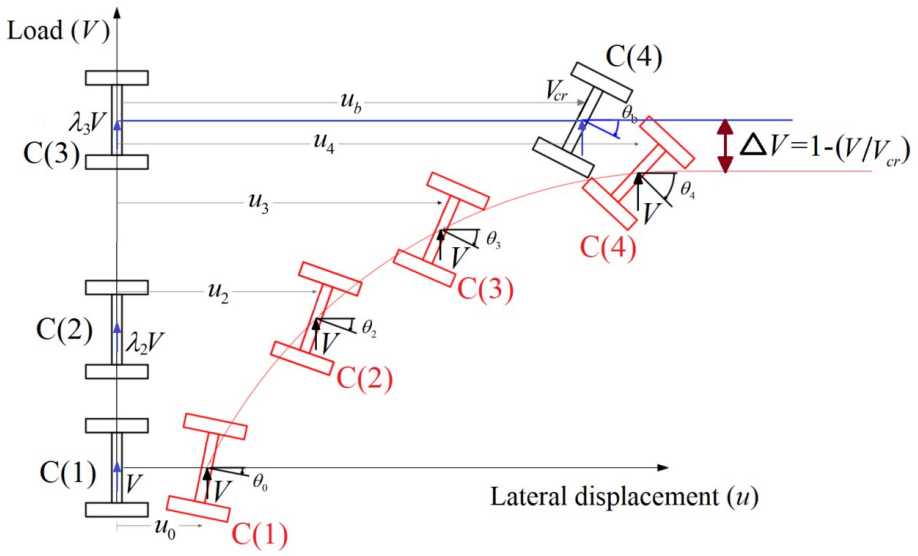

Fig. 1.1 Comparison of the lateral torsional buckling behavior of a straight beam versus beams with IOS.

1.3 Effect of Residual Stresses on Elastic LTB Strength

Residual stresses in steel members originate primarily from uneven cooling of rolled sections or following welding processes in fabricated sections. These locked-in stresses alter the stress distribution within the cross-section, thus reducing the effective yield strength and often leading to two detrimental effects: (1) Early yielding in zones of high residual stresses, and (2) Reduced elastic buckling resistance due to premature yielding before the attainment of the theoretical elastic limit. Design standards incorporate residual stresses into LTB calculations either explicitly, using calibrated buckling curves, or implicitly, by reducing the elastic stress limit. In the American specifications [1.3], residual stresses are addressed indirectly by limiting the elastic LTB stress to $0.7F_y$. This reduction, based on an assumed peak compressive residual stress of approximately $0.3F_y$, effectively lowers the point of onset of yielding by about 30%. This restriction is embedded

in the equation for the threshold span L_r , which defines the border between elastic and inelastic LTB regions. When the combined effect of applied stresses and residual stresses reach F_y , yielding is deemed to take place, and the member's inelastic LTB capacity is considered to drop below the elastic LTB critical moment.

The Canadian standard [1.2] adopts a more conservative approach by defining the point of onset of yielding as $0.67\,F_y$, which corresponds to a compressive residual stress of $0.33\,F_y$, a slightly higher residual stress value than that postulated in American specifications [1.3]. In contrast, both the Eurocode 3 [1.1] and the Australian standard [1.4] do not delineate a boundary between elastic and inelastic LTB. The Eurocode 3 defines four buckling curves *a–d* that represent various levels of detriment to the LTB resistance owing to the combined effect of IOS and residual stress effects. Rolled sections, which generally exhibit lower residual stress magnitudes, are assigned to curves *a* or *b*, while welded sections, with higher residual stresses, are assigned to curves *c* or *d*. In contrast, the AS 4100 has a unified expression. A comparative summary of residual stress treatment in all four steel design standards is presented in Table 1.1.

Table 1.1 Comparative summary of residual stress consideration in design standards

Standard	Residual Stress Consideration	Stress threshold for considering residual stresses
AISC 360-22	Only in the inelastic LTB range	>0.7Fy
CSA S16	Only in the inelastic LTB range	>0.67Fy
Eurocode 3	Elastic and inelastic LTB ranges	NA
AS 4100	Elastic and inelastic LTB ranges	NA

1.4 LTB Provisions in Design Standards

1.4.1 Elastic Critical Moment

The elastic critical moment M_u for LTB resistance is a key parameter in the design of laterally unbraced steel beams. For a perfectly straight member with a doubly symmetric section, it is determined by

$$M_u = \frac{C_b \pi}{L} \sqrt{EI_y GJ + \left(\frac{\pi E}{L}\right)^2 I_y C_w} \tag{1.1}$$

in which C_b is a moment gradient factor, I_y is the moment of inertia, J is the torsional constant, C_w is the warping constant, L is the laterally unbraced length of the beam, E is the modulus of elasticity, and G is the shear modulus. For a beam with a monosymmetric section, the elastic critical moment M_u takes the more general formula

$$M_u = \frac{C_b \pi^2 EI_y}{L^2} \left[\frac{\beta_x}{2} + \sqrt{\left(\frac{\beta_x}{2}\right)^2 + \left(\frac{GJL^2}{\pi^2 EI_y} + \frac{C_w}{I_y}\right)} \right] \tag{1.2}$$

For monosymmetric members, American and Canadian standards provide C_b in Eq. (1.2) only when the load is applied at the web mid-height, and β_x is the monosymmetric parameter about the bending axis in the American specifications [1.3] and the Canadian standard [1.2] calculated as:

$$\beta_x = \int_A y\left(x^2 + y^2\right) dA / I_x - 2p_y \tag{1.3}$$

in which p_y is the coordinate of the shear center S measured from the section centroid C (Fig. 1.2b). For I-shaped sections with unequal flanges, β_x takes the form (e.g., [1.5])

$$\beta_x = \frac{1}{I_x}\left[y_2\left(\frac{b_2^3 t_2}{12} + b_2 t_2 y_2^{\,2} + \frac{t_w}{4} y_2^{\,3} \right) - y_1\left(\frac{b_1^3 t_1}{12} + b_1 t_1 y_1^{\,2} + \frac{t_w}{4} y_1^{\,3} \right) \right] - 2p_y \tag{1.4}$$

in which y_1 is the distance from the top flange centroid to the section centroid, and y_2 is the distance from the bottom flange centroid to the section centroid, b_1 and t_1 are the width and thickness of the top flange, b_2 and t_2 are the width and thickness of the bottom flange, h and t_w are the web height (measured from the flange centroids) and thickness (Fig. 1.2b). The sign conventions and notations are depicted in Fig. 1.2.

The elastic critical moment expressions in Eqs. (1.1) and (1.2) are based on the perfectly straight member assumption, i.e., they exclude the effect of initial out-of-straightness, and may be considered as an upper-bound estimate of the elastic LTB resistance of actual members with IOS.

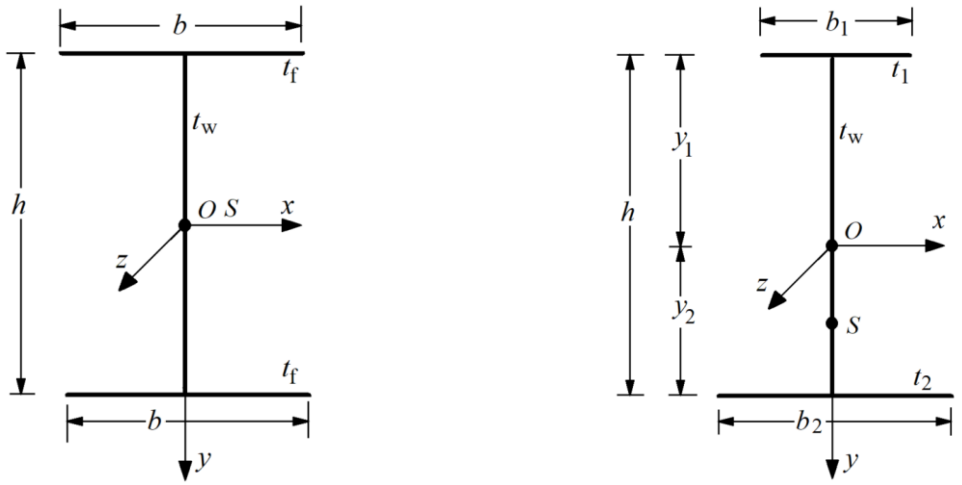

(a) (b)

Fig. 1.2 Sign convention and notation for (a) Doubly symmetric section, (b) Monosymmetric section

1.5 LTB Provisions in Canadian Standards

Based on the Canadian standard [1.2], the factored moment resistance M_r for a laterally unsupported beam under major axis bending, is given by

$$M_r = \phi M_n \tag{1.5}$$

in which $\phi = 0.9$ is a resistance factor that accounts for the variability in material and geometric properties and M_n is the nominal moment resistance. For a class 2 section, the nominal moment is given by

$$M_n = \begin{cases} M_P & M_u \geq 2.15M_p & \text{short span} & \text{plastic moment} \\ 1.15M_P\left[1-\dfrac{0.28M_P}{M_u}\right] & 2.15M_p \geq M_u \geq 0.67M_p & \text{intermediate span} & \text{inelastic LTB} \\ M_u & M_u \leq 0.67M_p & \text{long span} & \text{elastic LTB} \end{cases} \tag{1.6a-c}$$

in which M_P is the plastic moment of the cross-section, M_u is the elastic critical moment as given by Eq. (1.6) and the moment gradient factor C_b in the Canadian standard [1.2] is given by $C_b = C_{CAN} = 4M_{\max} \Big/ \sqrt{M_{\max}^2 + 4M_a^2 + 7M_b^2 + 4M_c^2} \leq 2.5$ in which M_{max} is the maximum moment within the unsupported length, and M_a, M_b, M_c are the moments at quarter-span, half-span, and three-quarter span, respectively. For Class 3 sections, the plastic moment M_p is replaced by the yield moment M_y.

The threshold span that separates the inelastic LTB and elastic LTB regions for a member with a doubly symmetric cross section is given in Clauses 13.5 and 13.6 of the Canadian standard [1.2] by setting $M_u = 0.67M_p$ for class 2 sections, (or $M_u = 0.67M_y$ for class 3 sections), which yields the following expression for threshold span L_t

$$L_t = \frac{\pi\sqrt{2EI_yEC_\omega}}{-EI_yGJ + \sqrt{\left(EI_yGJ\right)^2 + 4E^2I_yC_\omega\left(0.67M\right)^2}} \tag{1.7}$$

in which M depends on the section class and is equal to either the plastic moment $M_p = Z_xF_y$ or the yield moment is given $M_y = S_xF_y$, Z_x and S_x being the plastic and elastic section moduli. In a similar manner, by setting $M_u = 0.7S_{x\min}F_y$, the threshold span L_{ry} that separates of the inelastic LTB from the elastic LTB region for monosymmetric cross sections is obtained in the CISC commentary for Clause 13.6 of the Canadian standard [1.2] as

$$L_{ry} = \sqrt{\frac{2P\beta_x + Q + \sqrt{\left(2P\beta_x + Q\right)^2 + 4P^2R}}{2P^2}} \tag{1.8}$$

in which $P = \frac{1.4F_yS_{x,\min}}{C_b\pi^2EI_y}, Q = \frac{4GJ}{\pi^2EI_y}, R = \frac{4C_\omega}{I_y}$

As an illustrative example, consider a flexural member of W310x67 cross-section (flange width = $204\,mm$, web height = $306\,mm$, flange thickness = $14.6\,mm$, and a web thickness = $8.5\,mm$). Steel Young modulus is $E = 210GPa$ and its shear modulus is $G = 77GPa$. The member is subjected to uniform moments ($C_b = 1.00$). The flexural resistance (Fig. 1.3) is normalized with respect to the plastic moment M_p of the section.

For a laterally unbraced long-span beam subject to major axis bending (Fig. 1.3), the flexural resistance is governed by its elastic LTB resistance M_u as given by Eq. (1.6)c. Since this expression is based on a buckling eigenvalue analysis for a straight beam, the Canadian Standard implicitly omits the effect of initial out-of-straightness when computing a member's elastic LTB resistance.

Conversely, as presented in Fig. 1.3, in the inelastic LTB region, the resistance of the member is lower than that based on the elastic LTB resistance since it accounts for initial out-of-straightness and premature yielding due to residual stresses. Unlike Eq. (1.6)c, which omits the effect of initial out-of-straightness, Equation (1.6)b captures the effect of residual stresses and initial out-of-straightness when estimating the inelastic LTB resistance.

Yet, regardless of the member span, real members possess unavoidable initial out of straightness. In fact, the maximum allowable initial out-of-straightness amplitude δ for a wide flange section as given in [1.6] is specified as a fraction of the member span L as

$$\delta = \begin{cases} L/1000 & b \geq 150mm \\ L/500 & b < 150mm \end{cases} \tag{1.9}$$

in which b is the flange width. Also, according to [1.6] the permissible twist initial out-of-straightness for rectangular hollow structural members ranges from 1.3 to 3.1 mm per 1000 mm length, depending on the larger side dimension. Yet, no twist initial out-of-straightness threshold is specified for wide flange sections.

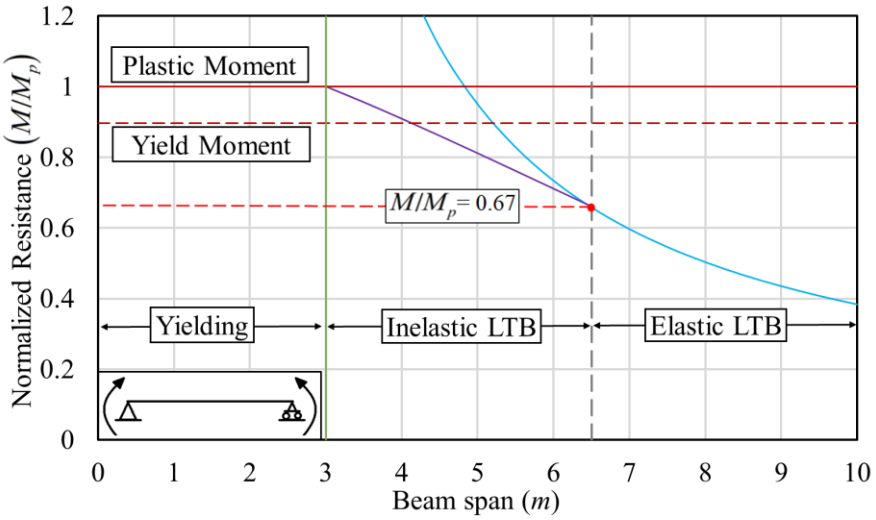

Fig. 1.3 Nominal flexural resistance for $W310\times67$ according to CAN/CSA S16-24

1.5.1 ANSI/AISC 360-22 Specifications

In a manner similar to the Canadian standards, the initial out-of-straightness amplitude in the American specifications [1.3] is specified as $\delta = L/1000$. The moment capacity, as in Table 1.2, M_n in the American specifications [1.3], similar to Canadian standards, is calculated based on the assumption of a perfectly straight beam without considering initial out-of-straightness.

$$M_r = \phi_b M_n \tag{1.10}$$

$$M_n = \begin{cases} M_P & L \le L_p & \text{short spans} & \text{plastic} \\ C_b\left[M_P - \left(M_P - 0.7F_yS_x\right)\left(\dfrac{L-L_P}{L_r-L_P}\right)\right] & L_p < L \le L_r & \text{intermediate spans} & \text{inelastic} \\ M_{cr} = S_xF_{cr} = C_bM_u & L > L_r & \text{long spans} & \text{elastic} \end{cases} \tag{1.11}$$

(1.11)a-c

in which the American specifications [1.3] moment gradient factor C_b is given by $C_b = 12.5M_{\max} \Big/ \left(2.5M_{\max} + 3M_{L/4} + 4M_{L/2} + 3M_{3L/4}\right)$ and the threshold spans L_r between the elastic and inelastic LTB regions and the threshold span L_p between the inelastic LTB and the yielding regions are given by

$$L_r = 1.95 r_{ts} \frac{E}{0.7F_y} \sqrt{\frac{Jc}{S_x h_0} + \sqrt{\left(\frac{Jc}{S_x h_0}\right)^2 + 6.76\left(\frac{0.7F_y}{E}\right)^2}} \qquad (1.12)\text{a-b}$$

$$L_p = 1.76 r_y \sqrt{E/F_y}$$

in which $r_{ts}^{\,2} = \sqrt{I_y C_w} \big/ S_x$, S_x being the elastic section modulus about the x axis, h_0 is the distance between the flange centroids, and the coefficient c takes the value $c = 1$ for doubly symmetric I-shapes, and F_{cr} is the critical stress given by

$$F_{cr} = \frac{M_{cr}}{A} = \frac{C_{US}\pi^2 E}{\left(L/r_{ts}\right)^2} \sqrt{1 + 0.078 \frac{Jc}{S_x h_0}\left(\frac{L_b}{r_{ts}}\right)^2} \qquad (1.13)$$

For monosymmetric sections, the limiting span L_r between the elastic and inelastic LTB regions is obtained by equating the critical moment M_{cr} in Eq.(1.2) for the case of uniform moment to $S_{x1}F_L$

$$M_{cr-US} = \frac{\pi^2 E I_y}{L_r^{\,2}} \left[\frac{\beta_x}{2} + \sqrt{\left(\frac{\beta_x}{2}\right)^2 + \frac{4}{4}\left(\frac{GJL_r^{\,2}}{\pi^2 E I_y} + \frac{C_w}{I_y}\right)} \right] = S_{xc} F_L \qquad (1.14)$$

in which $F_L = F_y - \alpha_1 F_y = F_y\left(1-0.3\right) = 0.7F_y$ is the yield stress F_y reduced for the presence of residual stress $\alpha_1 F_y = 0.3F_y$. By solving Eq. (1.14), one recovers the threshold span expression for L_r as provided in the American specifications [1.3] commentary clause for C-F4-4:

$$L_r = \frac{1.38E}{S_{xc}F_L}\sqrt{I_y J}\sqrt{\left[\frac{2.6F_L S_{xc}\beta_x}{EJ}+1\right]+0.192\pi^2\left(\frac{E}{F_L}\right)^2\frac{I_y J}{S_{xc}^{\ 2}}\sqrt{\left(\frac{2.6F_L S_{xc}\beta_x}{EJ}+1\right)^2+27\frac{C_\omega S_{xc}^{\ 2}F_L^{\ 2}}{I_y J^2 E^2}}} \tag{1.15}$$

Similar to Canadian standards [1.2], when $L \geq L_r$, the flexural resistance of the member (Fig. 1.4) is deemed to be governed by the elastic critical moment for a perfectly straight beam in the American specifications [1.3], which omits the effect of the member's initial out-of-straightness. This contrasts with the treatment of the Eurocode 3 [1.1] and the Australian Standard [1.4], both of which account for initial out-of-straightness, as discussed in the following sections.

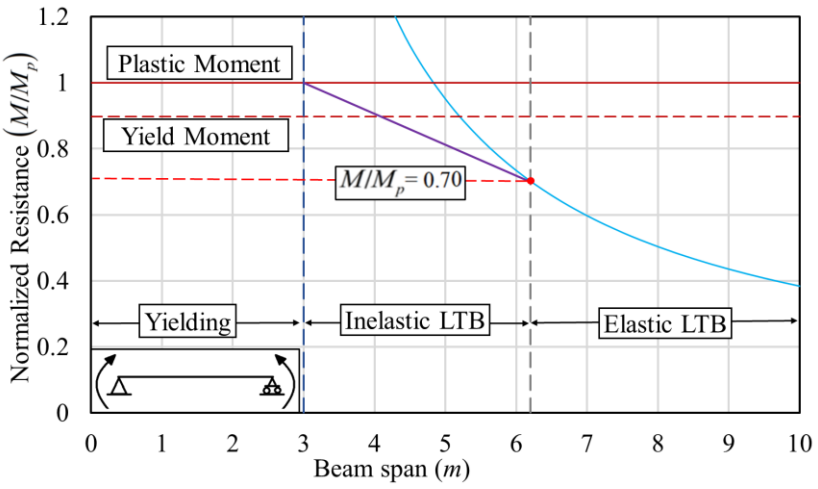

Fig. 1.4 Nominal flexural resistance for $W310\times67$ according to ANSI/AISC 360-22

1.5.2 Eurocode 3: Design of Steel Structures

The Eurocode 3 [1.1] guidelines for determining the flexural resistance of steel beams account for initial out-of-straightness across the entire range of spans. The flexural moment resistance of a laterally unbraced flexural member is given by

$$M_r = \chi W_y \frac{F_y}{\gamma_{M1}} \tag{1.16}$$

in which χ is a reduction factor that accounts for IOS and residual stresses, γ_{M1} a partial resistance factor, F_y is the yield stress, and W_y is the section modulus about the strong axis, which is taken as the plastic section modulus Z_x for classes 1 and 2 cross-sections, and S_x for class 3 sections, when the cross-section is doubly symmetric. For monosymmetric sections, the smaller section modulus $S_{x,\min}$ is taken. The reduction factor χ for LTB resistance as given by Clause 6.3.2.3 of the Eurocode 3 [1.1] is defined as

$$\chi = \frac{1}{\phi + \sqrt{\phi^2 - \lambda^2}} \tag{1.17}$$

in which ϕ is given by

$$\phi = \frac{1}{2}\left[1 + \alpha\left(\lambda_{LT} - 0.2\right) + {\lambda_{LT}}^2\right] \tag{1.18}$$

and λ_{LT} is the relative slenderness parameter defined by

$$\lambda_{LT} = \sqrt{\frac{W_y F_y}{M_{cr}}} \tag{1.19}$$

in which M_{cr} is the elastic critical moment. Since explicit expressions for M_{cr} are not provided in

the Eurocode, it can be determined from FEA analysis, local annexes, or Equations such as Eq. (1.1), where applicable. In Eq. (1.18), the imperfection factor α depends on the buckling curves (Table 8.2 and Figure 8.5 of Eurocode 3). Table 8.3 provides guidance on the selection of the buckling curve for flexural buckling. Table 1.2 presents the criteria for selecting lateral torsional buckling curves in general cases, as referenced in Table 8.6 of Eurocode 3.

Table 1.2 Selection of LTB curves for general cases in Eurocode 3 (Adapted from Table 8.6 of EN-1993-1-1-22

Cross-section		Limits	LTB curve
Rolled I- or H-sections	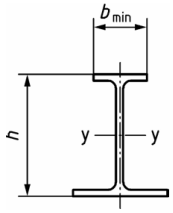	$h/b_{min} \leq 2.0$	a
		$h/b_{min} > 2.0$	b
Welded I-sections	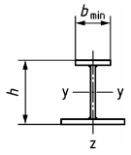	$h/b_{min} \leq 2.0$	c
		$h/b_{min} > 2.0$	d
Other sections (e.g. C-, U-, T-sections)	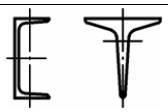	–	d

For doubly symmetric sections, the moment resistance M_r is given by

$$M_r = \chi_{LT} W_y \frac{F_y}{\gamma_{M1}} \tag{1.20}$$

and χ_{LT} is defined in Clause 8.3.2.3 (3) of the Eurocode 3 [1.1] as

$$\chi_{LT} = \frac{f_M}{\left(\phi_{LT} + \sqrt{\phi_{LT}^{\ 2} - f_M \bar{\lambda}_{LT}^{\ 2}}\right)} \leq 1.0 \tag{1.21}$$

in which

$$\phi_{LT} = 0.5\left[1 + f_M\left(\left(\bar{\lambda}_{LT}/\bar{\lambda}_y\right)^2 \alpha_{LT}\left(\bar{\lambda}_y - 0.2\right) + \bar{\lambda}_{LT}{}^2\right)\right] \tag{1.22}$$

and the relative slenderness parameter for lateral torsional buckling $\bar{\lambda}_{LT}$ is defined for Class 1 and 2 sections, as

$$\bar{\lambda}_{LT} = \sqrt{\frac{M_P}{M_{cr}}} \tag{1.23}$$

and f_M is a factor that accounts for the effect of the bending moment distribution as given in Table 1.3, which is based on Table 8.5 of the Eurocode 3 [1.1]. Also, in Eq. (1.22), the relative slenderness $\bar{\lambda}_y$ for the weak axis flexural buckling is given by Clause 8.3.1.2 as

$$\bar{\lambda}_y = \sqrt{N_{Rk}/N_{cr}} \tag{1.24}$$

and $N_{cry} = \pi^2 EI_y/L^2$ is the elastic flexural buckling resistance about the minor axis $N_{Rk} = AF_y$ is the characteristic compressive resistance (Clause 8.2.2.6), and A is the cross-sectional area. In Eq. (1.22), the imperfection factor for lateral torsional buckling α_{LT} for doubly symmetric sections is provided in Table 8.5 of the Eurocode 3 [1.1] (replicated as Table 1.3 herein) as a function of the manufacturing method (rolled versus welded), cross-section height-to-width ratio, and the ratio S_x / S_y of the section elastic moduli.

Table 1.3 Eurocode 3 recommended values $\alpha_{LT} \le 0.34$ for IOS factors α_{LT} (adapted from Table 8.5 of the Eurocode).

Cross-Section	height-to-width ratio		initial out-of-straightness factor α_{LT}
Rolled I-sections	$h/b > 1.2$	$t_f \le 40\,mm$	$0.12\sqrt{S_x/S_y}$ but
		$t_f > 40\,mm$	$0.16\sqrt{S_x/S_y}$ but $\alpha_{LT} \le 0.49$

	$h/b \le 1.2$	-	$0.16\sqrt{S_x/S_y}$ but $\alpha_{LT} \le 0.49$
Welded I-sections	$t_f \le 40\,mm$		$0.21\sqrt{S_x/S_y}$ but $\alpha_{LT} \le 0.64$
	$t_f > 40\,mm$		$0.25\sqrt{S_x/S_y}$ but $\alpha_{LT} \le 0.76$

As shown in Fig. 1.5, a beam with a $W310\times67$ cross-section spanning 6.5 m, subjected to uniform moment ($C_b = 1.00$, $f_M = 1.00$) with an imperfection factor $\alpha_{LT} = 0.22$ (for rolled sections) has a resistance that is 21% lower than that of an initially perfectly straight member.

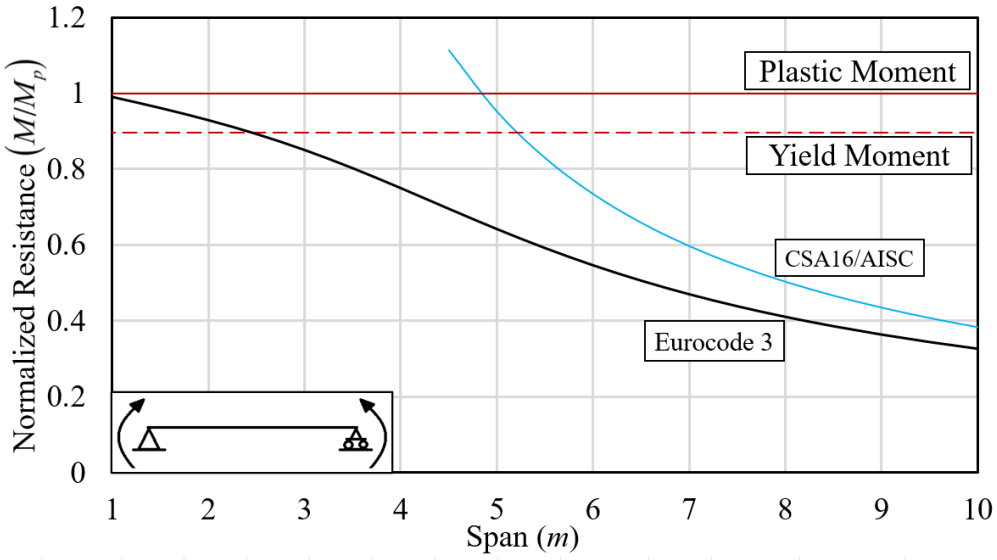

Fig. 1.5 Nominal flexural resistance for the $W310\times67$ beam according to Eurocode 3 ($\alpha_{LT} = 0.22$)

1.5.3 Australian Standards (AS 4100-2020)

According to Cl. 5.6.1.1(1) of the Australian Standard [1.4], the nominal moment capacity M_r for a laterally unbraced flexural member is

$$M_r = C_b\,\alpha_s\,M_s \le M_P \tag{1.25}$$

in which C_b is a moment modification factor which accounts for the effect of non-uniform moment distribution along the member, α_s is the slenderness reduction factor, which accounts for the reduction in strength due to lateral-torsional buckling (LTB), M_s is the nominal moment capacity of the section, calculated based on the yield stress and effective section modulus. The moment modification factor C_b (Cl. 5.6.1.1(1)) provided in the Australian standard is given by

$$C_b = \frac{1.7M_m^*}{\sqrt{\left(M_2^*\right)^2 + \left(M_3^*\right)^2 + \left(M_4^*\right)^2}} \leq 2.5 \tag{1.26}$$

in which M_m^* is the maximum moment within the unbraced segment and M_2^*, M_3^*, M_4^* are the moments at the quarter, midspan, and three-quarter points of the segment, respectively. The following sections outline the steps for determining the nominal moment capacity in accordance with the Australian Standard [1.4].

Nominal Section Capacity

The plasticity slenderness limit λ_{sp} and yield slenderness limit λ_{sy} for the section are those of the element (web or flange) with the larger slenderness to yield slenderness limit λ_e/λ_{ey} (Table 5.2 of the Australian Standard [1.4]). Given the section slenderness λ_s, the plasticity slenderness limit λ_{sp} and yield slenderness limit λ_{sy}, the effective section modulus Z_e is determined from:

$$Z_e = \begin{cases} \min\left(Z_x, 1.5S_x\right) & \lambda_s \leq \lambda_{sp} \quad \text{compact} \\ S_x + \left\{\dfrac{\left(\lambda_{sy} - \lambda_s\right)}{\left(\lambda_{sy} - \lambda_{sp}\right)}\left[\min\left(Z_x, 1.5S_x\right) - S_x\right]\right\} & \lambda_{sp} < \lambda_s \leq \lambda_{sy} \quad \text{non-compact where:} \\ S_x\left(\lambda_{sy}/\lambda_e\right)^2 & \lambda_{sy} < \lambda_s \quad \text{slender} \end{cases}$$

The nominal section moment capacity M_s (Cl. 5.2.1) is calculated by

$$M_s = Z_e F_y \tag{1.27}$$

in which F_y is the yield stress.

Reference Buckling moment

The reference buckling moment for LTB M_0 for a doubly symmetric section as given by Cl. 5.6.1.1(3) is

$$M_o = \frac{\pi}{L_e}\sqrt{EI_y GJ + \left(\frac{\pi E}{L_e}\right)^2 I_y C_w} \tag{1.28}$$

For a monosymmetric section, the elastic critical moment M_0 is given by

$$M_0 = \frac{\pi^2 EI_y}{L_e^{\,2}}\left[\frac{\beta_x}{2} + \sqrt{\left(\frac{\beta_x}{2}\right)^2 + \left(\frac{GJL_e^{\,2}}{\pi^2 EI_y} + \frac{C_w}{I_y}\right)}\right] \tag{1.29}$$

In the above two equations, L_e is the effective length of the member segment, determined as:

$$L_e = k_t k_l k_r L \tag{1.30}$$

in which k_t is a twist restraint factor given in Table 5.6.3(A), k_t is a load height factor given in Table 5.6.3(B) and k_r is the lateral rotation restraint factor given in Table 5.6.3(C) of the Australian Standard.

Slenderness Reduction Factor

The slenderness reduction factor α_s accounts for the reduction in strength due to lateral-torsional buckling (LTB) and is given by:

$$\alpha_s = 0.6\left[\sqrt{\left(M_s/M_0\right)^2 + 3} - \left(M_s/M_0\right)\right] \tag{1.31}$$

As presented in Fig. 1.6 for a 6.5 m span, the calculated resistance based on the Australian Standard is 26% lower than the elastic resistance of an initially perfectly straight beam, considering an initial out-of-straightness factor.

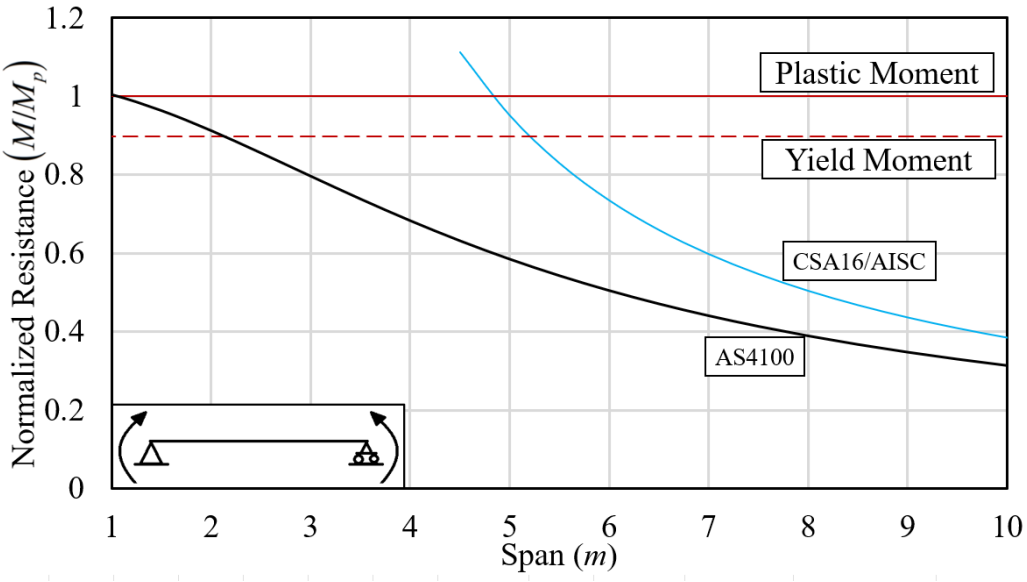

Fig. 1.6 Nominal flexural resistance for the $W310\times67$ **beam according to AS4100**

1.6 Objectives

The previous section discussed the differences in design philosophies among various standards for the lateral-torsional buckling strength of flexural members and illustrated the differences in their predictions. In this context, the present study aims to advance the understanding and prediction of the lateral-torsional buckling (LTB) behaviour of steel I-section members. Specifically, the present study seeks to:

1. Develop a geometrically nonlinear finite element formulation that predicts the response of long-span laterally unbraced flexural members with I-section subjected to major axis bending. The solution sought is to capture the detrimental effect of various IOS patterns (sweep, camber, twist, and combinations thereof) on the LTB resistance of the members.

2. Quantify the effect of IOS on the elastic LTB resistance of long-span, laterally unbraced members through a comprehensive parametric study. Parameters of interest include IOS patterns, amplitudes, load configurations, cross-sectional geometry, and member span. The results should be compared against the predictions of international design standards.

3. Propose simplified design equations for predicting the elastic LTB resistance of beams with different IOS characteristics, for the possible integration into the LTB provisions of North American design standards.

4. Extend the developed model to account for cross-sectional monosymmetric, load height effect, and residual stress effect, thus enabling the quantification of LTB resistance of long-span laterally unbraced monosymmetric flexural members under various loading types, load heights, IOS patterns and amplitudes.

Through these objectives, the research establishes a unified numerical and analytical framework that can assess the sensitivity of beam stability to imperfections, thereby contributing to the advancement of safe and economical design provisions for steel structures.

1.7 Dissertation Outline

The dissertation is organized into five chapters, each addressing a distinct aspect of the investigation. The dissertation was written in a paper-based format. Where appropriate, supplementary details of the investigations have been provided in the form of appendices.

Chapter 1: This introductory chapter provides the background of LTB in design provisions and outlines the objectives of the study.

Chapter 2 presents a geometric nonlinear formulation for doubly symmetric flexural members, based on the thin-walled beam theory. The validity of the model is established through comparisons against the results of thin-walled beam and shell models in ABAQUS. The chapter further quantifies the reduction in elastic LTB resistance due to various IOS patterns, amplitudes, and loading conditions.

In Chapter 3, the formulation developed in the previous chapter is adopted to generate a comprehensive parametric study to characterize the elastic LTB resistance, including the detrimental effect of IOS. The effects investigated include IOS patterns and amplitudes, as well as the combined effects of IOS, cross-sectional geometry, span, and load types. Regression models are subsequently developed to provide simplified design-oriented equations.

Chapter 4 extends the formulation developed in Chapter 2 by presenting a geometrically nonlinear finite element analysis for monosymmetric beams with initial out-of-straightness. The formulation captures the effect of load height and residual stresses. The enhanced model is numerically implemented and validated against ABAQUS shell element results, and it is employed to investigate key parameters influencing the LTB resistance of long-span monosymmetric members.

Chapter 5 summarizes the key findings and main conclusions of the study and offers recommendations for possible future research.

Finally, the appendices at the end of the dissertation provide relevant implementation details, algorithms, sensitivity analyses, additional verification studies, and sample calculations in support of the main body of the dissertation.

1.8 List of Symbols

a , n	Dimensionless regression coefficients
A	Cross-sectional area
b , t	Flange width and thickness
C_b	Moment gradient factor, moment modification factor
d , w	Web height and thickness
E	Young modulus
F_y	Yield strength
F_r	Compressive residual stresses at flange tips
f_M	Factor that accounts for the effect of the bending moment distribution
G	Shear modulus
I_y	Moment of inertia about the minor axis
I_x	Moment of inertia about the major axis
I_ω	Warping constant
J	Saint-Venant torsional constant
k_t	Twist restraint factor
k_t	Load height factor
k_t	Lateral rotation restraint factor
L	Span
L_t	Threshold span between inelastic and elastic LTB according to American specifications
L_{tc}	Threshold span between inelastic and elastic LTB according to Canadian standards
M_u	Critical moment for a perfectly straight beam
M_p	Plastic moment resistance
M_s	Nominal section moment capacity
M_0	Reference buckling moment for LTB
M	Bending moment obtained from the present FEA
N_{cry}	Elastic flexural buckling resistance about the minor axis
N_{Rk}	Characteristic compressive resistance
r^2	Coefficient of determination
S_x	Elastic section modulus about the major axis
u_b	Lateral displacement
Z_x	Plastic section modulus about the major axis
β_x	Monosymmetric parameter about the bending axis
α_s	Slenderness reduction factor

λ_{sp} Plastic χ ity slenderness limit

λ_{sy} Yield slenderness limit

$\overline{\lambda}_{LT}$ Slenderness parameter for lateral torsional buckling
Reduction factor for LTB resistance

δ Initial out-of-straightness amplitude

θ_b Twist angle

1.9 References

[1.1] EN-1993-1-1-22, *Eurocode 3: Design of Steel Structures-General Rules and Rules for Buildings*. Brussels, Belgium: European Committee of Standardization (CEN), 2020.

[1.2] CSA-Group, *CSA S16:24 Design and Construction of Steel Structures*, Tenth edit. CA: Canadian Institute of Steel Construction, 2024.

[1.3] ANSI/AISC 360-22, *Specification for structural steel buildings*. Chicago, IL: American Institute of Steel Construction (AISC), 2022.

[1.4] AS4100, *Steel structures*. Sydney: Standard Australia, 2020.

[1.5] ANDERSON JM and TRAHAIR NS, "Stability of Monosymmetric Beams and Cantilevers," *J. Struct. Div.*, vol. 98, no. 1, pp. 269–286, Jan. 1972, doi: 10.1061/JSDEAG.0003114.

[1.6] Canadian Institute of Steel Construction, "CISC, Handbook of steel construction, in: Canadian Institute of Steel Construction, 11th ed., Lakeside Group Inc, Ontario, Canada, 2017.," *Handb. Steel Constr.*, p. 1092, 2021.

Chapter 2: Geometrically Nonlinear Formulation for Doubly Symmetric Members with Initial out of Straightens

Abstract

Steel members possess unavoidable initial out-of-straightness (IOS), which can affect their lateral torsional buckling (LTB) resistance. Yet, when characterizing the LTB resistance of long-span members, current Canadian and American design standards omit IOS effects. Conversely, the Eurocode accounts for IOS effects for all spans based on Geometric and Material Nonlinear Analysis with Imperfections (GMNIA) philosophy. Within this context, the present study formulates a novel thin-walled beam finite element for the geometrically nonlinear analysis of steel members, that captures IOS effects. The formulation is then employed to characterize LTB resistance of long-span members expected to fail in an elastic LTB mode. For such members, the present study adopts a simplified first-yield criterion rather than the GMNIA approach and culminates in predictions comparable to those of the Eurocode and Australian standards. The effect of several IOS patterns and amplitudes are investigated, including pure lateral, pure twist, pure camber, lateral torsional, and biaxial IOS. Results reveal that pure twist IOS, a largely overlooked IOS pattern in previous studies, has the most detrimental impact on the LTB resistance of members.

Keywords

Nonlinear finite element analysis, Thin-walled members, Updated Lagrangian approach, Principle of virtual work, Initial out-of-straightness, I-sections. [1]

2.1 Introduction and Motivation

Structural steel members develop inevitable initial out-of-straightness (IOS) patterns throughout their manufacturing processes and transportation. The presence of IOS is recognized in structural construction practice (e.g., [2.1] and [2.2]), which provide limiting values for lateral IOS (sweep) and transverse IOS (camber) for steel members with I-sections as a fraction of the member span L such as $L/1000$ or $L/500$. The presence of IOS is expected to alter the lateral torsional buckling (LTB) resistance of such members compared to that of idealized, perfectly straight members. In the classical LTB treatment, members are assumed to be initially perfectly straight and to undergo sudden buckling once the applied loads attain a critical value as determined by an eigenvalue analysis. In contrast, members with IOS exhibit a gradual deformation pattern as the loads are increased and their full response can be determined only by a full geometric nonlinear analysis.

Present structural design standards take different approaches in addressing the effect of IOS on the elastic LTB resistance of flexural members. On one hand, the Canadian standards [2.3] and the American specifications [2.2] omit the effect of IOS in the elastic LTB failure region, by adopting the critical moment of a perfectly straight member. On the other hand, the Eurocode 3 [2.4] and Australian standards [2.5] are equipped with procedures that characterize the reduction in LTB

[1] This chapter has been submitted to an international journal for review and possible publication as Bhiri, M., Mohareb, M., and Attia, S., as Effects of Initial Out-of-Straightness on Lateral Torsional Buckling of I-Section Members

resistance owing to the presence of IOS. Within this context, the present study develops a thin-walled finite element for the geometrically nonlinear analysis of I-section members with IOS. The formulation is verified and subsequently used to trace the nonlinear equilibrium path for members with various IOS patterns under transversely and/or axially loading scenarios, up to the point of onset of yielding, while accounting for the presence of residual stresses. The study thus provides a basis to characterize the elastic LTB resistance for members with IOS and offers a means to assess the suitability of strength predictive procedures in existing design standards for various IOS patterns.

2.2 Literature Review

Thin-walled beams are known to undergo significant warping deformation as characterized by the theories of Vlasov [2.6] or Gjelsvik [2.7]. Several finite element solutions have been developed based on the kinematics of thin-walled beams. Such formulations were typically based on two-node elements with seven degrees of freedom (DOFs) per node, including a warping degree of freedom in addition to the six translational and rotational DOFs in solid beam elements. In a geometrically nonlinear context, such elements have been developed based on the Total Lagrangian (TL) approach or the Updated Lagrangian (UL) approach or the Co-Rotational (CR) approach. The relevant studies are summarized in Table 1 and are surveyed in the following.

Studies based on the TL approach include the work of Yang and Kuo [2.8] on horizontally curved beams and the shear deformable solution of Machado [2.9] who employed the Ritz method for the analysis of doubly symmetric sections. An extension of the work, Machado [2.10] incorporated IOS effects in composite beams. Mohri et al. [2.11] developed a TL solution for the geometrically nonlinear analysis of asymmetric beams, while Yang and Wang [2.12] extended the work to account for material nonlinearity.

Updated Lagrangian formulations include the work of Yang and McGuire [2.13] who developed a UL formulation for doubly symmetric straight members. Yang et al. [2.14] extended the work to horizontally curved members. Chan and Kitipornchai [2.15] and Al-Bermani and Kitipornchai [2.16] formulated solutions for asymmetric sections. Conci [2.17] formulated a solution for asymmetric sections that captures finite rotation effects. Using the external stiffness matrix approach of Yang and McGuire [2.13], Turkalj et al. [2.18] formulated a geometric nonlinear finite element for the analysis of non-colinear structures. Wang and Yang [2.19] formulated a shear deformable thin-walled finite element for monosymmetric members by introducing an additional midspan node in addition to end nodes. Lanc et al. [2.20] formulated a solution for the analysis of frame structures consisting of functionally graded thin-walled members with asymmetric cross sections. Liu et al. [2.21] developed a thin-walled finite element for members with asymmetric cross-sections. The formulation automated the computations of the Wagner coefficients and adopted the centroidal displacements as DOFs. Liu et al. [2.22] automated the computation of cross-sectional properties of asymmetric beam columns in the context of large deformation analysis. Based on the von Kármán strain approximation, Vo and Lee [2.23] developed a formulation for the analysis of open-section composite beams that captures local warping effects, and extended their work for box-section composite beams [2.24]. The effect of shear deformation was incorporated in the work of Vo and Lee [2.25]. Chen et al. [2.26] developed a formulation for the analysis of asymmetric sections that captures the span-wise variation of sectional properties along the member due to non-uniform torsion. Chen et al. [2.27] integrated the Modified Tangent Modulus approach, as proposed by Ziemian and McGuire [2.28], into the UL formulation to capture material nonlinear effects in members with asymmetric sections. Within the Generalized Beam Theory (GBT) framework, Silvestre and Camotim [2.29] studied the influence of global and

local IOS as well as sectional distortion on the post-buckling resistance of monosymmetric cold-formed beams. Their study was extended to include stiffened lipped channel columns [2.30] and beams [2.31].

A few studies adopted the CR approach for the geometric nonlinear analysis of thin-walled members. This includes the formulations of Lin and Hsiao [2.32] for doubly symmetric members and Lin and Hsiao [2.33] for monosymmetric members. Alsafadie et al. [2.34] incorporated shear deformation and plasticity effects in the analysis of monosymmetric members in a two-field mixed finite element. Du and Hajjar [2.35] and Rinchen et al. [2.36] adopted the CR approach for the elasto-plastic geometrically nonlinear analysis of asymmetric members. Chen et al. [2.37] incorporated thermal effects in the context of the CR approach for the analysis of asymmetric members.

Most IOS investigations adopted FEA models largely based on shell finite elements available in commercial software by assuming either lateral torsional IOS patterns based on the first buckling shape (e.g.,[2.38-2.48]) or pure lateral IOS (e.g., [2.41, 2.48-2.57]). Fewer studies considered pure twist IOS (e.g., [2.41, 2.48]), pure camber IOS (e.g., [2.58]), and combinations of IOS (e.g., [2.41]), although experimental measurements reported combinations of IOS in rolled members (e.g., [2.59]). Only a few thin-walled beam studies investigated IOS effects in rolled steel sections. Some of their limitations include omitting twist IOS effects, residual stress effects, being restricted to column members ([2.29], [2.30]) focussing exclusively on cold-formed members (e.g. [2.31]). In contrast, the present study develops a geometrically nonlinear thin-walled beam finite element that captures the effects of IOS and residual stresses in rolled sections. The formulation is then employed to investigate a wide range of IOS patterns, while adopting a first yield criterion to characterize the LTB resistance of long-span members.

Table 2.1 Comparative summary of geometric nonlinear formulations for thin-walled beam analysis

Author(s)	Material (1)	X-section (2)	Approach (3)	Effects Captured (4)						Additional aspects
				MN	SD	LH	IOS	RS	LW	
Yang and McGuire [2.13]	S	D	UL							Captures the rotational behaviour of joint moments in frames
Chan and Kitipornchai [2.15]	Al	A	UL			✓				Implements Arc-Length Method
Yang and Kuo [2.8]	S	D	TL							curved beams, geometric nonlinearity captured in variational principle but omitted in field equations.
Yang et al. [2.14]	S	D	UL							Finite element formulation for Curved-beams
Al-Bermani and Kitipornchai [2.16]	S	A	UL							Analysis of space frames, captures coupling between axial, lateral, and torsion deformation, omits warping
Conci [2.17]	S	M	UL							correction matrix to account for finite joint rotation in frames
Hsiao and Lin [2.33]	S, Al	M	CR			✓				Formulation retains third-order twist and curvature terms
Lin and Hsiao [2.32]	S, Al	D	CR			✓				Formulation retains third-order twist and curvature terms
Turkalj et al [2.18]	S	A	UL							Develops External Stiffness Matrix for joint equilibrium in non-collinear structures
Mohri et al. [2.11]	S	A	TL							Avoid moderate angle of twist simplifications
Machado [2.9]	S	D	TL		✓				✓	large angle of twist, Ritz method
Wang and Yang [2.19]	S	A	TL		✓					shear deformation Internal-node enhancement
Machado [2.10]	F	D	TL			✓	✓		✓	Captures large angles of twist, incorporates translational IOS, but does not capture twist IOS
Vo and Lee [2.23]	F	D	UL		✓	✓			✓	classical lamination theory, von Kármán geometric nonlinearity, open sections

Vo and Lee [2.24]	F	D	UL			✓			✓	Shear deformation, composite box beam sections
Yang and Wang [2.12]	S	A	TL	✓	✓					Avoids shear locking by introducing an intermediate node
Vo and Lee [2.25]	F	D	UL		✓	✓			✓	First-order shear deformation, von Kármán strain
Alsafadie et al. [2.34]	S	M	CR			✓				Two-field Hellinger–Reissner principle for large deformation, and elasto-plasticity.
Silvestre and Camotim [2.29]	S	M	UL				✓		✓	GBT, global and local IOS effects on cold-formed members
Silvestre and Camotim [2.30]	S	M	UL				✓		✓	GBT, stiffened lipped channel of cold-formed columns
Basaglia et al. [2.31]	S	A	UL				✓		✓	GBT, cold-formed I section columns and lipped channel columns and beams
Lanc et al. [2.20]	FG, S	A	UL			✓			✓	Functionally graded material, complex geometries, sandwich configurations.
Kim and Lee [2.60]	C-S, Al	M	UL			✓			✓	von Kármán-strain, FG sandwich I-beams, mono-symmetric cross-sections
Liu et al. [2.21]	S	A	UL			✓				Asymmetric, combining bifurcation and large-deflection analyses, LTB under eccentric loads
Liu et al. [2.22]	S	A	UL			✓	✓			axially loaded members with IOS
Rinchen et al. [2.36]	S	A	CR	✓		✓				Formulates the tangent matrix in local and global coordinates
Du and Hajjar [2.35]	S	A	CR	✓		✓				Devises a technique to avoid membrane-locking
Chen et al. [2.26]	S	A	UL			✓				Captures spanwise variation in sectional properties resulting from non-uniform torsion
Chen et al. [2.27]	S	A	UL	✓		✓		✓		material nonlinearity

Chen et al. [2.37]	S	A	CR			✓				beam-column element, material nonlinearity, and thermal effects
Present study	**S**	**D**	**UL**				✓	✓	✓	

(1) S=Steel, Al=Aluminum, F=FRP, C=Ceramic, FG=Functionally Graded

(2) D = doubly symmetric, M = monosymmetric, A = asymmetric.

(3) UL= updated Lagrangian, TL= total Lagrangian, CR= co-rotational

(4) MN= material nonlinearity, SD= shear deformation, LH= load height, IOS= initial out straightness, RS= residual stress, LW= local warping.

2.3 Assumptions

The FE formulation is based on the following assumptions:

1. The formulation follows the kinematics of Gjelsvik thin-walled beam theory, i.e.,
   1.1. The cross-section translates and twists as a rigid disk in its own plane,
   1.2. The shear strains within the middle surface are considered negligible,
   1.3. Straight lines normal to the undeformed middle surface remain straight and normal.
2. Rotations are assumed to be moderate, and strains are assumed to be small.
3. The nonlinear shear strain component is assumed negligible compared to the linear component for points offset from the middle surface.
4. The formulation is confined to doubly symmetric sections consisting of straight segments.
5. The coordinate system is chosen to satisfy the orthogonality conditions by adopting centroidal principal axes and selecting the pole and sectorial origin to coincide with the centroid.
6. The material is linearly elastic, isotropic, and follows the Saint–Venant–Kirchhoff model.
7. The formulation is first developed for a perfectly straight member in Section 2.4, and an IOS feature is subsequently added to the formulation in Section 2.5.

2.4 Formulation for Straight Member

2.4.1 Notation

Consider a thin-walled member in an undeformed state $C(0)$ at time $t = 0$. Under a specified load level at time t, the member is assumed to reach a known equilibrium state $C(t)$, such that the displacements of a generic point $B(z,s,n)$ within the member volume are characterized by longitudinal $\tilde{w}(z,s,n)$, tangential $\tilde{u}_t(z,s,n)$, and normal $\tilde{u}_n(z,s,n)$ displacements, defined from the undeformed state $C(0)$ to the deformed state $C(t)$, where z is a longitudinal coordinate, s is a tangential coordinate defined along the middle surface of the cross-section, n is a normal coordinate that denotes the offset of the point B from its projection B' on the middle surface, and the (z,s,n) coordinates form a right handed coordinate system (Fig. 2.1). The load level is then assumed to increase, such that a new unknown equilibrium state $C(t+\Delta t)$ is reached at time $t+\Delta t$. Under the load increase, the member undergoes additional unknown displacement increments ${}_t\tilde{w}(z,s,n)$, ${}_t\tilde{u}_t(z,s,n)$, and ${}_t\tilde{u}_n(z,s,n)$ from $C(t)$ to $C(t+\Delta t)$. In the framework of the updated Lagrangian formulation, the principle of virtual work is expressed as (e.g., [2.61])

$$ {}^{t+\Delta t}_{t}\overline{U} - {}^{t+\Delta t}_{t}\overline{R} = 0 \tag{2.1} $$

to characterize the displacement increments $({}_t\tilde{w}, {}_t\tilde{u}_t, {}_t\tilde{u}_n)$ by referring all field variables to the configuration at time t. In Eq. (2.1), ${}^{t+\Delta t}_{t}U$ is the internal work, ${}^{t+\Delta t}_{t}R$ is the external work, and overbars denote the variation of the argument functions. As a matter of convention, left subscripts denote the configuration to which the obj`ect is referred, and left superscripts denote configuration at which it is evaluated.

2.4.2 Thin-Walled Beam Kinematics

Consider a thin-walled member with a doubly symmetric cross-section (Assumption 4), in which the centroid O coincides with the shear center S (Fig. 2.1a). The displacement increments ${}_t\tilde{w}(z,s,n)$, ${}_t\tilde{u}_t(z,s,n)$, and ${}_t\tilde{u}_n(z,s,n)$ of a generic point $B(z,s,n)$ within the volume of the member can be expressed in terms of the displacement increments ${}_t\zeta(z)$, ${}_t\xi(z)$, and ${}_t\eta(z)$ of the shear center along the z, x, and y directions, and the angle of twist increment ${}_t\theta(z)$ of the cross-section (Assumption 1) through (e.g., [2.7])

$$
\begin{aligned}
{}_t\tilde{w} &= {}_t\zeta - \left[\partial_t\xi/\partial {}^t z\right] {}^t x - \left[\partial_t\eta/\partial {}^t z\right] {}^t y - \left[\partial_t\theta/\partial {}^t z\right] {}^t\omega \\
{}_t\tilde{u}_t &= {}_t\xi \cos {}^t\alpha + {}_t\eta \sin {}^t\alpha + {}_t\theta\left[{}^t h + {}^t n\right] \\
{}_t\tilde{u}_n &= {}_t\xi \sin {}^t\alpha - {}_t\eta \cos {}^t\alpha - {}_t\theta\, {}^t q
\end{aligned}
\qquad \text{(2.2)a-c}
$$

in which

$$
\left({}^t x, {}^t y, {}^t\omega\right) = \left({}^t\hat{x}, {}^t\hat{y}, {}^t\hat{\omega}\right) + \left({}^t\hat{\bar{x}}, {}^t\hat{\bar{y}}, {}^t\hat{\bar{\omega}}\right) \qquad \left({}^t\hat{\bar{x}}, {}^t\hat{\bar{y}}, {}^t\hat{\bar{\omega}}\right) = {}^t n\left(\sin {}^t\alpha, -\cos {}^t\alpha, -{}^t q\right) \qquad \text{(2.3)a-c}
$$

and ${}^t\hat{x}$ and ${}^t\hat{y}$ are the lateral and transverse coordinates, respectively, of point B' on the middle surface, ${}^t\alpha$ is the angle of the tangent to the middle surface at point B' relative to the positive direction of the ${}^t x$ axis, and ${}^t\hat{\omega} = \int_{s_0}^{{}^t s} {}^t h\, d\, {}^t s$ is the global warping function at point B' relative to the principal sectorial origin s_0, while ${}^t h$ and ${}^t q$ are the normal and tangential distances, respectively, from the shear center to point B' on the middle surface and are defined as

$$
\begin{aligned}
{}^t h &= {}^t\hat{x} \sin {}^t\alpha - {}^t\hat{y} \cos {}^t\alpha \\
{}^t q &= {}^t\hat{x} \cos {}^t\alpha + {}^t\hat{y} \sin {}^t\alpha
\end{aligned}
\qquad \text{(2.4)a-b}
$$

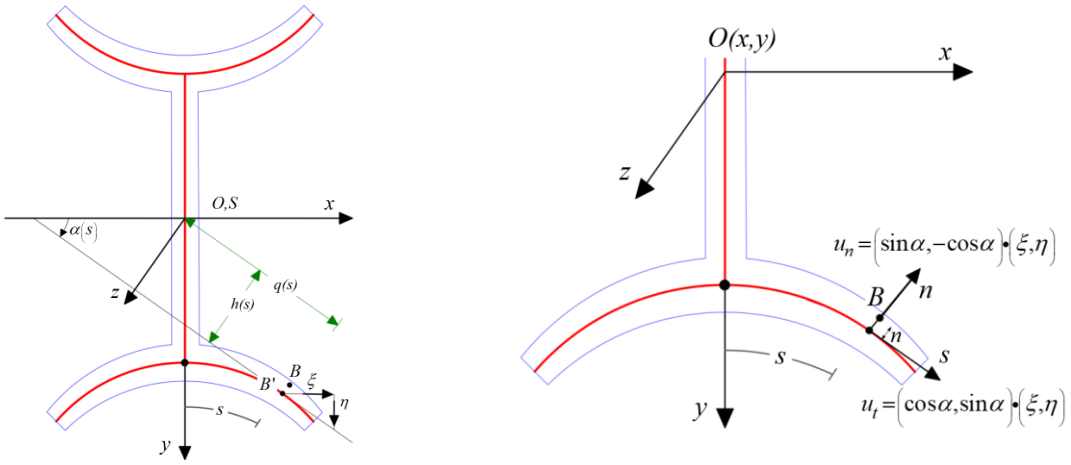

(a) (b)

Fig. 2.1 (a) Tangent and normal displacements (b) Point offset from contour in the normal direction and geometric parameters

2.4.3 Strain-Displacement Relations

The non-vanishing incremental components of the Green-Lagrange (GL) strain tensor ${}_t\varepsilon_{zz}$ and ${}_t\varepsilon_{zs}$ (Assumption 1) are expressed in terms of the longitudinal ${}_t\tilde{w}$, tangential ${}_t\tilde{u}_t$, and normal ${}_t\tilde{u}_n$ displacement increments as

$$ {}_t\varepsilon_{zz} = {}_t\varepsilon^L_{zz} + {}_t\varepsilon^N_{zz}, \qquad {}_t\varepsilon^L_{zz} = \frac{\partial_t \tilde{w}}{\partial^t z}, \qquad {}_t\varepsilon^N_{zz} = \frac{1}{2}\left[\left(\frac{\partial_t \tilde{w}}{\partial^t z}\right)^2 + \left(\frac{\partial_t \tilde{u}_t}{\partial^t z}\right)^2 + \left(\frac{\partial_t \tilde{u}_n}{\partial^t z}\right)^2\right] \tag{2.5}\text{a-c} $$

$$ {}_t\varepsilon_{zs} = {}_t\varepsilon^L_{zs} + {}_t\varepsilon^N_{zs}, \quad {}_t\varepsilon^L_{zs} = \frac{1}{2}\left(\frac{\partial_t \tilde{w}}{\partial^t s} + \frac{\partial_t \tilde{u}_t}{\partial^t z}\right), \quad {}_t\varepsilon^N_{zs} = \frac{1}{2}\left(\frac{\partial_t \tilde{w}}{\partial^t z}\frac{\partial_t \tilde{w}}{\partial^t s} + \frac{\partial_t \tilde{u}_t}{\partial^t z}\frac{\partial_t \tilde{u}_t}{\partial^t s} + \frac{\partial_t \tilde{u}_n}{\partial^t z}\frac{\partial_t \tilde{u}_n}{\partial^t s}\right) \tag{2.6}\text{a-c} $$

in which ${}_t\varepsilon^L_{zz}$ and ${}_t\varepsilon^L_{zs}$. are the linear components of the GL strain increments, while ${}_t\varepsilon^N_{zz}$ and ${}_t\varepsilon^N_{zs}$ are their nonlinear components. The term $\left(\partial_t \tilde{w}/\partial^t z\right)^2$ in Eq. (2.5)c is negligible compared to the linear strain increment ${}_t\varepsilon^L_{zz} = \left(\partial_t \tilde{w}/\partial^t z\right)$ (Assumption 2). Also, for a long-span beam, the nonlinear component of the shear strain ${}_t\varepsilon^N_{zs}$ is omitted (Assumption 3), yielding

$$ {}_t\varepsilon_{zz}^{L} = \frac{\partial_t \tilde{w}}{\partial^t z} \;,\; {}_t\varepsilon_{zz}^{N} \approx \frac{1}{2}\left[\left(\frac{\partial_t \tilde{u}_t}{\partial^t z}\right)^2 + \left(\frac{\partial_t \tilde{u}_n}{\partial^t z}\right)^2\right], {}_t\varepsilon_{zs}^{L} = \frac{1}{2}\left(\frac{\partial_t \tilde{w}}{\partial^t s} + \frac{\partial_t \tilde{u}_t}{\partial^t z}\right), \; {}_t\varepsilon_{zs}^{N} \approx 0 \qquad \text{(2.7)a-d} $$

2.4.4 Variational Formulation

The internal virtual work ${}^{t+\Delta t}_{t}\bar{U}$ due to the non-vanishing strains takes the form

$$ {}^{t+\Delta t}_{t}\bar{U} = \int_{{}^tV} \left({}^{t+\Delta t}_{t}\bar{\varepsilon}_{zz} \, {}^{t+\Delta t}_{t}S_{zz} + 2 \, {}^{t+\Delta t}_{t}\bar{\varepsilon}_{zs} \, {}^{t+\Delta t}_{t}S_{zs} \right) d^tV \qquad (2.8) $$

in which ${}^{t+\Delta t}_{t}S_{zz}$ and ${}^{t+\Delta t}_{t}S_{zs}$ are normal and shear components of the Second Piola-Kirchhoff (2PK) stress tensor, respectively, ${}^{t+\Delta t}_{t}\varepsilon_{zz}$ and ${}^{t+\Delta t}_{t}\varepsilon_{zs}$ are the corresponding components of the GL strain tensor, and the integration is performed over the deformed volume of the member at time t. For a linearly elastic isotropic material (Assumption 6), the Saint–Venant–Kirchhoff constitutive relations can be expressed as ${}^{t+\Delta t}_{t}S_{zz} = E \, {}^{t+\Delta t}_{t}\varepsilon_{zz}$ and ${}^{t+\Delta t}_{t}S_{zs} = G\left(2 \, {}^{t+\Delta t}_{t}\varepsilon_{zs}\right)$, in which E is the Young's modulus and G is the shear modulus, and the linearized form of the internal virtual work ${}^{t+\Delta t}_{t}\bar{U}$ (e.g., [2.61]) is expressed as

$$ {}^{t+\Delta t}_{t}\bar{U} \approx \int_{{}^tV} \left(E \, {}_t\bar{\varepsilon}_{zz}^{L} \, {}_t\varepsilon_{zz}^{L} + 4G \, {}_t\bar{\varepsilon}_{zs}^{L} \, {}_t\varepsilon_{zs}^{L} + {}_t\bar{\varepsilon}_{zz}^{L}\sigma_{zz} + 2 \, {}_t\bar{\varepsilon}_{zs}^{L}\sigma_{zs} + {}_t\bar{\varepsilon}_{zz}^{N}\sigma_{zz} + 2 \, {}_t\bar{\varepsilon}_{zs}^{N}\sigma_{zs} \right) d^tV \qquad (2.9) $$

in which $\sigma_{zz} = {}^{t}_{t}S_{zz}$ and $\sigma_{zs} = {}^{t}_{t}S_{zs}$ are normal and shear components of the Cauchy stress tensor, respectively. From Eqs. (2.9) and (2.7)d, by substituting into Eq. (2.1), the linearized virtual work principle for the member under consideration takes the form

$$ {}^{t+\Delta t}_{t}\bar{U}_1 + {}^{t+\Delta t}_{t}\bar{U}_2 + {}^{t+\Delta t}_{t}\bar{U}_3 = {}^{t+\Delta t}_{t}\bar{R} - {}^{t+\Delta t}_{t}\bar{U}_4 \qquad (2.10) $$

in which these quantities have been defined as

$$\left({}^{t+\Delta t}_{t}\bar{U}_1,\ {}^{t+\Delta t}_{t}\bar{U}_2,\ {}^{t+\Delta t}_{t}\bar{U}_3,\ {}^{t+\Delta t}_{t}\bar{U}_4\right)=\int_{{}^tV}\left[\left(E\,{}_t\varepsilon^L_{zz}\,{}_t\bar{\varepsilon}^L_{zz}\right),\left(4G\,{}_t\varepsilon^L_{zs}\,{}_t\bar{\varepsilon}^L_{zs}\right),\left({}_t\bar{\varepsilon}^N_{zz}\sigma_{zz}\right),\left({}_t\bar{\varepsilon}^L_{zz}\sigma_{zz}+2\,{}_t\bar{\varepsilon}^L_{zs}\sigma_{zs}\right)\right]d^tV \tag{2.11}$$

From Eq. (2.2), by substituting into Eq.(2.7), the GL strain components are expressed as

$$\begin{aligned}
&{}_t\varepsilon^L_{zz}={}_t\zeta'-{}_t\xi''\,{}^tx-{}_t\eta''\,{}^ty-{}_t\theta''\,{}^t\omega \qquad {}_t\varepsilon^L_{zs}={}_t\theta'\,{}^tn \qquad {}_t\varepsilon^N_{zs}\approx 0\\
&{}_t\varepsilon^N_{zz}=\frac{1}{2}\,{}_t\xi'^2+\frac{1}{2}\,{}_t\eta'^2+\frac{1}{2}\,{}_t\theta'^2\left({}^th^2+{}^tq^2+2{}^th{}^tn+{}^tn^2\right)-{}_t\xi'\,{}_t\theta'\,{}^ty+{}_t\eta'\,{}_t\theta'\,{}^tx
\end{aligned} \tag{2.12}\text{a-d}$$

in which all primes denote derivatives with respect to coordinate ${}^tz$. From Eqs. (2.12), by substituting into Eq. (2.10), performing all area integrals, and using the orthogonality conditions (Assumption 5) $\int_A\left(x,y,xy,\omega,\omega x,\omega y\right)dA=\left(0,0,0,0,0,0\right)$ where the approximation $A\approx {}^tA$ has been adopted (Assumption 1.1), one obtains

$$\begin{aligned}
&{}^{t+\Delta t}_{t}\bar{U}_1=E\int_{{}^tz=0}^{{}^tL}\left[A\,{}_t\bar{\zeta}'\,{}_t\zeta'+I_y\,{}_t\bar{\xi}''\,{}_t\xi''+I_x\,{}_t\bar{\eta}''\,{}_t\eta''+I_\omega\,{}_t\bar{\theta}''\,{}_t\theta''\right]d^tz\\
&{}^{t+\Delta t}_{t}\bar{U}_2=GJ\int_{{}^tz=0}^{{}^tL}{}_t\bar{\theta}'\,{}_t\theta' d^tz
\end{aligned}$$

$$\begin{aligned}
&{}^{t+\Delta t}_{t}\bar{U}_3=\int_{{}^tz=0}^{{}^tL}\left\langle {}_t\bar{\xi}' \quad {}_t\bar{\eta}' \quad {}_t\bar{\theta}'\right\rangle\begin{bmatrix} {}^tM_1 & 0 & {}^tM_3\\ 0 & {}^tM_1 & {}^tM_2\\ {}^tM_3 & {}^tM_2 & {}^tM_4\end{bmatrix}\begin{Bmatrix} {}_t\xi'\\ {}_t\eta'\\ {}_t\theta'\end{Bmatrix}d^tz\\
&{}^{t+\Delta t}_{t}\bar{U}_4=\int_{{}^tz=0}^{{}^tL}\left\langle {}_t\bar{\zeta}' \quad {}_t\bar{\xi}'' \quad {}_t\bar{\eta}'' \quad {}_t\bar{\theta}'' \quad {}_t\bar{\theta}'\right\rangle\left\langle {}^tM_1 \quad -{}^tM_1 \quad {}^tM_3 \quad {}^tM_5 \quad {}^tM_6\right\rangle^{\mathbf{T}}d^tz
\end{aligned} \tag{2.13}\text{a-d}$$

in which the cross-sectional properties $\left(A,I_y,I_x,I_\omega\right)=\int_A\left(1,x^2,y^2,\omega^2\right)dA$ and $J=\left(1/3\right)\int_{{}^ts}{}^te^3d^ts$, ${}^te$ being the thickness, and the stress resultants $\left({}^tM_1,{}^tM_2,{}^tM_3,{}^tM_4,{}^tM_5,{}^tM_6\right)=\int_A\left[\sigma_{zz},{}^tx\sigma_{zz},-{}^ty\sigma_{zz},\left({}^th^2+{}^tq^2+2{}^th{}^tn+{}^tn^2\right)\sigma_{zz},-{}^t\omega\sigma_{zz},4{}^tn\sigma_{zs}\right]dA$ have been defined.

2.4.5 Finite Element Formulation

A two-node finite element is developed with seven DOFs per node. The displacement field increments ${}_t\zeta$, ${}_t\xi$, ${}_t\eta$, and ${}_t\theta$ are related to the vectors of nodal DOFs at ends of the element (i.e., nodes *a* and *b*), i.e., ${}_t\boldsymbol{\zeta} = \langle {}_t\zeta_a \quad {}_t\zeta_b \rangle^{\mathbf{T}}$, ${}_t\boldsymbol{\xi} = \langle {}_t\xi_a \quad {}_t\xi'_a \quad {}_t\xi_b \quad {}_t\xi'_b \rangle^{\mathbf{T}}$, ${}_t\boldsymbol{\eta} = \langle {}_t\eta_a \quad {}_t\eta'_a \quad {}_t\eta_b \quad {}_t\eta'_b \rangle^{\mathbf{T}}$, and ${}_t\boldsymbol{\theta} = \langle {}_t\theta_a \quad {}_t\theta'_a \quad {}_t\theta_b \quad {}_t\theta'_b \rangle^{\mathbf{T}}$ through

$$ {}_t\zeta(z) = \mathbf{L}^{\mathbf{T}}(z)\,{}_t\boldsymbol{\zeta}, \quad {}_t\xi(z) = \mathbf{H_a}^{\mathbf{T}}(z)\,{}_t\boldsymbol{\xi}, \quad {}_t\eta(z) = \mathbf{H_b}^{\mathbf{T}}(z)\,{}_t\boldsymbol{\eta}, \quad {}_t\theta(z) = \mathbf{H_a}^{\mathbf{T}}(z)\,{}_t\boldsymbol{\theta} \qquad (2.14)\text{a-d} $$

in which

$$ \begin{aligned} \mathbf{L}^{\mathbf{T}} &= \langle \ (1-\varsigma) \quad \varsigma \ \rangle \\ \mathbf{H_a}^{\mathbf{T}} &= \langle 1-3\varsigma^2+2\varsigma^3 \ \vdots \ {}^tL\varsigma(1-\varsigma)^2 \ \vdots \ 3\varsigma^2-2\varsigma^3 \ \vdots \ {}^tL\varsigma^2(-1+\varsigma) \rangle \\ \mathbf{H_b}^{\mathbf{T}} &= \langle 1-3\varsigma^2+2\varsigma^3 \ \vdots \ -{}^tL\varsigma(1-\varsigma)^2 \ \vdots \ 3\varsigma^2-2\varsigma^3 \ \vdots \ -{}^tL\varsigma^2(-1+\varsigma) \rangle \end{aligned} \qquad (2.15)\text{a-c} $$

where $\varsigma = {}^tz/{}^tL$ is dimensionless finite length.

From Eqs. (2.14), by substituting into Eqs. (2.10) and (2.13), one obtains

$$ {}_t\bar{\mathbf{U}}^{\mathbf{T}}\left(\mathbf{K_E} + {}^t\mathbf{K_G}\right){}_t\mathbf{U} = {}_t\ \bar{\mathbf{U}}^{\mathbf{T}}\left({}^{(t+\Delta t)}\boldsymbol{\Delta}\mathbf{R} - {}^t\mathbf{F}\right)^{(2)} \qquad (2.16)\text{a-b} $$

---

(2) Appendix A outlines the algorithm for assembling and applying the geometric stiffness matrix and equivalent nodal forces. Appendix B provides a study on the number of integration points needed for convergence. Appendix C determines displacement- and force-based convergence tolerances. Appendix D provides a validation study for straight beams.

in which ${}_t\mathbf{U}^{\mathbf{T}} = \left\langle {}_t\boldsymbol{\zeta}^{\mathbf{T}} \;\vdots\; {}_t\boldsymbol{\xi}^{\mathbf{T}} \;\vdots\; {}_t\boldsymbol{\eta}^{\mathbf{T}} \;\vdots\; {}_t\boldsymbol{\theta}^{\mathbf{T}} \right\rangle$ is the vector of nodal displacements, ${}^{(t+\Delta t)}\mathbf{\Delta R}$ is the equivalent force vector from time t to $t+\Delta t$, and $\mathbf{K_E} = Diag\left[\mathbf{K_a}, \mathbf{K_b}, \mathbf{K_c}, \mathbf{K_d}\right]$ is the elastic stiffness matrix whose submatrices have been defined as

$$\begin{aligned} \mathbf{K_a} &= EA\int_{{}_tz=0}^{{}_tL} \left(\mathbf{L}'\right)\left(\mathbf{L}'\right)^{\mathbf{T}} d\,{}_tz \quad , \quad \mathbf{K_b} = EI_{yy}\int_{{}_tz=0}^{{}_tL} \left(\mathbf{H}_{\mathbf{a}}''\right)\left(\mathbf{H}_{\mathbf{a}}''\right)^{\mathbf{T}} d\,{}_tz \\ \mathbf{K_c} &= EI_{xx}\int_{{}_tz=0}^{{}_tL} \left(\mathbf{H}_{\mathbf{b}}''\right)\left(\mathbf{H}_{\mathbf{b}}''\right)^{\mathbf{T}} d\,{}_tz \quad , \quad \mathbf{K_d} = \int_{{}_tz=0}^{{}_tL} \left[EI_{\omega\omega}\left(\mathbf{H}_{\mathbf{a}}''\right)\left(\mathbf{H}_{\mathbf{a}}''\right)^{\mathbf{T}} + GJ\left(\mathbf{H}_{\mathbf{a}}'\right)\left(\mathbf{H}_{\mathbf{a}}'\right)^{\mathbf{T}}\right] d\,{}_tz \end{aligned} \tag{2.17a-f}$$

In Eq. (2.16), ${}^t\mathbf{K_G}$ is the geometric matrix at configuration $C(t)$ and takes the form

$${}^t\mathbf{K_G} = \begin{bmatrix} \mathbf{0} & \mathbf{0} & \mathbf{0} & \mathbf{0} \\ \mathbf{0} & {}^t\mathbf{K}_{\xi\xi} & \mathbf{0} & {}^t\mathbf{K}_{\xi\theta} \\ \mathbf{0} & \mathbf{0} & {}^t\mathbf{K}_{\eta\eta} & {}^t\mathbf{K}_{\eta\theta} \\ \mathbf{0} & {}^t\mathbf{K}_{\xi\theta} & {}^t\mathbf{K}_{\eta\theta}^{\mathbf{T}} & {}^t\mathbf{K}_{\theta\theta} \end{bmatrix} \tag{2.18}$$

and whose submatrices have been defined as

$$\begin{aligned} &{}^t\mathbf{K}_{\xi\xi} = \int_{{}_tz=0}^{{}_tL} {}^tM_1\left(\mathbf{H}_{\mathbf{a}}'\mathbf{H}_{\mathbf{a}}'^{\mathbf{T}}\right) d\,{}_tz,\ {}^t\mathbf{K}_{\eta\eta} = \int_{{}_tz=0}^{{}_tL} {}^tM_1\left(\mathbf{H}_{\mathbf{b}}'\mathbf{H}_{\mathbf{b}}'^{\mathbf{T}}\right) d\,{}_tz,\ {}^t\mathbf{K}_{\theta\theta} = \int_{{}_tz=0}^{{}_tL} {}^tM_4\left(\mathbf{H}_{\mathbf{a}}'\mathbf{H}_{\mathbf{a}}'^{\mathbf{T}}\right) d\,{}_tz \\ &{}^t\mathbf{K}_{\xi\theta} = \int_{{}_tz=0}^{{}_tL} {}^tM_3\left(\mathbf{H}_{\mathbf{a}}'\mathbf{H}_{\mathbf{a}}'^{\mathbf{T}}\right) d\,{}_tz,\ {}^t\mathbf{K}_{\eta\theta} = \int_{{}_tz=0}^{{}_tL} {}^tM_2\left(\mathbf{H}_{\mathbf{b}}'\mathbf{H}_{\mathbf{a}}'^{\mathbf{T}}\right) d\,{}_tz \end{aligned} \tag{2.19a-e}$$

Also, in Eq. (2.16), ${}^t\mathbf{F}^{\mathbf{T}} = \left\langle {}^t\mathbf{F}_{\zeta}^{\mathbf{T}} \quad {}^t\mathbf{F}_{\xi}^{\mathbf{T}} \quad {}^t\mathbf{F}_{\eta}^{\mathbf{T}} \quad {}^t\mathbf{F}_{\theta}^{\mathbf{T}} \right\rangle$ is the internal load vector at configuration $C(t)$ and whose sub-vectors have been defined as

$$\begin{aligned} &{}^t\mathbf{F}_{\zeta} = \int_{{}_tz=0}^{{}_tL} {}^tM_1\left(\mathbf{L}'\right) d\,{}_tz,\ {}^t\mathbf{F}_{\xi} = -\int_{{}_tz=0}^{{}_tL} {}^tM_2\left(\mathbf{H}_{\mathbf{a}}''\right) d\,{}_tz \\ &{}^t\mathbf{F}_{\eta} = \int_{{}_tz=0}^{{}_tL} {}^tM_3\left(\mathbf{H}_{\mathbf{b}}''\right) d\,{}_tz,\ {}^t\mathbf{F}_{\theta} = \int_{{}_tz=0}^{{}_tL} \left[{}^tM_5\left(\mathbf{H}_{\mathbf{a}}''\right) + {}^tM_6\left(\mathbf{H}_{\mathbf{a}}'\right)\right] d\,{}_tz \end{aligned} \tag{2.20a-c}$$

2.5 Incorporating Initial Out-of-Straightness Effects

In the most general case, a member is assumed to have a Lateral Initial Out-of-Straightness (L-IOS) $\xi_0(z)$, a Camber Initial Out-of-Straightness (C-IOS) $\eta_0(z)$, and a Twist Initial Out-of-Straightness (T-IOS) $\theta_0(z)$. Under loading, the member undergoes displacements $\left[\xi(z),\eta(z),\theta(z)\right]$ from its initially crooked position, such that the total out-of-straightness is $\left[\hat{\xi}(z),\hat{\eta}(z),\hat{\theta}(z)\right]=\left[\xi_0(z),\eta_0(z),\theta_0(z)\right]+\left[\xi(z),\eta(z),\theta(z)\right]$. The following section presents a technique to incorporates IOS into the FE formulation developed in Section 2.4 , in a manner akin to that introduced in [60], based on the multiplicative decomposition approach.

A member with IOS is assumed to have an undeformed configuration $C(0)$. Under loading, the member deforms to configuration $C(t)$. As the loading increases, the member continues to deform to configuration $C(t+\Delta t)$. Conventionally, the principle of virtual work for a perfectly straight member is referenced either to the undeformed configuration $C(0)$, as in the total Lagrangian approach, or to the previously deformed configuration $C(t)$, as in the updated Lagrangian approach. The present formulation adopts the updated Lagrangian approach to trace the nonlinear equilibrium path.

Under this approach, when applying the initial load increment (i.e., in going from $t=0$ to Δt_1) for a member with IOS, the corresponding conventional undeformed configuration $C(t=0)$ is relatively complex owing to the presence of IOS. In this case, it becomes expedient to avoid referring variables to configuration $C(t=0)$. This is achieved by introducing a fictitious, perfectly straight configuration $C(R)$ (excluding IOS) and adopting it as a reference configuration

(Fig. 2.2), thus exploiting the simplicity of the $C(R)$ geometry when evaluating the internal virtual work during the first loading increment (i.e., from $C(0)$ to $C(\Delta t_1)$). The corresponding internal virtual work expression takes the form

$$ {}^{\Delta t_1}_{R}\bar{U} = \int_{R_V} \left({}^{\Delta t_1}_{R}\bar{\boldsymbol{\varepsilon}}\, {}^{\Delta t_1}_{R}\mathbf{S} \right) d\, {}^{R}V \tag{2.21} $$

in which ${}^{\Delta t_1}_{R}\mathbf{S}$ is the 2PK stress tensor, ${}^{\Delta t_1}_{R}\bar{\boldsymbol{\varepsilon}}$ is the virtual GL strain tensor, both evaluated at $C(\Delta t_1)$ and referred to the fictitious reference configuration $C(R)$, and ${}^{R}V$ is the volume of the reference configuration (i.e., fictitious perfectly straight member). It is now required to determine the 2PK stress tensor ${}^{\Delta t_1}_{R}\mathbf{S}$ as the member undergoes from the undeformed configuration $C(0)$ to the deformed configuration $C(\Delta t_1)$, referred to configuration $C(R)$.

The GL strain tensor increment ${}_{\Delta t_1}\boldsymbol{\varepsilon} = {}^{\Delta t_1}_{0}\boldsymbol{\varepsilon}$ induced by the first load increment Δt_1, referenced to the undeformed configuration $C(0)$ is given by

$$ {}^{\Delta t_1}_{0}\boldsymbol{\varepsilon} = \frac{1}{2}\left[\mathbf{F}^{\mathbf{T}}_{(0,\Delta t_1)} \mathbf{F}_{(0,\Delta t_1)} - \mathbf{I} \right] \tag{2.22} $$

where $\mathbf{F}_{(0,\Delta t_1)}$ is the deformation gradient tensor relating a tangential vector $d\mathbf{X}^0$ in the undeformed configuration $C(0)$ to its image $d\mathbf{X}^{\Delta t_1}$ in the deformed configuration $C(\Delta t_1)$, and $\mathbf{I}$ is the identity tensor. The formulation adopts the Saint-Venant-Kirchhoff constitutive tensor (Assumption 6) ${}^{\Delta t_1}_{0}\mathbf{C} = \mathbf{C}$ to relate the 2PK stress tensor ${}^{\Delta t_1}_{0}\mathbf{S}$ to the GL strain tensor ${}^{\Delta t_1}_{0}\boldsymbol{\varepsilon}$ as expressed in Eq. (2.23) , i.e.,

$$ {}^{\Delta t_1}_{0}\mathbf{S} = \mathbf{C} : {}^{\Delta t_1}_{0}\boldsymbol{\varepsilon} = \frac{1}{2}\mathbf{C} : \left[\mathbf{F}^{\mathbf{T}}_{(0,\Delta t_1)} \mathbf{F}_{(0,\Delta t_1)} - \mathbf{I} \right] \tag{2.23} $$

The Cauchy stress tensor $\boldsymbol{\sigma}$ can be related to 2PK stress tensors ${}^{t+\Delta t}_{R}\mathbf{S}$ and ${}^{t+\Delta t}_{0}\mathbf{S}$ through

$$\boldsymbol{\sigma} = \left(1/\left\|\mathbf{F}_{(R,\Delta t_1)}\right\|\right)\mathbf{F}_{(R,\Delta t_1)}\,{}^{\Delta t_1}_{R}\mathbf{S}\mathbf{F}^{\mathbf{T}}_{(R,\Delta t_1)} \tag{2.24}$$

$$\boldsymbol{\sigma} = \left(1/\left\|\mathbf{F}_{(0,\Delta t_1)}\right\|\right)\mathbf{F}_{(0,\Delta t_1)}\,{}^{\Delta t_1}_{0}\mathbf{S}\mathbf{F}^{\mathbf{T}}_{(0,\Delta t_1)} \tag{2.25}$$

in which $\|\ \|$ denotes the determinant of the argument object. By equating Eqs. (2.24) and (2.25), one obtains

$${}^{\Delta t_1}_{R}\mathbf{S} = \left(\left\|\mathbf{F}_{(R,\Delta t_1)}\right\|/\left\|\mathbf{F}_{(0,\Delta t_1)}\right\|\right)\mathbf{F}^{-1}_{(R,\Delta t_1)}\mathbf{F}_{(0,\Delta t_1)}\,{}^{\Delta t_1}_{0}\mathbf{S}\mathbf{F}^{\mathbf{T}}_{(0,\Delta t_1)}\mathbf{F}^{-\mathbf{T}}_{(R,\Delta t_1)} \tag{2.26}$$

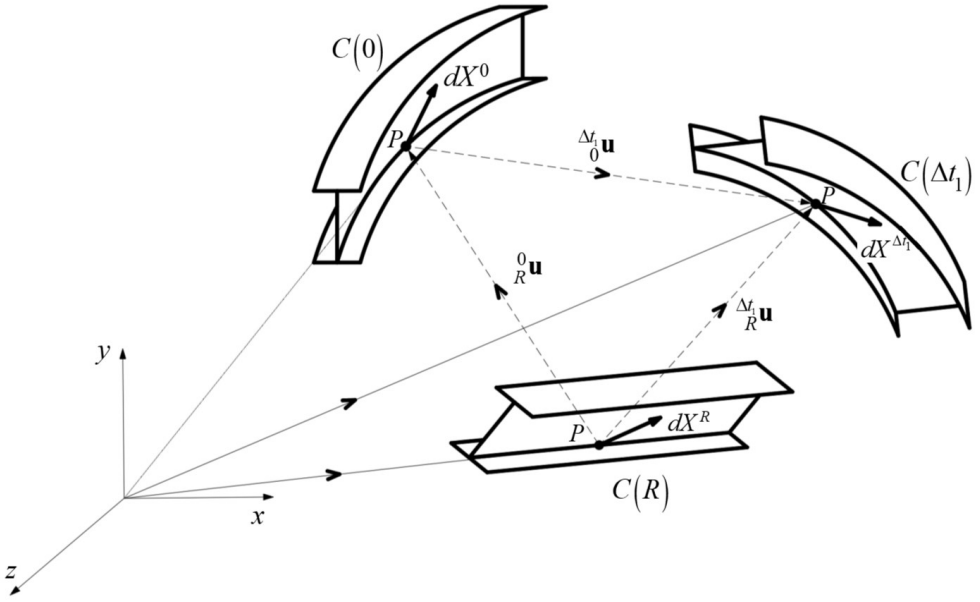

Fig. 2.2 Member at configuration C(0) with IOS deforming to first configuration C() referred to configuration C(R) with no IOS

The evaluation of ${}^{\Delta t_1}_{R}\mathbf{S}$ as defined in Eq. (2.26) requires the determination of deformation gradients $\mathbf{F}_{(R,\Delta t_1)}$ and $\mathbf{F}_{(0,\Delta t_1)}$. Under Cartesian coordinates, the deformation gradient tensor $\mathbf{F}_{(R,\Delta t_1)}$ can be expressed as

$$\mathbf{F}_{(R,\Delta t_1)}=\begin{bmatrix} 1+\dfrac{\partial \tilde{\tilde{w}}}{\partial^R z} & \dfrac{\partial \tilde{\tilde{w}}}{\partial^R s} & \dfrac{\partial \tilde{\tilde{w}}}{\partial^R n} \\ \dfrac{\partial \tilde{\tilde{u}}_t}{\partial^R z} & 1+\dfrac{\partial \tilde{\tilde{u}}_t}{\partial^R s} & \dfrac{\partial \tilde{\tilde{u}}_t}{\partial^R n} \\ \dfrac{\partial \tilde{\tilde{u}}_n}{\partial^R z} & \dfrac{\partial \tilde{\tilde{u}}_n}{\partial^R s} & 1+\dfrac{\partial \tilde{\tilde{u}}_n}{\partial^R n} \end{bmatrix} \tag{2.27}$$

where $\left(\tilde{\tilde{w}},\tilde{\tilde{u}}_t,\tilde{\tilde{u}}_n\right)=\left({}_0\tilde{w},{}_0\tilde{u}_t,{}_0\tilde{u}_n\right)+\left({}_R\tilde{w},{}_R\tilde{u}_t,{}_R\tilde{u}_n\right)$, in which $\left({}_0\tilde{w},{}_0\tilde{u}_t,{}_0\tilde{u}_n\right)$ is the incremental displacement vector from $C(0)$ to $C(\Delta t_1)$ and $\left[{}_R\tilde{w},{}_R\tilde{u}_t\left(\xi_0,\eta_0,\theta_0\right),{}_R\tilde{u}_n\left(\xi_0,\eta_0,\theta_0\right)\right]$ is the fictitious displacement vector from $C(R)$ to $C(0)$ (Fig. 2.2), which is determined based on the initial out-of-straightness $\left[\xi_0(z),\eta_0(z),\theta_0(z)\right]$. The deformation gradient tensor $\mathbf{F}_{(0,\Delta t_1)}$ appearing in Eq. (2.26) can be expressed in terms of the deformation gradient tensors $\mathbf{F}_{(R,\Delta t_1)}$ and $\mathbf{F}_{(R,0)}$ as described in the following. The tangential vectors $d\mathbf{X}^{\Delta t_1}$, $d\mathbf{X}^0$, and $d\mathbf{X}^R$ are inter-related through their respective deformation gradient tensors as

$$d\mathbf{X}^{\Delta t_1}=\mathbf{F}_{(0,\Delta t_1)}d\mathbf{X}^0,\quad d\mathbf{X}^0=\mathbf{F}_{(R,0)}d\mathbf{X}^R,\quad d\mathbf{X}^{\Delta t_1}=\mathbf{F}_{(R,\Delta t_1)}d\mathbf{X}^R \tag{2.28}$$a-c

in which $\mathbf{F}_{(a,b)}$ denotes the deformation gradient tensor corresponding to the deformation from $C(a)$ to $C(b)$. From Eq. (2.28)b, by substituting into Eq. (2.28)a, and subtracting from Eq. (2.28) c, one obtains the multiplicative identity of the deformation gradient tensors

$$\mathbf{F}_{(0,\Delta t_1)}=\mathbf{F}_{(R,\Delta t_1)}\mathbf{F}^{-1}_{(R,0)} \tag{2.29}$$

From Eq. (2.29), by substituting into Eq. (2.26), one obtains

$${}^{\Delta t_1}_{R}\mathbf{S}=\left\|\mathbf{F}_{(R,0)}\right\|\mathbf{F}^{-1}_{(R,0)}\left({}^{\Delta t_1}_{0}\mathbf{S}\right)\mathbf{F}^{-\mathbf{T}}_{(R,0)} \tag{2.30}$$

From Eqs.(2.29) and (2.23), by substituting into Eq. (2.30), one obtains

$$ {}^{\Delta t_1}_{R}\mathbf{S} = \frac{1}{2}\left\|\mathbf{F}_{(R,0)}\right\|\mathbf{F}^{-1}_{(R,0)}\left[\mathbf{C}:\left(\mathbf{F}^{-\mathbf{T}}_{(R,0)}\mathbf{F}^{\mathbf{T}}_{(R,\Delta t_1)}\mathbf{F}_{(R,\Delta t_1)}\mathbf{F}^{-1}_{(R,0)}-\mathbf{I}\right)\right]\mathbf{F}^{-\mathbf{T}}_{(R,0)} \tag{2.31} $$

Eq. (2.31) enables the computation of the 2PK stress tensor ${}^{\Delta t_1}_{R}\mathbf{S}$, evaluated at configuration $C(\Delta t_1)$ and referred to the configuration $C(R)$, given the deformation gradient tensors $\mathbf{F}_{(R,\Delta t_1)}$ as characterized by Eq. (2.27), and $\mathbf{F}_{(R,0)}$ which depends solely on the IOS pattern characterized by $\left[{}_R\tilde{w},\, {}_R\tilde{u}_t\left(\xi_0,\eta_0,\theta_0\right),\, {}_R\tilde{u}_n\left(\xi_0,\eta_0,\theta_0\right)\right]$.

2.6 Verification

2.6.1 Example 1: Beam with Lateral Torsional IOS

A reference member with an I-shaped cross-section has a span $L=5\ m$. Flange width is 100 mm and its thickness is 10 mm. Web height between flange mid-surface is 200 mm and its thickness is 10 mm. Cross-sectional properties are $A=4100\,mm^2$, I_x=$2.98\times10^7\ mm^4$, $I_y=1.68\times10^6\ mm^4$, $J=1.37\times10^5\ mm^4$, and $I_\omega=1.84\times10^{10}\ mm^6$. Material is steel with $E=200\,GPa$ and $G=77\,GPa$. Member ends are restrained against twist, transverse and lateral displacements at both ends, and a longitudinal restrain is provided at one end is i.e., $\zeta(0)=\xi(0)=\eta(0)=\theta(0)$ and $\xi(L)=\eta(L)=\theta(L)=0$. A midspan transverse point load V is applied at the shear center. The load is incrementally increased from 0 to $1.5V_{cr}$, V_{cr} being the load corresponding to the elastic critical moment of an initially straight member as determined from $M_u=\left(C_b\pi/L\right)\sqrt{EI_yGJ+\left(\pi E/L\right)^2 I_yI_\omega}=56.0\,kNm$, in which the moment gradient is taken as $C_b=1.35$, which corresponds to a critical load $V_{cr}=4M_u/L\simeq45.0\,kN$. The nonlinear response

of the member is sought by increasing the load from 0 to $1.5V_{cr} = 67.5\,kN$. The member is assumed to have a lateral torsional initial out-of-straightness (LT-IOS) based on the first mode shape $\left[\xi_0(z), \theta_0(z)\right]$ as determined from an eigenvalue buckling analysis for a perfectly straight member (i.e., an affine IOS pattern). The corresponding IOS is $u_{0T}(z) = \xi_0(z) + (d/2)\theta_0(z)$ at the top flange and $u_{0B}(z) = \xi_0(z) - (d/2)\theta_0(z)$ at the bottom flange, in which d is distance between flange centroids. In both the B31OS beam and S4 shell models, the IOS was applied using the *IMPERFECTION keyword in Abaqus, following an eigenvalue buckling analysis to extract the first buckling mode. The first eigenmode was then scaled so the target amplitude. Two LT-IOS magnitudes were investigated corresponding to an midspan IOS at the top flange of $u_{0T}(L/2) = L/1000$ and $u_{0T}(L/2) = L/400$.

Results of the present model are compared to the predictions of a S4 shell element model and a B31OS thin-walled beam model in Abaqus. The analysis is based on the generalized cross-section option of the B31OS model, which enables the user to directly enter cross-sectional properties. A mesh sensitivity analysis showed that the model based on the present formulation and the B31OS model attained convergence with 20 elements, while the S4 shell model attained convergence when 200 elements were taken along the span, 8 elements along the web height, and 6 elements along the flange width. Both the present and B31OS models have 147 DOFs, while the S4 model has 76,000 DOFs. Lateral restraints were provided along the entire web depth at both ends. Transverse restraints were imposed at the web–flange junctions at each end. Furthermore, longitudinal translation was restrained at one end to eliminate rigid-body motion.

For $u_{0T}(L/2) = L/400$, at a load level of $M/M_u = 1.5$, the present model predicts a midspan angle of twist within 2.0% of the prediction of the B31OS model and within 3.2% of the S4 model prediction. At $M/M_u = 1.0$, (Fig. 2.3a) shows that the midspan angle of twist for $u_{0T}(L/2) = L/1000$ is $0.021 rad$. This value significantly increases to $0.33 rad$ as the load level increases to $M/M_u = 1.5$. A similarly rapid increase is observed for the larger amplitude IOS $u_{0T}(L/2) = L/400$ i.e., the midspan angle of twist rapidly increases from $0.045 rad$ at $M/M_u = 1.0$ to $0.37 rad$ at $M/M_u = 1.5$. Similar observations are made for the lateral (Fig. 2.3b) and transverse (Fig. 2.3c) displacements. At $u_{0T}(L/2) = L/1000$, Fig. 2.4 shows that the peak normal stress attains $357 MPa$ at $M/M_u = 1.02$. For the larger IOS amplitude $u_{0T}(L/2) = L/400$, the peak normal stress significantly increases to $439 MPa$ at the same load level. For an IOS amplitude $u_{0T}(L/2) = L/400$, the peak compressive stress is observed to take place on the concave side of the top flange and to attain $439 MPa$ (Edge 4), while that on the convex side (Edge 3) is lower at $213 MPa$. The peak tensile stress of $334 MPa$ occurs on the convex side of the bottom flange (Edge 1), while that on concave side of the bottom flange (Edge 2) is $205 MPa$. In all cases, the displacements and stresses predicted agree well with both Abaqus models.

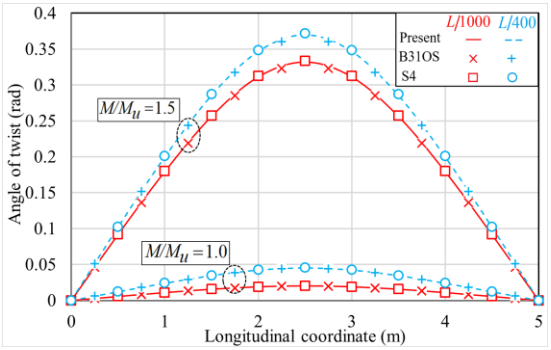

(a)

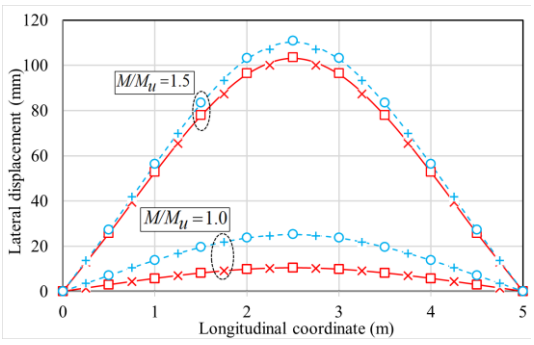

(b)

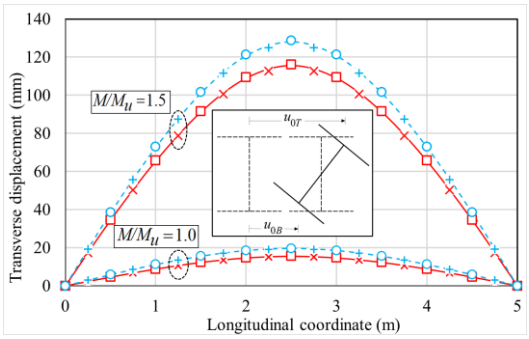

(c)

Fig. 2.3 Deformation for a beam with LT-IOS (a) Angle of twist (b) Lateral displacement, and (c) Transverse displacement.

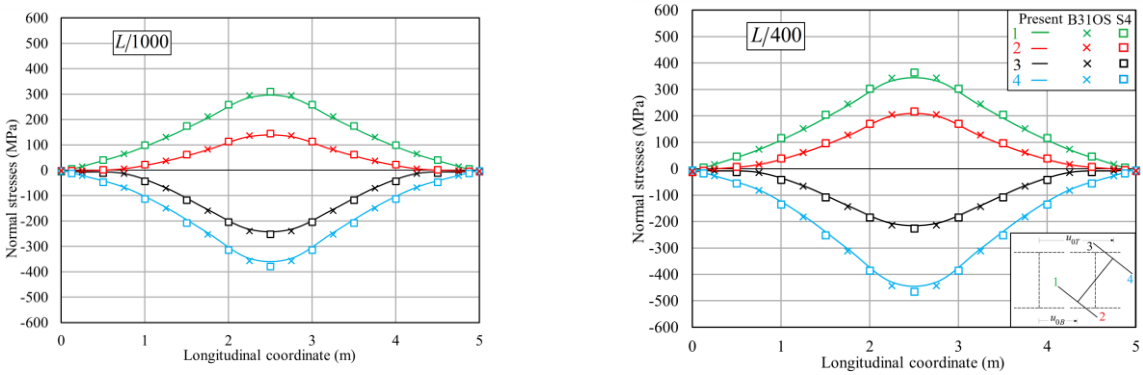

(a) (b)

Fig. 2.4 Normal stresses for a beam with LT-IOS for amplitudes of (a) $u_{0T} = L/1000$ and (b) $u_{0T} = L/400$ (moment ratio $M/M_u = 1.02$)

2.6.2 Example 2: Beam with Twist IOS

The reference member in Section 2.6.1 is assumed to have a T-IOS $\theta_0(z) = \gamma_\theta \sin(\pi z/L)$, with no L-IOS nor C-IOS, i.e., $\gamma_\xi = \gamma_\eta = 0$. For a section with a mid-surface depth d, an initial angle of twist $\theta_0(z)$ corresponds to an IOS $u_{0T}(z) = \gamma_\theta (d/2)\sin(\pi z/L)$ at the top flange, and $u_{0B}(z) = -\gamma_\theta (d/2)\sin(\pi z/L)$ at the bottom flange. Two amplitudes for the T-IOS are considered by setting the IOS of both flanges to $L/1000$ and $L/400$, which respectively correspond to peak T-IOS amplitudes of $\gamma_\theta = L/(500d)$ and $\gamma_\theta = L/(200d)$. It is noted that the T-IOS feature is not supported in the B31OS element implementation in Abaqus. As such, comparisons in this example are made solely against the S4 shell model predictions. As in Example 1, the member was subjected

to a midspan transverse force $V = 1.5V_{cr} = 67.5\ kN$. Fig. 2.5 shows close agreement between the angle-of-twist and normal-stress predictions from both models [3].

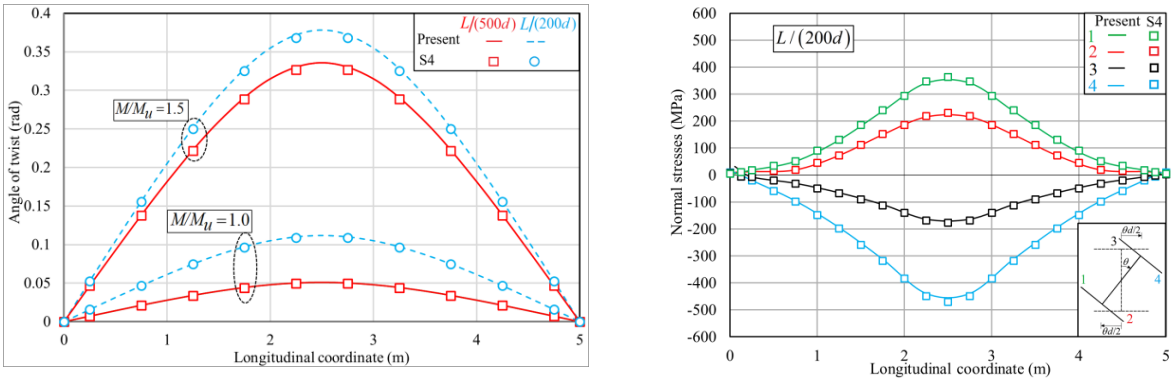

(a) (b)

Fig. 2.5 Response of a beam with T-IOS (a) Angle of twist (b) Normal stresses at $M/M_u = 0.96$ for $\gamma_\theta = L/(200d)$

2.7 Parametric Study

A reference beam with a W310x67 cross-section is considered. Cross-sectional properties are $A = 8434\,mm^2$, $I_x = 1.44\times10^8\ \text{mm}^4$, $I_y = 2.07\times10^7\ \text{mm}^4$, $J = 4.83\times10^5\ \text{mm}^4$, and $I_\omega = 4.39\times10^{11}\ \text{mm}^6$. Beam end restraints are $\zeta(0) = \xi(0) = \eta(0) = \theta(0) = \xi(L) = \eta(L) = \theta(L) = 0$. For a yield strength of $F_y = 350MPa$, the section meets compactness requirements (Class 2). Under the American specifications [2.2], the threshold span L_t delineating the inelastic LTB and elastic LTB regions is given by equating the elastic critical moment to 70% of the plastic moment, i.e., $M_u = (\pi/L_t)\sqrt{EI_yGJ + (\pi E/L_t)^2 I_y I_\omega} = 0.70M_p$, which yields $L_t = 6.4$

[3] Appendix E provides additional verifications for L-IOS, C-IOS for flexural members and L-IOS for axially loaded members

m. Four spans are considered in the elastic LTB range, $L = 7.00$, 8.75, 10.50, and 12.25 m which range from L/L_t =1.09 to 1.91. Three transverse loading cases were modelled per span: uniform moment (UM), midspan point loading (PL), and uniformly distributed loading (UD). Loads were assumed to act at the shear centre. For each loading case, three IOS patterns were investigated: L-IOS, T-IOS, and LT-IOS, each with two peak IOS amplitudes: $L/1000$ which represents the most severe scenario and $L/2000$ which is more reflective of a typical scenario, resulting in 4 spans $\times$ 3 loading cases $\times$ 3 IOS patterns $\times$ 2 IOS amplitudes = 72 cases. The elastic LTB resistance moment M_u is obtained from $M_u = \left(C_b \pi / L\right)\sqrt{EI_y GJ + \left(\pi E/L\right)^2 I_y I_\omega}$. In order to avoid approximations in moment gradient equations provided in the standards, the moment gradient factor C_b has been determined by conducting an eigenvalue buckling analysis based on the LTB-UO program [2.62] and computed by dividing the critical moment by the uniform critical moment, yielding $C_b = 1.0$ for UM, $C_b = 1.13$ for UD, and $C_b = 1.35$ for PL. A geometric nonlinear analysis was conducted up to the onset of first yield. In a manner consistent with the American specifications [2.2] provisions, it was assumed that the compressive residual stresses at the flange tips are $0.3F_y$, i.e., the first yield was deemed to have been attained when the compressive stress at one of the flange tips attains $0.7F_y$. The yield strength was taken as $F_y = 350MPa$.

2.7.1 Effects of IOS Pattern and Load Configurations

As a general observation in Fig. 2.6, the moment resistance values M based on the first yield for beams with IOS are consistently lower relative to the critical moment M_u of a perfectly straight beam. As the span ratio L/L_t increases, the moment ratio M/M_u increases, i.e., the effect of IOS becomes less pronounced.

Fig. 2.7 depicts the effect of loading type on the moment ratio. The lowest moment ratios correspond to members with midspan point loading, followed by uniformly distributed loading, whereas uniform moment loading corresponds to the highest moment ratios. Fig. 2.7c shows that the pure T-IOS pattern is more detrimental to the member resistance than the LT-IOS (Fig. 2.7b) which, in turn, is more detrimental than the pure L-IOS (Fig. 2.7a). For instance, for a span ratio L/L_t =1.09 with a T-IOS amplitude of $L/\gamma = 1000$, the moment ratio is 0.63 for midspan point loading, 0.68 for uniformly distributed loading, and 0.69 for uniform moments.

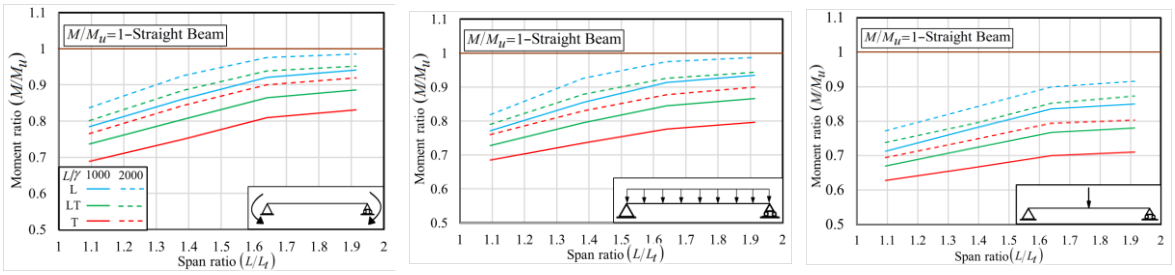

(a) (b) (c)

Fig. 2.6 Effect of IOS pattern on the moment ratio M/M_u : (a) Uniform moments, (b) Uniformly distributed load, and (c) midspan point load

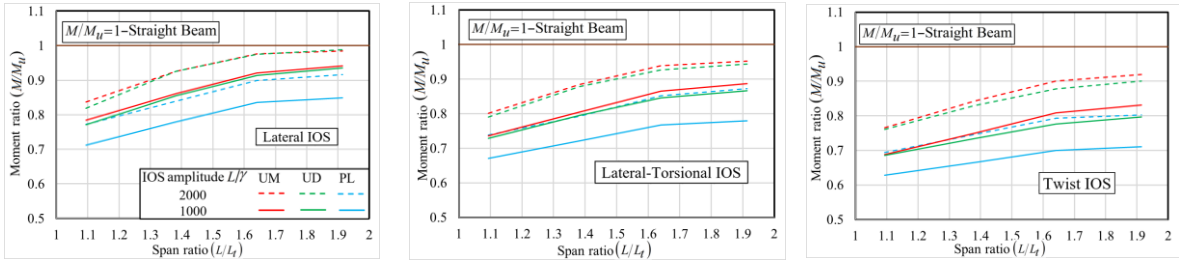

(a) (b) (c)

Fig. 2.7 Effect of loading type on moment ratio M/M_u for beams with: (a) Lateral IOS, (b) Lateral torsional IOS, and (c) Twist IOS

2.7.2 Effect of Biaxial IOS

A $7m$ span beam has a W310×67 cross-section with $(d, b, t_f, t_w) = (306, 204, 8.5, 14.6)mm$. The section meets Class 2 requirements for a yield strength of $F_y = 350MPa$. The beam is simply supported relative to transverse and lateral displacements and angle of twist and is subjected to

two equal end moments M . Ten IOS scenarios are considered: five uniaxial IOS involving only Camber and denoted **Cnn**, and five biaxial IOS involving combined Camber and Lateral IOS and denoted as **CnnL.** In the designations, the identifier **C** denotes a C-IOS characterized by $\eta_0(z) = \gamma_\eta \sin(\pi z/L)$, and **nn** denotes the camber amplitude $\gamma_\eta = \mathbf{nn}L/1000$ in which **nn** takes the values n =+2, +1, +0, -1, or -2. The identifier **nn** takes a positive sign when the member is upwardly cambered and a negative sign when the member is sagging. The presence of the letter **L** at the end of the designation indicates the presence of an additional L-IOS $\xi_0(z) = \gamma_\xi \sin(\pi z/L) = (L/2000)\sin(\pi z/L)$ and is taken as constant in all runs, while its absence indicates no L-IOS. For example, **C-2L** denotes a sagging member with an amplitude $\gamma_\eta = 2L/1000 = L/500$, combined with a L-IOS of an amplitude $\gamma_\xi = L/2000$. The applied end moments are gradually ramped up to the critical moment M_u for a perfectly straight beam, i.e., $M_u = (\pi/L)\sqrt{EI_yGJ + (\pi E/L)^2 (I_y I_\omega)} = 219.7kNm$. This moment level would correspond to a peak normal stress in a straight beam of $\sigma_u = (M_u/S_x) = 234\,MPa$, S_x being the elastic section modulus. For a yield stress F_y =350MPa, the elastic buckling stress σ_u in this example happens to coincide with the threshold stress $0.67F_y$ between elastic and inelastic LTB in the Canadian standards [2.3] and marginally inferior to the threshold $0.7F_y = 245MPa$ in the American specifications [2.2]. Fig. 2.8a-c shows the total COS for a load level of $M/M_u = 1$. For all scenarios considered, the predictions of the present solution, the B31OS model, and the shell FEA model are observed to be within 3%. In Fig. 2.8a, it can be verified that the difference between the total COS between any of the uniaxial IOS series Cnn and that of the perfectly straight beam (C+0) is nearly equal to the initial camber of each beam, i.e., the degree of camber/sag does not alter the

transverse deflection induced in the member. In contrast, the total COS for beams with biaxial IOS (the CnnL series) are observed to be lower than that of a straight beam (Fig. 2.8b). The figure shows that as the upward camber magnitude increases, the total COS increases, but the total LOS reduces (Fig. 2.8c).

Fig. 2.8d-e provide a comparison of the longitudinal stress distribution along the edges of C+2 and C+2L. In both cases, the moment was increased until a peak longitudinal stress of $0.67F_y$ is attained, which would yield the section in the presence of a residual stress at the section corners of $0.33F_y$. For C+2, the absence of L-IOS leads to a uniform stress distribution along the top and bottom edges (Fig. 2.8d), which corresponds to $M/M_u = 0.67S_xF_y/M_u = 1.0$. For C+2L, the stress distribution is non-uniform (Fig. 2.8e) and peaks at midspan. The corresponding end moment ratio thus reduces to $M/M_u = 0.838$. Fig. 2.8f provides a comparison of first yield moment ratios M/M_u for the five biaxial IOS scenarios. The moment ratio M/M_u attained is observed to range from 0.875 at C-2L down to 0.838 for C+2L, i.e., in the presence of L-IOS, positive cambering has a detrimental effect, while negative cambering (i.e., sag) has a favourable effect.

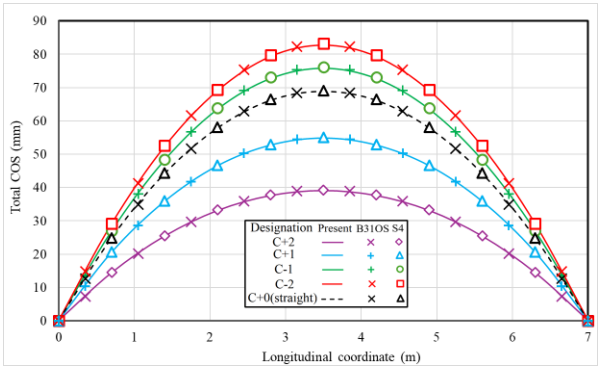

(a)

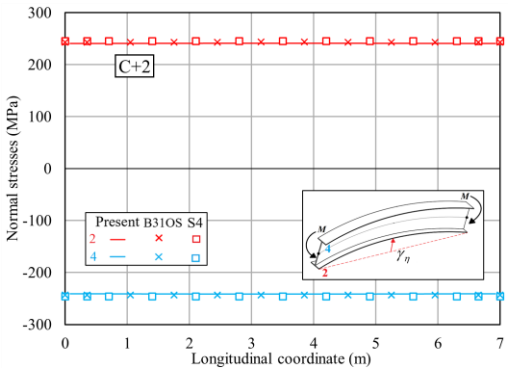

(d)

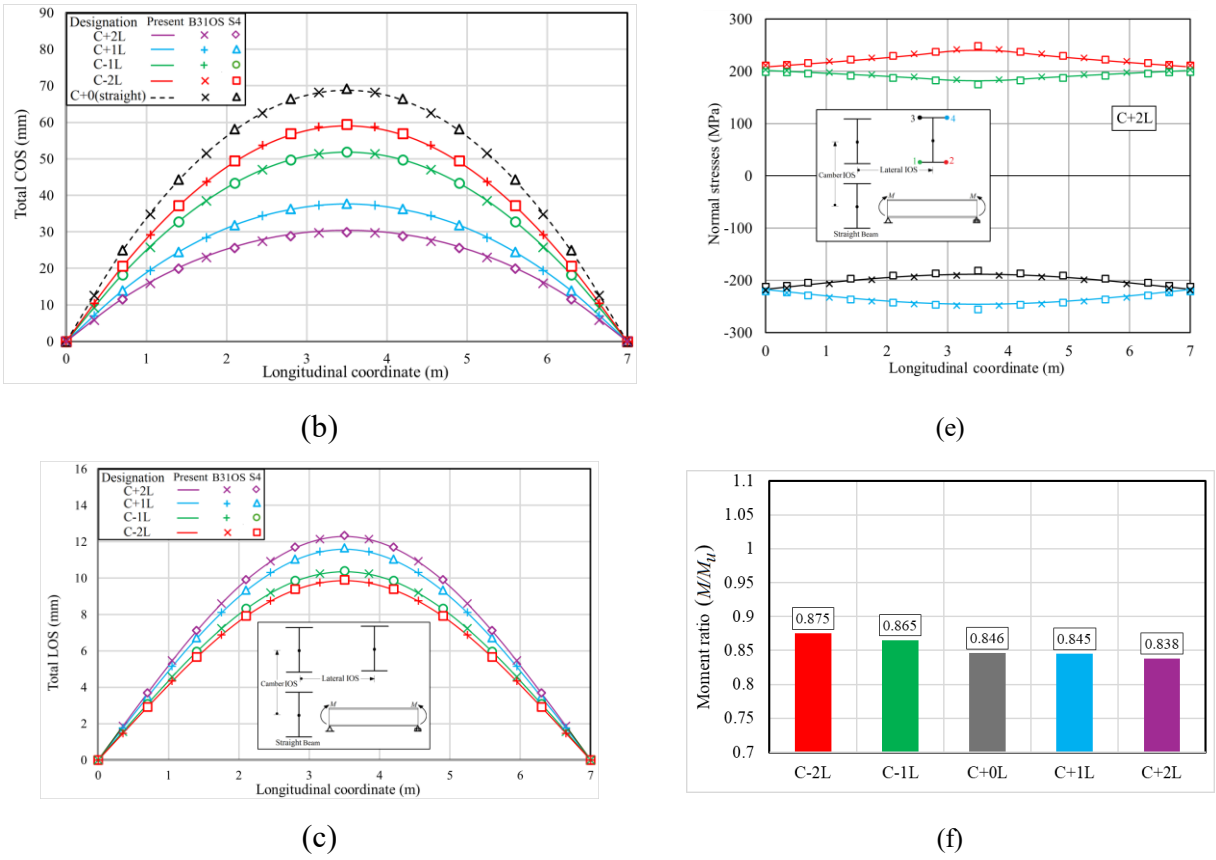

Fig. 2.8 Results for $M/M_u = 1$ (a) Total COS for uniaxial camber, (b) Total COS for biaxial IOS, (c) Total LOS for biaxial IOS, (d) Stresses at first yield for uniaxial camber, (e) Stresses at first yield for biaxial IOS, and (f) Comparison of first yield moment ratios for biaxial IOS

2.7.3 Comparison with Standard Predictions

The flexural resistance of the reference beam with various IOS and loading types is depicted in Fig. 2.9. The resistance is normalized with respect to the plastic moment M_p of the section. Under the American specifications [2.2], the elastic LTB resistance of a member with $L/L_t > 1$ is equal to the elastic buckling resistance $M_u = (C_b\pi/L)\sqrt{EI_yGJ + (\pi E/L)^2 I_y I_\omega}$ for a perfectly straight beam. The same resistance equation is essentially adopted in the Canadian standards [2.3] with the difference that the threshold span L_{tc} computed in Canadian standards [2.3] is obtained by equating the critical moment $M_u = (C_b\pi/L_{tc})\sqrt{EI_yGJ + (\pi E/L_{tc})^2 I_y I_\omega}$ to 67% of the plastic moment. For

the $W310\times67$ section considered, the threshold spans L_{tc} are 6.60, 7.22, and 8.30 m for uniform moment (UM), uniformly distributed load (UD), and midspan point load (PL), i.e., both standards omit the effect of IOS when characterizing the resistance of flexural members for $L/L_t > 1$ (or $L/L_{tc} > 1$). The normalized moment ratios versus L/L_t based on both standards are depicted in Fig. 2.9a-c along with the threshold spans $L = L_t$ and $L = L_{tc}$. Also shown on the figures are the normalized moment ratios based on the Eurocode 3 [2.4] and Australian standards [2.5] for comparison(4). Both standards account for IOS effects. Six IOS scenarios are considered, involving three IOS patterns: L-IOS, LT-IOS and T-IOS, and two amplitudes $L/2000$ and $L/1000$ per pattern. As a general observation, the Canadian and American equations overpredict the flexural resistance of the member compared to the predictions of the present model.

For UM (Fig. 2.9a), the Eurocode 3 [2.4] predictions are in a reasonable agreement with the normalized resistances for all types of IOS with an amplitude of $L/2000$. In contrast, the Australian standards [5] generally offer either accurate or conservative estimates of resistance for most patterns, except for the T-IOS configuration at an amplitude $L/1000$, where they tend to overpredict the moment resistance relative to the first yield moment as determined by the present model. For UD (Fig. 2.9b), the Eurocode 3 [2.4] predictions are generally consistent with the moment resistance predictions based on the first yield for all IOS patterns with an amplitude of $L/2000$. The Australian standards [2.5] provides a lower bound of the resistances for IOS patterns

(4) Appendix F provides the calculation steps for determining the lateral-torsional buckling resistance of a doubly symmetric beam as per Eurocode 3 and the Australian standards

with an amplitude of $L/2000$ and in a reasonable agreement for IOS patterns with an amplitude of $L/1000$, but slightly overestimates the resistance of T-IOS with an amplitude of $L/1000$.

For PL (Fig. 2.9c), the Eurocode 3 [2.4] overestimates the first yield moment for most IOS patterns and magnitudes considered, while the Australian standards [2.5] provides either a realistic or lower bound only for L-IOS and LT-IOS with an amplitude of $L/2000$. Both standards overestimate the resistance of members with T-IOS with an amplitude of $L/1000$.

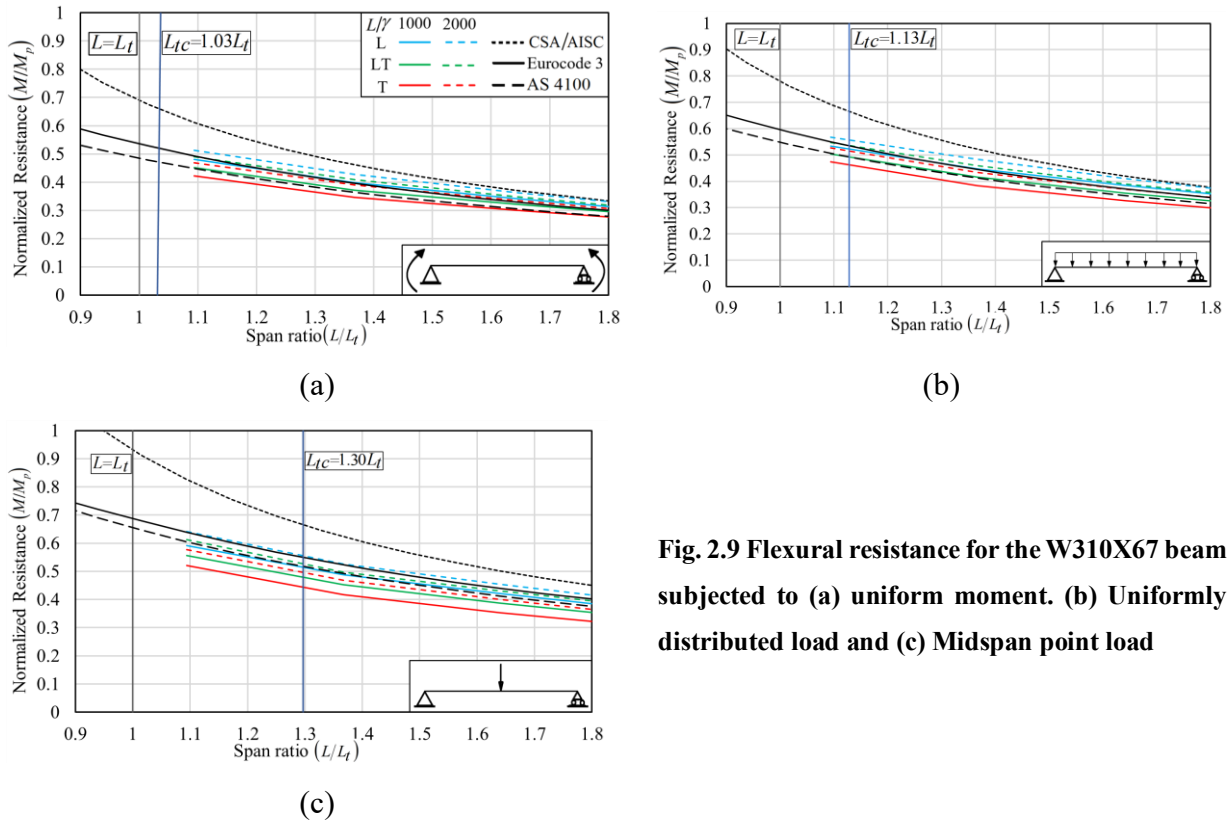

Fig. 2.9 Flexural resistance for the W310X67 beam subjected to (a) uniform moment. (b) Uniformly distributed load and (c) Midspan point load

2.8 Summary and Conclusions

The present study developed a geometrically nonlinear finite element formulation for thin-walled beams with L-IOS, T-IOS, C-IOS, and combinations thereof. The displacements and stresses predicted by the present model were found in agreement with those predicted by the S4 shell and B31OS thin-walled beam models in Abaqus. Using a first yield criterion while accounting for

typical residual stress patterns in rolled I sections, the present formulation was used to quantify the LTB resistance of long-span laterally unbraced members with various IOS patterns, magnitudes, and loading conditions. The main conclusions and observations are:

1. For the same IOS amplitude, T-IOS was found to have the most detrimental effect on the LTB resistance, followed by LT-IOS, and then by L-IOS, while pure C-IOS had virtually no impact on the LTB resistance of members bent about the major axis.
2. While pure C-IOS was found to have almost no impact on the LTB resistance of the member, when combined with L-IOS, it was observed to have a more detrimental effect in the case of upward camber on the LTB resistance than a downward camber (sag).
3. Based on the first yield criterion adopted in the present study, omitting the IOS effect in a manner consistent with the Canadian and American standards consistently overestimates the LTB resistance of the member.
4. For the most part, the Eurocode 3 procedure leads either to realistic or conservative estimates of the LTB resistance for members with L-IOS or LT-IOS with typical amplitudes of $L/2000$, but overestimates the resistances of members with the maximum admissible IOS amplitude of $L/1000$ when compared to the predictions of the present model based on the first yield criterion.
5. For the most part, the Australian standard equation leads to conservative estimates of the LTB resistance for members with typical IOS amplitudes of $L/2000$. Yet, in all loading cases examined, it was found to overestimate the LTB resistance of members with a T-IOS amplitude of $L/1000$.

List of Acronyms

L-IOS	Lateral Initial Out-of-straightness	Total LOS	Total Lateral Out-of-straightness
C-IOS	Camber Initial Out-of-Straightness	Total COS	Total Camber Out-of-straightness
T-IOS	Twist Initial Out-of-straightness	Total TOS	Total Twist Out-of-straightness

2.9 List of Symbols

${}^{t}A, A$	Cross-sectional area at the configuration $C(t)$
B'	Generic point lying on the middle surface
B	Generic point offset of the point B'
$C(a)$	The beam configuration at time a
C_b	Moment gradient factor
${}_0\mathbf{C}$	Saint-Venant-Kirchhoff constitutive tensor
d	Distance between flange centroids
$d\mathbf{X}^a$	Tangential vector in the deformed configuration $C(a)$
E	Young modulus
$\mathbf{F}_{(a,b)}$	Deformation gradient tensor corresponding to the deformation from $C(a)$ to $C(b)$
${}^{t}\mathbf{F}$	Internal force vector at time t
F_y	Yield stress of the cross-section
G	Shear modulus
$\mathbf{H}_a, \mathbf{H}_b$	Hermitian interpolation functions vectors
h	Normal distance from the shear center to point B' on the middle surface
I_y	Moment of inertia about the minor axis
I_x	Moment of inertia about the major axis
I_ω	Warping constant
J	Saint-Venant torsional constant
$\mathbf{K_E}$	Elastic stiffness matrix
$\mathbf{K_G}$	Geometric stiffness matrix at time t
$\mathbf{L}$	Vector of Lagrangian interpolation functions
${}^{t}L$	Length of the member at configuration $C(t)$
L_t	Threshold span L_t between inelastic and elastic LTB in American specifications
L_{tc}	Threshold span L_{tc} between the inelastic and elastic LTB in Canadian standards
M_i	The $C(\Delta t_1)$th stress resultant
M	Bending moment
M_u	Elastic critical moment of an initially straight member
M_p	Plastic moment
n	Coordinate normal to the contour
O	Cross section centroid
P	Applied axial force
P_{cr}	Critical load of an initially straight member
q	Tangential distance from the shear center to a point on the middle surface

${}_a^b R$	External work at configuration $C(b)$ referred to configuration $C(a)$
${}^{(t+\Delta t)}\mathbf{\Delta R}$	Equivalent force vector from time t to $t+\Delta t$
${}_a^b \mathbf{S}$	Second Piola-Kirchhoff stress tensor at configuration $C(b)$ referred to configuration $C(a)$
${}_a^b S_{zz}$, ${}_a^b S_{zs}$	Normal and shear components of the Second Piola-Kirchhoff stress tensor at configuration $C(b)$ referred to configuration $C(a)$
S_x	Elastic section modulus
S	Shear center
s	Tangential coordinate
s_o	Principal sectorial origin
t	Time
Δt	Time increment
Δt_1	Initial time increment
${}_a^b U$	Internal work at configuration $C(b)$ referred to configuration $C(a)$
${}_t\mathbf{U}$	Vector of total nodal displacement
${}_t\bar{\mathbf{U}}$	Vector of total virtual nodal displacement
$\tilde{u}_t$	Tangential displacement of a generic point from the undeformed state $C(0)$ to the Deformed state $C(t)$
${}_t\tilde{u}_t$	Tangential displacement increment of a generic point
$\tilde{u}_n$	Normal displacement of a generic point from the undeformed state $C(0)$ to the deformed state $C(t)$
${}_t\tilde{u}_n$	Normal displacement increment of a generic point
u_{0T}, u_{0B}	Lateral out-of-straightness LOS at the top and bottom flanges
${}^R V$	Member volume at the reference perfectly straight configuration
${}^t V$	Member volume at configuration $C(t)$
V	Applied transverse force
V_{cr}	Critical transverse buckling force corresponding to the elastic critical moment
$\tilde{w}$	Longitudinal displacement of a generic point from configuration $C(0)$ to $C(t)$
${}_t\tilde{w}$	Longitudinal displacement increments for a generic point
x	Lateral coordinate
y	Transverse coordinate
z	Longitudinal coordinate
α	Angle between tangent to the middle surface relative to the x axis
$(\gamma_\xi, \gamma_\eta, \gamma_\theta)$	Lateral, transverse, and twist initial out-of-straightness amplitudes
${}_t\varepsilon_{zz}$, ${}_t\varepsilon_{zs}$	Longitudinal and shear increments components of the Green-Lagrange strains
${}_t\varepsilon^L{}_{zz}$, ${}_t\varepsilon^N{}_{zz}$	Linear and nonlinear components of the longitudinal Green-Lagrange strain increment

${}_t\varepsilon^L{}_{zs}, {}_t\varepsilon^N{}_{zs}$	Shear linear and nonlinear increment components of the Green-Lagrange strain
${}^{t+\Delta t}_{\ t}\varepsilon_{zz}, {}^{t+\Delta t}_{\ t}\varepsilon_{zs}$	Normal and shear components of the Green-Lagrange strain tensor at configuration $C(t+\Delta t)$ referred to configuration $C(t)$
${}^b_a\boldsymbol{\varepsilon}$	Green-Lagrange strain tensor at configuration $C(b)$ referred to configuration $C(a)$
ξ_0, η_0, θ_0	L-IOS, C-IOS, and T-IOS
ς	Dimensionless longitudinal coordinate.
${}_t\boldsymbol{\zeta}, {}_t\boldsymbol{\xi}, {}_t\boldsymbol{\eta}, {}_t\boldsymbol{\theta}$	Vectors of nodal degrees of freedom
${}_t\zeta, {}_t\xi, {}_t\eta$	Shear center displacement increments along the z, x, and y directions
${}_t\theta$	Angle of twist increment
σ_{zz}, σ_{zs}	Normal and shear components of the Cauchy stress tensor
$\boldsymbol{\sigma}$	Cauchy stress tensor F
ω	Sectorial coordinate

2.10 References

[2.1] Canadian Institute of Steel Construction, "CISC, Handbook of steel construction, in: Canadian Institute of Steel Construction, 11th ed., Lakeside Group Inc, Ontario, Canada, 2017.," *Handb. Steel Constr.*, p. 1092, 2021.

[2.2] ANSI/AISC 360-22, *Specification for structural steel buildings*. Chicago, IL: American Institute of Steel Construction (AISC), 2022.

[2.3] CSA-Group, *CSA S16:24 Design and Construction of Steel Structures*, Tenth edit. CA: Canadian Institute of Steel Construction, 2024.

[2.4] EN-1993-1-1-22, *Eurocode 3: Design of Steel Structures-General Rules and Rules for Buildings*. Brussels, Belgium: European Committee of Standardization (CEN), 2020.

[2.5] AS4100, *Steel structures*. Sydney: Standard Australia, 2020.

[2.6] V. Z. Vlasov, *Thin walled elastic beams*, 2d ed. Jerusalem, Published for the National Science Foundation, Washington, D.C., by the Israel Program for Scientific Translations, available from the Office of Technical Services, U.S. Dept. of Commerce, Washington, 1961.

[2.7] A. Gjelsvik, *The Theory of Thin Walled Bars*. New York: John Wiley & Sons, 1981.

[2.8] Y. Yang and S. Kuo, "Effect of curvature on stability of curved beams," *J. Struct. Eng.*, vol. 113, no. 6, pp. 1185–1202, 1987, doi: 10.1061/(asce)0733-9445(1987)113:6(1185).

[2.9] S. P. Machado, "Non-linear buckling and postbuckling behavior of thin-walled beams considering shear deformation," *Int. J. Non. Linear. Mech.*, vol. 43, no. 5, pp. 345–365, 2008, doi: 10.1016/j.ijnonlinmec.2007.12.019.

[2.10] S. P. Machado, "Non-linear stability analysis of imperfect thin-walled composite beams," *Int. J. Non. Linear. Mech.*, vol. 45, no. 2, pp. 100–110, 2010, doi: 10.1016/j.ijnonlinmec.2009.09.006.

[2.11] F. Mohri, A. Eddinari, N. Damil, and M. Potier Ferry, "A beam finite element for non-linear analyses of thin-walled elements," *Thin-Walled Struct.*, vol. 46, no. 7–9, pp. 981–990, 2008, doi: 10.1016/j.tws.2008.01.028.

[2.12] Q. S. Yang and X. F. Wang, "A geometrical and physical nonlinear finite element model for spatial thin-walled beams with arbitrary section," *Sci. China Technol. Sci.*, vol. 53, no. 3, pp. 829–838, 2010, doi: 10.1007/s11431-010-0065-9.

[2.13] Y. Yang and W. McGuire, "Stiffness matrix for geometric nonlinear analysis," *J. Struct. Eng.*, vol. 112, no. 4, pp. 853–877, 1986, doi: 10.1061/(asce)0733-9445(1986)112:4(853).

[2.14] Y. Yang, S. Kuo, and Y. Cherng, "Curved beam elements for nonlinear analysis," *J. Eng. Mech.*, vol. 115, no. 4, pp. 840–855, 1989, doi: 10.1061/(asce)0733-9399(1989)115:4(840).

[2.15] S. L. Chan and S. Kitipornchai, "Geometric nonlinear analysis of asymmetric thin-walled beam-columns," *Eng. Struct.*, vol. 9, no. 4, pp. 243–254, 1987, doi: 10.1016/0141-0296(87)90023-X.

[2.16] B. F. G. A. Al-bermani and S. Kitipornchai, “Nonlinear analysis of thin-walled structures using least element/member,” vol. 116, no. 1, pp. 215–234, 1990.
[2.17] B. A. Conci, “Stiffness matrix for nonlinear analysis of thin-walled frames,” vol. 118, no. 9, pp. 1859–1875, 1993.
[2.18] G. Turkalj, J. Brnic, and J. Prpic-Orsic, “Large rotation analysis of elastic thin-walled beam-type structures using ESA approach,” *Comput. Struct.*, vol. 81, no. 18–19, pp. 1851–1864, 2003, doi: 10.1016/S0045-7949(03)00206-2.
[2.19] X. Wang and Q. Yang, “Geometrically nonlinear finite element model of spatial thin-walled beams with general open cross section,” *Acta Mech. Solida Sin.*, vol. 22, no. 1, pp. 64–72, 2009, doi: 10.1016/S0894-9166(09)60091-4.
[2.20] D. Lanc, G. Turkalj, T. P. Vo, and J. Brnić, “Nonlinear buckling behaviours of thin-walled functionally graded open section beams,” *Compos. Struct.*, vol. 152, pp. 829–839, 2016, doi: 10.1016/j.compstruct.2016.06.023.
[2.21] S. W. Liu, R. D. Ziemian, L. Chen, and S. L. Chan, “Bifurcation and large-deflection analyses of thin-walled beam-columns with non-symmetric open-sections,” *Thin-Walled Struct.*, vol. 132, no. 135, pp. 287–301, 2018, doi: 10.1016/j.tws.2018.07.044.
[2.22] S. W. Liu, W. L. Gao, and R. D. Ziemian, “Improved line-element formulations for the stability analysis of arbitrarily-shaped open-section beam-columns,” *Thin-Walled Struct.*, vol. 144, no. July, p. 106290, 2019, doi: 10.1016/j.tws.2019.106290.
[2.23] T. P. Vo and J. Lee, “Geometrically nonlinear analysis of thin-walled open-section composite beams,” *Comput. Struct.*, vol. 88, no. 5–6, pp. 347–356, 2010, doi: 10.1016/j.compstruc.2009.11.007.
[2.24] T. P. Vo and J. Lee, “Geometrically nonlinear theory of thin-walled composite box beams using shear-deformable beam theory,” *Int. J. Mech. Sci.*, vol. 52, no. 1, pp. 65–74, 2010, doi: 10.1016/j.ijmecsci.2009.10.005.
[2.25] T. P. Vo and J. Lee, “Geometrical nonlinear analysis of thin-walled composite beams using finite element method based on first order shear deformation theory,” *Arch. Appl. Mech.*, vol. 81, no. 4, pp. 419–435, 2011, doi: 10.1007/s00419-010-0407-x.
[2.26] L. Chen, A. H. A. Abdelrahman, S.-W. Liu, R. D. Ziemian, and S.-L. Chan, “Gaussian beam–column element formulation for large-deflection analysis of steel members with open sections subjected to torsion,” *J. Struct. Eng.*, vol. 147, no. 12, pp. 1–14, 2021, doi: 10.1061/(asce)st.1943-541x.0003185.
[2.27] L. Chen, W. L. Gao, S. W. Liu, R. D. Ziemian, and S. L. Chan, “Geometric and material nonlinear analysis of steel members with nonsymmetric sections,” *J. Constr. Steel Res.*, vol. 198, Nov. 2022, doi: 10.1016/j.jcsr.2022.107537.
[2.28] R. D. Ziemian and W. McGuire, “Modified Tangent Modulus Approach, A Contribution to Plastic Hinge Analysis,” *J. Struct. Eng.*, vol. 128, no. 10, pp. 1301–1307, 2002, doi: 10.1061/(asce)0733-9445(2002)128:10(1301).
[2.29] N. Silvestre and D. Camotim, “NONLINEAR GENERALIZED BEAM THEORY FOR COLD-FORMED STEEL MEMBERS,” *Int. J. Struct. Stab. Dyn.*, vol. 3, no. 4, pp. 461–490, 2003.
[2.30] N. Silvestre, D. Camotim, and M. Asce, “Local-Plate and Distortional Postbuckling Behavior of Cold-Formed Steel Lipped Channel Columns with,” *J. Struct. Eng. (New York, N.Y.)*, vol. 132, no. 4, pp. 529–540, 2006, doi: 10.1061/(ASCE)0733-9445(2006)132.
[2.31] C. Basaglia, D. Camotim, and N. Silvestre, “Non-linear GBT formulation for open-section thin-walled members with arbitrary support conditions,” *Comput. Struct.*, vol. 89, no. 21–22, pp. 1906–1919, 2011, doi: 10.1016/j.compstruc.2011.07.001.
[2.32] W. Y. Lin and K. M. Hsiao, “Co-rotational formulation for geometric nonlinear analysis of doubly symmetric thin-walled beams,” *Comput. Methods Appl. Mech. Eng.*, vol. 190, no. 45, pp. 6023–6052, 2001, doi: 10.1016/S0045-7825(01)00212-2.
[2.33] K. M. Hsiao and W. Y. Lin, “A co-rotational formulation for thin-walled beams with monosymmetric open section,” *Methods*, vol. 190, pp. 1163–1185, 2000.
[2.34] R. Alsafadie, M. Hjiaj, and J. M. Battini, “Three-dimensional formulation of a mixed corotational thin-walled beam element incorporating shear and warping deformation,” *Thin-Walled Struct.*, vol. 49, no. 4, pp. 523–533, 2011, doi: 10.1016/j.tws.2010.12.002.
[2.35] X. Du and J. Hajjar, “Three-dimensional nonlinear displacement-based beam element for members with angle and tee sections,” *Eng. Struct.*, vol. 239, no. March, p. 112239, 2021, doi: 10.1016/j.engstruct.2021.112239.
[2.36] Rinchen, G. J. Hancock, and K. J. R. Rasmussen, “Geometric and material nonlinear analysis of thin-walled members with arbitrary open cross-section,” *Thin-Walled Struct.*, vol. 153, no. May, p. 106783, 2020, doi: 10.1016/j.tws.2020.106783.

[2.37] L. Chen, S. W. Liu, and S. L. Chan, “Geometrically nonlinear analysis of steel structures with nonsymmetric sections under elevated temperatures,” *J. Constr. Steel Res.*, vol. 211, no. April, p. 108205, 2023, doi: 10.1016/j.jcsr.2023.108205.
[2.38] J. Szalai and F. Papp, “On the theoretical background of the generalization of Ayrton-Perry type resistance formulas,” *J. Constr. Steel Res.*, vol. 66, no. 5, pp. 670–679, 2010, doi: 10.1016/j.jcsr.2009.12.013.
[2.39] A. Agüero, F. J. Pallarés, and L. Pallarés, “Equivalent geometric imperfection definition in steel structures sensitive to lateral torsional buckling due to bending moment,” *Eng. Struct.*, vol. 96, pp. 41–55, 2015, doi: 10.1016/j.engstruct.2015.03.066.
[2.40] A. Agüero, L. Pallarés, and F. J. Pallarés, “Equivalent geometric imperfection definition in steel structures sensitive to flexural and/or torsional buckling due to compression,” *Eng. Struct.*, vol. 96, pp. 160–177, 2015, doi: 10.1016/j.engstruct.2015.03.065.
[2.41] N. Boissonnade and H. Somja, “Influence of imperfections in FEM modeling of lateral torsional buckling,” in *Structural Stability Research Council Annual Stability Conference 2012*, 2012, pp. 399–413.
[2.42] D. Dubina and V. Ungureanu, “Effect of imperfections on numerical simulation of instability behaviour of cold-formed steel members,” *Thin-Walled Struct.*, vol. 40, no. 3, pp. 239–262, 2002, doi: 10.1016/S0263-8231(01)00046-5.
[2.43] C. Nguyen, J. Moon, V. N. Le, and H. E. Lee, “Lateral-torsional buckling of I-girders with discrete torsional bracings,” *J. Constr. Steel Res.*, vol. 66, no. 2, pp. 170–177, 2010, doi: 10.1016/j.jcsr.2009.09.011.
[2.44] T. T. Nguyen, T. M. Chan, and J. T. Mottram, “Influence of boundary conditions and geometric imperfections on lateral-torsional buckling resistance of a pultruded FRP I-beam by FEA,” *Compos. Struct.*, vol. 100, pp. 233–242, 2013, doi: 10.1016/j.compstruct.2012.12.023.
[2.45] T. T. Nguyen, T. M. Chan, and J. T. Mottram, “Lateral – Torsional Buckling design for pultruded FRP beams,” *Compos. Struct.*, vol. 133, pp. 782–793, 2015, doi: 10.1016/j.compstruct.2015.07.079.
[2.46] H. H. Snijder, R. P. van der Aa, H. Hofmeyer, and B. W. E. M. van Hove, “Lateral torsional buckling design imperfections for use in non-linear FEA,” *Steel Constr.*, vol. 11, no. 1, pp. 49–56, 2018, doi: 10.1002/stco.201810015.
[2.47] R. Stroetmann and S. Fominow, “Imperfections for the LTB-design of Members with I-sections,” *ce/papers*, vol. 5, no. 4, pp. 290–299, 2022, doi: 10.1002/cepa.1758.
[2.48] M. Li, “Effect of the Initial Out-of-Straightness on the Lateral Torsional Buckling Strength of Steel Beams,” *(masters Sci. Diss. Univ. d’Ottawa/University Ottawa)*, 2017.
[2.49] H. Yoshida and K. Maegawa, “Lateral instability of I-beams with imperfections,” *J. Struct. Eng.*, vol. 110, no. 8, pp. 1875–1892, 1984, doi: 10.1061/(asce)0733-9445(1984)110:8(1875).
[2.50] A. Agüero and F. J. Pallarés, “Proposal to evaluate the ultimate limit state of slender structures. Part 1: Technical aspects,” *Eng. Struct.*, vol. 29, no. 4, pp. 483–497, 2007, doi: 10.1016/j.engstruct.2006.05.014.
[2.51] A. Agüero, I. Baláž, and Y. Koleková, “New method for metal beams sensitive to lateral torsional buckling with an equivalent geometrical UGLI imperfection,” *Structures*, vol. 29, no. November 2020, pp. 1445–1462, 2021, doi: 10.1016/j.istruc.2020.11.047.
[2.52] F. Ascione, “Influence of initial geometric imperfections in the lateral buckling problem of thin walled pultruded GFRP I-profiles,” *Compos. Struct.*, vol. 112, no. 1, pp. 85–99, 2014, doi: 10.1016/j.compstruct.2014.02.002.
[2.53] M. Fortan and B. Rossi, “Lateral Torsional Buckling of Welded Stainless-Steel I-Profile Beams: Design and Reliability,” *J. Struct. Eng.*, vol. 146, no. 12, pp. 1–12, 2020, doi: 10.1061/(asce)st.1943-541x.0002830.
[2.54] M. Fortan and B. Rossi, “Lateral Torsional Buckling of Welded Stainless Steel I-Profile Beams: Experimental Study,” *J. Struct. Eng.*, vol. 147, no. 3, pp. 1–12, 2021, doi: 10.1061/(asce)st.1943-541x.0002927.
[2.55] I. Kabir and A. K. Bhowmick, “Applicability of North American standards for lateral torsional buckling of welded I-beams,” *J. Constr. Steel Res.*, vol. 147, pp. 16–26, 2018, doi: 10.1016/j.jcsr.2018.03.029.
[2.56] I. Kabir and A. K. Bhowmick, “Lateral torsional buckling of welded wide flange beams under constant moment,” *Can. J. Civ. Eng.*, vol. 45, no. 9, pp. 766–779, 2018, doi: 10.1139/cjce-2017-0499.
[2.57] C. Quan, F. Walport, and L. Gardner, “Equivalent geometric imperfections for the design of steel and stainless steel beam-columns by GMNIA,” *J. Constr. Steel Res.*, vol. 215, no. September 2023, p. 108502, 2024, doi: 10.1016/j.jcsr.2024.108502.
[2.58] J. P. Smith-Pardo and J. D. Aristizábal-Ochoa, “Buckling reversals of axially restrained imperfect beam-column,” *J. Eng. Mech.*, vol. 125, no. 4, pp. 401–409, 1999, doi: 10.1061/(asce)0733-9399(1999)125:4(401).
[2.59] X. L. “Dimple” Ji, S. C. Twizell, R. G. Driver, and A. Imanpour, “Lateral Torsional Buckling Response of Compact I-Shaped Welded Steel Girders,” *J. Struct. Eng.*, vol. 148, no. 10, pp. 1–13, 2022, doi: 10.1061/(asce)st.1943-541x.0003431.

[2.60] N. Il Kim and J. Lee, “Nonlinear analysis of thin-walled Al/Al2O3 FG sandwich I-beams with mono-symmetric cross-section,” *Eur. J. Mech. A/Solids*, vol. 69, no. January 2017, pp. 55–70, 2018, doi: 10.1016/j.euromechsol.2017.11.010.
[2.61] Bathe, *Finite Element Procedures*. 1996. [Online]. Available: http://www.amazon.com/Finite-Element-Procedures-Part-1-2/dp/0133014584
[2.62] A. Sahraei, A. Iranpour, and M. Mohareb, “User manual for LTB-UO V3.0 (LTB-UO is a computer program for Lateral Torsional Buckling analysis of beams/beam-columns, written at the University of Ottawa),” 2020, *University of Ottawa*.

Chapter 3: Parametric Investigation for W-shaped Members

Abstract

Structural steel design standards provide analytical procedures for determining the lateral torsional (LTB) resistance of long-span unbraced members subjected to factored design actions within the framework of ultimate limit state design. In a class of design problems, in addition to satisfying ultimate LTB limit state requirements as established by design standards under factored loads, operational conditions may require the member to remain in the elastic range of deformation under service load levels to avoid permanent deformation or yielding. In this context, the present study aims to establish serviceability criteria for the LTB of long-span unbraced members with hot-rolled wide-flange sections that account for Initial Out-of-Straightness (IOS), to determine the service load level that the member can sustain while remaining within the elastic range.

Towards this goal, a finite element parametric investigation comprising 504 simulations is conducted on long-span hot-rolled wide-flange members whose capacities are governed by elastic LTB. The analyses account for geometric nonlinearity, IOS, and residual stress effects. The study investigates the influence of IOS characteristics—including IOS patterns (symmetric vs. asymmetric), types (lateral, twist, and lateral torsional), amplitudes, member spans, cross-sectional geometries, and loading conditions—on the lateral torsional buckling resistance of long-span members. Regression equations are developed to characterize the LTB resistance of members with various ISO types and amplitudes, and their application is illustrated through a design example.

Keywords: Lateral torsional buckling, Initial out-of-Straightness, Residual Stresses, Geometric nonlinear analysis, finite element

3.1 Introduction

Current structural steel design standards employ distinct approaches to estimate the flexural resistance of laterally unbraced beams bent about their major axis. The Canadian standard [3.1] and American specifications [3.2] adopt a piecewise characterization, the resistance of short-span members is governed by yielding, intermediate-span members by inelastic lateral torsional buckling (LTB), and long-span members by elastic LTB. In the elastic regime, both standards rely on the full elastic critical moment for perfectly straight members, thereby neglecting the influence of initial out-of-straightness (IOS). In contrast, Eurocode 3 [3.3] and the Australian standard [3.4] adopt unified equations that transition smoothly across all three regimes while capturing IOS effects.

A key distinction between the Canadian standard [3.1], and American specifications [3.2], versus Eurocode 3 [3.3] and the Australian standard [3.4], lies in their treatment of elastic lateral-torsional buckling (LTB) resistance. The former base their resistance equations on the elastic LTB capacity of perfectly straight members, neglecting initial out-of-straightness (IOS). In contrast, the latter standards explicitly account for IOS, resulting in reduced flexural resistances relative to those of idealized members.

The Eurocode approach is based on a generalization of the classical Ayrton-Perry formula [3.5], originally developed for the flexural buckling resistance of imperfect columns, to laterally unbraced flexural members. The procedure underlying the Eurocode design equations is based on Geometrically and Materially Nonlinear Analysis with Imperfection (GMNIA) and thus accounts

for residual stresses, IOS patterns and magnitudes, loading and support conditions, cross-sectional geometry, and whether the member is hot-rolled or welded. The Australian standard also captures the reduction in LTB flexural resistance due to the presence for IOS and residual stresses, while offering a less elaborate but more conservative procedure. Regardless of the design philosophy adopted, current provisions for lateral torsional buckling resistance are intended to guard against the attainment of the ultimate limit state under factored loading conditions. In this context, the present study aims to develop complementary LTB design criteria to ensure that the member remains within the elastic range of deformation under service load levels, in applications where member plastification or excessive deformation could impair the structural functionality and serviceability. Towards this objective, the present study conducts a parametric investigation based on the geometric nonlinear analysis of members with various IOS patterns to quantify their LTB resistance at the onset of first yield, while accounting for the presence of residual stresses. Simplified expressions are subsequently derived to quantify the LTB resistance corresponding to the onset of yield.

3.2 Literature Review

The effect of IOS on the LTB resistance of steel members has been investigated experimentally in

(e.g., [3.6-3.9]), and analytically (e.g.,[3.5, 3.10-3.19]). Numerical solutions based on thin-walled beam finite element models include [3.5, 3.11-3.22], and those based on shell element models include [3.9, 3.18-3.20, 3.23-3.32]. Some studies adopted the residual stress patterns of hot-rolled sections [3.6, 3.9-3.10, 3.18, 3.22, 3.24-3.26, 3.31-3.32] while others focused on welded sections [3.6-3.8, 3.10, 3.24-3.25, 3.27-3.32] Most investigations on the effect of Initial out of straightness (IOS) on the LTB resistance adopted Lateral Initial out of Straightness patterns (L-IOS) (e.g., [3.5, 3.7-3.8, 3.12, 3.14, 3.17-3.20, 3.22-3.32]) or affine eigenmode imperfections, i.e., Lateral

Torsional Initial out of straightness (LT-IOS) patterns based on the fundamental buckling mode as determined by a buckling eigenvalue analysis (e.g., [3.5, 3.7-3.9, 3.12-3.13, 3.16-3.18, 3.20-3.32]). Analyses based on other IOS patterns are scarce and include twist initial out of straightness (T-IOS) [3.18, 3.24], Camber Initial out-of-straightness (C-IOS) [3.11], plate out-of-flatness [3.7, 3.15, 3.20, 3.24], and non-orthogonality of flange to web [3.7, 3.25]. Most previous studies focused on the LTB of steel members, except for [3.15, 3.17, 3.20] which focused on pultruded FRP beams. Also, apart from the studies in [3.5, 3.7, 3.11-3.12, 3.23, 3.32] which centered on beam-columns, most previous studies focused on pure flexural members. Table 3.1 provides a comparative summary of analytical and numerical studies that account for IOS effects on hot rolled steel sections in the context of lateral torsional buckling.

Table 3.1 Comparative summary of studies on IOS effects on LTB of steel members

Author(s)	Solution type(1)	element type(2)	IOS type(3)	RS	Section type(4)	Material nonlinearity	Additional aspects of the study
Yoshida and Maegawa [3.10]	N	B	L	Yes	R	No	Determined LTB resistance of horizontally curved beams with combined IOS
Stroetmann and Fominow [3.9]	N	B, S	L, LT	Yes	W,R		GNIA calibration of LTB imperfection amplitudes
Smith and Aristizábal [3.11]	A	B	C		R		LTB under UD, PL, and moment with sinusoidal IOS
Nguyen et al. [3.13]	N	S	LT		R	No	Analytical solution for LTB of beams with discrete partial twist restraints
MaCann [3.14]	N	B	L		R		Closed-form solutions with Fourier series displacement functions
Agüero et al. [3.16]	A, N	S	LT		R		defines geometric imperfections consistent with Eurocode
Li [3.18]	A,N	B	L, LT,T	Yes	R	No	Approximate Second Order Analysis
Agüero et al. [3.22]	N	S	L	Yes	W,R		Generalized Eurocode UGLI to bending members
Boissonnade and Somja [3.24]	N	S	L, LT, T	Yes	W,R	Yes	Numerical study modelling IOS with sinusoidal midspan waves

Subramanian and White [3.25]	E, N	S	L	Yes	W,R	Yes	Defined IOS consistent with Experiments
Snijder et al. [3.26]	N	S	LT		R	Yes	Define imperfection consistent with Eurocode and GMNIA
Fortan and Rossi [3.29]	E, N	S	L	Yes	W,R		Stainless steel, Digital image correlation, Defined slenderness-imperfection relationships for design
Quan et al. [3.31]	N	B	LT	Yes	W,R	Yes	Mild and Stainless Steel, GMNIA-based equivalent IOS for out-of-plane stability
Present	**N**	**B**	**L,LT, T**	**Yes**	**R**	**No**	**Geometric nonlinear Analysis with RS and various IOS patterns**

(1) N= Numerical, E = Experimental, A= Analytical. (2) B= Beam, S= Shell.
(3) L= Lateral-IOS, LT= Lateral-Torsional-IOS, RS= Residual stress. (4) R= Hot Rolled sections, W= Welded sections.

3.3 Parametric Study

3.3.1 Reference Case

A member with a W310x67 cross-section and span $L = 8\,m$ is selected as a reference member. Flange width is $b = 204mm$, thickness is $t = 14.6mm$ and web height is $d = 306\,mm$ and thickness $w = 8.5mm$, which correspond to the dimensionless parameters $(b/d, b/t, d/w, L/d) = (0.667, 14.0, 36.0, 26.1)$. Cross-sectional properties are $A = 8434\,mm^2$, $I_x = 1.44\times10^8$ mm^4, $I_y = 2.07\times10^7$ mm^4, $J = 4.83\times10^5$ mm^4, and $I_\omega = 4.39\times10^{11}$ mm^6. All three displacements and the angle of twist are restrained at one end, while the lateral and transverse displacements and the angle of twist are restrained at the other end. For a yield strength of $F_y = 350MPa$, the section meets compactness requirements (Class 2). Under the American specifications [3.2], the threshold span L_t delineating the inelastic and elastic LTB regions is determined by equating the uniform elastic critical moment $M_u = (\pi/L_t)\sqrt{EI_yGJ + (\pi E/L_t)^2 I_y I_\omega}$ to 70% of the plastic moment M_p, yielding L_t = 6.4 m. A similar approach is adopted in the Canadian standards [3.1], except that the Canadian threshold spans L_{tc} are computed by equating the critical moment

$M_u = \left(C_b \pi / L_{tc}\right) \sqrt{EI_y GJ + \left(\pi E / L_{tc}\right)^2 I_y I_\omega}$ to 67% of the plastic moment. For the W310×67 section considered, the threshold spans L_{tc} are 6.60, 7.22, and 8.30 m respectively for uniform moment, uniformly distributed load, and midspan point load. The moment gradient factors are taken as $C_b = 1.0, 1.13, 1.35$, as determined from thin-walled beam finite element buckling analysis ([3.33]) in order to avoid approximations associated with applying the quarter-point moment gradient equation in the Canadian standards.

The flexural resistance of the member based on elastic LTB is to be determined based on the onset of yield in compression criterion while accounting for the presence of residual stresses. The compressive residual stresses at flange tips are assumed to be $0.3\, F_y = 105\ MPa$. As a result, the first-yield condition occurs when the additional compressive stresses induced by external loads induce an additional compressive stress of $0.7\, F_y = 245\ MPa$ at the flange tips. This approach is consistent with the methodology adopted in the American specifications [3.2] to compute the threshold span L_t i.e., by equating the LTB moment of a perfectly straight beam to 70% of its cross-sectional strength.

3.3.2 Model Description

The analysis is based on a thin-walled beam finite element developed in Chapter 2, which captures geometric nonlinear effects, IOS, and warping deformations. The element is based on the kinematics of Gjelsvik's thin-walled beam theory, in which (a) the cross-section is assumed to move as a rigid disk in its own plane with no distortion, (b) shear strains in the middle surface are negligible, and (c) lines normal to the middle surface preserve their normality throughout deformation. The element features two nodes with seven degrees of freedom per node: three translations, three rotations, and a warping degree of freedom. The formulation is based on small

strains and moderate rotations. A mesh sensitivity analysis has shown that convergence is attained with 20 beam elements along the span. Thus, 20 elements are used to mesh each parametric run in the present study.

3.3.3 Designations

A series of parametric runs is conducted. Each run is assigned a designation of the form XXNNLL, in which XX denotes the type of IOS and takes the value (L) for lateral IOS (i.e., sweep), (LT) for lateral-torsional IOS (i.e., affine eigenmode imperfections), or (T) for twist IOS. Symbol NN denotes the span to peak IOS magnitude ratio, and LL designates the loading pattern and takes the values (UM) for uniform moment, (PL) for midspan point load, or (UD) for uniformly distributed load. For example, LT2000PL denotes a beam with a lateral torsional type of IOS having a maximum IOS amplitude of $L/2000$ subjected to a midspan point load.

3.3.4 Effect of IOS Pattern

Three types of IOS are considered for the reference beam: L, T, and LT. For each IOS type, three patterns are examined: $\xi(z)=\xi_1\sin(\pi z/L)$, $\xi(z)=\xi_2\left[\sin(\pi z/L)+\sin(2\pi z/L)\right]$, and $\xi(z)=\xi_3\left[\sin(\pi z/L)-\sin(3\pi z/L)\right]$, in which constants ξ_i are chosen in each case so that the peak IOS at the top flange is equal to the target IOS value. For example, if a target IOS of $L/1000$ .is sought at the top flange, ξ_i is set to $L/1000$. The above three patterns are denoted respectively as P1, P1+2, and P1-3. While patterns P1 and P1-P3 are symmetric about the member midspan, pattern P1+2 is asymmetric.

A geometrically nonlinear analysis is conducted in each case to obtain the moment M corresponding to the onset of yield in compression within the cross-section in the presence of residual stresses. Since the compressive residual stresses at flange tips are assumed to be

$F_r = 0.30F_y$, the corresponding onset of yield in compression is assumed to occur when one of tips of the compression flange attains $F_y - F_r = 0.70F_y$. The moment M thus obtained is normalized relative to the elastic critical moment $M_u = \left(C_b\pi/L\right)\sqrt{EI_yGJ + \left(\pi E/L\right)^2 I_y I_\omega}$. The ratio M/M_u is indicative of the reduction in moment capacity caused by the presence of IOS. The results in Table 3.2 show that, irrespective of the load configuration, Pattern P1 consistently corresponds to the lowest M/M_u ratio (i.e., causing the largest detrimental effect on the resistance), followed by P1-3 and then by P1+2 (inducing the lowest detrimental effect). For example, for L1000UM, Pattern P1 had $M/M_u = 0.86$. This ratio increased to 0.88 for Pattern P1-3 and further increased to 0.89 for Pattern P1+2.

Table 3.2 Effect of IOS patterns on moment ratio M/M_u

IOS Pattern	L1000UM	LT1000UM	T1000UM	L1000UD	LT1000UD	T1000UD	L1000PL	LT1000PL	T1000PL
P1	0.86	0.81	0.76	0.85	0.79	0.74	0.76	0.71	0.66
P1-3	0.88	0.86	0.79	0.87	0.83	0.76	0.78	0.75	0.68
P1+2	0.89	0.87	0.8	0.88	0.84	0.78	0.79	0.76	0.69

Note: L =Lateral IOS, LT = lateral-torsional IOS, and T = twist IOS. 1000 is the span to IOS amplitude.

UM =uniform moment, UD =uniformly distributed load, and PL = midspan point load

The total out-of-straightness TOS at both flanges (defined as the sum of the initial out-of-straightness and the displacements induced by loading) are generated for L1000UM, LT1000UM, and T1000UM for three IOS patterns considered: P1, P1+2, and P1-3 and normalized with respect to the peak lateral IOS under zero load (Fig.3.1a-i). For comparison, the TOS are provided at the moment M corresponding to the onset of yield ($m = \tilde{M}/M = 1$), at the intermediate loading stage $m = 0.5$, and at the initial stage $m = 0$.

Irrespective of whether the starting IOS pattern is symmetric (P1, P1-3) or asymmetric (P1+2), the TOS distribution gradually approaches a symmetric pattern relative to midspan, as the applied moments approach the onset of yield moment ($m \to 1.0$). In particular, the asymmetric patterns P1+2 depicted in Fig.3.1c, f, i gradually unwind towards a symmetrical configuration for all patterns considered, L, LT, or T as the applied moments increase.

At $m = 1.0$, pattern P1 induces the highest normalized total IOS with top and bottom lateral displacements $(u_T, u_B) = (3.12, 2.60)\,mm$, followed by P1-3 with $(u_T, u_B) = (2.34, 1.94)\,mm$, and then by P1+2 with $(u_T, u_B) = (2.03, 1.69)\,mm$, i.e., the largest lateral displacements correspond to the P1 pattern. Thus, following parametric runs will be based on pattern P1.

Also, for Pattern P1, the normalized TOS at both flanges corresponding to the peak load $m = 1.0$, are $(u_T, u_B) = (3.12, 2.60)\ mm$ for L1000UM, $(u_T, u_B) = (3.33, 2.57)\ mm$ for LT1000UM, and $(u_T, u_B) = (3.69, 1.49)\ mm$ for T1000UM, i.e., the normalized TOS at the top flange is lowest for L-IOS and highest for T-IOS. Conversely, the normalized TOS at the bottom flange is highest for L-IOS and lowest for T-IOS. Similar trends are observed for Patterns P1-3 and P1+2.

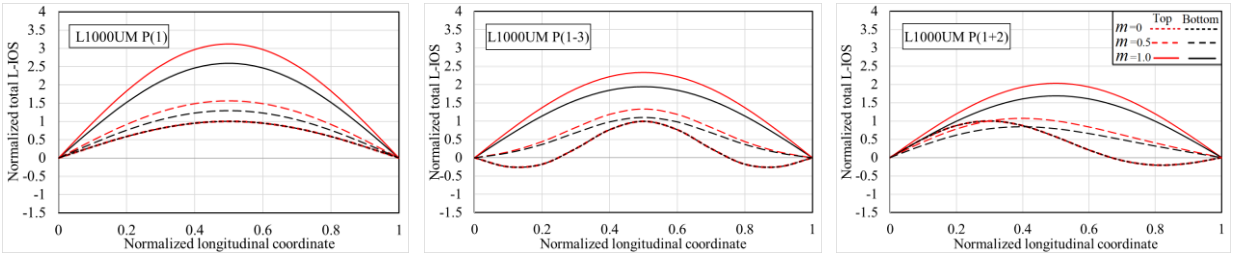

(a) (b) (c)

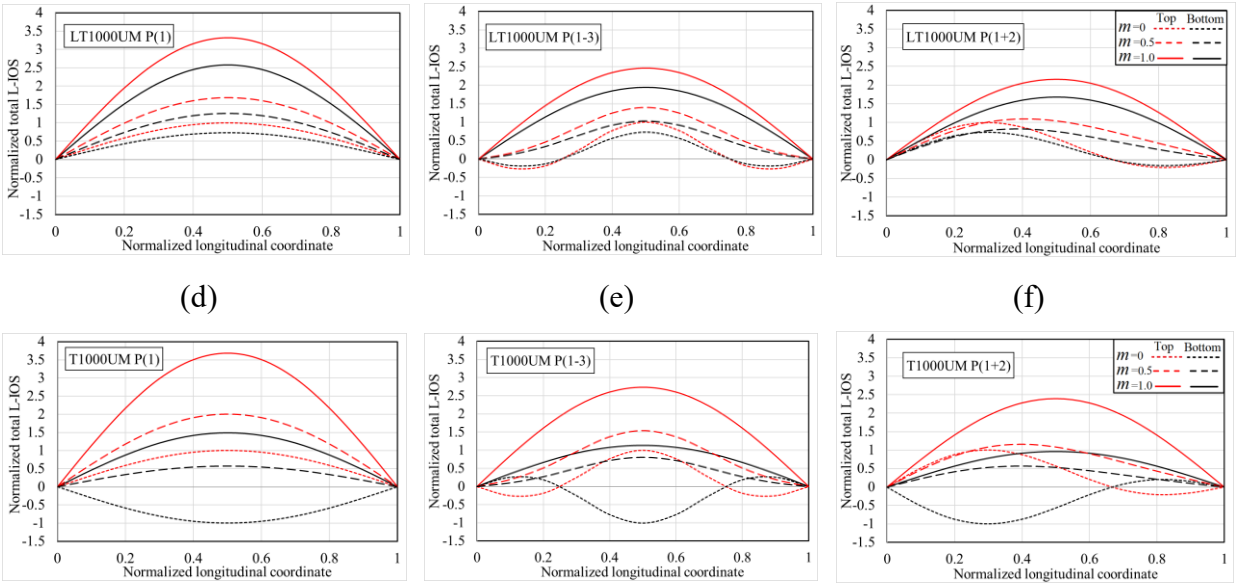

Fig.3.1 Progression of normalized total lateral out of straightness at both flanges for (a–c) L1000UM, (d–f) LT1000UM, and (g–i) T1000UM for Patterns P1, P1-3 and P1+2

3.3.5 Parametric Combinations

A total of 24 Reference Load Imperfection Combinations (RLIC) are examined, involving three load configurations; UM, PL, and UD, three IOS patterns per loading configuration; L, LT, or T. For L and LT IOS patterns, two IOS amplitudes are investigated $L/1000$ to represent the maximum allowable value in [3.34] and $L/2000$ to representative of a typical IOS magnitude [3.25], while for T-IOS patterns, four amplitudes were considered $L/1000$, $L/1500$, $L/2000$, and $L/3000$. Thus, the L and LT IOS cases account for 3 loading cases × 2 IOS patterns × 2 amplitudes =12 RLIC, and the T IOS cases account for an additional 3 loading cases × 4 amplitudes =12 RLIC.

For each of the 24 RLIC, the geometry of the problem was varied so that three of the reference dimensionless parameters $(b/d, b/t, d/w, L/d)$ provided in Section 3.3.1 are kept constant, while varying the fourth dimensionless parameter within the ranges of available cross-sections in the Handbook of Steel Construction [3.34], resulting in four clusters of runs.

In the first cluster, five b/d values were considered in the 0.5-0.9 range, in addition to the reference value. In the second cluster, five additional values of b/t were considered between 10 and 16. The third cluster had five additional d/w values ranging from 15 to 55, while the fourth cluster considered five additional values for L/d ranging from 24 to 36. The four clusters resulted in a total of 21 geometric variations per RLIC, resulting in a total of 21×24= 504 parametric cases[5].

3.3.6 Effect of IOS Type and Magnitude

Section 3.3.4 has shown that, irrespective of the type of IOS (L, LT, or T), pattern P1 has the most detrimental effect on the onset yield moment. As such, the parametric runs in the present section will conservatively adopt the P1 pattern for all types of imperfections.

Across all loading scenarios considered: UM, UD, PL, Fig. 3.2 and Fig. 3.3 show that for a given IOS magnitude, T-IOS has the most detrimental effects as reflected by the lowest moment ratios M/M_u, followed by LT-IOS, while L-IOS has the least detrimental effect.

As expected, for a given type of IOS (L, LT, or T), a higher IOS magnitude corresponds to a lower yield moment ratio M/M_u. On average, for L1000, the moment ratio M/M_u is found to be 7.23% lower that of L2000. Also, for LT1000, the moment ratio is 8.68% lower that of LT2000 and for T1000, the moment ratio is 11.97% lower that of T2000.

Also shown on Fig. 3.2 and Fig. 3.3 are the M/M_u ratios predicted by Eurocode and AS4100 for comparison. The predictions of both codes are observed to lie within the band defined by the upper

[5] Appendix G presents the numerical database of results for the present study.

bound defined by L2000 and the lower bound corresponding to T1000. In all cases, the AS4100 predictions are more conservative than those of the Eurocode.

For a maximum IOS amplitude of L/1000, the Eurocode provisions overestimate the LTB resistance of members by 3.1% on average for L1000, by 9.9% for LT1000, and by 19% for T1000, compared to the onset yield moments computed by the present study. For the more typical IOS magnitude of L/2000, the Eurocode provisions underestimate the LTB resistance of members on average by 2.9% for L2000, but overestimates it by 1.1% for LT2000, and by 6.2% for T2000. In comparison, AS4100 underestimates the LTB resistance of L1000 by 4.2%, but overestimates that of LT1000 by 2.1% and T1000 by 10.5%. For the typical IOS magnitude of L/2000, it underestimates L2000 by 10.7%, LT200 by 6.0% and T2000 by 1.3% on average (Table 3.3).

Table 3.3 Ratio of moment capacities predicted by the present study and Eurocode and AS4100 predictions

		LT1000	**T1000**	**L1000**	**LT2000**	**T2000**	**L2000**	**T1500**	**T3000**
Present/ Eurocode3	Average	1.099	1.190	1.031	1.011	1.062	0.961	1.131	0.976
	Standard deviation	0.043	0.055	0.037	0.034	0.041	0.029	0.047	0.033
Present/ AS4100	Average	1.021	1.105	0.958	0.940	0.987	0.893	1.051	0.906
	Standard deviation	0.051	0.062	0.043	0.040	0.049	0.035	0.054	0.039

3.3.7 Effect of Geometric Parameters

Fig. 3.2a-c depicts the results for the first cluster of runs in which parameters $(b/t, d/w, L/d) = (14.0, 36.0, 26.1)$ were kept constant, while varying the width-to-depth ratio b/d. An increase in b/d is observed to reduce the ratio of the onset yield moment to the critical moment M/M_u. For example, for T1000UM. Fig. 3.2a shows that the normalized moment ratio M/M_u of 0.81 at b/d =0.5 reduces notably to 0.58 when b/d = 0.9. Similar trends, though less severe, are observed for LT1000UM and L1000UM. This negative trend is confirmed by the Eurocode 3 and AS4100 predictions.

In the second cluster of runs (Fig. 3.2d–f) parameters $(b/d, d/w, L/d)$ were kept constant at $(0.667, 36.0, 26.1)$, while varying the ratio of flange width-to-thickness b/t. An increase in b/t is observed to consistently increase the ratio of the onset yield to critical moment ratio. For example, the normalized moment ratio for T1000UM (Fig. 3.2d) is 0.68 at b/t =10. This value increases to 0.79 at b/t =18. Similar trends are observed for LT1000UM and L1000UM, which are also consistent with those of the Eurocode 3 and AS4100.

Fig. 3.3a–presents the third cluster of runs, in which the span ratio L/L_t was varied while the remaining parameters $(b/d, b/t, d/w)$ remained constant at $(0.667, 14.0, 36.0)$. Increasing the span ratio is observed to increase the moment ratio, suggesting that the detrimental effect induced by IOS becomes less pronounced. For example, the normalized moment ratio for T1000UM (increases from 0.73 at L/L_t =1.16 to 0.78 when the span ratio is increased to L/L_t =1.74 (Fig. 3.3a). Similar patterns are observed for L1000UM and LT1000UM, and the trends remain consistent with predictions of Eurocode 3 and AS4100.

Fig. 3.3d-f depicts the fourth cluster of runs. The variation in d/w has a minimal influence on the normalized moment ratio M/M_u, with values remaining nearly constant across the examined range.

For members subjected to UM and UD loading, the Eurocode-based moment ratios are observed to be higher than those predicted by the present study for members with maximum allowable lateral and lateral-torsional initial out-of-straightness (i.e., L1000 and LT1000). Instead, the Eurocode predictions are closer to those of members with more typical lateral torsional IOS amplitudes of LT2000. This observation is consistent with the findings in [3.25]. For members under PL loading,

the Eurocode predictions are higher than those of LT2000 and closer to L2000. The higher Eurocode moment ratios stem from its consideration of beneficial material plasticity, whereas the present study is based on the onset of yield criterion. While the Eurocode standard is intended to characterize the ultimate limit state of the member under factored load levels, the limits predicted in the present study are appropriate for serviceability limit states, in which operational conditions under regular service loads, require the member to remain in the elastic range, avoiding permanent deformation or yielding.

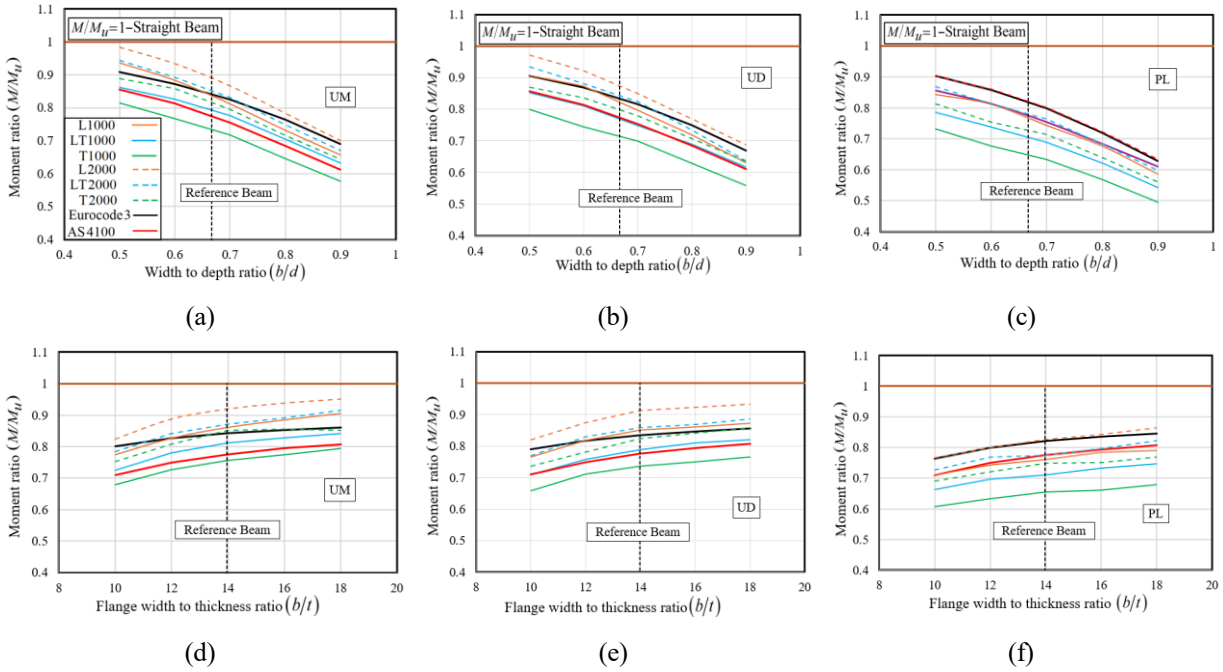

Fig. 3.2 Moment ratio versus flange width to depth ratio (a-c) and flange width to thickness ratio (d-f)

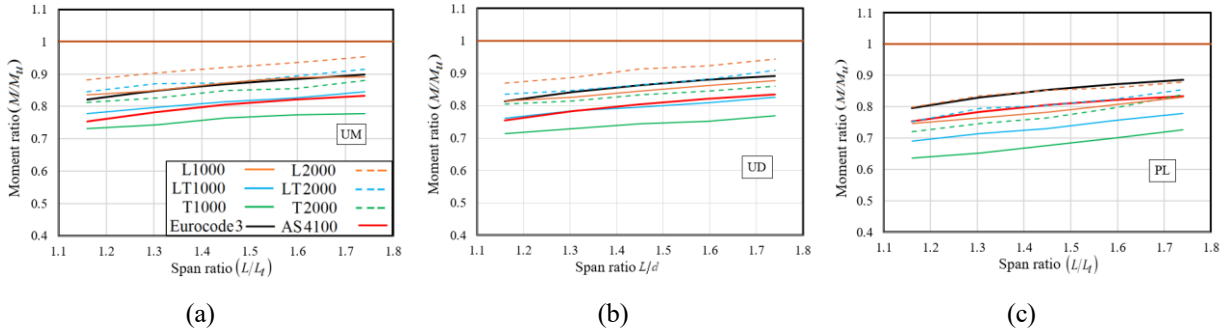

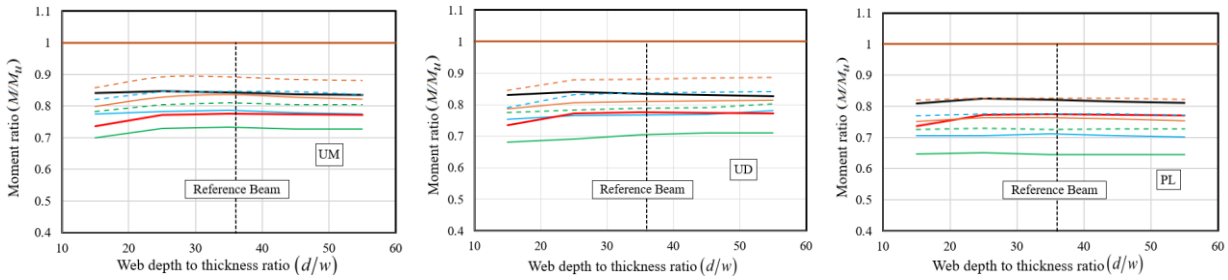

(d) (e) (f)

Fig. 3.3 Moment ratio versus span ratio (a-c), and web depth to thickness ratio (d-f)

3.4 Threshold for Twist IOS

As discussed in the literature review, the IOS research underlying the Eurocode is based either on Lateral-Torsional IOS with an L/1000 amplitude [3.5, 3.7-3.9, 3.12-3.13, 3.16-3.18, 3.20-3.32] or on Lateral IOS with an L/1000 amplitude [3.5, 3.7-3.8, 3.12, 3.14, 3.17-3.20, 3.22-3.32]. The threshold of L/1000 is also consistent with the limiting sweep criterion provided in the Handbook of Steel Construction [3.34]. However, no T-IOS criteria are currently provided in design standards. As shown in the previous section, T-IOS has a higher detrimental effect on LTB resistance than L-IOS or LT-IOS of the same amplitude.

As discussed in the literature review, the initial out-of-straightness (IOS) research underlying the Eurocode is primarily based on two types of IOS: LT-IOS [3.5, 3.7-3.9, 3.12-3.13, 3.16-3.18, 3.20-3.32] or and L-IOS [3.5, 3.7-3.8, 3.12, 3.14, 3.17-3.20, 3.22-3.32], both typically modeled with an amplitude of L/1000. This L/1000 threshold aligns with the limiting sweep criterion recommended in [3.34]. However, current design standards do not provide criteria for T-IOS**.** As demonstrated in the previous section, T-IOS has a more pronounced adverse impact on lateral-torsional buckling (LTB) resistance than either L-IOS or LT-IOS of the same amplitude. Given this heightened sensitivity**,** it becomes of interest to propose T-IOS amplitude limits that result in strength reductions comparable to those caused by LT-IOS with an L/1000 amplitude**.** This would help ensure consistency in design assumptions.

Fig. 3.4 and Fig. 3.5 depict the normalized moment ratio M/M_u versus section aspect ratio b/d (Fig. 3.4a–c) , flange slenderness b/t (Fig. 3.4d-f) , span ratio L/L_t (Fig. 3.5a–c), and web slenderness (Fig. 3.5d–f) for various T-IOS amplitudes ranging from $L/3000$ up to $L/1000$. Overlaid for comparison are the predictions of Eurocode 3, AS4100 and LT1000. Across all cases, the slopes of the response M/M_u plots predicted by the present study for T1000, T1500, T2000, T3000, and LT1000 specimens closely align with those based on AS4100 provisions. Conversely, while the present solution exhibits close agreement with Eurocode slopes for the midspan point load scenario, it tends to yield comparatively milder slope predictions under uniformly distributed load and uniform moment conditions. In all cases, the moment ratios for LT1000 consistently fall between those of T2000 and T1500, indicating that a T-type initial out-of-straightness (IOS) with an amplitude of approximately L/1700 produces, on average, a detrimental effect comparable to that of an LT-type IOS with an amplitude of LT/1000.

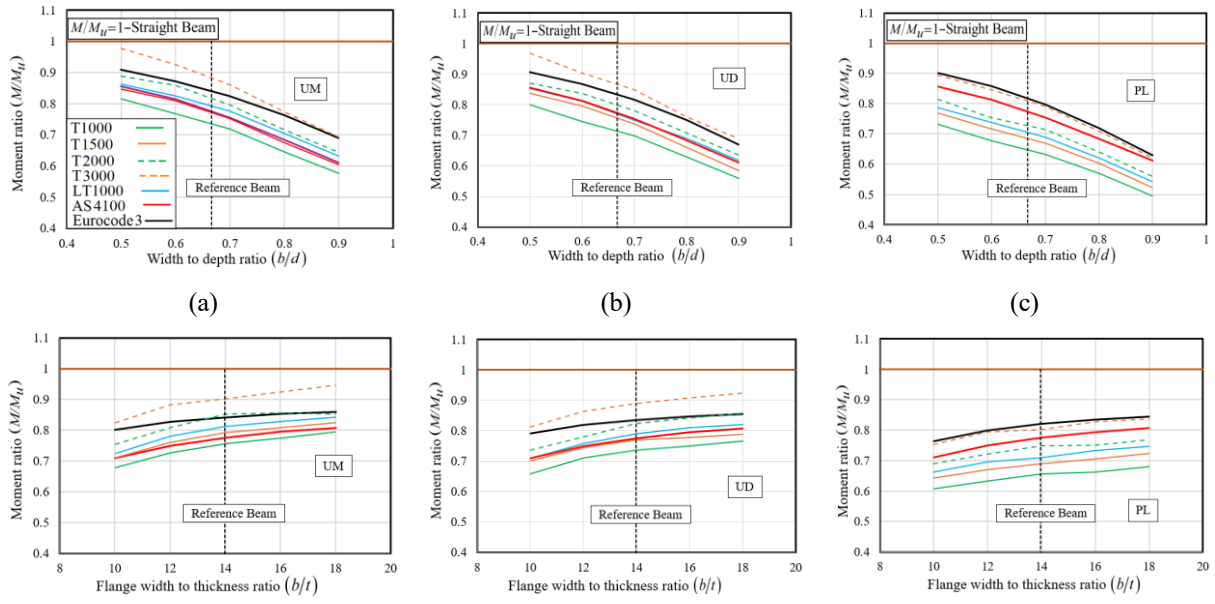

Fig. 3.4 (a-c) Moment ratio versus section aspect ratio and (d-f) Moment ratio versus flange slenderness

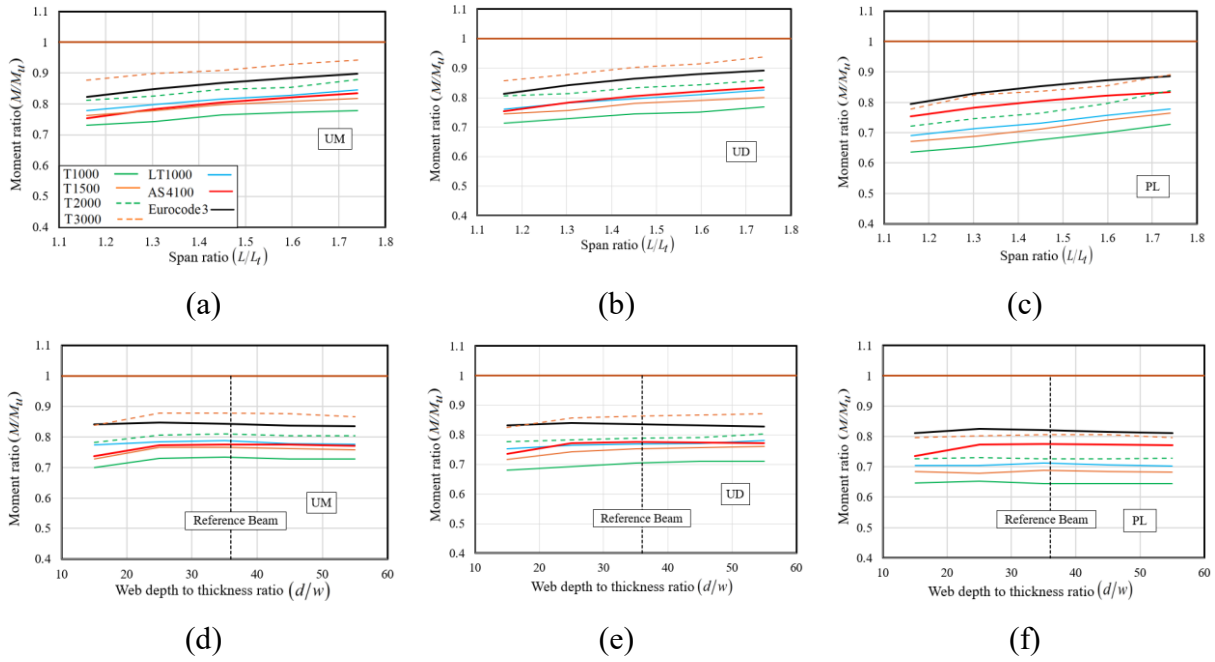

Fig. 3.5 (a-c) Moment ratio versus Span ratio (d-f) Moment Ratio versus web slenderness

3.5 Regression Analysis

The database of nominal LTB moment resistances generated throughout the previous parametric study is used to develop simplified regression equations to characterize the LTB resistance while accounting for the reduction induced by IOS. Since such reductions are analogous to those of the compressive strength in columns induced by IOS, the equation proposed herein adopts a form analogous to that the column strength equation in CAN-CSA S16, by multiplying the cross-sectional flexural strength $S_x F_y$ by a reduction factor $\left(1+\lambda^{an}\right)^{-1/n}$ that depends on a slenderness parameter λ related to lateral torsional buckling, i.e.,

$$M = S_x F_y \left(1+\lambda^{an}\right)^{-1/n} \tag{3.1}$$

in which S_x is the major axis elastic section modulus, a and n are dimensionless regression coefficients that depend on the IOS pattern and magnitude, and $\lambda = \sqrt{S_x F_y / M_u}$ is a slenderness

parameter defined in terms of the ratio of the cross-section flexural strength $S_x F_y$ to elastic critical moment $M_u = (C_b \pi / L)\sqrt{EI_y GJ + (\pi E / L)^2 I_y I_\omega}$ for a perfectly straight member. Separate regression coefficients were obtained for each of the patterns considered: L1000, L2000, LT1000, LT2000, T1000, T1500, T2000, T3000 (Table 3.4). For all IOS patterns, a coefficient of determination of 0.99 was achieved. The plots confirm the close fit in Fig. 3.6 which shows that the regression equations closely replicate the finite element results, irrespective of the loading pattern.

Table 3.4 Regression coefficients a, n and coefficient of variation R^2 for various IOS patterns and amplitudes

IOS Pattern	L1000	L2000	LT1000	LT2000	T1000	T1500	T2000	T3000
a	2.14	2.17	2.15	2.20	2.14	2.17	2.20	2.21
n	1.90	2.45	1.60	2.05	1.32	1.48	1.76	2.34
R^2	0.99	0.99	0.99	0.99	0.99	0.99	0.99	0.99

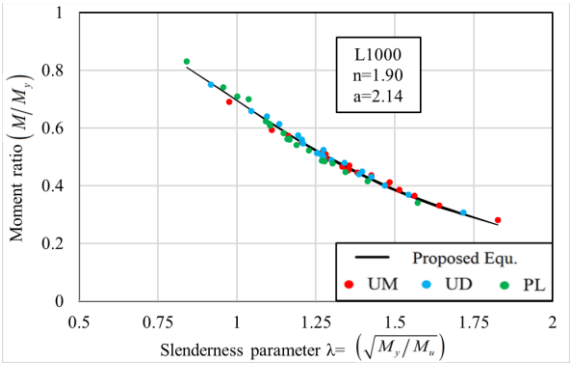

(a)

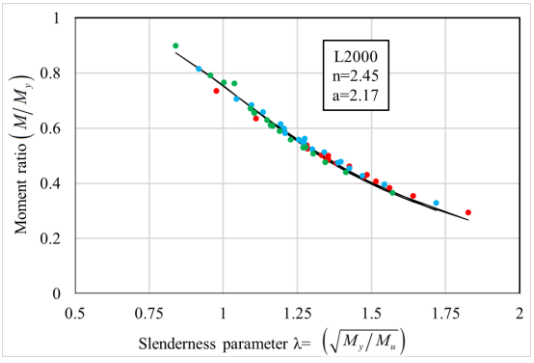

(b)

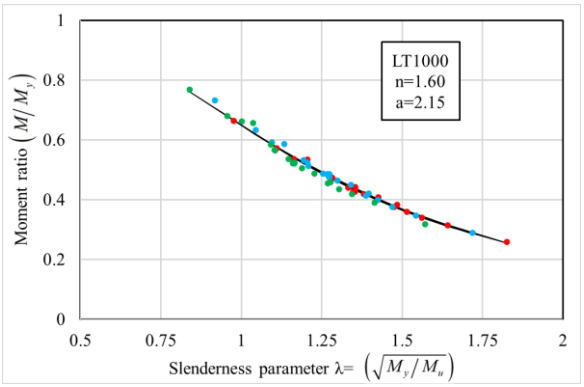

(c)

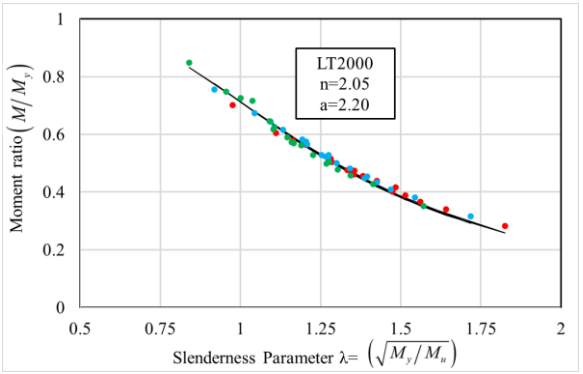

(d)

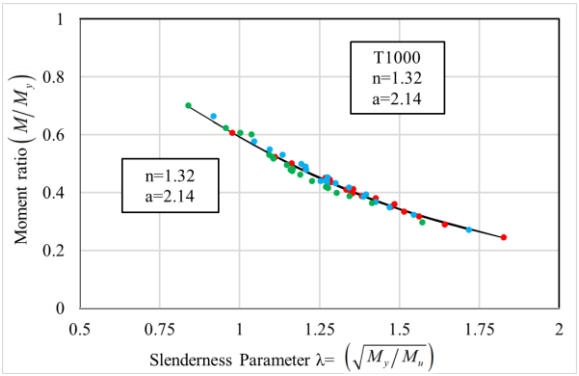

(e)

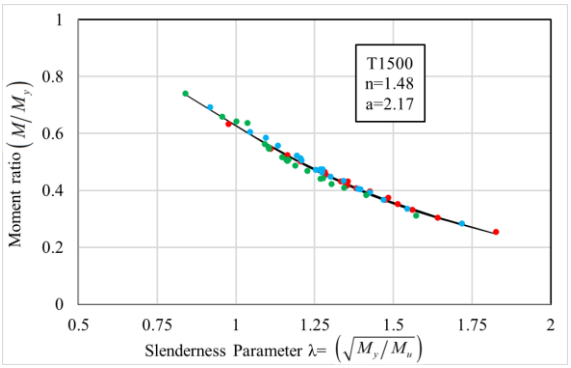

(f)

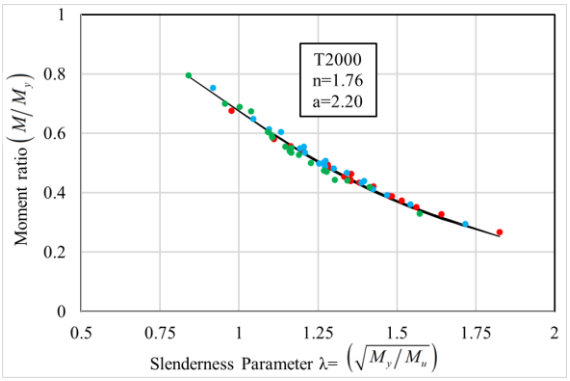

(g)

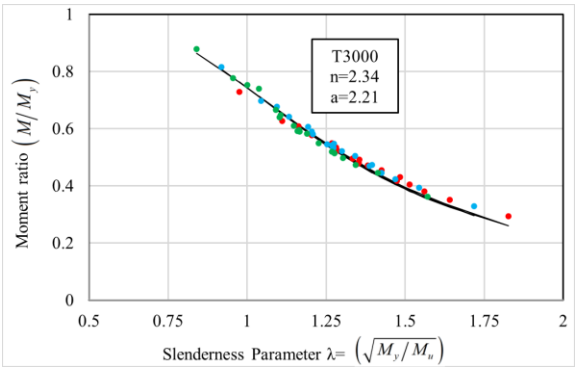

(h)

Fig. 3.6 Comparison of regression and finite element predictions versus slenderness ratio for (a) L1000, (b) L2000, (c) LT1000, (d) LT2000, (e) T1000, (f) T1500, (g) T2000, and (h) T3000.

3.6 Comparison with Standard Predictions

The flexural resistances for the reference W310×67 beam is evaluated under UM, UD, and PL. Beam span is varied from the threshold span $L_t = 6.33\,m$ based on American standards to $1.8L_t$.

As discussed under Section 3.1, the Canadian standard threshold span L_{tc} is load dependent and takes the values $6.60m$ for UM, $7.22m$ for UD, and $8.30m$ for midspan point load PL. The predicted moment resistance M is normalized relative to the plastic moment M_p and the ratio M / M_p is plotted against the normalized span L / L_t (Fig. 3.7a–c).

Comparisons are provided between the present FEA solution based of the onset of yield criterion for L1000, LT1000, and T1000 IOS scenarios and the regression equation proposed for LT1000 (with a=2.15, n=1.60), the American and Canadian standards solutions which omit IOS effects and the Eurocode 3 and AS 4100 both of which capturing IOS effects.

For all three loading cases and across all spans considered, the FEA solutions incorporating L/1000 imperfections, both L-IOS and LT-IOS, consistently fall below the predictions of the Canadian and American standards, which do not account for IOS effects in the elastic lateral-torsional buckling (LTB) region. Both FEA solutions also fall slightly below the Eurocode 3 predictions, despite the Eurocode accounting for IOS effects. The difference is primarily attributed to the different criteria used: the present study uses an onset of yielding criterion, whereas the Eurocode provisions are based on geometric and material nonlinear analysis with imperfections (GMNIA), which allows the member to deform into the plastic range, thereby increasing its apparent resistance. Both L-IOS and LT-IOS curves lie above the Australian Standard predictions for UM, UD loading but lie below it for PL loading. For all cases, the regression equation (a=2.15, n=1.60) closely replicates the FEA analysis for LT1000.

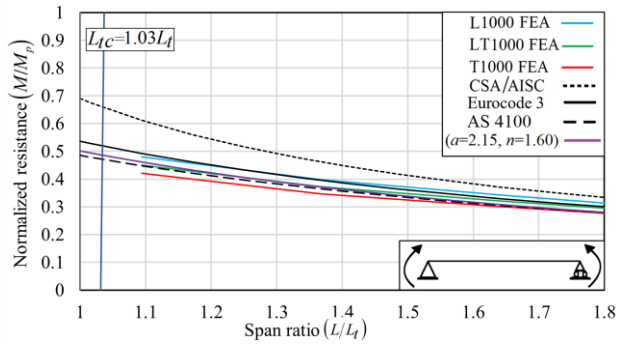

(a)

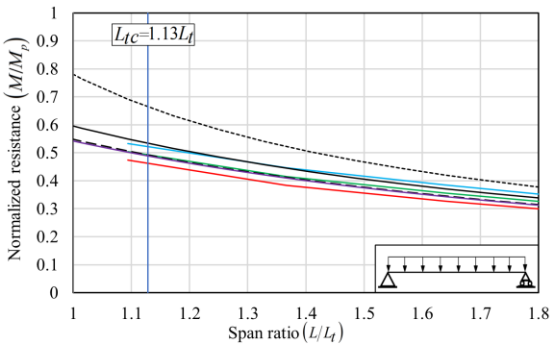

(b)

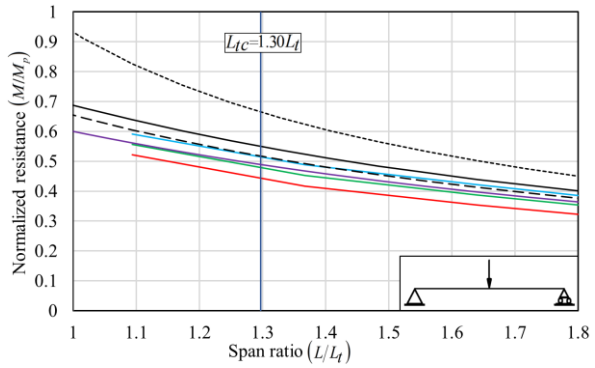

(c)

Fig. 3.7 Flexural resistance of W310X67 beam using the proposed equation compared to the developed model and design standards, subjected to (a) uniform moment. (b) Uniformly distributed load and (c) Midspan point load

3.7 Design Example

A 10 *m* span beam is laterally and torsionally unbraced at both ends and laterally unbraced along its span. The beam is subjected to a factored midspan point load $P_f = 61kN$. As the beam is carrying sensitive equipment, it is required to sustain a service load level of $P_s = 47kN$ without experiencing permanent deformations. IOS can be assumed on the fundamental buckling mode (LT) with an amplitude L/1000. Steel yield strength is $F_y = 350MPa$ and the maximum compressive residual stresses at the flange tips is $0.3F_y$. The designer attempts a W250x58 with $(b,t,d,w) = (203,13.5,252,8.0)mm$ and cross-sectional properties $I_y = 1.88\times10^7\ \text{mm}^4$, $J = 4.09\times10^5\ \text{mm}^4$, $I_\omega = 2.68\times10^{11}\ \text{mm}^6$, $Z_x = 7.70\times10^5\ \text{mm}^4$, and $S_x = 6.93\times10^5\ \text{mm}^6$.

Determine whether the nominal resistances for the beam exceed the LTB ultimate and serviceability demands.

For $F_y = 350MPa$, it is found that the section meets compactness requirements (Class 2) and its span exceeds the elastic LTB thresholds of the American and Canadian standards. The nominal LTB resistance under both standards is $M_u = \left(C_b \pi / L_{tc}\right)\sqrt{EI_y GJ + \left(\pi E / L_{tc}\right)^2 I_y I_\omega} = 158kNm$ which exceeds the midspan factored moment $P_f L/4 = 153\,kNm$. Yet, this value exceeds the LTB nominal resistance of the Eurocode of $135\,kNm$ and that based on the Australian standards i.e., $124\,kNm$. Eq. (3.1) is applied for an LT1000 (i.e., $135\,kNm$ in which *a*=2.15, *n*=1.60) to conduct the serviceability limit state check, which yields a serviceability moment resistance of $111kNm$ compare to $114\,kNm$ that is based on the developed model. This value falls below the mid-span service moment demand of $P_s L/4 = 118\,kNm$.

A second trial is attempted with a W250X67 cross-section $\left(b,t,d,w\right) = \left(204,15.7,257,8.9\right)mm$ and cross-sectional properties $I_y = 2.22\times10^7\ mm^4$, $J = 6.25\times10^5\ \text{mm}^4$, $I_\omega = 3.24\times10^{11}\ \text{mm}^6$, $Z_x = 9.01\times10^5\ \text{mm}^4$, and $S_x = 8.06\times10^5\ \text{mm}^6$. Again, the section meets the compactness requirement, and its span exceeds the elastic LTB thresholds for the American and Canadian standards. The nominal LTB resistance under both standards is $209\,kNm$ which compares to $179\,kNm$ based on the Eurocode, and $162\,kNm$ based on the Australian Standards, i.e., the new nominal resistances exceed the ultimate LTB moment demand under all four standards. The serviceability limit state check based on Equ (3.1) yields a serviceability moment resistance of

$138\,kNm$ compared to $142\,kNm$ from the developed model, which also exceeds the serviceability demand.

3.8 Summary and Conclusions

The present study conducted a parametric investigation on the elastic LTB resistance of long span beams with hot rolled I sections whose resistance is expected to be governed by elastic LTB resistance. The underlying model captures geometric nonlinear effects, initial out of straightness, and residual stresses and is based on the onset of yielding failure criterion. Following are the main findings of the study:

1. Among IOS types, twist imperfections (T-IOS) have the most detrimental effect, followed by lateral-torsional (LT-IOS) and lateral (L-IOS) imperfections.

2. Symmetric IOS patterns (P1) consistently lead to the greatest reduction in moment capacity, while asymmetric patterns (P1+2) are less detrimental.

3. Increasing flange width-to-depth ratio reduces LTB resistance, while increasing flange slenderness and span ratio improves it. Web slenderness has a minimal impact. These trends align with the Eurocode and Australian Standards.

4. The Canadian and American standards, which neglect IOS, consistently overpredict LTB resistance in the elastic LTB regime, when compared to the predictions of the present study which captures IOS effects.

5. A new threshold for twist IOS is proposed: an amplitude of L/1700 produces strength reductions comparable to LT-IOS with L/1000 amplitude. This fills a gap in current design standards and supports more consistent imperfection modeling.

6. A family of simplified regression equations is developed to predict LTB resistance under serviceability conditions. It achieves a high accuracy (R^2 = 0.99) across all IOS types and amplitudes, offering a practical tool for engineers to assess elastic LTB capacity with imperfections.

3.9 List of Symbols

a , n	Dimensionless regression coefficients
A	Cross-sectional area
b , t	Flange width and thickness
C_b	Moment gradient factor
d , w	Web height and thickness
E	Young modulus
F_y	Yield strength
F_r	Compressive residual stresses at flange tips
G	Shear modulus
I_y	Moment of inertia about the minor axis
I_x	Moment of inertia about the major axis
I_ω	Warping constant
J	Saint-Venant torsional constant
L	Span
L_t	Threshold span between inelastic and elastic LTB according to American specifications
L_{tc}	Threshold span between inelastic and elastic LTB according to Canadian standards
M_u	Critical moment for a perfectly straight beam
M_p	plastic moment resistance
M	Bending moment obtained from the present FEA
r^2	Coefficient of determination
S_x	Elastic section modulus about the major axis
u_T	Top flange lateral TOS
u_B	Bottom flange lateral TOS

3.10 References

[3.1] CSA-Group, *CSA S16:24 Design and Construction of Steel Structures*, Tenth edit. CA: Canadian Institute of Steel Construction, 2024.
[3.2] ANSI/AISC 360-22, *Specification for structural steel buildings*. Chicago, IL: American Institute of Steel Construction (AISC), 2022.

[3.3] EN-1993-1-1-22, *Eurocode 3: Design of Steel Structures-General Rules and Rules for Buildings*. Brussels, Belgium: European Committee of Standardization (CEN), 2020.
[3.4] AS4100, *Steel structures*. Sydney: Standard Australia, 2020.
[3.5] J. Szalai and F. Papp, "On the theoretical background of the generalization of Ayrton-Perry type resistance formulas," *J. Constr. Steel Res.*, vol. 66, no. 5, pp. 670–679, 2010, doi: 10.1016/j.jcsr.2009.12.013.
[3.6] Y. Fukumoto and Y. Itoh, "EVALUATING THE ULTIMATE STRENGTH OF STEEL STRUCTURAL MEMBERS," *Japan Soc. Civ. Eng.*, vol. 1981, no. 312, p. pp.59-72, 1981, doi: 10.2208/jscej1969.1981.312_59.
[3.7] A. S. Hasham and K. J. R. Rasmussen, "Member capacity of thin-walled I-sections in combined compression and major axis bending," *Univ. Sydney, Dept. Civ. Eng.*, 1997.
[3.8] M. Fortan and B. Rossi, "Lateral Torsional Buckling of Welded Stainless Steel I-Profile Beams: Experimental Study," *J. Struct. Eng.*, vol. 147, no. 3, pp. 1–12, 2021, doi: 10.1061/(asce)st.1943-541x.0002927.
[3.9] R. Stroetmann and S. Fominow, "Imperfections for the LTB-design of Members with I-sections," *ce/papers*, vol. 5, no. 4, pp. 290–299, 2022, doi: 10.1002/cepa.1758.
[3.10] H. Yoshida and K. Maegawa, "Lateral instability of I-beams with imperfections," *J. Struct. Eng.*, vol. 110, no. 8, pp. 1875–1892, 1984, doi: 10.1061/(asce)0733-9445(1984)110:8(1875).
[3.11] J. P. Smith-Pardo and J. D. Aristizábal-Ochoa, "Buckling reversals of axially restrained imperfect beam-column," *J. Eng. Mech.*, vol. 125, no. 4, pp. 401–409, 1999, doi: 10.1061/(asce)0733-9399(1999)125:4(401).
[3.12] A. Agüero and F. J. Pallarés, "Proposal to evaluate the ultimate limit state of slender structures. Part 1: Technical aspects," *Eng. Struct.*, vol. 29, no. 4, pp. 483–497, 2007, doi: 10.1016/j.engstruct.2006.05.014.
[3.13] C. Nguyen, J. Moon, V. N. Le, and H. E. Lee, "Lateral-torsional buckling of I-girders with discrete torsional bracings," *J. Constr. Steel Res.*, vol. 66, no. 2, pp. 170–177, 2010, doi: 10.1016/j.jcsr.2009.09.011.
[3.14] F. McCann, M. A. Wadee, and L. Gardner, "Lateral Stability of Imperfect Discretely Braced Steel Beams," *J. Eng. Mech.*, vol. 139, no. 10, pp. 1341–1349, 2013, doi: 10.1061/(asce)em.1943-7889.0000586.
[3.15] F. Ascione, "Influence of initial geometric imperfections in the lateral buckling problem of thin walled pultruded GFRP I-profiles," *Compos. Struct.*, vol. 112, no. 1, pp. 85–99, 2014, doi: 10.1016/j.compstruct.2014.02.002.
[3.16] A. Agüero, F. J. Pallarés, and L. Pallarés, "Equivalent geometric imperfection definition in steel structures sensitive to lateral torsional buckling due to bending moment," *Eng. Struct.*, vol. 96, pp. 41–55, 2015, doi: 10.1016/j.engstruct.2015.03.066.
[3.17] T. T. Nguyen, T. M. Chan, and J. T. Mottram, "Lateral – Torsional Buckling design for pultruded FRP beams," *Compos. Struct.*, vol. 133, pp. 782–793, 2015, doi: 10.1016/j.compstruct.2015.07.079.
[3.18] M. Li, "Effect of the Initial Out-of-Straightness on the Lateral Torsional Buckling Strength of Steel Beams," *(masters Sci. Diss. Univ. d'Ottawa/University Ottawa)*, 2017.
[3.19] S. P. Machado, "Non-linear stability analysis of imperfect thin-walled composite beams," *Int. J. Non. Linear. Mech.*, vol. 45, no. 2, pp. 100–110, 2010, doi: 10.1016/j.ijnonlinmec.2009.09.006.
[3.20] T. T. Nguyen, T. M. Chan, and J. T. Mottram, "Influence of boundary conditions and geometric imperfections on lateral-torsional buckling resistance of a pultruded FRP I-beam by FEA," *Compos. Struct.*, vol. 100, pp. 233–242, 2013, doi: 10.1016/j.compstruct.2012.12.023.
[3.21] A. Agüero, L. Pallarés, and F. J. Pallarés, "Equivalent geometric imperfection definition in steel structures sensitive to flexural and/or torsional buckling due to compression," *Eng. Struct.*, vol. 96, pp. 160–177, 2015, doi: 10.1016/j.engstruct.2015.03.065.
[3.22] A. Agüero, I. Baláž, and Y. Koleková, "New method for metal beams sensitive to lateral torsional buckling with an equivalent geometrical UGLI imperfection," *Structures*, vol. 29, no. November 2020, pp. 1445–1462, 2021, doi: 10.1016/j.istruc.2020.11.047.
[3.23] D. Dubina and V. Ungureanu, "Effect of imperfections on numerical simulation of instability behaviour of cold-formed steel members," *Thin-Walled Struct.*, vol. 40, no. 3, pp. 239–262, 2002, doi: 10.1016/S0263-8231(01)00046-5.
[3.24] N. Boissonnade and H. Somja, "Influence of imperfections in FEM modeling of lateral torsional buckling," in *Structural Stability Research Council Annual Stability Conference 2012*, 2012, pp. 399–413.
[3.25] L. Subramanian and D. W. White, "Resolving the disconnects between lateral torsional buckling experimental tests, test simulations and design strength equations," *J. Constr. Steel Res.*, vol. 128, pp. 321–334, 2017, doi: 10.1016/j.jcsr.2016.08.009.
[3.26] H. H. Snijder, R. P. van der Aa, H. Hofmeyer, and B. W. E. M. van Hove, "Lateral torsional buckling design imperfections for use in non-linear FEA," *Steel Constr.*, vol. 11, no. 1, pp. 49–56, 2018, doi: 10.1002/stco.201810015.
[3.27] I. Kabir and A. K. Bhowmick, "Lateral torsional buckling of welded wide flange beams under constant moment," *Can. J. Civ. Eng.*, vol. 45, no. 9, pp. 766–779, 2018, doi: 10.1139/cjce-2017-0499.

[3.28] I. Kabir and A. K. Bhowmick, “Applicability of North American standards for lateral torsional buckling of welded I-beams,” *J. Constr. Steel Res.*, vol. 147, pp. 16–26, 2018, doi: 10.1016/j.jcsr.2018.03.029.
[3.29] M. Fortan and B. Rossi, “Lateral Torsional Buckling of Welded Stainless-Steel I-Profile Beams: Design and Reliability,” *J. Struct. Eng.*, vol. 146, no. 12, pp. 1–12, 2020, doi: 10.1061/(asce)st.1943-541x.0002830.
[3.30] X. L. “Dimple” Ji, S. C. Twizell, R. G. Driver, and A. Imanpour, “Lateral Torsional Buckling Response of Compact I-Shaped Welded Steel Girders,” *J. Struct. Eng.*, vol. 148, no. 10, pp. 1–13, 2022, doi: 10.1061/(asce)st.1943-541x.0003431.
[3.31] C. Quan, F. Walport, and L. Gardner, “Equivalent imperfections for the out-of-plane stability design of steel beams by second-order inelastic analysis,” *Eng. Struct.*, vol. 251, no. PB, p. 113481, 2022, doi: 10.1016/j.engstruct.2021.113481.
[3.32] C. Quan, F. Walport, and L. Gardner, “Equivalent geometric imperfections for the design of steel and stainless steel beam-columns by GMNIA,” *J. Constr. Steel Res.*, vol. 215, no. September 2023, p. 108502, 2024, doi: 10.1016/j.jcsr.2024.108502.
[3.33] A. Sahraei, A. Iranpour, and M. Mohareb, “User manual for LTB-UO V3.0 (LTB-UO is a computer program for Lateral Torsional Buckling analysis of beams/beam-columns, written at the University of Ottawa),” 2020, *University of Ottawa*.
[3.34] Canadian Institute of Steel Construction, “CISC, Handbook of steel construction, in: Canadian Institute of Steel Construction, 11th ed., Lakeside Group Inc, Ontario, Canada, 2017.,” *Handb. Steel Constr.*, p. 1092, 2021.

Chapter 4: Geometrically Nonlinear Analysis of Monosymmetric Members with Imperfections

Abstract

The present study develops a finite element formulation for the geometrically nonlinear analysis of thin-walled beams with I-shaped monosymmetric cross-sections. Based on the updated Lagrangian approach, the formulation incorporates key effects, including initial out-of-straightness, residual stresses, and load height effect. The developed solution is employed in conjunction with an onset-of-yielding criterion to characterize the lateral–torsional buckling resistance of long-span, laterally unbraced monosymmetric members subjected to major axis bending. The model is further utilized to examine the effects of load type, initial out-of-straightness amplitudes and patterns, including lateral, lateral-torsional, and torsional, and configurations in which either the smaller or larger flange is subjected to compression. The resulting database enables comparisons between computed buckling resistances and predictions from design equations in the Eurocode and the American, Canadian, and Australian standards.

Keywords

Lateral torsional buckling, geometric nonlinear analysis, finite element, monosymmetric beams, residual stresses, and initial out-of-straightness.

4.1 Introduction and Motivation

Monosymmetric I-shaped beams with unequal flanges offer an efficient solution for roof structures in buildings where gravity-induced positive bending moments typically exceed the negative moments caused by wind uplift. Their use in such scenarios allows for optimized material usage and potential cost savings. In addition to their use in building roofs, wide flange monosymmetric

beams are commonly employed as girders in steel bridge construction. When the top flange is connected to a concrete deck to form a composite section, using girders with smaller top flanges can be a cost-effective choice. In these cases, the concrete deck typically provides continuous lateral and torsional restraint in the completed structure, which helps prevent lateral-torsional buckling. However, this form of buckling may still occur during construction, prior to the placement of concrete. Therefore, it is essential to quantify the lateral-torsional buckling resistance of monosymmetric beams. This resistance is significantly affected by unavoidable imperfections introduced during manufacturing, handling, and erection. These imperfections include residual stresses resulting from uneven cooling after hot-rolling or welding. Imperfections also include initial out-of-straightness (IOS), which may manifest as lateral sweep, camber, twist, or cross-section distortion. Steel construction standards specify allowable IOS limits for camber and sweep, typically expressed as proportions of the member span. Yet, current structural steel design standards differ significantly in how they estimate the flexural resistance of laterally unbraced monosymmetric beams subjected to major axis bending. The Canadian standard [4.1] and American specifications [4.2] use a segmented approach, categorizing beam behaviour into three regimes: short-span members governed by yielding, intermediate spans by inelastic lateral-torsional buckling (LTB), and long spans by elastic LTB. In the elastic regime, both standards assume ideal conditions by using the full elastic critical moment for perfectly straight members, thereby overlooking the impact of initial out-of-straightness (IOS). In contrast, Eurocode 3 [4.3] and the Australian standard [4.4] adopt unified design equations that smoothly transition across all three regimes. A key distinction lies in their treatment of elastic LTB resistance: while the Canadian and American standards base their provisions on idealized perfectly straight members, Eurocode

3 and the Australian standard explicitly incorporate IOS effects, resulting in more conservative flexural resistance estimates that reflect real imperfections.

Loading height relative to the shear center is known to alter the LTB resistance of beams. Applying gravity loads above the shear center results in a reduction in the elastic critical moment compared to shear center loading, while applying them below the shear center enhances the elastic critical moment. Yet, the LTB design provisions for monosymmetric members in current standards have limitations related to the treatment of load height effects. Both Canadian and American standards incorporate moment gradient factors in the elastic critical moment equations, but these are limited to loading applied at the cross-section's mid-height. While both standards do not offer explicit guidance on how to account for load eccentricity for monosymmetric members, [4.5] has provided an empirical approach based on shell finite element simulations. In contrast, the Australian standard recommends the use of advanced buckling analysis to capture the effects of load height effect through available computational tools based on eigenvalue buckling analysis for perfectly straight members (e.g., [4.6]). Yet, the interaction between load eccentricity, residual stresses, and IOS in the context of monosymmetric cross-sections has received little attention and is the scope of the present study.

4.2 Literature Review

The following literature surveys focus on studies that developed geometrically nonlinear solutions for monosymmetric and asymmetric structural members. Following this, it provides investigations that specifically address the influence of residual stress and load height effects on member behaviour.

4.2.1 Geometrically Nonlinear Formulations for Monosymmetric Beams

Geometrically nonlinear finite element formulations for monosymmetric members have been developed based on the Total Lagrangian (TL), Updated Lagrangian (UL), and Co-Rotational (CR) approaches. Studies based on the TL approach include the work of Kitipornchai and Chan [4.7] which captured the effect of cross-section asymmetry, Yang et al. [4.8] which extended the formulation to horizontally curved members while accounting for shear deformation and Wang and Yang [4.9] which developed a shear-deformable thin-walled finite element with an additional mid-span node alongside the conventional end nodes.

Studies adopting the CR approach include the work of Hsiao and Lin [4.10] on channel sections. Chen et al. [4.11] extended the approach using a second-order linearization to tackle more general monosymmetric and asymmetric or cross-sections. Battini and Pacoste [4.12] formulated a 3D beam formulation capturing large-rotation and plastic in asymmetric members. Alsafadie et al. [4.13] developed a two-field Hellinger–Reissner co-rotational element incorporating plasticity and large rotations. Du and Hajjar [4.14] formulated a 3D displacement-based beam element for non-symmetric open sections tailored for angle, tee, and channel profiles. Jonker [4.15] developed a generalized strain-based FE formulation for monosymmetric and asymmetric cross-sections that captures coupled bending–torsion–warping behavior.

Updated Lagrangian formulations include the work of Conci [4.16] on the analysis of space frames composed of thin-walled members. Vo and Lee [4.17] adopted the von Kármán strain approximation within a first-order shear deformable theory to formulate a solution for monosymmetric composite I-beams. Kim and Lee [4.18] and Phi et al. [4.19] formulated solutions that capture the shear deformation effects of functionally graded sandwich monosymmetric I-beam

sections. Chen et al. [4.20] adopted the Modified Tangent Modulus method to account for material nonlinearity in asymmetric members.

The Generalized Beam Theory (GBT) provides a viable framework to formulate geometrically nonlinear solutions for monosymmetric members. This includes the work of Silvestre and Camotim [4.19, 4.20] who formulated a GBT solution to investigate local–distortional interactions with imperfections in lipped-channel columns. Also, Basaglia et al. [4.23] developed a GBT solution within the updated Lagrangian scheme to directly incorporate IOS into the geometric nonlinear analysis of monosymmetric and asymmetric members.

4.2.2 Effect of Residual Stresses

Residual stress can notably affect the buckling strength of steel beams and should be assessed with geometric nonlinearities. Hot-rolled sections typically exhibit nearly symmetric residual stress patterns in doubly symmetric members, whereas monosymmetric sections display distinct and often asymmetric stress distributions [4.24]. In contrast, welded members tend to develop localized residual stress peaks near weld lines and heat-affected zones, which can significantly intensify torsion–bending coupling during lateral–torsional buckling (LTB), as reported by Hsiao [4.11], Hajjar [4.14]. When combined with initial geometric imperfections, residual stresses have been reported to further reduce the effective stiffness and critical moment, producing strength losses greater than the sum of individual effects [4.21], an aspect that is numerically assessed in the present study.

4.2.3 Load-Height Effect

While numerous studies addressed the load height effect on the elastic critical moment of doubly symmetric members, fewer studies have focused on load height effects on monosymmetric members. This includes the work of Helwig et al. [4.5] who conducted a shell-based finite-

element-parametric study based on elastic eigenvalue analysis, and provided recommendations to capture the load height effect on the LTB resistance of monosymmetric I beams. Also, nonlinear analyses (e.g., Basaglia [4.23]) have shown that top-flange loading lowers the lateral–torsional buckling resistance, especially when combined with residual stresses

Table 4.1 provides a comparative summary of thin-walled beam studies focused on the geometrically nonlinear analysis of monosymmetric members. A key commonality across all the studies listed is their incorporation of global warping and geometric nonlinearity**.** Beyond these shared features, the table outlines and contrasts additional analytical considerations addressed in the literature, including material nonlinearity**,** shear deformation effects**,** load height influence**,** initial out-of-straightness**,** residual stress effects**,** and the treatment of local warping phenomena.

Among these studies, only the GBT studies in [4.18], [4.19], [4.20] examined the effects of IOS on the flexural resistance of the member. However, these studies focused on cold-formed members. A shell-based analysis [4.25] examined the impact of lateral (L-IOS), lateral-torsional (LT-IOS), and torsional (T-IOS) initial out-of-straightness imperfections on the lateral-torsional buckling resistance of monosymmetric I-shaped members, while other studies on the effect of IOS effect on LTB resistance has been directed to doubly symmetric beams, as presented in the literature surveys of Chapter 2 and Chapter 3. In this context, the present study contributes to state knowledge by formulating a geometrically nonlinear analysis for monosymmetric members that captures the effect of residual stresses and initial of straightness. The model is subsequently used to investigate the effects of IOS on the LTB resistance of long-span laterally unbraced flexural monosymmetric members.

Table 4.1 Comparative summary of geometric nonlinear formulations of monosymmetric thin-walled beam

Author(s)	X-section (1)	Approach (2)	Effects Captured (3)						Core idea / method
			MN	SD	LH	IOS	RS	LW	
Kitipornchai & Chan [4.7]	M	TL						✓	Geometric stiffness; leg asymmetry effects
Conci [4.16]	M/A	UL							UL stiffness for large-displacement thin-walled frames.
Vo & Lee [4.17]	M	UL		✓				✓	von Kármán strain; local warping & shear; laminate theory.
Alsafadie et al. [4.13]	M	CR	✓	✓					Two-field Hellinger–Reissner element with plasticity
Phi et al. [4.19]	M	UL						✓	Buckling/lateral buckling of FG mono I-beams.
Kim & Lee [4.18]	M	UL		✓				✓	GNL of FG sandwich I-beams (mono cross-section).
Hsiao & Lin [4.10]	M	CR						✓	Warping DOF; 3rd-order twist/curvature captured
Chen, Lin & Hsiao [4.11]	A	CR						✓	Efficient geometric NL with warping torsion
Du & Hajjar [4.14]	A	CR						✓	Geom. exact element; OpenSees implementation; frame-scale
Silvestre & Camotim [4.21]	M	UL				✓		✓	GBT, global and local IOS effects on cold-formed members
Wang and Yang [4.9]	A	TL		✓					Shear deformation Internal-node enhancement
Silvestre & Camotim [4.22]	M	UL				✓		✓	GBT, stiffened lipped channel of cold-formed columns
Yang and Wang [4.8]	A	TL	✓	✓					Avoids shear locking by introducing an intermediate node
Basaglia et al. [4.23]	M/A	UL				✓		✓	GBT, cold-formed I-section columns and lipped channel columns and beams
Chen et al. [4.26]	A	UL			✓				Captures variation of sectional properties along the span due to non-uniform torsional deformation
Battini & Pacoste [4.12]	M/A	CR						✓	3D co-rotational beam elements, including branch-switching
Jonker [4.15]	A	CR			✓				Generalized strain-based finite element for nonlinear
Present study	**M**	**UL**			✓	✓	✓	✓	

(1) D = doubly symmetric, M = monosymmetric, A = asymmetric.
(2) UL= updated Lagrangian, TL= total Lagrangian, CR= co-rotational
(3) MN= material nonlinearity, SD= shear deformation, LH= load height, IOS= initial out straightness, RS= residual stress, LW= local warping

4.3 Assumptions

The finite element (FE) formulation is developed based on the following assumptions:

1. Kinematic Framework: The formulation adheres to the kinematics of Gjelsvik's thin-walled beam theory, which includes:

    1.1 Rigid cross-sectional motion: The cross-section translates and rotates as a rigid disk within its own plane.

    1.2 Negligible shear strains: Shear deformation within the middle surface is considered insignificant.

    1.3 Preservation of normal: Lines initially normal to the undeformed middle surface remain straight and perpendicular after deformation.

2. Geometric Nonlinear Effects: The formulation captures moderate rotations and small strains.

3. Shear Strain Simplification: For points offset from the middle surface, the nonlinear component of shear strain is assumed negligible compared to the linear component.

4. Section Geometry: The formulation is restricted to mono-symmetric I-sections with unequal flanges.

5. Coordinate System: The coordinate system is defined to satisfy orthogonality conditions by employing centroidal principal axes, a principal sectorial origin, and locating the at the shear centre.

6. Constitutive Behavior: The material is modeled as linearly elastic and isotropic, following the Saint–Venant–Kirchhoff constitutive law while representing the longitudinal residual stress effects as an initial stress field.

7. Development Sequence: The formulation is initially developed for a perfectly straight member without residual stresses in Section 4. Enhancements to include initial out-of-straightness (IOS) and residual stress effects are introduced in Section 5.

4.4 Formulation for Members with No Imperfections

4.4.1 General

Consider a thin-walled member in an undeformed state $C(0)$ at time $t = 0$. Under a specified load level at time t, the member is assumed to have attained a known equilibrium state $C(t)$, such that the displacements of a generic point for a generic point $B(z,s,n)$ within the member volume are characterized by longitudinal, tangential, and normal displacements $\tilde{w}(z,s,n)$ $\tilde{u}_t(z,s,n)$ $\tilde{u}_n(z,s,n)$, where z is a longitudinal coordinate, s is a tangential coordinate defined along the middle surface of the cross-section, n is a normal coordinate that denotes the offset of the point B from its projection B' on the middle surface, and the (z,s,n) coordinates form a right-handed coordinate system (Fig. 4.1a). The load level is then incremented, such that a new unknown equilibrium state $C(t+\Delta t)$ is reached at the time $t+\Delta t$. Under the load increase, the member undergoes additional unknown displacement increments ${}_t\tilde{w}(z,s,n)$, ${}_t\tilde{u}_t(z,s,n)$, and ${}_t\tilde{u}_n(z,s,n)$ from $C(t)$ to $C(t+\Delta t)$.

4.4.2 Thin-walled Beam Kinematics

Consider a prismatic thin-walled member with a mono-symmetric cross-section (Fig. 4.1c). A Cartesian coordinate system x, y, z is defined such that its origin O coincides with the section centroid, i.e., $\int_A (x, y)\, dA = (0,0)$. Axes orientations are selected such that the axis of symmetry y of the cross-section coincides with the web, i.e., $\int_A xy dA = 0$. A principal sectorial origin is adopted such that $\int_A \omega dA = 0$, and the pole P is taken to coincide with the shear centre S. Owing to the symmetry of the cross-section about the y axis, the orthogonality conditions $\int_A (\omega, \omega y)\, dA = (0,0)$ imply that the principal sectorial origin and the shear centre lie on the axis of symmetry, and the remaining orthogonality condition $\int_A \omega x d^t A = 0$ yields coordinate y_{sc} of the shear centre along the y axis relative to the centroid. For an I-shaped cross-section (Fig. 4.1c) with a top flange dimensions $b_t \times e_f$, bottom flange dimensions $b_b \times e_f$ and web dimensions $d \times e_w$, coordinate y_{sc} [6] is given by

$$y_{sc} = \frac{b_b^{\,3}(d - y_t) - b_t^{\,3} y_t}{b_b^{\,3} + b_t^{\,3}} \tag{4.1}$$

in which the distance from the top flange to the section centroid is $y_t = \left(b_b e_f d + 0.5 e_w d^2\right) \Big/ \left(b_t e_f + b_b e_f + d e_w\right)$. The displacement increments from $C(t)$ to $C(t + \Delta t)$ of a generic point $B(z, s, n)$ within the volume of the member are denoted as ${}_t\tilde{w}(z, s, n)$, ${}_t\tilde{u}_t(z, s, n)$, ${}_t\tilde{u}_n(z, s, n)$ and are expressed in terms of the incremental shear centre displacements

[6] Appendix H derives expressions for the centroidal and shear centre coordinates for monosymmetric I-sections

${}_t\xi(z)$, ${}_t\eta(z)$ along the x, y directions, longitudinal displacement ${}_t\zeta(z)$ at the centroid, and the angle of twist ${}_t\theta(z)$ of the cross-section through (Assumptions 1.1-1) (e.g., [4.27])

$$
\begin{aligned}
{}_t\tilde{w} &= {}_t\zeta - \left[\partial_t\xi/\partial {}^t z\right] {}^t x - \left[\partial_t\eta/\partial {}^t z\right] {}^t y - \left[\partial_t\theta/\partial {}^t z\right] {}^t\omega \\
{}_t\tilde{u}_t &= {}_t\xi\cos {}^t\alpha + {}_t\eta\sin {}^t\alpha + {}_t\theta\left[{}^t h + {}^t n\right] \\
{}_t\tilde{u}_n &= {}_t\xi\sin {}^t\alpha - {}_t\eta\cos {}^t\alpha - {}_t\theta\, {}^t q
\end{aligned}
\qquad (4.2)\text{a-c}
$$

in which coordinates $\left({}^t x, {}^t y, {}^t\omega\right)$ of point B are the sum of the global coordinates $\left({}^t\hat{x}, {}^t\hat{y}, {}^t\hat{\omega}\right)$ of its projection on the middle surface and $\left({}^t\hat{\hat{x}}, {}^t\hat{\hat{y}}, {}^t\hat{\hat{\omega}}\right)$ of point B' relative to point B, i.e.,

$$
\left({}^t x, {}^t y, {}^t\omega\right) = \left({}^t\hat{x}, {}^t\hat{y}, {}^t\hat{\omega}\right) + \left({}^t\hat{\hat{x}}, {}^t\hat{\hat{y}}, {}^t\hat{\hat{\omega}}\right) \qquad \left({}^t\hat{\hat{x}}, {}^t\hat{\hat{y}}, {}^t\hat{\hat{\omega}}\right) = {}^t n\left(\sin {}^t\alpha, -\cos {}^t\alpha, -{}^t q\right) \qquad (4.3)\text{a-c}
$$

and ${}^t\hat{x}$, ${}^t\hat{y}$ are the lateral and transverse coordinates, ${}^t\alpha$ is the angle of the tangent to the middle surface at B' relative to the ${}^t x$ axis, ${}^t\hat{\omega} = \int_{s_0}^{{}^t s} {}^t h\, d\, {}^t s$ is the global warping function at B' relative to the principal sectorial origin s_0, ${}^t h$ and ${}^t q$ are the normal and tangential distances from the shear center to point B'. For a section symmetric about the y axis, ${}^t h$ and ${}^t q$ are given by

$$
{}^t h = {}^t\hat{x}\sin {}^t\alpha - \left({}^t\hat{y} - y_{sc}\right)\cos {}^t\alpha \qquad {}^t q = {}^t\hat{x}\cos {}^t\alpha + \left({}^t\hat{y} - y_{sc}\right)\sin {}^t\alpha \qquad (4.4)\text{a-b}
$$

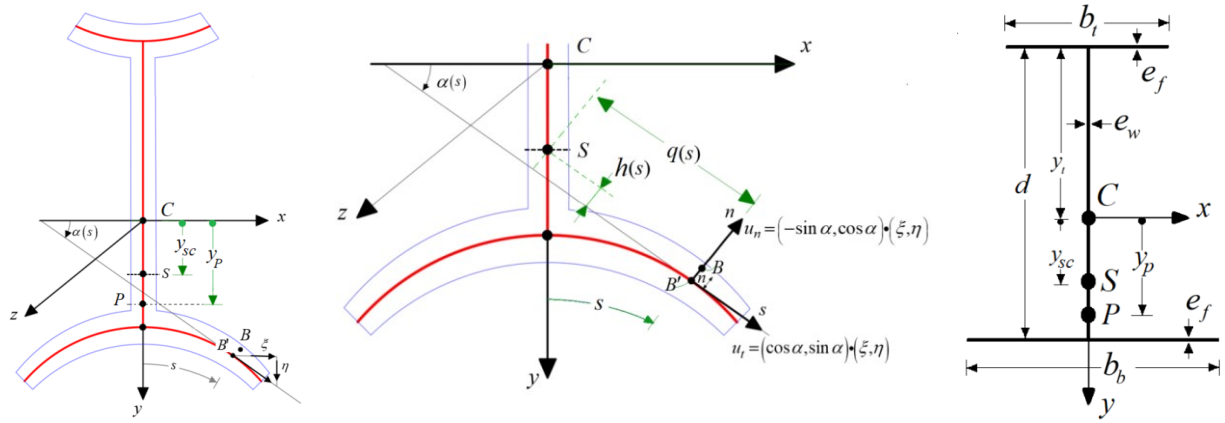

(a) **(b)** **(c)**

Fig. 4.1 (a) Cartesian Coordinates and displacements, (b) Curvilinear Coordinates and displacements, and (c) Cross-sectional dimensions

4.4.3 Strain-Displacement Relationships

The non-vanishing incremental components of the Green-Lagrange (GL) strain tensor ${}_t\varepsilon_{zz}$ and ${}_t\varepsilon_{zs}$ are expressed in terms of the displacement increments ${}_t\tilde{w}$, ${}_t\tilde{u}_t$, ${}_t\tilde{u}_n$ and noting that $\left(\partial_t\tilde{w}/\partial^t z\right)$ is negligible compared to unity (Assumption 3), and that for a long-span member, the nonlinear component of the shear strain can be omitted (Assumptions 1.1-2), one obtains

$$ {}_t\varepsilon_{zz} = {}_t\varepsilon^L_{zz} + {}_t\varepsilon^N_{zz}, \qquad {}_t\varepsilon^L_{zz} = \frac{\partial_t\tilde{w}}{\partial^t z}, \qquad {}_t\varepsilon^N_{zz} \approx \frac{1}{2}\left[\left(\frac{\partial_t\tilde{u}_t}{\partial^t z}\right)^2 + \left(\frac{\partial_t\tilde{u}_n}{\partial^t z}\right)^2\right] \tag{4.5)a-c} $$

$$ {}_t\varepsilon_{zs} \approx {}_t\varepsilon^L_{zs} = \frac{1}{2}\left(\frac{\partial_t\tilde{w}}{\partial^t s} + \frac{\partial_t\tilde{u}_t}{\partial^t z}\right) \tag{4.6} $$

in which ${}_t\varepsilon^L_{zz}$ and ${}_t\varepsilon^L_{zs}$ are the linear components of the GL strain increments and ${}_t\varepsilon^N_{zz}$ and ${}_t\varepsilon^N_{zs}$ are the nonlinear components. From Eq. (4.2)-(4.4) by substituting into Eq. (4.5),(4.6) the GL strain components are expressed as

$$
{}_t\varepsilon_{zz}^{L} = {}_t\zeta' - {}_t\xi''\,{}^t x - {}_t\eta''\,{}^t y - {}_t\theta''\,{}^t\omega \qquad {}_t\varepsilon_{zs}^{L} = {}_t\theta'\,{}^t n
$$
$$
{}_t\varepsilon_{zz}^{N} = \frac{1}{2}\,{}_t\xi'^2 + \frac{1}{2}\,{}_t\eta'^2 + \frac{1}{2}\,{}_t\theta'^2\left({}^t\hat{x}^2 + {}^t\hat{y}^2 + 2\,{}^t h\,{}^t n + {}^t n^2\right) - {}_t\xi'\,{}_t\theta'\,{}^t y + {}_t\eta'\,{}_t\theta'\,{}^t x \tag{4.7}\text{a-c}
$$

in which all primes denote derivatives with respect to coordinate ${}^t z$.

4.4.4 Variational Principle

Within the updated Lagrangian framework, the principle of virtual work is expressed as (e.g., [4.28])

$$
{}^{t+\Delta t}_{t}\bar{U} - {}^{t+\Delta t}_{t}\bar{R} = 0 \tag{4.8}
$$

in which ${}^{t+\Delta t}_{t}U$ is the internal work, ${}^{t+\Delta t}_{t}R$ is the external work by the forces, and all overbars denote virtual quantities, and the left subscripts denote the configuration to which the object is referred, and left superscripts denote the configuration at which it is evaluated.

4.4.5 Internal Virtual Work

For a Saint–Venant–Kirchhoff constitutive material (Assumption 6), the linearized form of the internal virtual work ${}^{t+\Delta t}_{t}\bar{U}$ for the incremental deformation configuration for $C(t)$ to $C(t+\Delta t)$ (e.g., Chapter 2) can be expressed as

$$
{}^{t+\Delta t}_{t}\bar{U} = {}^{t+\Delta t}_{t}\bar{U}_1 + {}^{t+\Delta t}_{t}\bar{U}_2 + {}^{t+\Delta t}_{t}\bar{U}_3 + {}^{t+\Delta t}_{t}\bar{U}_4
$$
$$
\left({}^{t+\Delta t}_{t}\bar{U}_1, {}^{t+\Delta t}_{t}\bar{U}_2, {}^{t+\Delta t}_{t}\bar{U}_3, {}^{t+\Delta t}_{t}\bar{U}_4\right) = \int_{{}^tV}\left[\left(E\,{}_t\varepsilon_{zz}^{L}\,{}_t\bar{\varepsilon}_{zz}^{L}\right), \left(4G\,{}_t\varepsilon_{zs}^{L}\,{}_t\bar{\varepsilon}_{zs}^{L}\right), \left({}_t\bar{\varepsilon}_{zz}^{N}\sigma_{zz}\right), \left({}_t\bar{\varepsilon}_{zz}^{L}\sigma_{zz} + 2\,{}_t\bar{\varepsilon}_{zs}^{L}\sigma_{zs}\right)\right] d\,{}^tV \tag{4.9}\text{a-e}
$$

in which all overbars denote virtual quantities, and σ_{zz} and σ_{zs} are normal and shear components of the Cauchy stress tensor. As will be discussed under Section 5, the normal stress σ_{zz} has a component induced by load effects and an additional component due to initial stresses. From Eq.

Eqs (4.7)a-c, by substituting into Eq. (4.9)a-e, performing all area integrals, using the orthogonality conditions (Assumption 5) $\int_A \left(x, y, xy, \omega, \omega x, \omega y\right) dA = \left(0,0,0,0,0,0\right)\text{m}$ and adopting the approximation $A \approx {}^{t}A$, one obtains

$$
\begin{aligned}
{}^{t+\Delta t}_{t}\bar{U}_1 &= E\int_{{}^{t}z=0}^{{}^{t}L}\left[\left(A\,{}_{t}\bar{\zeta}'\,{}_{t}\zeta'\right)+\left(I_y\,{}_{t}\bar{\xi}''\,{}_{t}\xi''\right)+\left(I_x\,{}_{t}\bar{\eta}''\,{}_{t}\eta''\right)+\left(I_\omega\,{}_{t}\bar{\theta}''\,{}_{t}\theta''\right)\right]d\,{}^{t}z \\
{}^{t+\Delta t}_{t}\bar{U}_2 &= GJ\int_{{}^{t}z=0}^{{}^{t}L}\left({}_{t}\bar{\theta}'\,{}_{t}\theta'\right)d\,{}^{t}z \\
{}^{t+\Delta t}_{t}\bar{U}_3 &= \int_{{}^{t}z=0}^{{}^{t}L}\left[\left({}_{t}\bar{\xi}'\,{}_{t}\xi'+{}_{t}\bar{\eta}'\,{}_{t}\eta'\right){}^{t}N+\left({}_{t}\bar{\theta}'\,{}_{t}\xi'+{}_{t}\bar{\xi}'\,{}_{t}\theta'\right){}^{t}M_x+\left({}_{t}\bar{\theta}'\,{}_{t}\eta'+{}_{t}\bar{\eta}'\,{}_{t}\theta'\right){}^{t}M_y+\left({}_{t}\bar{\theta}'\,{}_{t}\theta'\right){}^{t}B_s\right]d\,{}^{t}z \\
{}^{t+\Delta t}_{t}\bar{U}_4 &= \int_{{}^{t}z=0}^{{}^{t}L}\left({}_{t}\bar{\zeta}'\,{}^{t}N-{}_{t}\bar{\xi}''\,{}^{t}M_y+{}_{t}\bar{\eta}''\,{}^{t}M_x+{}_{t}\bar{\theta}''\,{}^{t}B+{}_{t}\bar{\theta}'\,{}^{t}T_{sv}\right)d\,{}^{t}z
\end{aligned}
$$

(4.10)a-d

in which the cross-sectional properties $\left(A, I_y, I_x, I_\omega\right) = \int_A \left(1, x^2, y^2, \omega^2\right) dA$ and $J = \left(1/3\right)\int_{{}^{t}s} {}^{t}e^3\, d\,{}^{t}s$ have been defined and ${}^{t}e = {}^{t}e\left(s\right)$ is the thickness. Also, in Eq. (4.10) ${}^{t}N, {}^{t}M_y, {}^{t}M_x, {}^{t}B, {}^{t}T_{sv}, {}^{t}B_s$ are the stress resultants at configuration $C\left(t\right)$ and are defined as

$$\left({}^{t}N, {}^{t}M_y, {}^{t}M_x, {}^{t}B, {}^{t}T_{sv}\right) = \int_A \left(\sigma_{zz}, {}^{t}x\sigma_{zz}, -{}^{t}y\sigma_{zz}, -{}^{t}\omega\sigma_{zz}, 4\,{}^{t}n\sigma_{zs}\right) dA \tag{4.11}$$

$${}^{t}B_s = \int_A \left({}^{t}\hat{x}^2 + {}^{t}\hat{y}^2 + {}^{t}n^2\right)\sigma_{zz} dA + 2y_{sc}\,{}^{t}M_x + {y_{sc}}^2\,{}^{t}N \tag{4.12}$$

4.4.6 External Virtual Work

Consider a member subjected to a transverse line load $q_y\left(z\right)$ acting located at a vertical distance $\left({}^{0}y_p - y_{sc}\right)$ below the shear centre axis. The line of action of the load is denoted by the coordinates $\left({}^{0}x_p = 0, {}^{0}y_p\right)$ in the undeformed state $C\left(0\right)$. The member is assumed to be in a known equilibrium state $C\left(t\right)$ under a load level ${}^{t}q_y\left(z\right)$. In the updated Lagrangian formulation, a finite

element's local coordinate system rotates along with its deformed configuration. Hence the deformed coordinates of the line of action at $C(t)$ remain unchanged, i.e., $\left({}^{t}x_p, {}^{t}y_p, {}^{t}z_p\right) = \left({}^{0}x_p, {}^{0}y_p, {}^{0}z_p\right) = \left(0, y_p, z_p\right)$. Under an additional load increment ${}_{t}q_y(z)$, the $C(t)$ to $C(t+\Delta t)$, the line of action of the load undergoes displacement increments $\left[{}_{t}\xi_p(z), {}_{t}\eta_p(z), {}_{t}\zeta_p(z)\right]$, in which the transverse component is ${}_{t}\eta_p(z) = {}_{t}\eta(z) + {}^{t}x_p\,{}_{t}\theta(z) = {}_{t}\eta(z) - \left(y_p - y_{sc}\right){}^{t}\theta(z)\,{}_{t}\theta(z)$. The external virtual work done by the load increment ${}_{t}q_y(z)$ is given by

$$ {}^{t+\Delta t}_{t}\overline{R} = \int_0^L q_y\left({}^{t}z\right)\left[{}_{t}\eta\left({}^{t}z\right) - \left(y_p - y_{sc}\right){}^{t}\theta(z)\,{}_{t}\theta\left({}^{t}z\right)\right]dz \tag{4.13} $$

For the special case of a point load P_y acting at a longitudinal coordinate ${}^{t}z = {}^{t}z_P$, one has $q_y\left({}^{t}z\right) = P_y\delta\left({}^{t}z - {}^{t}z_e\right)$, in which δ is the Dirac delta function, and Eq. (4.13) yields

$$ {}^{t+\Delta t}_{t}\overline{R} = P_y\left[{}_{t}\eta\left({}^{t}z_e\right) - \left(y_p - y_{sc}\right){}^{t}\theta\left({}^{t}z_e\right){}_{t}\theta\left({}^{t}z_e\right)\right] \tag{4.14} $$

4.4.7 Finite Element Formulation

A two-node finite element is developed with seven DOFs per node. The displacement field increments ${}_{t}\zeta$, ${}_{t}\xi$, ${}_{t}\eta$, and ${}_{t}\theta$ are related to the vectors of nodal DOFs at ends of the element (i.e., nodes *a* and *b*), i.e., ${}_{t}\boldsymbol{\zeta} = \left\langle {}_{t}\zeta_a \quad {}_{t}\zeta_b \right\rangle^{\mathbf{T}}$, ${}_{t}\boldsymbol{\xi} = \left\langle {}_{t}\xi_a \quad {}_{t}\xi'_a \quad {}_{t}\xi_b \quad {}_{t}\xi'_b \right\rangle^{\mathbf{T}}$, ${}_{t}\boldsymbol{\eta} = \left\langle {}_{t}\eta_a \quad {}_{t}\eta'_a \quad {}_{t}\eta_b \quad {}_{t}\eta'_b \right\rangle^{\mathbf{T}}$, and ${}_{t}\boldsymbol{\theta} = \left\langle {}_{t}\theta_a \quad {}_{t}\theta'_a \quad {}_{t}\theta_b \quad {}_{t}\theta'_b \right\rangle^{\mathbf{T}}$ through

$$ {}_{t}\zeta\left({}^{t}z\right) = \mathbf{L}^{\mathbf{T}}\left({}^{t}z\right){}_{t}\boldsymbol{\zeta}, \quad {}_{t}\xi\left({}^{t}z\right) = \mathbf{H_a}^{\mathbf{T}}\left({}^{t}z\right){}_{t}\boldsymbol{\xi}, \quad {}_{t}\eta(z)\,{}^{t}z = \mathbf{H_b}^{\mathbf{T}}\left({}^{t}z\right){}_{t}\boldsymbol{\eta}, \quad {}_{t}\theta\left({}^{t}z\right) = \mathbf{H_a}^{\mathbf{T}}\left({}^{t}z\right){}_{t}\boldsymbol{\theta} $$

(4.15)a-d

in which,

$$\mathbf{L}^{\mathrm{T}} = \left\langle \ (1-\varsigma) \quad \varsigma \right\rangle$$
$$\mathbf{H_a}^{\mathrm{T}} = \left\langle 1-3\varsigma^2+2\varsigma^3 \ \middle| \ {}^tL\varsigma(1-\varsigma)^2 \ \middle| \ 3\varsigma^2-2\varsigma^3 \ \middle| \ {}^tL\varsigma^2(-1+\varsigma) \right\rangle \qquad (4.16)\text{a-c}$$
$$\mathbf{H_b}^{\mathrm{T}} = \left\langle 1-3\varsigma^2+2\varsigma^3 \ \middle| \ -{}^tL\varsigma(1-\varsigma)^2 \ \middle| \ 3\varsigma^2-2\varsigma^3 \ \middle| \ -{}^tL\varsigma^2(-1+\varsigma) \right\rangle$$

where $\varsigma = {}^tz/{}^tL$. From Eqs. (4.16), by substituting into Eqs (4.10), (4.13) one obtains

$${}_t\bar{\mathbf{U}}^{\mathrm{T}}\left(\mathbf{K_E}+{}^t\mathbf{K_G}\right){}_t\mathbf{U} = {}_t\ \bar{\mathbf{U}}^{\mathrm{T}}\left({}^{(t+\Delta t)}\mathbf{\Delta R}-{}^t\mathbf{F}\right) \ {}^{(7)} \qquad (4.17)\text{a-b}$$

in which ${}_t\mathbf{U}^{\mathrm{T}} = \left\langle {}_t\boldsymbol{\zeta}^{\mathrm{T}} \ \middle| \ {}_t\boldsymbol{\xi}^{\mathrm{T}} \ \middle| \ {}_t\boldsymbol{\eta}^{\mathrm{T}} \ \middle| \ {}_t\boldsymbol{\theta}^{\mathrm{T}} \right\rangle$ is the vector of nodal displacements $\mathbf{K_E}$ is the elastic stiffness matrix defined as

$$\mathbf{K_E} = \int_{{}_tz=0}^{{}^tL} \left[\begin{array}{c|c|c|c} EA\mathbf{L}'\mathbf{L}'^{\mathrm{T}} & \mathbf{0} & \mathbf{0} & \mathbf{0} \\ \hline \mathbf{0} & EI_{yy}\mathbf{H}''_{\mathbf{a}}\mathbf{H}''^{\mathrm{T}}_{\mathbf{a}} & \mathbf{0} & \mathbf{0} \\ \hline \mathbf{0} & \mathbf{0} & EI_{xx}\mathbf{H}''_{\mathbf{b}}\mathbf{H}''^{\mathrm{T}}_{\mathbf{b}} & \mathbf{0} \\ \hline \mathbf{0} & \mathbf{0} & \mathbf{0} & \left(EI_{\omega\omega}\mathbf{H}''_{\mathbf{a}}\mathbf{H}''^{\mathrm{T}}_{\mathbf{a}}+GJ\mathbf{H}'_{\mathbf{a}}\mathbf{H}'^{\mathrm{T}}_{\mathbf{a}}\right) \end{array}\right] d\,{}^tz \qquad (4.18)\text{a-f}$$

${}^t\mathbf{K_G}$ is the geometric matrix at configuration $C(t)$ which takes the form

$${}^t\mathbf{K_G} = \left[\begin{array}{c|c|c|c} \mathbf{0} & \mathbf{0} & \mathbf{0} & \mathbf{0} \\ \hline \mathbf{0} & {}^t\mathbf{K}_{\xi\xi} & \mathbf{0} & {}^t\mathbf{K}_{\xi\theta} \\ \hline \mathbf{0} & \mathbf{0} & {}^t\mathbf{K}_{\eta\eta} & {}^t\mathbf{K}_{\eta\theta} \\ \hline \mathbf{0} & {}^t\mathbf{K}_{\xi\theta} & {}^t\mathbf{K}^{\mathrm{T}}_{\eta\theta} & {}^t\mathbf{K}_{\theta\theta} \end{array}\right] = \int_{{}_tz=0}^{{}^tL} \left[\begin{array}{c|c|c|c} \mathbf{0} & \mathbf{0} & \mathbf{0} & \mathbf{0} \\ \hline \mathbf{0} & {}^tN\left(\mathbf{H}'_{\mathbf{a}}\mathbf{H}'^{\mathrm{T}}_{\mathbf{a}}\right) & \mathbf{0} & {}^tM_x\left(\mathbf{H}'_{\mathbf{a}}\mathbf{H}'^{\mathrm{T}}_{\mathbf{a}}\right) \\ \hline \mathbf{0} & \mathbf{0} & {}^tN\left(\mathbf{H}'_{\mathbf{b}}\mathbf{H}'^{\mathrm{T}}_{\mathbf{b}}\right) & {}^tM_y\left(\mathbf{H}'_{\mathbf{b}}\mathbf{H}'^{\mathrm{T}}_{\mathbf{a}}\right) \\ \hline \mathbf{0} & {}^tM_x\left(\mathbf{H}'_{\mathbf{a}}\mathbf{H}'^{\mathrm{T}}_{\mathbf{a}}\right) & {}^tM_y\left(\mathbf{H}'_{\mathbf{a}}\mathbf{H}'^{\mathrm{T}}_{\mathbf{b}}\right) & {}^tB_s\left(\mathbf{H}'_{\mathbf{a}}\mathbf{H}'^{\mathrm{T}}_{\mathbf{a}}\right) \end{array}\right] d\,{}^tz$$

(4.19)

(7) Appendix I provides a verification study for perfectly straight monosymmetric beams.

and ${}^{t}\mathbf{F}^{\mathbf{T}} = \left\langle {}^{t}\mathbf{F}_{\zeta}^{\mathbf{T}} \quad {}^{t}\mathbf{F}_{\xi}^{\mathbf{T}} \quad {}^{t}\mathbf{F}_{\eta}^{\mathbf{T}} \quad {}^{t}\mathbf{F}_{\theta}^{\mathbf{T}} \right\rangle$ is the internal load vector at configuration $C(t)$ and whose sub-vectors have been defined as

$$ {}^{t}\mathbf{F}^{\mathbf{T}} = \int_{{}^{t}z=0}^{{}^{t}L} \left\langle {}^{t}N\mathbf{L}'^{\mathbf{T}} \;\vdots\; -{}^{t}M_{y}\mathbf{H}_{\mathbf{a}}''^{\mathbf{T}} \;\vdots\; {}^{t}M_{x}\mathbf{H}_{\mathbf{b}}''^{\mathbf{T}} \;\vdots\; \left({}^{t}B\mathbf{H}_{\mathbf{a}}''^{\mathbf{T}} + {}^{t}T_{sv}\mathbf{H}_{\mathbf{a}}'^{\mathbf{T}} \right) \right\rangle d\,{}^{t}z \tag{4.20a-c} $$

and the equivalent force vector from time t to $t+\Delta t$ is,

$$ {}^{(t+\Delta t)}\mathbf{\Delta R} = \int_{0}^{L} \begin{Bmatrix} \mathbf{0} \\ \mathbf{0} \\ q_{y}\left({}^{t}z\right)\mathbf{H}_{\mathbf{b}}\left({}^{t}z\right) \\ q_{y}\left({}^{t}z\right)\left(y_{p}-y_{sc}\right)\mathbf{H}_{\mathbf{a}}\left({}^{t}z\right)\mathbf{H}_{\mathbf{a}}^{\mathbf{T}}\left({}^{t}z\right)\,{}_{t}\boldsymbol{\theta} \end{Bmatrix} dz \tag{4.21} $$

4.5 Incorporating Imperfections in First Loading Increment

In the most general case, the member is assumed to possess an initial stress state due to residual stress**.** Additionally, the member may exhibit initial out-of-straightness**,** arising from manufacturing or handling processes, and typically characterized by lateral (L-IOS)**,** camber (C-IOS)**,** and twist (T-IOS) deviations, respectively denoted by symbols $\xi_{0}(z)$, $\eta_{0}(z)$, $\theta_{0}(z)$. Under loading, the member undergoes displacements $\left[\xi(z),\eta(z),\theta(z)\right]$ from its initially crooked position, such that the total out-of-straightness is $\left[\hat{\xi}(z),\hat{\eta}(z),\hat{\theta}(z)\right]=\left[\xi_{0}(z),\eta_{0}(z),\theta_{0}(z)\right]+\left[\xi(z),\eta(z),\theta(z)\right]$. Under the updated Lagrangian approach, when applying the first load increment from the initial configuration to the deformed configuration, the conventional undeformed geometry at the initial state is relatively complex due to the presence of initial out-of-straightness (IOS) and an initial stress state.

Thus, rather than referring variables to configuration $C(0)$, a fictitious, perfectly straight and stress free configuration $C(R)$ is introduced and adopted as a reference configuration (Fig. 4.2). The adoption of $C(R)$ as a reference configuration simplifies the evaluation of internal virtual work integrals during the first loading increment from the reference configuration $C(0)$ to the configuration corresponding to the first load increment $C(\Delta t_1)$. This section presents a generalized methodology for evaluating internal virtual work integrals using the multiplicative decomposition of the deformation gradient, building on the foundational approach introduced in Chapter 2 and [4.29].The internal virtual work referred to the perfectly straight configuration takes the form

$$ {}^{\Delta t_1}_{R}\bar{U} = \int_{R_V} \left({}^{\Delta t_1}_{R}\bar{\boldsymbol{\varepsilon}}\, {}^{\Delta t_1}_{R}\mathbf{S} \right) d\, {}^{R}V \tag{4.22} $$

in which ${}^{\Delta t_1}_{R}\mathbf{S}$ is the 2PK stress tensor, ${}^{\Delta t_1}_{R}\bar{\boldsymbol{\varepsilon}}$ is the virtual GL strain tensor, both evaluated at $C(\Delta t_1)$ and referred to the fictitious reference configuration $C(R)$, and ${}^{R}V$ is the volume of the reference configuration (i.e., fictitious, perfectly straight and stress-free). It is now required to determine the 2PK stress tensor ${}^{\Delta t_1}_{R}\mathbf{S}$ as the member undergoes deformation from $C(0)$ to $C(\Delta t_1)$ while adopting $C(R)$ as a reference configuration. The GL strain tensor increment ${}_{\Delta t_1}\boldsymbol{\varepsilon} = {}^{\Delta t_1}_{0}\boldsymbol{\varepsilon}$ induced by the first load increment, referenced to the undeformed configuration $C(0)$ is given by

$$ {}^{\Delta t_1}_{0}\boldsymbol{\varepsilon} = \frac{1}{2}\left[\mathbf{F}^{\mathbf{T}}_{(0,\Delta t_1)} \mathbf{F}_{(0,\Delta t_1)} - \mathbf{I} \right] \tag{4.23} $$

where $\mathbf{F}_{(0,\Delta t_1)}$ is the deformation gradient tensor relating a tangential vector $d\mathbf{X}^0$ in the undeformed configuration $C(0)$ to its image $d\mathbf{X}^{\Delta t_1}$ in the deformed configuration $C(\Delta t_1)$, and $\mathbf{I}$ is the identity

tensor. The formulation adopts the Saint-Venant-Kirchhoff constitutive tensor (Assumption 6) ${}^{\Delta t_1}_{0}\mathbf{C} = \mathbf{C}$ to relate the 2PK stress tensor ${}^{\Delta t_1}_{0}\mathbf{S}$ to the GL strain tensor ${}^{\Delta t_1}_{0}\boldsymbol{\varepsilon}$ as expressed in Eq. (4.23) in the presence of initial stresses $\boldsymbol{\sigma}_\mathbf{0}$ yielding

$$ {}^{\Delta t_1}_{0}\mathbf{S} = \boldsymbol{\sigma}_\mathbf{0} + \mathbf{C} : {}^{\Delta t_1}_{0}\boldsymbol{\varepsilon} = \boldsymbol{\sigma}_\mathbf{0} + \frac{1}{2}\mathbf{C} : \left[\mathbf{F}^{\mathbf{T}}_{(0,\Delta t_1)} \mathbf{F}_{(0,\Delta t_1)} - \mathbf{I} \right] \tag{4.24} $$

For the case where only the non-vanishing component of the initial stress tensor is the longitudinal residual stresses, one has

$$ \boldsymbol{\sigma}_\mathbf{0} = \sigma_r(s)\, \mathbf{e}_\mathbf{1} \otimes \mathbf{e}_\mathbf{1} \tag{4.25} $$

in which the through-thickness variation of the residual stresses has been assumed negligible $\sigma_r(s,n) \approx \sigma_r(s)$

The Cauchy stress tensor $\boldsymbol{\sigma}$ is related to 2PK stress tensors ${}^{t+\Delta t}_{R}\mathbf{S}$ and ${}^{t+\Delta t}_{0}\mathbf{S}$ through

$$ \boldsymbol{\sigma} = \left(1 \Big/ \left\| \mathbf{F}_{(R,\Delta t_1)} \right\| \right) \mathbf{F}_{(R,\Delta t_1)}\, {}^{\Delta t_1}_{R}\mathbf{S}\, \mathbf{F}^{\mathbf{T}}_{(R,\Delta t_1)} \tag{4.26} $$

$$ \boldsymbol{\sigma} = \left(1 \Big/ \left\| \mathbf{F}_{(0,\Delta t_1)} \right\| \right) \mathbf{F}_{(0,\Delta t_1)}\, {}^{\Delta t_1}_{0}\mathbf{S}\, \mathbf{F}^{\mathbf{T}}_{(0,\Delta t_1)} \tag{4.27} $$

in which $\| \ \|$ denotes the determinant of the argument object. By equating Eqs. (4.26) and (4.27), one obtains

$$ {}^{\Delta t_1}_{R}\mathbf{S} = \left(\left\| \mathbf{F}_{(R,\Delta t_1)} \right\| \Big/ \left\| \mathbf{F}_{(0,\Delta t_1)} \right\| \right) \mathbf{F}^{-1}_{(R,\Delta t_1)} \mathbf{F}_{(0,\Delta t_1)}\, {}^{\Delta t_1}_{0}\mathbf{S}\, \mathbf{F}^{\mathbf{T}}_{(0,\Delta t_1)} \mathbf{F}^{-\mathbf{T}}_{(R,\Delta t_1)} \tag{4.28} $$

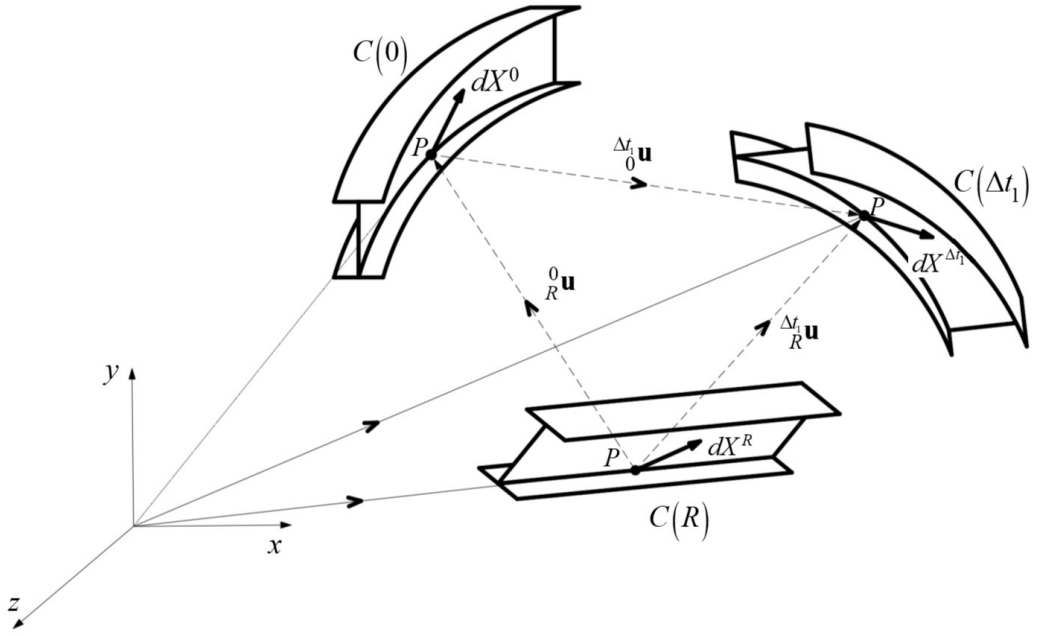

Fig. 4.2 Member at configuration C(0) with IOS deforming to first configuration C() referred to configuration C(R) with no IOS

The evaluation of ${}^{\Delta t_1}_{R}\mathbf{S}$ as defined in Eq. (4.28) requires the evaluation of deformation gradients $\mathbf{F}_{(R,\Delta t_1)}$ and $\mathbf{F}_{(0,\Delta t_1)}$. Under Cartesian coordinates, the deformation gradient tensor $\mathbf{F}_{(R,\Delta t_1)}$ is

$$\mathbf{F}_{(R,\Delta t_1)} = \begin{bmatrix} 1+\dfrac{\partial \tilde{\tilde{w}}}{\partial^R z} & \dfrac{\partial \tilde{\tilde{w}}}{\partial^R s} & \dfrac{\partial \tilde{\tilde{w}}}{\partial^R n} \\ \dfrac{\partial \tilde{\tilde{u}}_t}{\partial^R z} & 1+\dfrac{\partial \tilde{\tilde{u}}_t}{\partial^R s} & \dfrac{\partial \tilde{\tilde{u}}_t}{\partial^R n} \\ \dfrac{\partial \tilde{\tilde{u}}_n}{\partial^R z} & \dfrac{\partial \tilde{\tilde{u}}_n}{\partial^R s} & 1+\dfrac{\partial \tilde{\tilde{u}}_n}{\partial^R n} \end{bmatrix} \tag{4.29}$$

in which $\left(\tilde{\tilde{w}},\tilde{\tilde{u}}_t,\tilde{\tilde{u}}_n\right)=\left({}_0\tilde{w},{}_0\tilde{u}_t,{}_0\tilde{u}_n\right)+\left({}_R\tilde{w},{}_R\tilde{u}_t,{}_R\tilde{u}_n\right)$, $\left({}_0\tilde{w},{}_0\tilde{u}_t,{}_0\tilde{u}_n\right)$ is the incremental displacement vector from $C(0)$ to $C(\Delta t_1)$, and $\left[{}_R\tilde{w},{}_R\tilde{u}_t(\xi_0,\eta_0,\theta_0),{}_R\tilde{u}_n(\xi_0,\eta_0,\theta_0)\right]$ is the fictitious displacement vector from $C(R)$ to $C(0)$ (Fig. 4.2) computed based on the initial out-of-straightness $\left[\xi_0(z),\eta_0(z),\theta_0(z)\right]$.

The deformation gradient tensor $\mathbf{F}_{(0,\Delta t_1)}$ appearing in Eq.(4.29) can be expressed in terms of the deformation gradient tensors $\mathbf{F}_{(R,\Delta t_1)}$ and $\mathbf{F}_{(R,0)}$ by relating the tangential vectors $d\mathbf{X}^{\Delta t_1}$, $d\mathbf{X}^0$, and $d\mathbf{X}^R$ through their respective deformation gradient tensors as

$$d\mathbf{X}^{\Delta t_1} = \mathbf{F}_{(0,\Delta t_1)} d\mathbf{X}^0, \quad d\mathbf{X}^0 = \mathbf{F}_{(R,0)} d\mathbf{X}^R, \quad d\mathbf{X}^{\Delta t_1} = \mathbf{F}_{(R,\Delta t_1)} d\mathbf{X}^R \tag{4.30)a-c}$$

in which $\mathbf{F}_{(a,b)}$ denotes the deformation gradient corresponding to the deformation from $C(a)$ to $C(b)$. From Eq. (4.30)b, by substituting into Eq. (4.30)a, and subtracting from Eq. (4.30)c, one recovers the multiplicative identity of the deformation gradient

$$\mathbf{F}_{(0,\Delta t_1)} = \mathbf{F}_{(R,\Delta t_1)} \mathbf{F}^{-1}_{(R,0)} \tag{4.31}$$

From Eq. (4.29), by substituting into Eq.(4.28), one obtains

$${}^{\Delta t_1}_{R}\mathbf{S} = \left\| \mathbf{F}_{(R,0)} \right\| \mathbf{F}^{-1}_{(R,0)} \, {}^{\Delta t_1}_{0}\mathbf{S} \mathbf{F}^{-\mathbf{T}}_{(R,0)} \tag{4.32}$$

From Eqs. (4.31), (4.24) by substituting into Eq. (4.32), one obtains

$${}^{\Delta t_1}_{R}\mathbf{S} = \left\| \mathbf{F}_{(R,0)} \right\| \mathbf{F}^{-1}_{(R,0)} \left[\boldsymbol{\sigma}_{\mathbf{0}} + \frac{1}{2} \mathbf{C} : \left(\mathbf{F}^{-\mathbf{T}}_{(R,0)} \mathbf{F}^{\mathbf{T}}_{(R,\Delta t_1)} \mathbf{F}_{(R,\Delta t_1)} \mathbf{F}^{-1}_{(R,0)} - \mathbf{I} \right) \right] \mathbf{F}^{-\mathbf{T}}_{(R,0)} \tag{4.33}$$

Eq. (4.33) enables the computation of the 2PK stress tensor ${}^{\Delta t_1}_{R}\mathbf{S}$ at configuration $C(\Delta t_1)$, based on the deformation gradient tensors $\mathbf{F}_{(R,\Delta t_1)}$ given by Eq. (4.29), and $\mathbf{F}_{(R,0)}$ which depends solely on the IOS pattern $\left[{}_R\tilde{w}, {}_R\tilde{u}_t(\xi_0, \eta_0, \theta_0), {}_R\tilde{u}_n(\xi_0, \eta_0, \theta_0) \right]$. This in turn enables the computation of the internal virtual work expression in Eq. (4.22).

For the special case of no initial out of straightness, the 2PK stress tensor at $C(\Delta t_1)$ in Eq. (4.33) can be shown to take the form ${}^{\Delta t_1}_{0}\mathbf{S} = \left[\boldsymbol{\sigma}_\mathbf{0} + 0.5\mathbf{C} : \left(\mathbf{F}^{\mathbf{T}}_{(0,\Delta t_1)}\mathbf{F}_{(0,\Delta t_1)} - \mathbf{I}\right)\right]$ and the corresponding Cauchy stress takes the form

$$\boldsymbol{\sigma} = \frac{\mathbf{F}_{(0,\Delta t_1)}}{\left\|\mathbf{F}_{(0,\Delta t_1)}\right\|}\left[\boldsymbol{\sigma}_\mathbf{0} + \frac{1}{2}\mathbf{C} : \left(\mathbf{F}^{\mathbf{T}}_{(0,\Delta t_1)}\mathbf{F}_{(0,\Delta t_1)} - \mathbf{I}\right)\right]\mathbf{F}^{\mathbf{T}}_{(0,\Delta t_1)} \tag{4.34}$$

The bracketed term in Eq. (4.34) is the sum of two stress components, the first being the initial stress $\boldsymbol{\sigma}_\mathbf{0}$ and the second is induced by the deformation gradient $\mathbf{F}_{(0,\Delta t_1)}$ of the load increment from $C(0)$ to $C(t)$. Also, the deformation gradient transformation of the bracketed quantity captures coupling between both components.

4.6 Verification

4.6.1 Reference Beam

A verification study was conducted on a 10.0 m span monosymmetric I-beam. Member ends are restrained against twist, transverse and lateral displacements at both ends, and a longitudinal restrain is provided at one end i.e., $\zeta(0) = \xi(0) = \eta(0) = \theta(0)$ and $\xi(L) = \eta(L) = \theta(L) = 0$. Top Flange dimensions are $b_t \times e = 150 \times 16.0 mm$ and bottom flange dimensions are $b_2 \times e = 300 \times 16.0 mm$. The distance between flange centroids is $d = 400\,mm$ and the web thickness is $e_w = 10.0\,mm$. The distance from the top flange to section centroid is $y_t = 242.9\,mm$. The coordinate of the shear center relative to the centroid is $y_{sc} = 112.7 mm$ (Fig. 4.3a). Sectional properties are $I_x = 3.21 \times 10^8\,mm^4$, $I_y = 4.06 \times 10^7\,mm^4$, $C_\omega = 6.42 \times 10^{11} mm^6$, $J = 7.48 \times 10^5\,mm^4$, $S_{x1} = 1.32 \times 10^6\,mm^3$ and $S_{x2} = 2.04 \times 10^6\,mm^3$. The monosymmetric parameter β_x as given by

$$\begin{aligned}\beta_x &= \int_A y\left(x^2+y^2\right)dA/I_x - 2p_y \\ &= \frac{1}{I_x}\left[\left(d-y_t\right)\left(\frac{b_b^3 e}{12}+be\left(d-y_t\right)^2+\frac{e_w}{4}\left(d-y_t\right)^3\right)-y_t\left(\frac{b_t^3 e}{12}+b_t e y_t^{\,2}+\frac{e_w}{4}y_t^{\,3}\right)\right]-2y_{sc}\end{aligned} \tag{4.35}$$

is found to be $-282mm$. Material is steel with a Young's modulus $E=200\,GPa$ and a shear modulus $G=77.0\,GPa$. The residual stress pattern is taken to conform to that reported in [4.24], with a peak compressive stress of $0.3F_y$ at the tips of the larger flange and $\left(0.3\times b_s/b_l\right)F_y$ at the tips of the compression flange, which corresponds to $0.15F_y$ for the given cross-section. A bilinear residual stress distribution is assumed to take place in the web such that it satisfies the self-equilibrating conditions $\int_A \sigma_r dA = \int_A y\sigma_r dA = 0$ [8]. Both conditions result in a peak residual stress in the web of $0.20F_y$ (Fig. 4.3c) at a height $y_g = 133.3\,mm$ from the bottom flange.

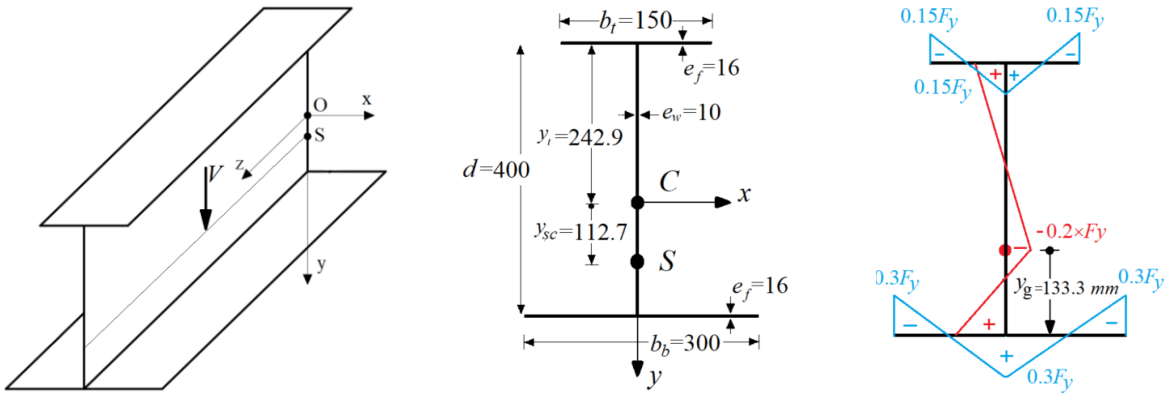

(a) (b) (c)

Fig. 4.3 (a) Monosymmetric beam (b) Notation and dimensions (c) Residual stress pattern

4.6.2 Designations

Each parametric run is assigned an identifier of the type **F-Ann-(R)**, in which symbol **F** denotes the compressed flange and is taken as S when the smaller flange is in compression and taken as L

[8] Appendix J provides an evaluation of the residual stress distribution in monosymmetric I-sections.

otherwise. Symbol **A** denotes the type of initial out of straightness, and takes the value L for lateral IOS, LT for lateral torsional IOS affine to the fundamental eigen mode, and T for pure twist IOS. Symbol **nn** denotes the ratio of span to peak IOS amplitude. A value of 1000 corresponds to the allowable amplitude as stipulated in [4.30]. The presence of R at the end of an identifier denotes that the residual stresses in the member are modelled as initial stresses. In this case, the load is incrementally increased until the total stresses (due to the combined effect of loading and residual stresses) attain the yield strength at the tip of the compression flange. Conversely, the absence of R from an identifier denotes that residual stresses are not modelled as initial stress. Instead, the load is incremented until the longitudinal stress at the tip of the compression flange attains the yield strength minus the residual stress.

4.6.3 Verification 1 – Effect of IOS

4.6.3.1 Description

A mid-span load is applied at the shear center for three IOS scenarios: S-L1000-R, S-L500-R, S-L1000, S-L500. For comparison, the case of minimal IOS amplitude S-L-20,000-R is considered. The problem is modelled using the present solution and the Abaqus shell model. An upper bound on the member's expected resistance is obtained by performing an elastic buckling eigenvalue analysis for a perfectly straight member, using LTB-UO [4.31]—an in-house program based on the thin-walled beam finite element formulation by Barsoum and Gallagher [4.6], hereafter referred to as BG. The element is based on the kinematics of the Vlasov beam and has two nodes with seven degrees of freedom per node, including a warping degree of freedom. A mesh study has shown that convergence is attained by subdividing the member into 30 elements. The critical moment predicted by the BG model is $305kNm$, which corresponds to a critical load of $122\,kN$. Thus, a midspan transverse point load of $V = 122\,kN$ was targeted under the present nonlinear solution and Abaqus shell model.

The shell model is based on the S4 element in Abaqus, a four-node shell element with six degrees of freedom per node, three translations and three rotations, based on full integration. In the shell model, convergence is attained with 6 elements along the small flange width, 8 elements along the large flange width, 10 elements along the web height, and 200 elements along the span. Residual stresses are modelled as initial stresses at integration points within the elements using the predefined field option (Initial step, Type=Stress), in Abaqus, to emulate the residual stress pattern in Fig. 4.3c.

In the present solution and the Abaqus shell models, the load was incrementally increased until the Cauchy stress at one of the corners of the compression flange, including residual stress effects, attains the yield stress . The corresponding moment capacities are summarized in Table 4.2. Close agreement is observed between the predictions of the present model and those of the Abaqus S4 shell element model across all scenarios considered, with a maximum discrepancy of approximately 1.0%. As expected, both sets of results are consistently lower than those predicted by the BG solution. The onset of yield moment predicted by the present model ranges from 73% to 95% of the elastic critical moment, depending on the amplitude of the initial out-of-straightness (IOS). For the minimal IOS amplitude S-L20,000-R, the ratio of onset of yield to critical moment reaches 95%. This ratio decreases significantly to 80% for the more representative amplitude S-L1,000-R and further drops to 73% for S-L100-R.

By treating the residual stresses as an initial stress in S-L1000R, while targeting a peak compressive stress of F_y at the corners of the compression flange, the present solution predicts a critical moment of $242.5\,kNm$, which compares to $250.1\,kNm$ based on S-L1000, a 3.0% difference. Similarly, the percentage difference between S-L500-R and S-L500 is found to be 4.6%

Table 4.2 Effect of residual stress and IOS pattern on critical moments

IOS Pattern	Critical Moments (kNm)			Moment ratios	
	BG	Present solution	Shell model	Present/BG	Present/Shell model
S-L20,000-R	305	289	288	0.95	1.005
S-L1000	305	250	250	0.82	1.000
S-L1000-R	305	242	241	0.79	1.005
S-L500	305	232	231	0.76	1.001
S-L500-R	305	222	220	0.73	1.010

At $M/M_u = 0.79$ (Fig. 4.4a), the Total L-IOS at midspan for S-L1000-R is 27.9 mm at the top flange (TF) and 17.1 mm at the bottom flange (BF). For S-L500-R at $M/M_u = 0.73$, the total L-IOS increases to 33.1 mm at TF and 20.2 mm at BF. The lateral displacements predicted by the present model agree with those of the shell model within 4.2%.

Fig. 4.4b shows that the midspan transverse displacement slightly increases from 34.1 mm for S-L1000-R to 37.0 mm for S-L500-R and Fig. 4.4c-d shows that the midspan peak compressive stress attains $F_y = 350MPa$ at $M/M_u = 0.79$ for a S-L1000-R and at $M/M_u = 0.73$ for a S-L500-R. In S-L1000-R, the midspan peak compressive stress of $F_y = 350MPa$ occurs on the concave side of the top flange (Edge 4 in Fig. 4.4c) which compares to a compressive stress of $272\,MPa$ on the convex side (Edge 3). Conversely, the bottom flange experiences a tensile stress of $104\,MPa$ on the concave side (Edge 2) and $67\,MPa$ on the convex side (Edge 1). For the S-L1000-R, the peak normal stress at midspan predicted by the present model and Abaqus S4 differ by no more than 5.7%.

In Fig. 4.4e, since the S-L1000 run does not model the residual stresses as an initial stress, the point of onset of yielding was deemed to occur when the compressive stresses at edge 4 attains F_y. As a result, the normal stresses are lower than those in Fig. 4.4c. By adding a compressive residual stress of 0.30Fy to the tips of the larger flange and 0.15Fy to the tips of the small flange, one obtains the dashed lines on Fig. 4.4e. One can observe that the total stresses, in this case are close to those shown in Fig. 4.4c. Similar observations are made for S-L500 and S-L500-R when comparing Fig. 4.4f and Fig. 4.4e. The results suggest that the detrimental effect induced by the interaction between initial stresses and IOS is rather minor, and their combined effect can be reasonably approximated by superposition.

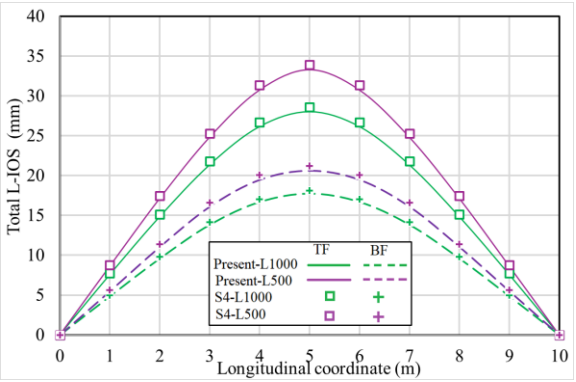

(a)

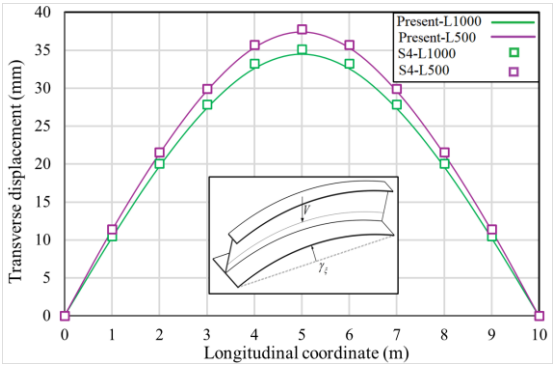

(b)

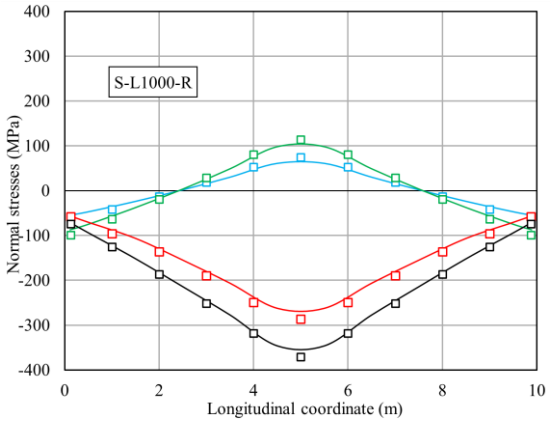

(c)

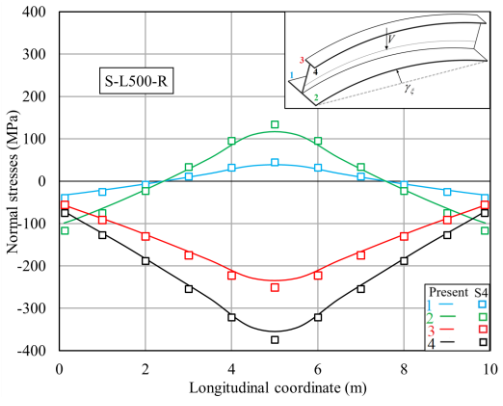

(d)

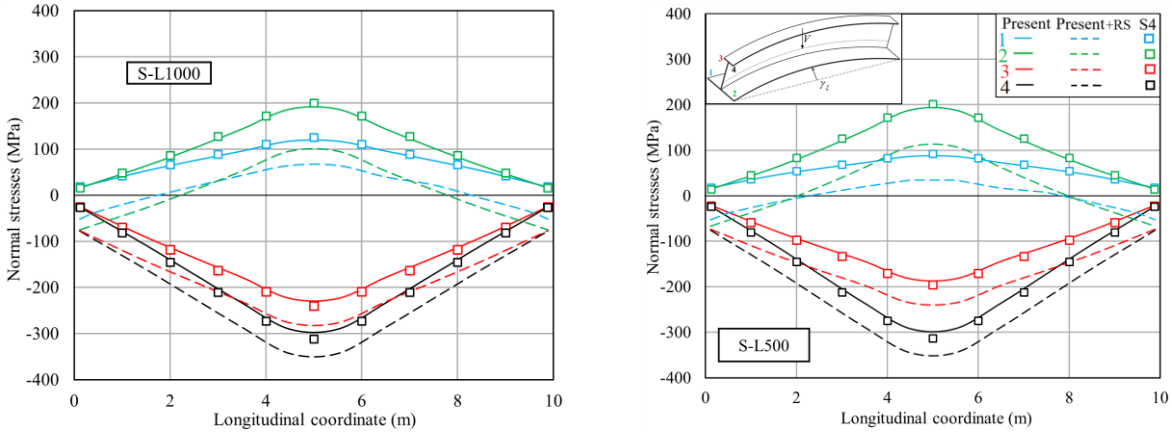

(e) (f)

Fig. 4.4 (a) Total L-IOS for S-L1000-R (b) Transverse displacement for S-L1000-R (c) Normal stresses for S-L1000-R (d) Normal stresses for S-L500-R (e) Normal stresses for S-L-1000, (f) Normal stresses of for S- L-500.

4.6.4 Verification 2 - Effect of Load Height

The reference beam under midspan point load in the previous section is re-examined for two configurations: one with the small flange in compression (S-L1000-R), and the other with the large flange in compression (L-L1000-R). In both configurations, the point load is applied at various heights along the web: bottom flange (BF), shear center (SC), centroid (CT), section mid-height (MH), and top flange (TF). The corresponding elastic critical moment M_u based on an eigenvalue buckling analysis as predicted by the BG solution and the moment resistance M based on the onset of yielding as predicted by the present solution and the shell model are summarized in Table 4.3 and Table 4.4..

For S-L1000-R, Table 4.3 shows that the resisting moments in all three solutions increase as the point of load application shifts from the top flange to the bottom flange, as expected. For the case of mid-height load (MH), the Canadian and American standards equation $M_u = C_b\pi^2 EI_y/2L^2\left[\beta_x + \sqrt{\beta_x^2 + 4\left(GJL^2/\pi^2 EI_y + C_\omega/I_y\right)}\right]$ predict an elastic critical moment $M_u\left(\text{CSA}\right)$=202kNm , which coincides with that predicted by the BG solution. In general, the

predictions of the present solution and Abaqus agree within 3%. An exception is observed for the case of top flange loading, in which the difference between both models is 6%. The ratio of the onset of yielding moments predicted by the present solution to those based on elastic critical moment range from 0.78 to 0.81%.

For L-L1000-R, Table 4.4 shows that the resisting moments reduce as the point of load application shifts downwards. The elastic critical moment equation $M_u = C_b \pi^2 EI_y / 2L^2 \left[\beta_x + \sqrt{\beta_x^2 + 4\left(GJL^2 / \pi^2 EI_y + C_\omega / I_y \right)} \right]$ predicts a value of $508 kNm$ for the case of mid-height (MH) loading which, again, coincides with the that computed by the BG eigenvalue solution. The predictions of the present solution and Abaqus are within 2% in all five load heights considered. The ratio of the onset of yielding moments predicted by the present solution to those based on elastic critical moment range from 0.76% to 0.79%. These lower values compared to those of S-L1000-R indicate that the detrimental effect of IOS is slightly more pronounced when the larger flange is in compression.

Table 4.3 Moment resistance for various load heights – small flange in compression

Load height	Moments (kNm)			Moment ratios		
	BG	Present	Shell	Present/BG	Present/Shell	
TF	148	115	122	0.78	0.94	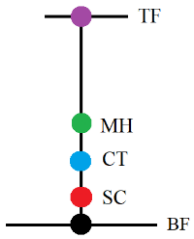
MH	202	159	163	0.78	0.97	
CT	221	176	177	0.79	0.99	
SC	305	242	241	0.79	1.00	
BF	310	250	250	0.81	1.00	

TF = top flange, BF = bottom flange, SC = shear center, CT= centroid, MH = mid height

Table 4.4 Moment resistance for various load heights – large flange in compression

Load height	Moments (kNm)			Moment ratios	
	BG	Present	Shell	Present/BG	Present/Shell
TF	361	283	285	0.78	0.99
SC	391	299	301	0.76	0.99
CT	475	364	368	0.76	0.99
MH	508	389	391	0.76	0.98
BF	678	513	518	0.76	0.98

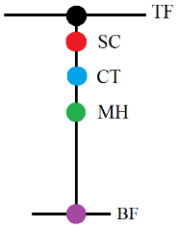

TF = top flange, BF = bottom flange, SC = shear center, CT= centroid, MH = mid height

4.7 Parametric Study

The onset of yielding moments for a parametric series of beams with the reference cross-section defined in the previous section is determined based on the present model. The end restraints are $\zeta(0)=\xi(0)=\eta(0)=\theta(0)=\xi(L)=\eta(L)=\theta(L)=0$. The yield strength is taken as $F_y=350MPa$. Three loading cases are considered: uniform moment (UM), midspan point loading (PL), and uniformly distributed loading (UD), all applied at web mid-height. Both possible orientations of the cross-section are examined: small flange in compression and large flange in compression. Four spans L are chosen within the elastic lateral torsional buckling range: For cases where the small flange is in compression, the span lengths were varied within the range $1\le L/L_{ts}\le 2$ where L_{ts} represents the threshold between elastic and inelastic lateral-torsional buckling (LTB) under bending moments inducing compression in the small flange. Similarly, for cases where the large flange is in compression, the spans were varied within the range $1\le L/L_{tl}\le 2$ with L_{tl} being the corresponding threshold for LTB when the large flange is in compression [9].

[9] Appendix K determines the threshold span of a monosymmetric beam that delineates the elastic LTB from the inelastic LTB region

The residual stress pattern is taken identical to that defined in Fig. 4.3c., i.e., the peak residual stresses at the tip of the shorter flange is $0.15F_y$ and that at tip of the larger flange is of $0.30F_y$. Three IOS patterns are investigated: pure lateral, pure torsional, and lateral torsional, affine to the fundamental eigenmode. Two IOS amplitudes; are considered; (a) $L/1000$ which represents the most adverse scenario based on present sweep limits [4.30] and (b) $L/2000$ which is reflective of a more typical amplitude. The corresponding permutations yield 3 loading cases x 2 cross-section orientations $\times$ 4 spans $\times$3 IOS patterns $\times$ 2 IOS amplitudes = 144 parametric cases. Geometric nonlinear analyses are conducted based on the present solution and the moment resistance M at the onset of yield was determined. The moment resistances are then normalized by dividing them by the elastic critical moment M_u as obtained from $M_u = C_b\pi^2 EI_y/2L^2\left[\beta_x + \sqrt{\beta_x{}^2 + 4\left(GJL^2/\pi^2 EI_y + C_\omega/I_y\right)}\right]$. In order to avoid approximations in moment gradient equations provided in standards, the moment gradient factor C_b has been determined by conducting an buckling eigenvalue analyses using BG model and computed by dividing the critical moment for the loading under consideration by the uniform critical moment yielding $C_b = 1.0$ for UM, $C_b = 1.13$ for UD, and $C_b = 1.35$ for PL. To distinguish between the various loading cases, the notation **F-Ann-(R)** defined in Section 4.5.2 is extended to **F-Ann-(R)-L**, where **L** denotes the type of loading and takes the values **UM**, **UD**, or **PL**.

4.7.1 Effect of IOS Pattern -Small Flange in Compression

As a general observation in Fig. 4.5, the moment resistances M based on the onset of yield for beams with IOS are consistently lower than the critical moment M_u of analogous perfectly straight beams. As the span-to-depth ratio L/d increases, the moment ratio M/M_u increases, i.e., the effect of IOS becomes less pronounced. As shown consistently across Fig. 4.5a-c, irrespective of

the applied load type, T-IOS has the most detrimental effect, followed by LT-IOS, while L-IOS has the least detrimental impact. Fig. 4.6 a-c also shows that, regardless of the IOS pattern and amplitude, UM exhibits the least detrimental effect due to IOS, as indicated by its relatively high moment ratio. This is followed by UD, with PL showing the most pronounced reduction.

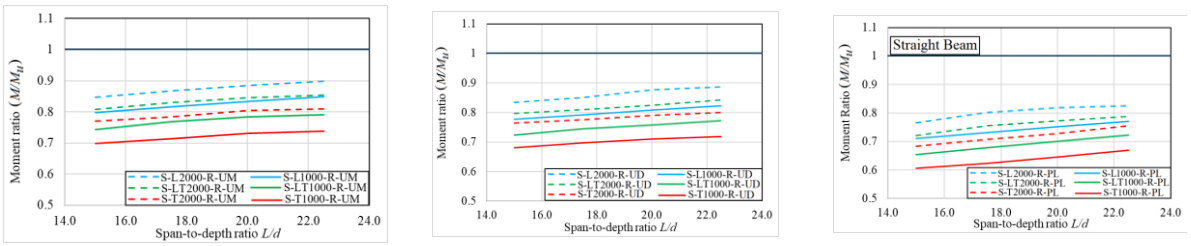

(a) **(b)** **(c)**

Fig. 4.5 Moment ratio versus Normalized Span -Small Flange in Compression- Effect of loading type: (a) Uniform moments UM, (b) Uniformly Distributed Load UD, and (c) Midspan Point Load PL

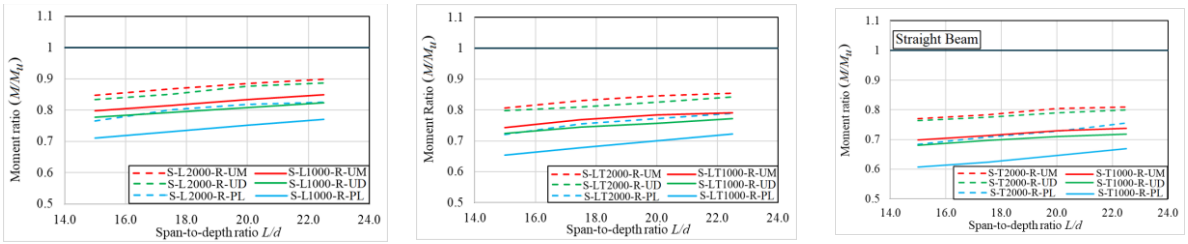

(a) **(b)** **(c)**

Fig. 4.6 Moment ratio versus Normalized Span- Small Flange in Compression- Effect of IOS pattern and amplitude: (a) Members with Lateral IOS, (b) Members with Lateral torsional IOS, and (c) Members with Twist IOS

4.7.2 Effect of IOS Pattern -Large Flange in Compression

Fig. 4.7 shows that, in cases where the large flange is in compression, the moment ratios are consistently higher than in cases where the small flange is in compression (Fig. 4.6) within their respective elastic LTB ranges as characterized by the member slenderness ratio L/d. This suggests that the detrimental effect of initial out-of-straightness (IOS) is less severe when the large flange is in compression compared to when the small flange is in compression. The ranking of IOS patterns remains unchanged: T-IOS results in the lowest resistance, followed by LT-IOS, and then L-IOS, which has the least detrimental effect. Similarly, point loading results in the lowest moment

ratios, while uniform moments produce the highest. However, the differences in moment ratios between the loading cases are smaller (Fig. 4.8) than those observed when the small flange is in compression.

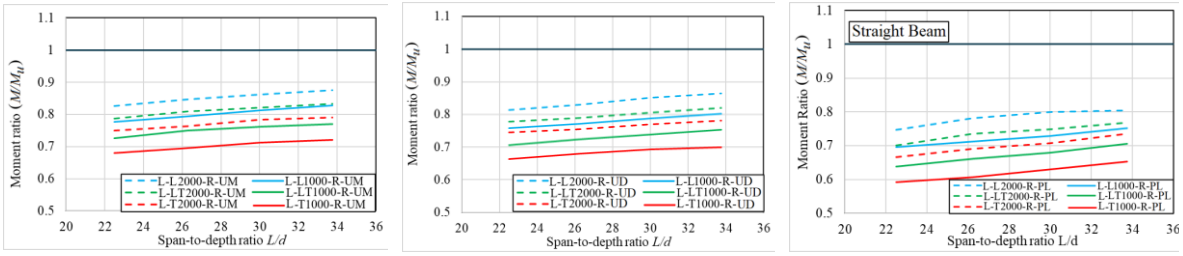

(a) **(b)** **(c)**

Fig. 4.7 Moment ratio versus Normalized Span -Large Flange in Compression- Effect of loading type: (a) Uniform moments UM, (b) Uniformly Distributed Load UD, and (c) Midspan Point Load PL

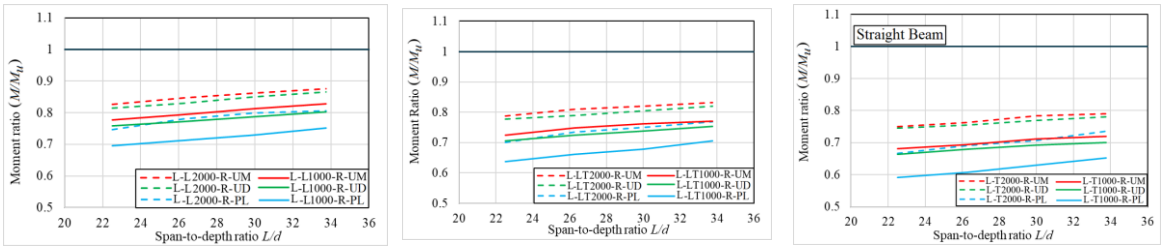

(a) (b) (c)

Fig. 4.8 Moment ratio versus Normalized Span- Large Flange in Compression- Effect of IOS pattern and amplitude: (a) Members with Lateral IOS, (b) Members with Lateral torsional IOS, and (c) Members with Twist IOS

4.7.3 Comparison with Standard Predictions

The flexural resistance of the reference beam under various IOS patterns and loading types is illustrated in Fig. 4.9 for the case where the small flange is in compression, and in Fig. 4.10 for the case where the large flange is in compression. The flexural resistance is normalized with respect to the plastic moment M_p of the cross-section. Under the American specifications [4.2], the LTB resistance of a member with a normalized span $L/L_t > 1$ is given by its the elastic critical moment resistance for a perfectly straight member. For a compact section, the threshold span L_t is determined by equating the elastic uniform

$M_0 = \pi^2 EI_y / 2L^2 \left[\beta_x + \sqrt{\beta_x^{\,2} + 4\left(GJL^2 / \pi^2 EI_y + C_\omega / I_y \right)} \right]$ to 70% of its elastic moment resistance $S_{x1}F_y$, which yields a threshold span $L_t = 4.10m$ when the small flange is in compression. When the large flange is in compression, equating M_0 to $S_{x2}F_y$ yields $L_t = 10.90m$. A similar approach is adopted by the Canadian standards [4.1]. Yet, the threshold span L_{tc} under the Canadian standard is determined by equating the elastic critical moment $M_u = C_b M_0$ (including the moment gradient effect) to 70% of the elastic moment resistance. When the small flange is in compression, the threshold spans L_{tc} are $4.10\,m$ for UM, $4.50\,m$ for UD, and $5.30\,m$ for PL and when the large flange is in compression, the threshold spans L_{tc} increase to $10.90\,m$ for UM, $11.50\,m$ for UD, and $13.30\,m$ for PL. The normalized moment ratios versus L/L_t are shown in Fig. 4.9a–c for the cases where the small flange is in compression, and in Fig. 4.10a–c for the cases where the large flange is in compression. Also, shown as vertical lines the Canadian threshold span L_{tc} on each figure. The normalized moment ratios based on the Eurocode 3 [4.3] and Australian standards [4.4] for comparison[10]. Unlike the American and Canadian standards, both the Eurocode and the Australian standards account for IOS effects in their provisions. Six IOS scenarios are examined, involving three IOS patterns: L-IOS, LT-IOS and T-IOS, and two amplitudes per pattern. As a general observation, the Canadian and American equations overpredict the flexural resistance of the member compared to the predictions of the present model.

[10] Appendix L provides the steps for calculating the lateral-torsional buckling resistance of a monosymmetric beam as per Eurocode 3 and the Australian standards

The moment ratios M / M_y versus normalized span L/L_t loading are depicted in Fig. 4.9 for the case where the small flange is in compression, and in Fig. 4.10 for the case where the large flange is in compression. In all cases, the American and Canadian standards overpredict the flexural resistance. This outcome is expected, as these standards do not account for the effects of IOS. The Eurocode predictions are significantly lower than the American and Canadian Standard solutions, while the Australian standard predictions are slightly above those of the Eurocode. For the most part, flexural resistances computed by the present solution are clustered around the predictions of the Eurocode and Australian standards and far below the American and Canadian standards. For most IOS patterns and amplitudes investigated, the Eurocode either reasonably approximates or underpredicts the flexural resistances computed based on the onset of yielding. An exception is observed for the cases where the small flange is in compression with a T-IOS of $L/1000$, in which the Eurocode tends to overpredict the computed flexural resistance in most instances.

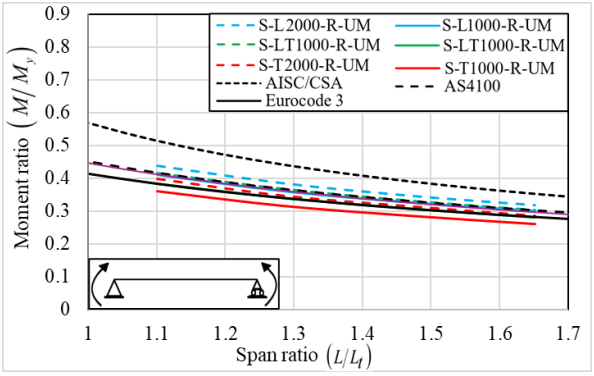

(a)

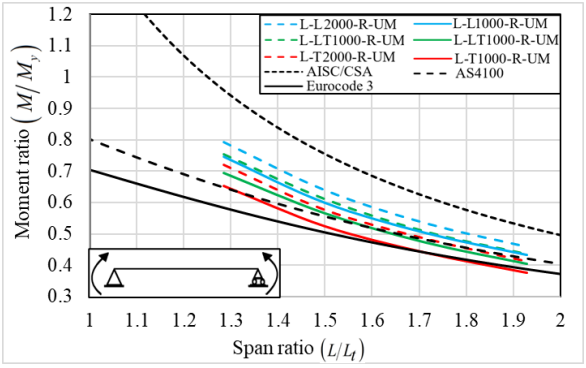

(d)

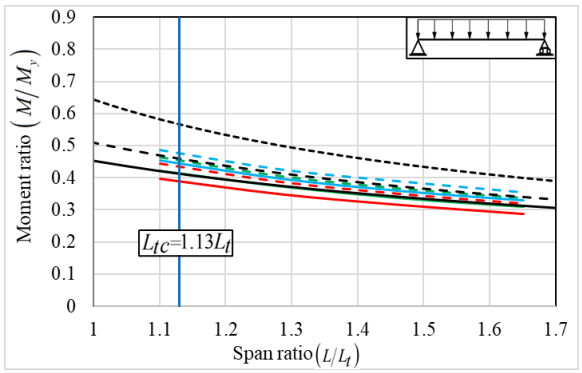

(b)

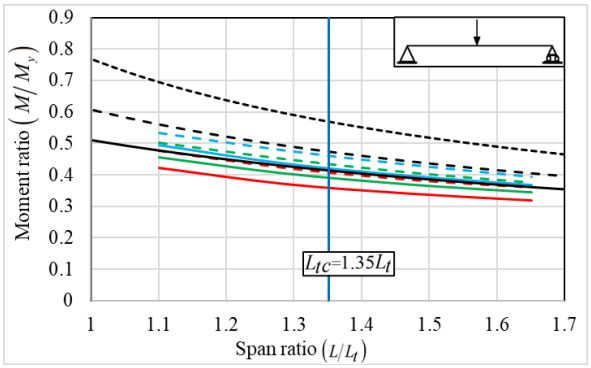

(c)

Fig. 4.9 Flexural resistance for the reference beam with SFIC (a) UM, (b) UD and (c) PL

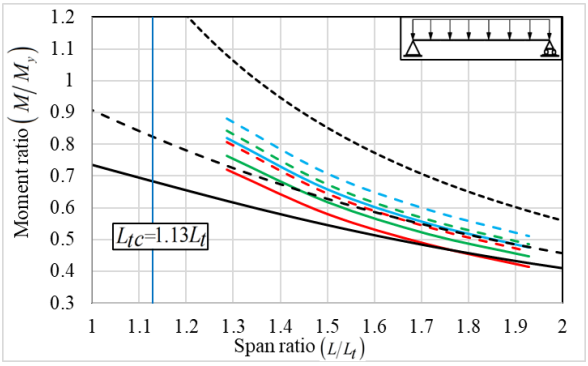

(e)

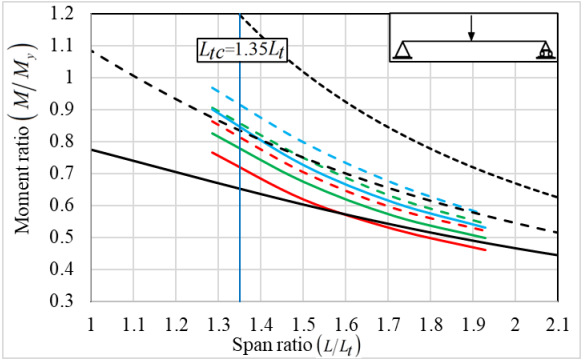

(f)

Fig. 4.10 Flexural resistance for the reference beam with LFIC (d) UM, (e) UD and (f) PL

4.8 Summary and Conclusions

The present study develops a geometrically nonlinear finite element formulation tailored for thin-walled monosymmetric I-shaped beams subjected to major axis bending. Using the updated Lagrangian approach, the model captures the load height effect and incorporates imperfection effects including initial out-of-straightness (IOS) and residual stresses. The formulation is validated against shell finite element models. A parametric study is conducted to assess the influence of IOS patterns; lateral (L-IOS), lateral-torsional (LT-IOS), and torsional (T-IOS) as well as different load types (uniform moment, point load, distributed load) and compression flange (small vs. large flange in compression). The model predictions are compared to those based on the

Canadian, American, Eurocode, and Australian LTB resistance provisions for monosymmetric members. The main findings of the study are:

1. Initial out-of-straightness significantly reduces the lateral-torsional buckling resistance for long-span, laterally unbraced monosymmetric beams.

2. Torsional IOS (T-IOS) has the most detrimental effect on buckling resistance, followed by lateral-torsional (LT-IOS) and lateral (L-IOS) imperfections.

3. Uniform moment loading is least sensitive to IOS effects, while midspan point loading is associated with the greatest reduction in moment resistance.

4. Beams with the large flange in compression show slightly higher moment ratios than those with the small flange in compression, indicating reduced sensitivity to initial out-of-straightness.

5. For the reference section examined in the present study, the combined effect of initial out-of-straightness and residual stresses can be approximated by superposition.

6. Canadian and American standards tend to overestimate flexural resistance due to neglecting IOS and residual stress effects, while Eurocode 3 and AS 4100 provide more conservative and accurate predictions by explicitly accounting for imperfections

4.9 List of Symbols

${}^{t}A \approx A$	Cross-sectional area at the configuration $C(t)$
B	Generic point within the member volume
B'	Projection of B on the middle surface
b_t, b_b	Top and bottom flange widths
${}_0\mathbf{C}$	Saint-Venant-Kirchhoff constitutive tensor
$d\mathbf{X}^a$	Tangential vector in the deformed configuration $C(a)$
E	Young's modulus
e, e_w	Flange and web thickness
$\mathbf{F}_{(a,b)}$	Deformation gradient tensor from $C(a)$ to $C(b)$
${}^{t}\mathbf{F}$	Internal force vector at time t
G	Shear modulus
$\mathbf{H}_a, \mathbf{H}_b$	Vectors of Hermitian interpolation functions
h	Normal distance from the shear center to the tangent of B' on the middle surface
I_{yy}	Moment of inertia about the y axis
I_{xx}	Moment of inertia about the x axis
$I_{\omega\omega}$	Warping constant
J	Saint-Venant torsional constant
$\mathbf{K_E}$	Elastic stiffness matrix
$\mathbf{K_G}$	Geometric stiffness matrix at time t
$\mathbf{L}$	Vector of Lagrangian interpolation functions
${}^{t}L$	Length of the member at configuration $C(t)$
n	Normal coordinate
q	Tangential distance from the shear center to the point B' on the middle surface
$q_y(z)$	Transverse line load
${}^{b}_{a}R$	External work at the configuration $C(b)$ referred to the configuration $C(a)$
${}^{b}_{a}\bar{R}$	External virtual work at $C(b)$ referred to $C(a)$
${}^{b}_{a}\mathbf{S}$	Second Piola-Kirchhoff stress tensor at $C(b)$ referred to $C(a)$
${}^{b}_{a}S_{zz}$, ${}^{b}_{a}S_{zs}$	Normal and shear components of the Second Piola-Kirchhoff stress tensor at $C(b)$ referred to $C(a)$
s	Tangential coordinate
s_0	Principal sectorial origin
t	Time
Δt	Time increment
Δt_1	Initial Time increment
${}^{b}_{a}U$	Internal work at the configuration $C(b)$ referred to the configuration $C(a)$

${}_{a}^{b}\bar{U}$	Internal virtual work at configuration $C(b)$ referred to the configuration $C(a)$
$\tilde{u}_t$	Tangential displacement from $C(0)$ to $C(t)$
${}_t\tilde{u}_t$	Tangential displacement increment
$\tilde{u}_n$	Normal displacement of a generic point from $C(0)$ to $C(t)$
${}_t\tilde{u}_n$	Normal displacement increment
${}^{R}V$	Member volume in the perfectly straight reference configuration
${}^{t}V$	Member volume at configuration $C(t)$
$\tilde{w}$	Longitudinal displacement from $C(0)$ to $C(t)$
${}_t\tilde{w}$	Longitudinal displacement increment
${}_{R}^{\Delta t_1}\bar{U}$	Virtual work referred to the reference configuration
${}_t\mathbf{U}$	Vector of nodal displacement
x	Lateral coordinate
y	Transverse coordinate
y_t	Distance from the top flange to the section centroid
y_{sc}	Shear center coordinate relative to the section centroid
${}^{0}y_p$	Load height
z	Longitudinal coordinate
${}^{0}z_p$	Load location in beam longitudinal distance
α	Angle of the tangent to the middle surface relative to the x axis
${}_t\xi, {}_t\eta$	Displacement increments of the shear center along x, and y directions
${}_t\zeta$	Longitudinal displacement increment of the centroid
${}_t\theta$	Angle of twist increment
${}^{(t+\Delta t)}\mathbf{\Delta R}$	Nodal Equivalent force vector from time t to $t+\Delta t$
ω	Sectorial coordinate
${}_t\varepsilon_{zz}, {}_t\varepsilon_{zs}$	Longitudinal and shear Green-Lagrange strain increments
${}_t\varepsilon^{L}{}_{zz}, {}_t\varepsilon^{N}{}_{zz}$	Linear and nonlinear components of longitudinal Green-Lagrange strain increment
${}_t\varepsilon^{L}{}_{zs}, {}_t\varepsilon^{N}{}_{zs}$	Linear and nonlinear components of Green-Lagrange shear strain increment
${}_{t}^{t+\Delta t}\varepsilon_{zz}, {}_{t}^{t+\Delta t}\varepsilon_{zs}$	Normal and shear components of Green-Lagrange strain tensor at configuration $C(t+\Delta t)$ referred to configuration $C(t)$
${}_{a}^{b}\boldsymbol{\varepsilon}$	Green-Lagrange strain tensor at $C(b)$ referred to configuration $C(a)$
σ_{zz}, σ_{zs}	Normal and shear components of the Cauchy stress tensor
$\boldsymbol{\sigma}$	Cauchy stress tensor
$\boldsymbol{\sigma}_0$	Initial yielding stresses due residual stresses
${}_t\boldsymbol{\zeta}, {}_t\boldsymbol{\xi}, {}_t\boldsymbol{\eta}, {}_t\boldsymbol{\theta}$	Vectors of nodal degrees of freedom
ς	Dimensionless longitudinal coordinate

4.10 References

[4.1] CSA-Group, *CSA S16:24 Design and Construction of Steel Structures*, Tenth edit. CA: Canadian Institute of Steel Construction, 2024.

[4.2] ANSI/AISC 360-22, *Specification for structural steel buildings*. Chicago, IL: American Institute of Steel Construction (AISC), 2022.

[4.3] EN-1993-1-1-22, *Eurocode 3: Design of Steel Structures-General Rules and Rules for Buildings*. Brussels, Belgium: European Committee of Standardization (CEN), 2020.

[4.4] AS4100, *Steel structures*. Sydney: Standard Australia, 2020.

[4.5] T. A. Helwig, K. H. Frank, and J. A. Yura, "Lateral-Torsional Buckling of Singly Symmetric I-Beams," *J. Struct. Eng.*, vol. 123, no. 9, pp. 1172–1179, 1997, doi: 10.1061/(asce)0733-9445(1997)123:9(1172).

[4.6] R. S. Barsoum and R. H. Gallagher, "Torsional-Flexural Stability Problems," *Int. J. Numer. Methods Eng.*, vol. 2, no. August 1969, pp. 335–352, 1970.

[4.7] S. L. Chan and S. Kitipornchai, "Geometric nonlinear analysis of asymmetric thin-walled beam-columns," *Eng. Struct.*, vol. 9, no. 4, pp. 243–254, 1987, doi: 10.1016/0141-0296(87)90023-X.

[4.8] Y. Yang, S. Kuo, and Y. Cherng, "Curved beam elements for nonlinear analysis," *J. Eng. Mech.*, vol. 115, no. 4, pp. 840–855, 1989, doi: 10.1061/(asce)0733-9399(1989)115:4(840).

[4.9] X. Wang and Q. Yang, "Geometrically nonlinear finite element model of spatial thin-walled beams with general open cross section," *Acta Mech. Solida Sin.*, vol. 22, no. 1, pp. 64–72, 2009, doi: 10.1016/S0894-9166(09)60091-4.

[4.10] K. M. Hsiao and W. Y. Lin, "A co-rotational formulation for thin-walled beams with monosymmetric open section," *Methods*, vol. 190, pp. 1163–1185, 2000.

[4.11] H. H. Chen, W. Y. Lin, and K. M. Hsiao, "Co-rotational finite element formulation for thin-walled beams with generic open section," *Comput. Methods Appl. Mech. Eng.*, vol. 195, no. 19–22, pp. 2334–2370, 2006, doi: 10.1016/j.cma.2005.05.011.

[4.12] J. M. Battini and C. Pacoste, "Co-rotational beam elements with warping effects in instability problems," *Comput. Methods Appl. Mech. Eng.*, vol. 191, no. 17–18, pp. 1755–1789, 2002, doi: 10.1016/S0045-7825(01)00352-8.

[4.13] R. Alsafadie, M. Hjiaj, and J. M. Battini, "Three-dimensional formulation of a mixed corotational thin-walled beam element incorporating shear and warping deformation," *Thin-Walled Struct.*, vol. 49, no. 4, pp. 523–533, 2011, doi: 10.1016/j.tws.2010.12.002.

[4.14] X. Du and J. Hajjar, "Three-dimensional nonlinear displacement-based beam element for members with angle and tee sections," *Eng. Struct.*, vol. 239, no. March, p. 112239, 2021, doi: 10.1016/j.engstruct.2021.112239.

[4.15] J. B. Jonker, "Three-dimensional beam element for pre- and post-buckling analysis of thin-walled beams in multibody systems," *Multibody Syst. Dyn.*, vol. 52, no. 1, pp. 59–93, 2021, doi: 10.1007/s11044-021-09777-x.

[4.16] B. A. Conci, "Stiffness matrix for nonlinear analysis of thin-walled frames," vol. 118, no. 9, pp. 1859–1875, 1993.

[4.17] T. P. Vo and J. Lee, "Geometrical nonlinear analysis of thin-walled composite beams using finite element method based on first order shear deformation theory," *Arch. Appl. Mech.*, vol. 81, no. 4, pp. 419–435, 2011, doi: 10.1007/s00419-010-0407-x.

[4.18] N. Il Kim and J. Lee, "Nonlinear analysis of thin-walled Al/Al2O3 FG sandwich I-beams with mono-symmetric cross-section," *Eur. J. Mech. A/Solids*, vol. 69, no. January 2017, pp. 55–70, 2018, doi: 10.1016/j.euromechsol.2017.11.010.

[4.19] L. T. M. Phi, T. T. Nguyen, and J. Lee, "Buckling analysis of open-section beams with thin-walled functionally graded materials along the contour direction," *Eur. J. Mech. A/Solids*, vol. 88, no. December 2020, p. 104217, 2021, doi: 10.1016/j.euromechsol.2021.104217.

[4.20] L. Chen, W. L. Gao, S. W. Liu, R. D. Ziemian, and S. L. Chan, "Geometric and material nonlinear analysis of steel members with nonsymmetric sections," *J. Constr. Steel Res.*, vol. 198, Nov. 2022, doi: 10.1016/j.jcsr.2022.107537.

[4.21] N. Silvestre and D. Camotim, "NONLINEAR GENERALIZED BEAM THEORY FOR COLD-FORMED STEEL MEMBERS," *Int. J. Struct. Stab. Dyn.*, vol. 3, no. 4, pp. 461–490, 2003.

[4.22] N. Silvestre, D. Camotim, and M. Asce, “Local-Plate and Distortional Postbuckling Behavior of Cold-Formed Steel Lipped Channel Columns with,” *J. Struct. Eng. (New York, N.Y.)*, vol. 132, no. 4, pp. 529–540, 2006, doi: 10.1061/(ASCE)0733-9445(2006)132.
[4.23] C. Basaglia, D. Camotim, and N. Silvestre, “Non-linear GBT formulation for open-section thin-walled members with arbitrary support conditions,” *Comput. Struct.*, vol. 89, no. 21–22, pp. 1906–1919, 2011, doi: 10.1016/j.compstruc.2011.07.001.
[4.24] N. S. Trahair, “Inelastic buckling design of monosymmetric I-beams,” *Eng. Struct.*, vol. 34, pp. 564–571, 2012, doi: 10.1016/j.engstruct.2011.10.021.
[4.25] N. Boissonnade and H. Somja, “Influence of imperfections in FEM modeling of lateral torsional buckling,” in *Structural Stability Research Council Annual Stability Conference 2012*, 2012, pp. 399–413.
[4.26] L. Chen, A. H. A. Abdelrahman, S.-W. Liu, R. D. Ziemian, and S.-L. Chan, “Gaussian beam–column element formulation for large-deflection analysis of steel members with open sections subjected to torsion,” *J. Struct. Eng.*, vol. 147, no. 12, pp. 1–14, 2021, doi: 10.1061/(asce)st.1943-541x.0003185.
[4.27] A. Gjelsvik, *The Theory of Thin Walled Bars*. New York: John Wiley & Sons, 1981.
[4.28] Bathe, *Finite Element Procedures*. 1996. [Online]. Available: http://www.amazon.com/Finite-Element-Procedures-Part-1-2/dp/0133014584
[4.29] S. Attia, M. Mohareb, M. Martens, and S. Adeeb, “Shell finite element formulations of ovalized thin-walled pipes,” *Mech. Based Des. Struct. Mach.*, vol. 0, no. 0, pp. 1–22, 2025, doi: 10.1080/15397734.2025.2505190.
[4.30] Canadian Institute of Steel Construction, “CISC, Handbook of steel construction, in: Canadian Institute of Steel Construction, 11th ed., Lakeside Group Inc, Ontario, Canada, 2017.,” *Handb. Steel Constr.*, p. 1092, 2021.
[4.31] A. Sahraei, A. Iranpour, and M. Mohareb, “User manual for LTB-UO V3.0 (LTB-UO is a computer program for Lateral Torsional Buckling analysis of beams/beam-columns, written at the University of Ottawa),” 2020, *University of Ottawa*.

Chapter 5: Summary, Conclusions and Recommendations

5.1 Summary

The present dissertation formulates two geometrically nonlinear finite element solutions for the analysis of laterally unbraced long span members. The first formulation is tailored for the analysis of doubly symmetric members and adopts the updated Lagrangian approach, the kinematics of the thin-walled beam theory to capture local and global warping effects, while exploiting the multiplicative property of the deformation gradient to capture initial out-of-straightness effects. The second formulation extends the analysis to monosymmetric members, accounts for the effect of residual stresses by treating them as initial stresses, and accounts for load height effects. The formulations were implemented and verified against Abaqus shell and thin-walled beam finite element solutions.

The first formulation is used in conjunction with the onset of yield criterion to conduct a parametric study consisting of 504 numerical simulations on flexural members with doubly symmetric hot-rolled W-shaped sections to examine the effects of various IOS patterns (lateral, lateral torsional, twist, camber, and combinations thereof), IOS amplitudes, span-to-depth ratios, cross-sectional proportions, and loading types (uniform moment, uniform load, and mid-span point load). Regression analyses based on the database of runs were conducted to derive simple equations predicting elastic LTB resistance that capture the detrimental effects of IOS and residual stresses.

The second formulation is used to conduct a parametric study to assess the detrimental effects of various IOS patterns and amplitudes, load height, and whether the small or the large flange is in compression on the LTB moment resistance of long-span laterally unbraced flexural members with monosymmetric sections.

5.2 Conclusions

The main conclusions of the study are summarized in the following:

5.2.1 Rolled Members with Doubly Symmetric Sections

1- Accuracy: The displacements and normal stresses predicted by the formulation in Chapter 2 were found to be generally within 2–3% of those predicted by the Abaqus shell model.

2- Comparison against design standards: When applying the current formulation in conjunction with the first yield criterion, the predicted moment resistances were consistently lower than the American and Canadian standard predictions for spans governed by elastic lateral-torsional buckling, and, for the most part, higher than the Australian standard predictions. In most cases, the results were on par with the Eurocode predictions.

3- Effect of IOS pattern: Among the IOS patterns examined, twist IOS produced the largest reduction in LTB capacity, followed by lateral torsional-IOS and then by lateral-IOS. Camber alone in IOS had a negligible effect on LTB strength. Yet, when combined with L-IOS, upward camber was shown to reduce the LTB resistance.

4- Effect of IOS pattern and symmetry: For the load types and IOS considered, initial out of straightness in the form of a single half-wave IOS shape resulted in the lowest moment resistance, whereas multi-wave symmetric patterns are less detrimental and asymmetric IOS shapes were found to be the least detrimental to the LTB capacity.

5- Cross-section proportions and span: The ratio of the predicted moment resistance to the elastic critical moment is found to reduce with the flange width-to-depth ratio and to increase with flange slenderness and span-to-depth ratio, while remaining insensitive to web slenderness.

6- Influence of loading type: The detrimental effect of initial out-of-straightness (IOS) was found to be smallest for members subjected to uniform moment, greatest for those under mid-span point loading, and intermediate for members subjected to uniformly distributed loading. These trends were consistent across all doubly symmetric sections analyzed.

5.2.2 Rolled Members with Monosymmetric I Sections

1- Model verification and accuracy: The displacements and normal stresses predicted by the formulation in Chapter 4 were found to lie generally within 3-5% of those predicted by the Abaqus shell model.

2- Effect of compression flange proportion: Members with the small flange in compression exhibited greater sensitivity to IOS than those with the large flange in compression.

3- Effect of load height: Initial out-of-straightness (IOS) has the most detrimental effect on LTB resistance when the load is acting on the shear centre, as reflected by the lower M/M_u ratios. This detrimental effect diminishes slightly as the load height moves towards or below the shear

4- Interaction of IOS and residual stresses: For the cases investigated, the combined detrimental effect of residual stresses and IOS on the LTB strength is 2-3% above the sum of both effects, suggesting that the interaction between the two types of imperfections may be negligible.

5- Loading type sensitivity: In a manner similar to doubly symmetric beams, uniform moment loading showed minimal sensitivity to IOS, while mid-span point loading was most sensitive. The difference between the two cases was found to be more pronounced in monosymmetric sections.

5.3 Recommendations for Future Research

1- Extension of the study to intermediate spans: The present study has focused on the flexural resistance of long-span members whose capacities are primarily governed by elastic LTB. It is recommended that future research focus on intermediate spans, whose resistance is governed by inelastic LTB. This would necessitate incorporating the effect of material nonlinearity into the formulation in addition to features already implemented (IOS, residual stresses, load height effect).

2- Effects of other types of IOS: The present study focused on lateral, lateral torsional, twist and camber IOS. It is recommended to investigate other types of IOS, such as the non-orthogonality between the flange and web, plate out-of-flatness/initial distortions of the web and/or flanges.

3- Integration in design standards: It is recommended to conduct a probabilistic reliability analysis to establish appropriate resistance factors and/or IOS design amplitudes. Emphasis should be placed on refining the proposed twist-imperfection (T-IOS) amplitude threshold and integrating the regression-based equations into current design provisions.

4- Experimental verification: While the present numerical formulations have been thoroughly verified against shell and beam finite-element benchmark solutions, carefully designed experiments are recommended to validate the predicted LTB resistance of flexural members under carefully measured IOS patterns. Comparing the load-deformation predictions of the present models with experimentally measured results would provide an additional assessment of the models' validity.

5- Boundary conditions and intermediate restraints: The present study focused exclusively on simply supported members. It is of interest to expand the parametric studies to other boundary conditions involving fixity relative to minor-axis and major-axis rotations and/or warping. Also, it

is of interest to extend the study to continuous beams and cantilevers. Investigating the interaction between IOS and lateral and torsional braces on the member LTB resistance is also of practical interest.

6-Combined loading effects: The models implemented in the present study can capture interactions among major and minor axis bending, axial force, and torsion, and can serve as a basis for developing and assessing various interaction equations among these effects and their interplay with initial out-of-straightness and residual stresses.

Appendix A: Algorithm for Computing the Geometric Stiffness Matrix and Force Vector

The objective of this appendix is to illustrate the algorithm for computing the geometric stiffness matrix and force vector derived in Chapters 2 and 4. Starting with the converged displacement vector after increment n, this appendix outlines the steps for computing the geometric stiffness matrix and the energy equivalent load vector within the framework of the updated Lagrangian Formulation.

A.1 Key Equations

A.1.1 Geometric Matrix Definition

The geometric stiffness matrix at configuration $C(t)$ in local coordinates takes the form (Equation 16 in Chapter 2)

$$ {}^{t}\mathbf{K}_{\mathbf{G}} = \begin{bmatrix} \mathbf{0} & \mathbf{0} & \mathbf{0} & \mathbf{0} \\ \mathbf{0} & {}^{t}\mathbf{K}_{\xi\xi} & \mathbf{0} & {}^{t}\mathbf{K}_{\xi\theta} \\ \mathbf{0} & \mathbf{0} & {}^{t}\mathbf{K}_{\eta\eta} & {}^{t}\mathbf{K}_{\eta\theta} \\ \mathbf{0} & {}^{t}\mathbf{K}_{\xi\theta}^{\mathbf{T}} & {}^{t}\mathbf{K}_{\eta\theta}^{\mathbf{T}} & {}^{t}\mathbf{K}_{\theta\theta} \end{bmatrix} \tag{A.1} $$

in which

$$ {}^{t}\mathbf{K}_{\xi\xi} = \int_{{}^{t}z=0}^{{}^{t}L} {}^{t}M_1 \left(\mathbf{H}_{\mathbf{a}}' \mathbf{H}_{\mathbf{a}}'^{\mathbf{T}} \right) d\,{}^{t}z,\ {}^{t}\mathbf{K}_{\eta\eta} = \int_{{}^{t}z=0}^{{}^{t}L} {}^{t}M_1 \left(\mathbf{H}_{\mathbf{b}}' \mathbf{H}_{\mathbf{b}}'^{\mathbf{T}} \right) d\,{}^{t}z,\ {}^{t}\mathbf{K}_{\theta\theta} = \int_{{}^{t}z=0}^{{}^{t}L} {}^{t}M_4 \left(\mathbf{H}_{\mathbf{a}}' \mathbf{H}_{\mathbf{a}}'^{\mathbf{T}} \right) d\,{}^{t}z $$

$$ {}^{t}\mathbf{K}_{\theta\xi} = \int_{{}^{t}z=0}^{{}^{t}L} {}^{t}M_3 \left(\mathbf{H}_{\mathbf{a}}' \mathbf{H}_{\mathbf{a}}'^{\mathbf{T}} \right) d\,{}^{t}z,\ {}^{t}\mathbf{K}_{\theta\eta} = \int_{{}^{t}z=0}^{{}^{t}L} {}^{t}M_2 \left(\mathbf{H}_{\mathbf{a}}' \mathbf{H}_{\mathbf{b}}'^{\mathbf{T}} \right) d\,{}^{t}z $$

$$ \mathbf{L}^{\mathbf{T}} = \left\langle \ (1-\varsigma) \quad \varsigma \right\rangle \qquad\qquad \varsigma = {}^{t}z / {}^{t}L $$

$$ \mathbf{H}_{\mathbf{a}}{}^{\mathbf{T}} = \left\langle 1-3\varsigma^2+2\varsigma^3 \ \middle\vdots\ {}^{t}L\varsigma(1-\varsigma)^2 \ \middle\vdots\ 3\varsigma^2-2\varsigma^3 \ \middle\vdots\ {}^{t}L\varsigma^2(-1+\varsigma) \right\rangle $$

$$ \mathbf{H}_{\mathbf{b}}{}^{\mathbf{T}} = \left\langle 1-3\varsigma^2+2\varsigma^3 \ \middle\vdots\ -{}^{t}L\varsigma(1-\varsigma)^2 \ \middle\vdots\ 3\varsigma^2-2\varsigma^3 \ \middle\vdots\ -{}^{t}L\varsigma^2(-1+\varsigma) \right\rangle $$

and

$$ {}^{t}M_1 = \int_A \sigma_{zz} dA,\ {}^{t}M_2 = \int_A {}^{t}x\sigma_{zz} dA,\ {}^{t}M_3 = -\int_A {}^{t}y\sigma_{zz} dA,\ {}^{t}M_4 = \int_A \left({}^{t}h^2 + {}^{t}q^2 + 2{}^{t}h\,{}^{t}n + {}^{t}n^2 \right) \sigma_{zz} dA $$

A.1.2 Load Vector Definition

The nodal force vector at the configuration $C(t)$ in local coordinates is

$$ \begin{aligned} {}^{t+\Delta t}_{t}\bar{U}_4 &= \int_{{}^{t}z=0}^{{}^{t}L} \left({}_{t}\bar{\zeta}' {}^{t}M_1 - {}_{t}\bar{\xi}'' {}^{t}M_2 + {}_{t}\bar{\eta}'' {}^{t}M_3 + {}_{t}\bar{\theta}'' {}^{t}M_5 + {}_{t}\bar{\theta}' {}^{t}M_6 \right) d\,{}^{t}z \\ &= \left\langle {}_{t}\bar{\boldsymbol{\zeta}}^{\mathbf{T}} \quad {}_{t}\bar{\boldsymbol{\xi}}^{\mathbf{T}} \quad {}_{t}\bar{\boldsymbol{\eta}}^{\mathbf{T}} \quad {}_{t}\bar{\boldsymbol{\theta}}^{\mathbf{T}} \right\rangle \int_{{}^{t}z=0}^{{}^{t}L} \begin{Bmatrix} {}^{t}M_1 \mathbf{L}' \\ -{}^{t}M_2 \mathbf{H_a}'' \\ +{}^{t}M_3 \mathbf{H_b}'' \\ +\left({}^{t}M_5 \mathbf{H_a}'' + {}^{t}M_6 \mathbf{H_a}' \right) \end{Bmatrix} d\,{}^{t}z \end{aligned} \qquad \text{(A.2)} $$

in which

$$ {}^{t}M_1 = \int_A \sigma_{zz} dA\ ,\ {}^{t}M_2 = \int_A {}^{t}x\sigma_{zz} dA,\ {}^{t}M_3 = -\int_A {}^{t}y\sigma_{zz} dA,\ {}^{t}M_5 = -\int_A {}^{t}\omega\sigma_{zz} dA,\ {}^{t}M_6 = \int_A 4\,{}^{t}n\sigma_{zs} dA $$

A.1.3 Deformation gradient

$$ {}^{t+\Delta t}\mathbf{F}^{(i)} = \begin{bmatrix} 1 + \dfrac{\partial}{\partial\,{}^{t}z}\left({}^{t+\Delta t}\tilde{w} \right) & \dfrac{\partial}{\partial\,{}^{t}s}\left({}^{t+\Delta t}\tilde{w} \right) & \dfrac{\partial}{\partial\,{}^{t}n}\left({}^{t+\Delta t}\tilde{w} \right) \\ \dfrac{\partial}{\partial\,{}^{t}z}\left({}^{t+\Delta t}\tilde{u}_t \right) & 1 + \dfrac{\partial}{\partial\,{}^{t}s}\left({}^{t+\Delta t}\tilde{u}_t \right) & \dfrac{\partial}{\partial\,{}^{t}n}\left({}^{t+\Delta t}\tilde{u}_t \right) \\ \dfrac{\partial}{\partial\,{}^{t}z}\left({}^{t+\Delta t}\tilde{u}_n \right) & \dfrac{\partial}{\partial\,{}^{t}s}\left({}^{t+\Delta t}\tilde{u}_n \right) & 1 + \dfrac{\partial}{\partial\,{}^{t}n}\left({}^{t+\Delta t}\tilde{u}_n \right) \end{bmatrix} = \begin{bmatrix} 1 + \dfrac{\partial}{\partial z}\left({}^{t+\Delta t}\tilde{w} \right) & \dfrac{\partial}{\partial s}\left({}^{t+\Delta t}\tilde{w} \right) & \dfrac{\partial}{\partial n}\left({}^{t+\Delta t}\tilde{w} \right) \\ \dfrac{\partial}{\partial z}\left({}^{t+\Delta t}\tilde{u}_t \right) & 1 + \dfrac{\partial}{\partial s}\left({}^{t+\Delta t}\tilde{u}_t \right) & \dfrac{\partial}{\partial n}\left({}^{t+\Delta t}\tilde{u}_t \right) \\ \dfrac{\partial}{\partial z}\left({}^{t+\Delta t}\tilde{u}_n \right) & \dfrac{\partial}{\partial s}\left({}^{t+\Delta t}\tilde{u}_n \right) & 1 + \dfrac{\partial}{\partial n}\left({}^{t+\Delta t}\tilde{u}_n \right) \end{bmatrix} $$

(A.3)

in which the displacement derivatives in Eq.(A.3) are computed as

$$\frac{\partial}{\partial z}\left[{}^{t+\Delta t}\tilde{w}(z,s,n)\right] = {}^{t+\Delta t}\zeta'(z) - {}^{t+\Delta t}\xi''(z)\,x(s,n) - {}^{t+\Delta t}\eta''(z)\,y(s,n) - {}^{t+\Delta t}\theta''(z)\,\omega(s,n)$$
$$\frac{\partial}{\partial s}\left[{}^{t+\Delta t}\tilde{w}(z,s,n)\right] = -{}^{t+\Delta t}\xi'(z)\cos\alpha(s) - {}^{t+\Delta t}\eta'(z)\sin\alpha(s) - {}^{t+\Delta t}\theta'(z)\left[h(s)-n\right]$$
$$\frac{\partial}{\partial n}\left({}^{t+\Delta t}\tilde{w}\right) = -{}^{t+\Delta t}\xi'(z)\sin\alpha(s) + {}^{t+\Delta t}\eta'(z)\cos\alpha(s) + {}^{t+\Delta t}\theta'(z)\,t(s)$$

$$\frac{\partial}{\partial z}\left({}^{t+\Delta t}\tilde{u}_t\right) = {}^{t+\Delta t}\xi'(z)\cos\alpha(s) + {}^{t+\Delta t}\eta'(z)\sin\alpha(s) + {}^{t+\Delta t}\theta'(z)\left[h(s)+n\right]$$
$$\frac{\partial}{\partial s}\left({}^{t+\Delta t}\tilde{u}_t\right) = 0$$
$$\frac{\partial}{\partial n}\left({}^{t+\Delta t}\tilde{u}_t\right) = {}^{t+\Delta t}\theta(z)$$

$$\frac{\partial}{\partial z}\left({}^{t+\Delta t}\tilde{u}_n\right) = {}^{t+\Delta t}\xi'(z)\sin\alpha(s) - {}^{t+\Delta t}\eta'(z)\cos\alpha(s) - {}^{t+\Delta t}\theta'(z)\,t(s)$$
$$\frac{\partial}{\partial s}\left({}^{t+\Delta t}\tilde{u}_n\right) = -{}^{t+\Delta t}\theta(z)$$
$$\frac{\partial}{\partial n}\left({}^{t+\Delta t}\tilde{u}_n\right) = 0$$

and the coordinates of the point of interest are

$$\begin{aligned} x(s,n) &= \bar{x}(s) + n\sin\alpha(s) \\ y(s,n) &= \bar{y}(s) - n\cos\alpha(s) \\ \omega(s,n) &= \bar{\omega}(s) - nt(s) \end{aligned} \qquad \text{(A.4)a-c}$$

and the displacements and their derivatives are related to the nodal displacements through

$${}^{t+\Delta t}\zeta'(z) = \mathbf{L}^{\mathrm{T}}(z)\,{}^{t+\Delta t}\boldsymbol{\zeta}'$$

$${}^{t+\Delta t}\xi(z) = \mathbf{H_a}^{\mathrm{T}}(z)\,{}^{t+\Delta t}\boldsymbol{\xi} \qquad {}^{t+\Delta t}\eta(z) = \mathbf{H_b}^{\mathrm{T}}(z)\,{}^{t+\Delta t}\boldsymbol{\eta} \qquad {}^{t+\Delta t}\theta(z) = \mathbf{H_a}^{\mathrm{T}}(z)\,{}^{t+\Delta t}\boldsymbol{\theta}$$
$${}^{t+\Delta t}\xi'(z) = \mathbf{H_a}'^{\mathrm{T}}(z)\,{}^{t+\Delta t}\boldsymbol{\xi} \qquad {}^{t+\Delta t}\eta'(z) = \mathbf{H_b}'^{\mathrm{T}}(z)\,{}^{t+\Delta t}\boldsymbol{\eta} \qquad {}^{t+\Delta t}\theta(z) = \mathbf{H_a}'^{\mathrm{T}}(z)\,{}^{t+\Delta t}\boldsymbol{\theta}$$
$${}^{t+\Delta t}\xi''(z) = \mathbf{H_a}''^{\mathrm{T}}(z)\,{}^{t+\Delta t}\boldsymbol{\xi} \qquad {}^{t+\Delta t}\eta''(z) = \mathbf{H_b}''^{\mathrm{T}}(z)\,{}^{t+\Delta t}\boldsymbol{\eta} \qquad {}^{t+\Delta t}\theta''(z) = \mathbf{H_a}''^{\mathrm{T}}(z)\,{}^{t+\Delta t}\boldsymbol{\theta}$$

(A.5)a-d

in which

$$\mathbf{L}^{\mathrm{T}} = \begin{bmatrix} (1-\varsigma) & \varsigma \end{bmatrix} \qquad \varsigma = {}^{t}z/{}^{t}L$$

$$\mathbf{H_a}^{\mathrm{T}} = \begin{bmatrix} 1-3\varsigma^2+2\varsigma^3 & {}^{t}L\varsigma(1-\varsigma)^2 & 3\varsigma^2-2\varsigma^3 & {}^{t}L\varsigma^2(-1+\varsigma) \end{bmatrix}$$

$$\mathbf{H_b}^{\mathrm{T}} = \begin{bmatrix} 1-3\varsigma^2+2\varsigma^3 & -{}^{t}L\varsigma(1-\varsigma)^2 & 3\varsigma^2-2\varsigma^3 & -{}^{t}L\varsigma^2(-1+\varsigma) \end{bmatrix}$$

A.1.4 Transformation Matrix

The member nodal displacement vector in local coordinates ${}^{t+\Delta t}\tilde{\mathbf{u}}_{\mathbf{e}14\times1}$ is obtained its nodal displacement vector in global coordinates ${}^{t+\Delta t}\tilde{\mathbf{u}}_{\mathbf{G}14\times1}$ using the transformation ${}^{t+\Delta t}\tilde{\mathbf{u}}_{\mathbf{e}14\times1} = {}^{t+\Delta t}\mathbf{T}\,{}^{t+\Delta t}\tilde{\mathbf{u}}_{\mathbf{G}}$ in which the transformation matrix ${}^{t+\Delta t}\mathbf{T}_{14\times14}$ is given by

$${}^{t+\Delta t}\mathbf{T}_{14\times14} = \left[\begin{array}{cc:c:cc:c} {}^{t+\Delta t}\mathbf{r}_{3\times3} & \mathbf{0} & 0 & \mathbf{0} & \mathbf{0} & 0 \\ \mathbf{0} & {}^{t+\Delta t}\mathbf{r}_{3\times3} & 0 & \mathbf{0} & \mathbf{0} & 0 \\ \hdashline 0 & 0 & 1 & 0 & 0 & 0 \\ \hdashline \mathbf{0} & \mathbf{0} & 0 & {}^{t+\Delta t}\mathbf{r}_{3\times3} & \mathbf{0} & 0 \\ \mathbf{0} & \mathbf{0} & 0 & \mathbf{0} & {}^{t+\Delta t}\mathbf{r}_{3\times3} & 0 \\ \hdashline 0 & 0 & 0 & 0 & 0 & 1 \end{array}\right] \tag{A.6}$$

in which the nodal orientation matrix ${}^{t+\Delta t}\mathbf{r}_{3\times3}$ at time $t+\Delta t$ is given by (e.g.,[2.22])

$$\mathbf{r} = \begin{bmatrix} r_{xX} & r_{xY} & r_{xZ} \\ \dfrac{-r_{xX}r_{xY}\cos\varphi - r_{xZ}\sin\varphi}{\sqrt{{r_{xX}}^2+{r_{xZ}}^2}} & \sqrt{{r_{xX}}^2+{r_{xZ}}^2}\cos\varphi & \dfrac{-r_{xY}\,r_{xZ}\cos\varphi + r_{xX}\sin\varphi}{\sqrt{{r_{xX}}^2+{r_{xZ}}^2}} \\ \dfrac{r_{xX}r_{xY}\sin\varphi - r_{xZ}\cos\varphi}{\sqrt{{r_{xX}}^2+{r_{xZ}}^2}} & -\sqrt{{r_{xX}}^2+{r_{xZ}}^2}\sin\varphi & \dfrac{r_{xY}\,r_{xZ}\sin\varphi + r_{xX}\cos\varphi}{\sqrt{{r_{xX}}^2+{r_{xZ}}^2}} \end{bmatrix} \tag{A.7}$$

in which (r_{xX}, r_{xY}, r_{xZ}) are the direction cosines of the local axis x of the member in the deformed configuration $C(t)$ and the global axes (X, Y, Z) of the structure and φ is the angle of twist of the member.

A.2 Pseudo-code for Computing Geometric Stiffness Matrix and Load Vector

Loop on elements e

Extract element nodal displacements in global coordinates ${}^{t+\Delta t}(\tilde{\mathbf{u}}_{\mathbf{G}})$ from structure nodal vector

Transform displacements from global to local coordinates ${}^{t+\Delta t}(\tilde{\mathbf{u}}_e) = {}^{t+\Delta t}\mathbf{T}\,{}^{t+\Delta t}(\tilde{\mathbf{u}}_{\mathbf{G}})$

Loop on Gauss points i along the span

Compute z_i

Given ${}^{t+\Delta t}(\tilde{\mathbf{u}}_e)$ and z_i obtain all Four displacements, 1st and 2nd z derivatives at z_i

Loop on the three segments of cross-section $j = 1, 2, 3$

Compute $h, q, \sin\alpha, \cos\alpha$ for segment j

Loop on all Simpson points k along segment width

Given k compute the tangential coordinate $s = s_{e,i,j,k,l}$

Loop on through thickness Gauss points l

Compute $x(s,n), y(s,n), \omega(s,n)$ at (i, j, k, l)

Given the displacements+ derivatives and coordinates compute the deformation gradient ${}^{t+\Delta t}\mathbf{F}^{\mathbf{T}(i)}$ at point (i,j,k,l)

Compute the Green Lagrange strain

$${}^{t+\Delta t}\boldsymbol{\varepsilon}^{(i)} = \frac{1}{2}\left({}^{t+\Delta t}\mathbf{F}^{\mathbf{T}(i)}\, {}^{t+\Delta t}\mathbf{F}^{(i)} - \mathbf{I} \right)$$

Compute the 2PK stress tensor ${}^{t+\Delta t}\mathbf{S}^{(i)}$

$${}^{t+\Delta t}\mathbf{S}^{(i)} = \begin{bmatrix} {}^{t+\Delta t}S_{11} & {}^{t+\Delta t}T_{12} & 0 \\ {}^{t+\Delta t}T_{12} & {}^{t+\Delta t}S_{22} & 0 \\ 0 & 0 & 0 \end{bmatrix}$$

$${}^{t+\Delta t}\hat{\mathbf{S}}^{(i)} = \begin{bmatrix} E & 0 & 0 \\ 0 & E & 0 \\ 0 & 0 & G \end{bmatrix} \begin{Bmatrix} {}^{t+\Delta t}\varepsilon_{11} \\ {}^{t+\Delta t}\varepsilon_{22} \\ 2\,{}^{t+\Delta t}\varepsilon_{12} \end{Bmatrix} = \begin{Bmatrix} {}^{t+\Delta t}S_{11} \\ {}^{t+\Delta t}S_{22} \\ 2\,{}^{t+\Delta t}T_{12} \end{Bmatrix}$$

Compute and store the Cauchy stress ${}^{t+\Delta t}\boldsymbol{\sigma}$ for (i,j,k,l)

$${}^{t+\Delta t}\boldsymbol{\sigma}^{(i)} = \frac{1}{\left\| {}^{t+\Delta t}\mathbf{F}^{(i)} \right\|} \left({}^{t+\Delta t}\mathbf{F}^{(i)} \right) \left({}^{t+\Delta t}\mathbf{S}^{(i)} \right) \left({}^{t+\Delta t}\mathbf{F}^{\mathbf{T}(i)} \right)$$

Close loop on through thickness Gauss points l

Close loop on Simpson points along the width k

Close loop on segment j

Numerically perform and store the following integrals at location z_i

$$
{}^{t}M_1 = \int_A \sigma_{zz} dA, \qquad {}^{t}M_2 = \int_A {}^{t}x\sigma_{zz} dA,
$$

$$
{}^{t}M_3 = -\int_A {}^{t}y\sigma_{zz} dA \qquad , {}^{t}M_4 = \int_A \left({}^{t}h^2 + {}^{t}q^2 + 2{}^{t}h\,{}^{t}n + {}^{t}n^2 \right) \sigma_{zz} dA
$$

$$
{}^{t}M_5 = -\int_A {}^{t}\omega\sigma_{zz} dA, \qquad {}^{t}M_6 = \int_A 4{}^{t}n\sigma_{zs} dA
$$

Close loop on the Gauss points i

1. Numerically perform the Gauss integral along the span to form the geometric stiffness matrix in local coordinates $ {}^{t}\mathbf{K}_{\mathbf{G}} = f\left({}^{t}\mathbf{K}_{\xi\xi}, {}^{t}\mathbf{K}_{\eta\eta}, {}^{t}\mathbf{K}^{\mathbf{T}}_{\xi\theta}, {}^{t}\mathbf{K}^{\mathbf{T}}_{\eta\theta}, {}^{t}\mathbf{K}_{\theta\theta} \right)$
2. Numerically perform the Gauss integral along the span to form the element energy equivalent load vector $ {}^{t+\Delta t}\mathbf{f}_l $
3. Perform the transformation of the element stiffness matrix from local coordinates to global coordinates

   $$ {}^{t}\mathbf{K}_{\mathbf{e}} = {}^{t}\mathbf{T}^{\mathbf{T}} \left\{ \mathbf{K}_{\mathbf{E(e)}} + {}^{t}\mathbf{K}_{\mathbf{G(e)}} \right\} {}^{t}\mathbf{T} $$

4. Perform the transformation of the element load vector from local coordinates to global coordinates

   $$ {}^{t+\Delta t}\mathbf{f}_g = \left({}^{t}\mathbf{T}^{\mathbf{T}} \right) \left({}^{t+\Delta t}\mathbf{f}_l \right) $$

5. Send element matrix $ \mathbf{K}_{\mathbf{e}}^{(n)} $ to the structure stiffness matrix

Close loop on element e

Appendix B: Number of Integration Points Needed for Convergence

B.1 Scope

The present appendix examines the number of integration points required for convergence of the model developed in Chapters 2- 4. In the implementation of volume integrals, integration along the longitudinal direction and across the thickness are conducted using Gauss quadrature while the Simpson integration is adopted along the flange width and web height.

B.2 Statement of the Problem

Geometrically nonlinear analyses are performed on a cantilever steel beam with a 4 m span. Beam cross-section is I-shaped with a flange width of 100 mm and thicknesses of 10 mm and a web height of 200 mm, and a thickness of 10mm. The corresponding cross-sectional properties presented in Table B.1. Material is steel with a Young modulus $E = 200GPa$ and a shear modulus $G = 77GPa$ The beam spans and is subjected to combined loading conditions acting at the cantilever tip:

(1) A transverse load V equal to half of the LTB critical load $V = V_c/2 = 11kN$ where V_c was determined through a buckling eigenvalue analysis; and

(2) An axial load P equal to half of the buckling load $P_{crx} = \pi^2 EI_x/4L^2$, i.e., $P = P_{crx}/2 = 450\,kN$

A mesh sensitivity analysis indicated that convergence is achieved with 10 elements along the beam span. The load is applied in 20 increments. All results reported in the following section correspond to a load level $V = 11kN$ and $P = 450\,kN$.

Table B.1 Sectional properties for cross-section

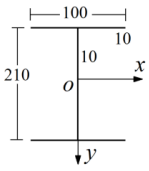	$A\left(\text{mm}^2\right)$	4100	$J\left(\text{mm}^4\right)$	1.3667×10^5
	$I_{xx}\left(\text{mm}^4\right)$	2.9784×10^7	$I_{\omega}\left(\text{mm}^6\right)$	1.8434×10^{10}
	$I_{yy}\left(\text{mm}^4\right)$	1.6841×10^6		

B.3 Number of Gauss Points Along the Longitudinal Direction

Numerical integration along the longitudinal direction was conducted using Gauss quadrature. To identify the optimal number of Gauss points required for accurately predicting stress and displacement, the analysis was conducted using three and four Gauss points. Meanwhile, the Simpson integration points along the flanges and web width were seven, and the number of Gauss points across the thickness was limited to two. The results in Fig. B.1. correspond to a transverse load of $V = 11kN$ and axial load lever of $P = 450\,kN$. As illustrated in Fig. B.1.a, the transverse displacement predictions at the cantilever tip using three and four Gauss points are in close agreement. Similar agreement is also observed for the longitudinal stress predictions (Fig. B.1.b). Three Gauss points per element are thus judged to be enough to attain convergence

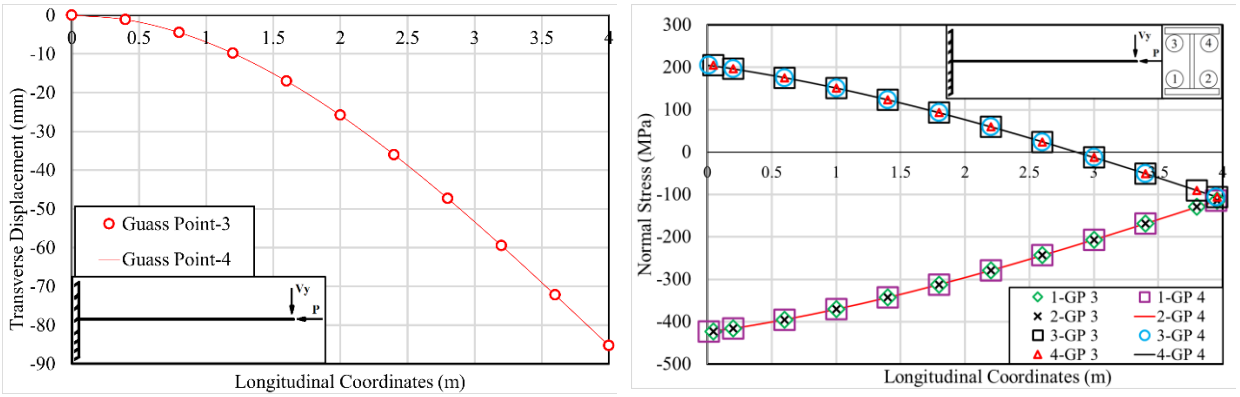

(a) (b)

Fig. B.1 Sensitivity analysis of number of gauss integration points along longitudinal direction (a) Transverse displacement and (b) Longitudinal Stresses

B.4 Number of Simpson Points Along the Web Height and Flange Width

Numerical integration over the flange width and web height was performed using Simpson integration. To determine the appropriate number of Simpson integration points for convergence, the analysis was conducted with 5, 7, 9, and 11 points. Meanwhile, the Gauss integration points were kept at four along the longitudinal direction and two across the thickness.

Fig. B.2a shows that the transverse displacement predictions at the cantilever tip using 9 and 11 Simpson points are indistinguishable. A similar conclusion can be drawn from Fig. B.2.b regarding the stresses at the corner points of the cantilever root. Fewer Simpson points result in inaccuracies, while more Simpson points provide only a marginal improvement. Nine Simpson points are thus judged to strike an optimal balance between accuracy and computational efficiency.

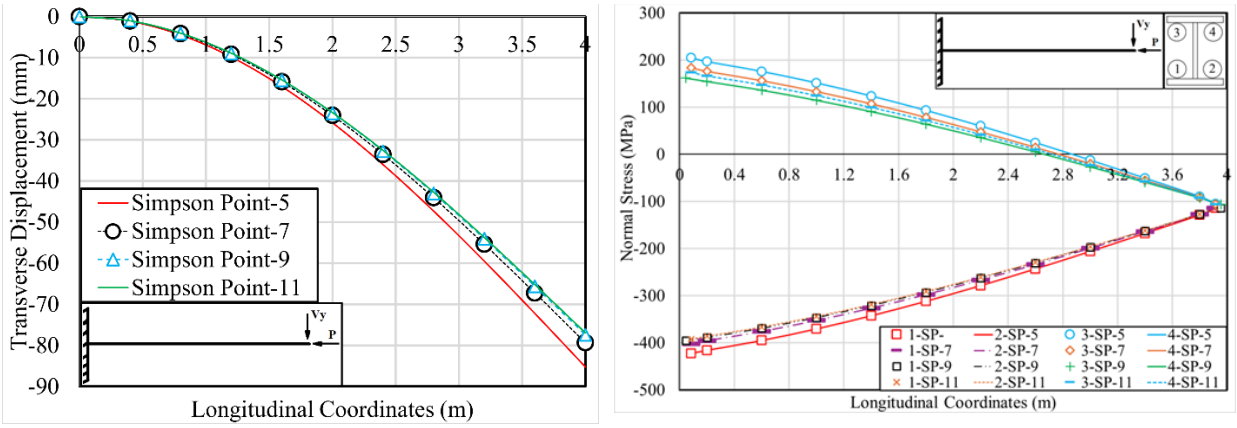

(a) (b)

Fig. B.2 Sensitivity analysis of the number of Simpson points along the web height (a) Transverse displacement. (b) Longitudinal Stresses

B.5 Number of Gauss Points Across the Thickness

Numerical integration across the thickness was conducted using Gauss quadrature. To determine the appropriate number of Gauss points across the thickness, two- and three-point Gauss integration were used, while keeping the number of Simpson points constant along the flange width

and web height at 9, and setting the number of Gauss points across the thickness to three. As illustrated in Fig. B.3a, the transverse displacements at the cantilever tip predicted by the present model with two and three through-thickness Gauss integration points are in excellent agreement. Very close agreement is observed between the two solutions for the longitudinal stresses at the cantilever roots at the four corners of the flanges (Fig. B.3b).

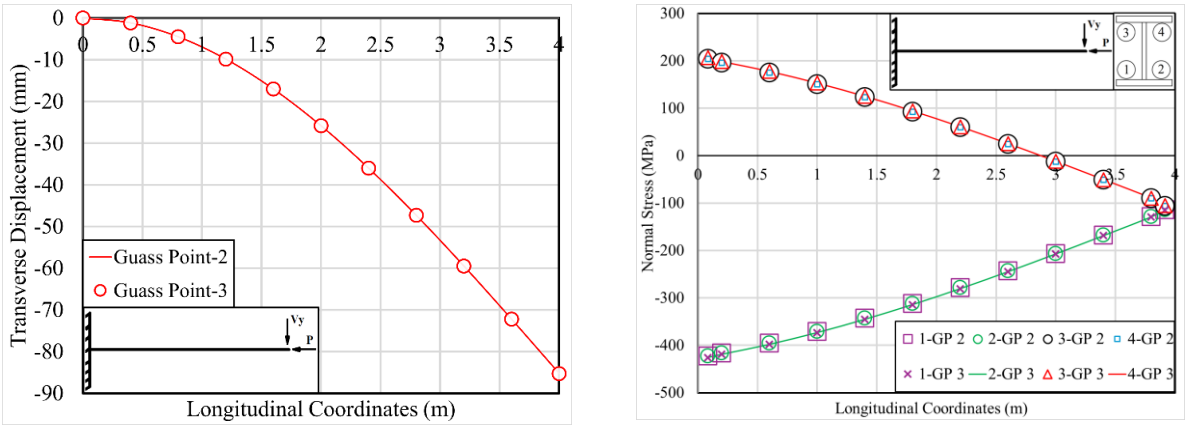

(a) (b)

Fig. B.3 Sensitivity analysis of Gauss integration points in the thickness direction of the cross-section of the cantilever beam under combined loading (a) Transverse displacement. (b) Stress.

B.6 Conclusion

In conclusion, the above results show that convergence is attained with:

a) three Gauss points along the longitudinal directions

b) nine Simpson points along the flange width and web height, and

c) two Gauss integration points across the thickness

The parametric runs in the study have thus been based on the above number of integration points.

Appendix C: Study of Convergence Tolerance

Starting with the prescribed convergence criteria of the developed model used in Chapters 2, 3, and 4, this appendix outlines the procedure and results for evaluating displacement- and force-based tolerances for members with three IOS patterns and three representative cross-sections. The discussion aims to determine the number of increments and iterations required to reach the target load, and tolerance values for subsequent analyses.

C.1 Statement of the Problem

Flexural members with $\mathrm{W310\times67}$, $\mathrm{W250\times45}$, and $\mathrm{W200\times36}$ cross-sections are considered. Cross-sectional dimensions and properties are provided in Table C.1. The beams meet Class 2 requirements for a yield strength F_y =350MPa. The beams are restrained transversely and laterally against twist at both ends and subjected to uniform moment loading. The target moment applied is $1.5M_{cr}$ where M_{cr} is the critical moment through eigenvalue buckling analysis. The threshold length L_t between the elastic and inelastic lateral torsional buckling regions is determined from

$$L_t = \frac{\pi\sqrt{2EI_yEC_\omega}}{-EI_yGJ+\sqrt{\left(EI_yGJ\right)^2+4E^2I_yC_\omega\left(0.67M_p\right)^2}} \tag{C.1}$$

where $E=200GPa$ is the modulus of elasticity, I_y is the weak-axis moment of inertia, $G=77GPa$ is the shear modulus, and is J the torsional constant, and C_ω is the warping constant. The spans chosen were about $1.5L_t$.

Three initial out-of-straightness (IOS) patterns are considered: (1) lateral IOS with an amplitude $L/1000$, (2) pure torsional IOS with an amplitude $L/1000$ at top flange and $-L/1000$ at bottom

flange , and (3) combined lateral-torsional IOS according to the first mode shape. The first mode shape is obtained from an eigenvalue buckling analysis in Abaqus. The IOS is applied using the *IMPERFECTION keyword in Abaqus, with an amplitude value at the top flange of $L/1000$. This was accomplished using the relationship $u_{TF} = u_0 + (d/2)\theta_0$ where u_{TF} represents the lateral out-of-straightness of the top flange, u_0 the lateral out-of-straightness at the shear center, θ_0 is the angle of twist at the cross-section, and d is the cross-sectional depth. Similarly, the bottom flange lateral IOS in the case of lateral-torsional IOS is determined from $u_{TF} = u_0 - (d/2)\theta_0$. The analysis begins with an eigenvalue analysis for a perfectly straight beam to determine from

$$M_{cr} = \frac{C\pi}{L}\sqrt{EI_y GJ + \left(\frac{\pi E}{L}\right)^2 I_y C_w} \tag{C.2}$$

The load is incrementally increased from 0 to $1.5M_{cr}$.

Table C.1 Beam dimensions and geometric properties for the examined cross-sections

Designation	d mm	b mm	t mm	w mm	L mm	$I_x \times 10^6$ mm^4	$I_y \times 10^5$ mm^4	$C_\omega \times 10^{10}$ mm^6	$J \times 10^4$ mm^4
W200×36	201	165	10.2	6.2	5220	34.4	76.4	6.96	14.5
W250×45	266	148	13	7.6	4250	71.1	70.3	11.3	26.1
W310×67	306	204	14.6	8.5	5620	144	207	43.9	52.2

Two convergence tolerance types were considered in the present model nonlinear solution: the displacement tolerance ε_d and the force tolerance ε_f. Each analysis run used a specific pair of tolerance values, as summarized in Table C.2. For each run, tolerance was adjusted according to the values shown below, and the comparison of displacement and stress results was conducted at the target load level of $1.5M_{cr}$.

Table C.2 Adopted displacement and force tolerances

displacement tolerance ε_d	force tolerance ε_f .
1/50	1/100
1/100	1/500
1/1000	1/1000

C.2 Present Model

A mesh sensitivity analysis indicated that convergence is achieved with 10 elements along the beam span. Therefore, 10 elements were used in all runs. Integration points consist of 4 Gauss quadrature points in the longitudinal direction, 8 Simpson's integration points along the width and height directions, and 2 Gauss quadrature points across the thickness direction.

Table C.3 Moment and IOS of each cross-section

Designation	$1.5M_{cr}$ (kNm)	Threshold span L_t (m)	Chosen span L (m)	L / L_t	Lateral IOS (mm)		Lateral-Torsional IOS (mm)		Torsional Pure Twist IOS (mm)	
					TF LIOS	BF LIOS	TF LIOS	BF LIOS	TF LIOS	BF LIOS
W200×36	120	5.22	8.00	1.53	8	8	8	2.117	8	-8
W250×45	190	4.25	6	1.41	6	6	6	1.588	6	-6
W310×67	320	5.62	8	1.42	8	8	8	2.117	8	-8
					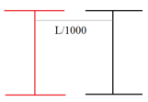		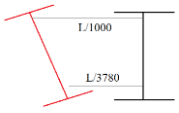		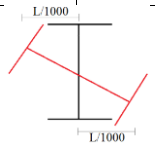	

*Threshold span Lt from Eq. (C.1)

C.3 B31OS Model

The B31OS element is a thin-walled beam element with two nodes. Each node possesses seven degrees of freedom: three translations, three rotations, and a warping degree of freedom. It captures shear deformation caused by bending but does not account for shear deformation due to warping. A mesh study was conducted, indicating that 16- 20 elements were needed to accurately predict stress and displacement generalized cross-section feature in Abaqus was used to input the member's cross-sectional properties (Table C.4).

Table C.4 Mesh sensitivity analysis of the B31OS beam element

Beam cross-section	Transverse displacement[(1)] (mm)	Normal stress[(2)] (MPa)	Number of Elements
W200×36	80.3	241	14
	81.3	249	16
	81.4	252	18
W250×45	33.1	243	14
	34.3	248	17
	34.4	250	20
W310×67	51.3	239	16
	53.8	247	20
	54.0	249	24

(1) At the cantilever tip
(2) Peak normal stress at the extreme fiber at the cantilever root

C.4 S4 Model

The S4 element is a general-purpose doubly curved shell (S) element with four (4) nodes and full integration. Each node has three translational and three rotational degrees of freedom per node. Full integration ensures the element accurately captures the strains and stresses while avoiding hourglassing that may occur in lower-integration elements. A mesh convergence study showed that a minimum of 100 elements were required along the span, and 6 elements along the flange to 8 elements along the web (Table C.5).

Table C.5 Mesh sensitivity analysis of the S4 shell element

Beam cross-section	Elements Along Length	Elements Across Flange	Elements Across web	Total Elements
W200×36	80	6	8	3840
W250×45	80	6	8	3840
W310×67	100	6	8	4800

An IOS was introduced into the model to account for lateral out-of-straightness. It was incorporated into the weak-axis coordinate at midspan, with an amplitude of L/1000, in the Abaqus S4 and B31OS element input files. Similarly, pure torsional IOS was assigned directly to the S4 input file by setting the amplitude at the midspan of the top flange to L/1000 and the bottom flange

to -L/1000. For lateral-torsional IOS, the analysis started with an eigenvalue analysis. The first mode shape from this analysis was used in conjunction with the *IMPERFECTION keyword in Abaqus, with the amplitude set to introduce a peak lateral imperfection at the top flange of L/1000.

C.5 Results

A convergence tolerance study was conducted on beams with three IOS patterns—lateral, lateral-torsional, and twist—applied to three cross-sections (W200×36, W250×45, and W310×67). Specifically:

1. Lateral IOS (Fig. C.1, Fig. C.2 and Fig. C.3)
2. Lateral-torsional IOS (Fig. C.4, Fig. C.5 and Fig. C.6)
3. Twist IOS (Fig. C.7, Fig. C.8 and Fig. C.9)

The results in Table C.6 show that a displacement tolerance of $\varepsilon_d = 1/100$ is both acceptable and efficient. It requires fewer than 18 increments to reach the targeted load of 1.5Mcr. The 1st increment converges in 6 iterations, while subsequent increments require 2-4 iterations each. In contrast, increasing the tolerance to $\varepsilon_d = 1/1000$ yields similar results but requires over 30 increments. In this case, the 1st increment requires 10 iterations to converge, with the remaining increments taking 4 to 7 iterations each.

Force tolerances were found to demand more increments for convergence. For a force tolerance of $\varepsilon_f = 1/100$, 36 increments are needed, with the 1st increment taking 11 iterations to converge and subsequent increments requiring 4 to 8 iterations. For a force tolerance of $\varepsilon_f = 1/1000$, 52 increments are necessary, with the 1st increment taking 19 iterations to converge, while the remaining increments require 5-10 iterations each.

Figures C.1 through C.9 show comparisons of displacement and stress for all nine cases considered. In all cases, close agreement is attained between the predictions of the converged present solution and those based on Abaqus S4 models. The results in Table C.6 reflect the L-IOS case, with a similar convergence trend noted for the LT-IOS and T-IOS cases across both initial and subsequent load increments.

Table C.6 Number of iterations requeued to attain convergence for L-IOS

increment	W200×36	W250×45	W310×67	
1st	4-6	3-6	3-5	$\varepsilon_d = 1/50$
subsequent	1-3	2-3	1-3	
1st	5-8	7-8	4-7	$\varepsilon_d = 1/100$
subsequent	2-4	3-5	3-4	
1st	9-12	10-12	8-11	$\varepsilon_d = 1/1000$
subsequent	4-8	5-8	4-7	
1st	8-12	9-12	7-11	$\varepsilon_f = 1/100$
subsequent	4-6	5-7	4-5	
1st	11-15	14-16	9-13	$\varepsilon_f = 1/500$
subsequent	5-8	7-9	3-6	
1st	17-20	20-24	16-19	$\varepsilon_f = 1/1000$
subsequent	5-12	7-13	4-8	

C.5.1 W200x36 with Lateral IOS $\delta_\xi = (L/1000)$

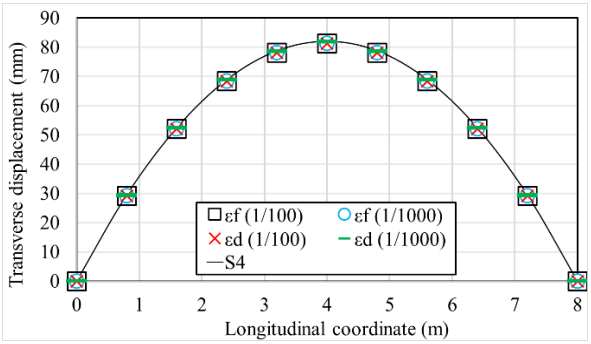

(a)

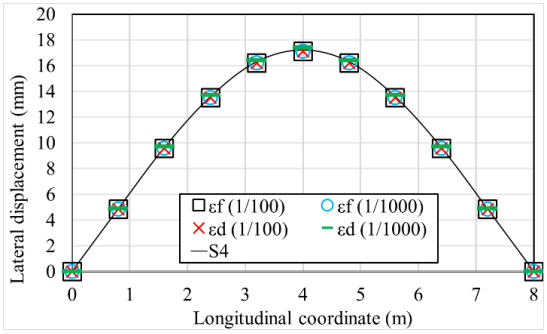

(b)

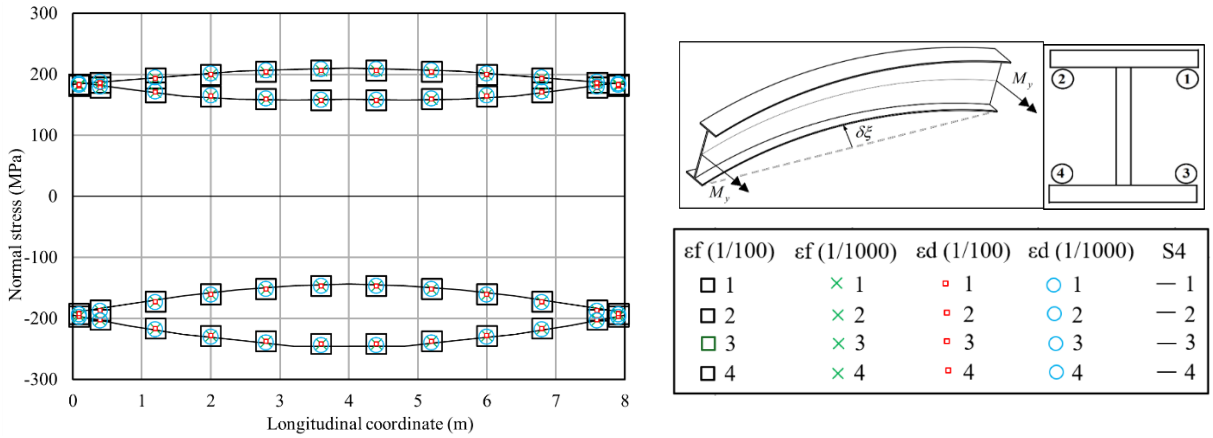

Fig. C.1 (a) Transverse displacement. (b) Lateral displacement of beam L-IOS of $\delta_\xi = (L/1000)$, (c) Normal stress, and (d) Legend of stress and IOS and loading type.

C.5.2 W250x45 with Lateral IOS $\delta_\xi = (L/1000)$

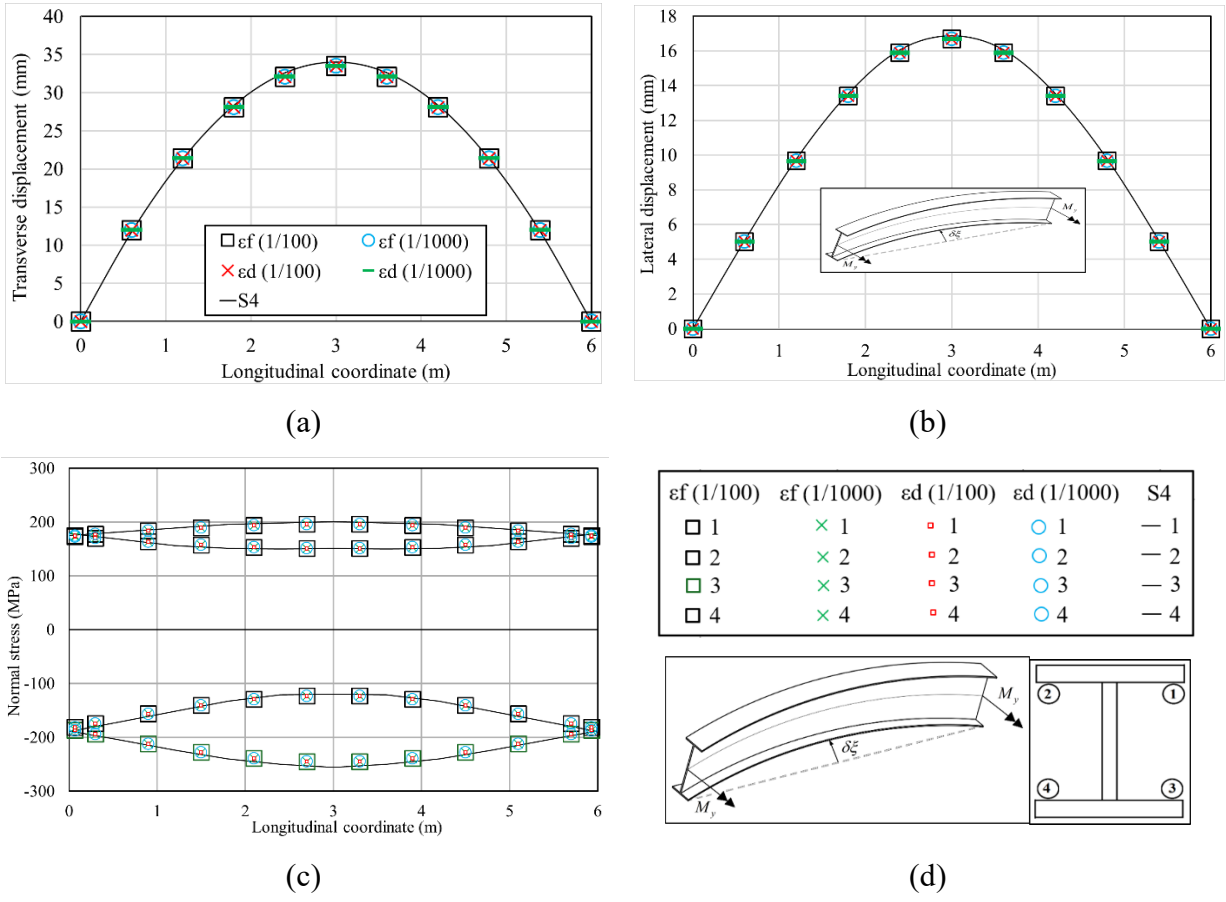

Fig. C.2 (a) Transverse displacement. (b) Lateral displacement of beam L-IOS of $\delta_\xi = (L/1000)$, (c) Normal stress, and (d) Legend of stress and IOS and loading type.

C.5.3 W310x67 with Lateral IOS $\delta_\xi = (L/1000)$

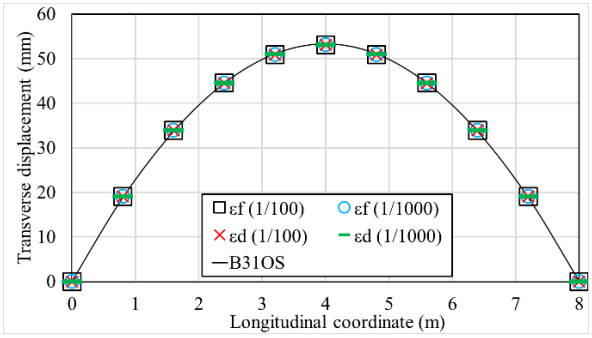

(a)

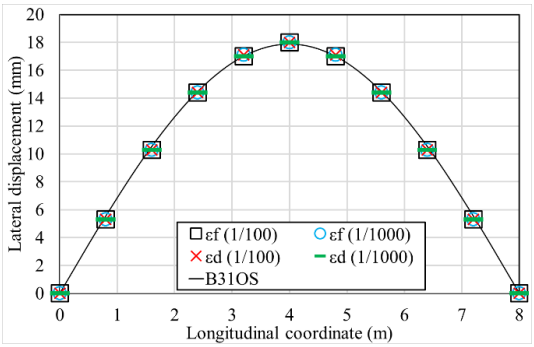

(b)

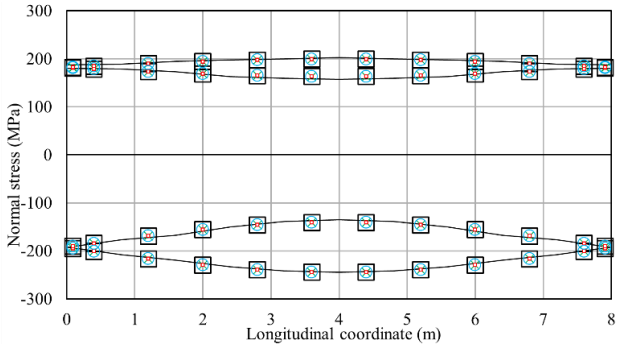

(a)

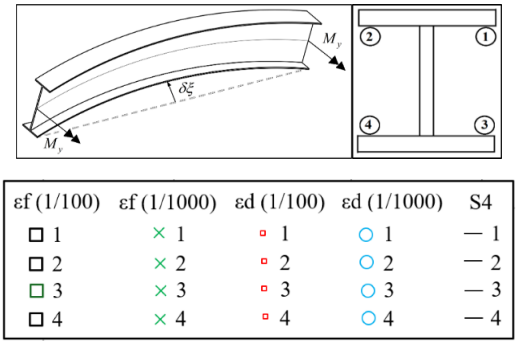

(b)

Fig. C.3 (a) Transverse displacement. (b) Lateral displacement of beam L-IOS of $\delta_\xi = (L/1000)$, (c) Normal stress, and (d) Legend of stress and IOS and loading type

C.5.4 W200x36 Lateral-Torsional IOS with Top Flange $\delta_\xi = (L/1000)$

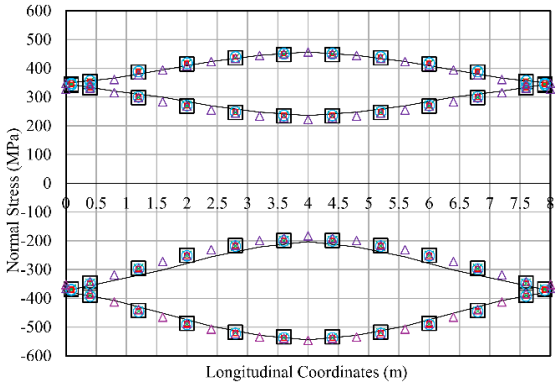

(a)

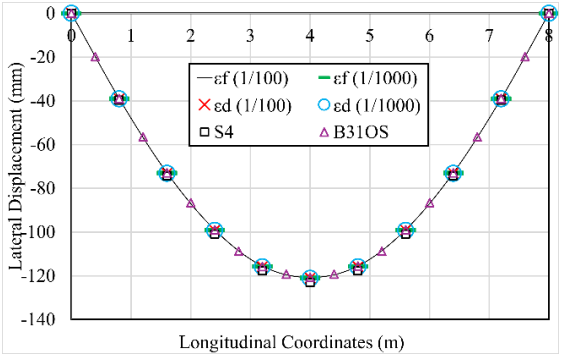

(b)

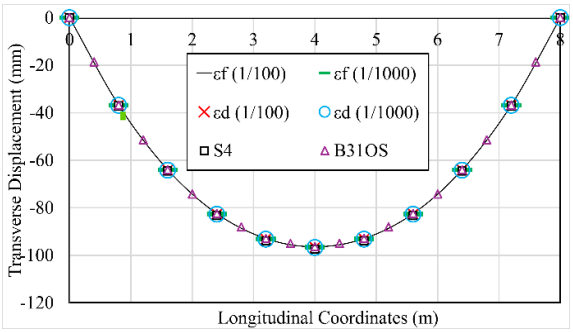

(c)

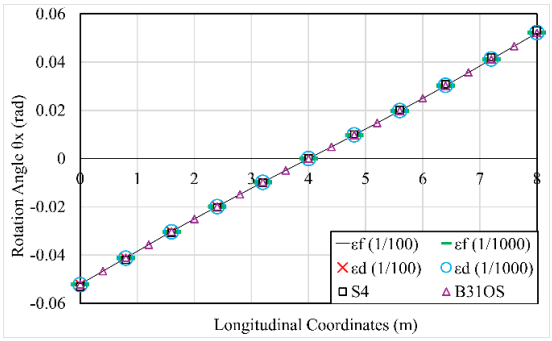

(d)

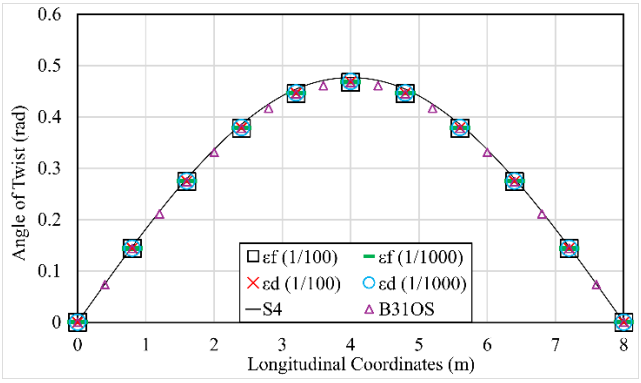

(e)

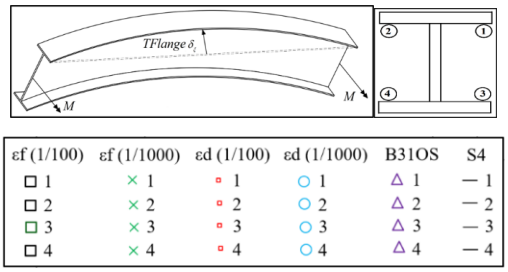

(f)

Fig. C.4 (a) Pinned Roller Beam with $\delta_\xi = (L/1000)$ of first mode shape initial out-of-straightness (a) Normal Stress. (b) Lateral displacement ξ. (c) Transverse displacement η. (d) Rotation angle θ_y. (e) Angle of twist. (f) Legend of stress and IOS, and loading type

C.5.5 W250x45 Lateral-Torsional IOS with Top Flange $\delta_\xi = (L/1000)$

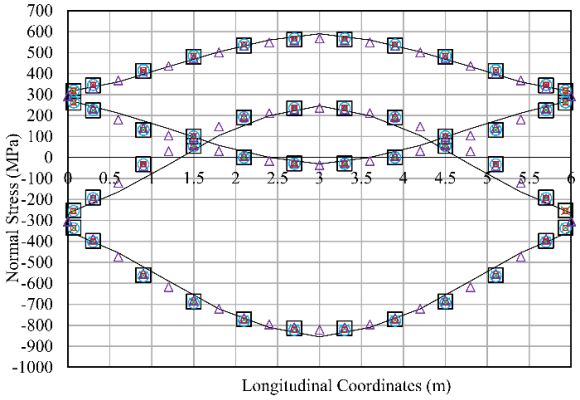

(a)

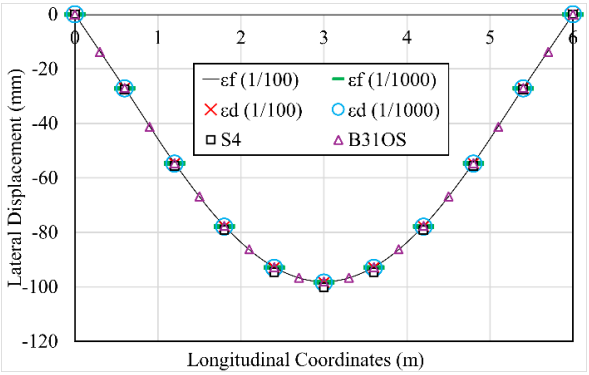

(b)

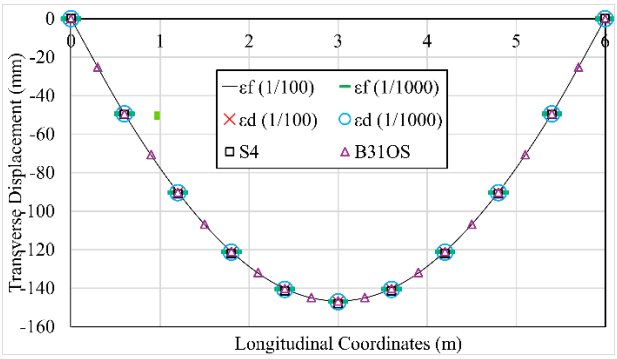

(c)

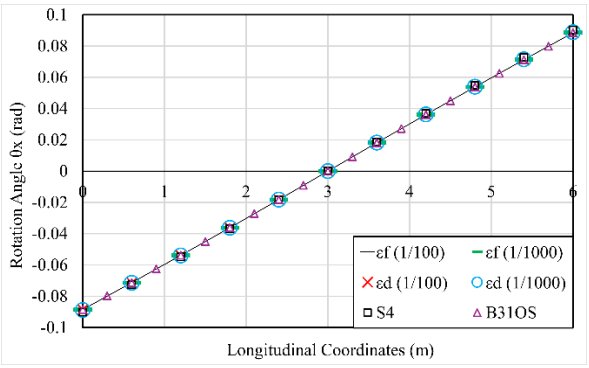

(d)

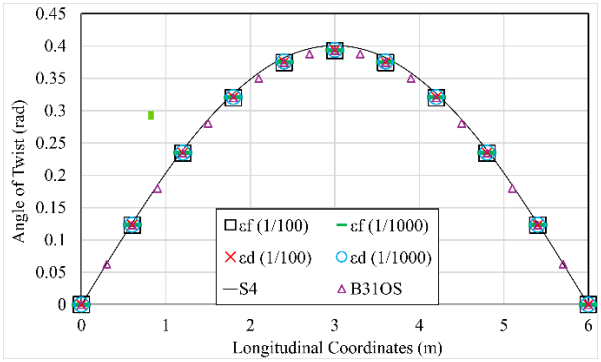

(e)

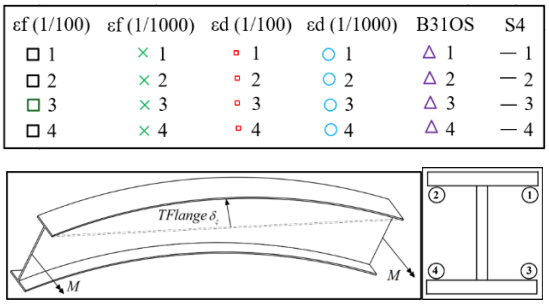

(f)

Fig. C.5 Pinned Roller Beam with $\delta_\xi = (L/1000)$ of first mode shape initial out-of-straightness (a) Normal Stress. (b) Lateral displacement ξ. (c) Transverse displacement η. (d) Rotation angle θ_y. (e) Angle of twist. (f) Legend of stress and IOS and loading type.

C.5.6 W310x67 Lateral-Torsional IOS with Top Flange $\delta_\xi = (L/1000)$

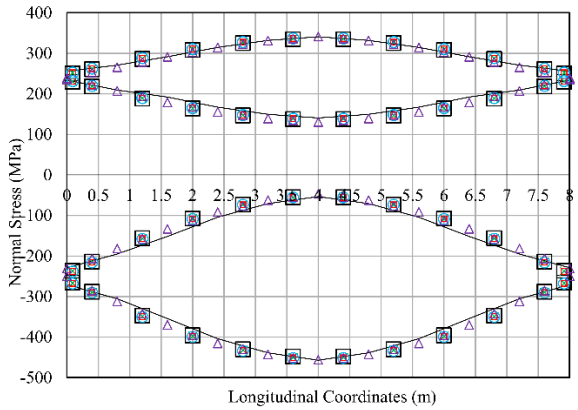

(a)

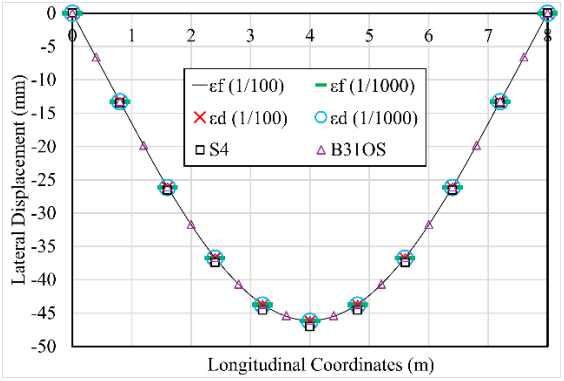

(b)

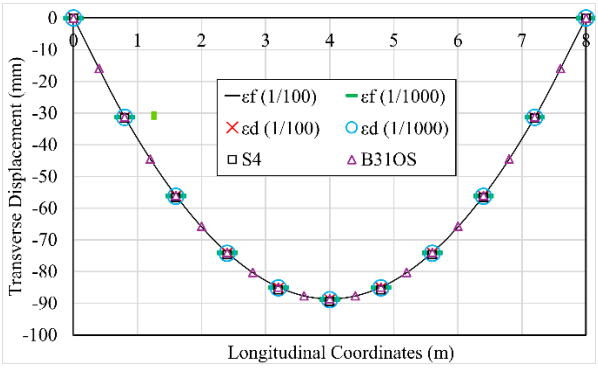

(c)

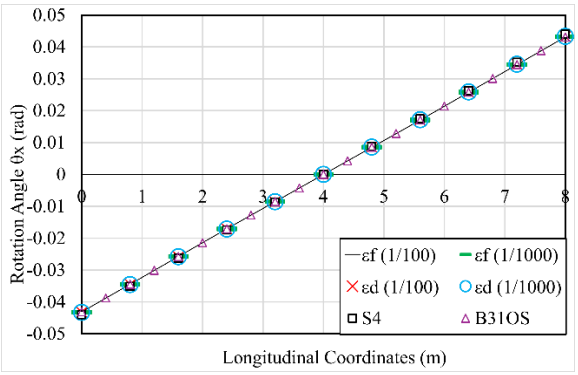

(d)

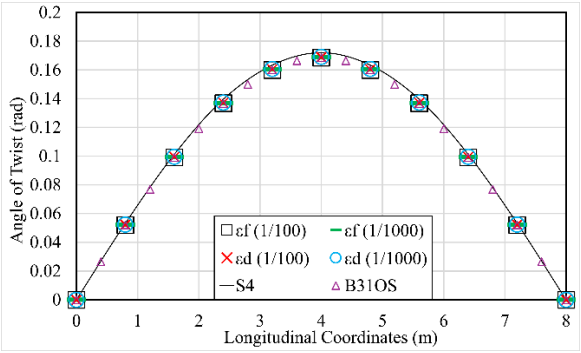

(e)

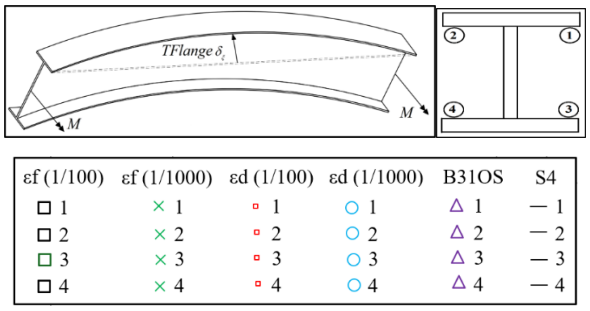

(f)

Fig. C.6 (a). Pinned Roller Beam with $\delta_\xi = (L/1000)$ of first mode shape initial out-of-straightness (a) Normal Stress. (b) Lateral displacement ξ. (c) Transverse displacement η. (d) Rotation angle θ_y. (e) Angle of twist. (f) Legend of stress and IOS and loading type.

C.5.7 W200x36 Twist IOS with Top Flange $\delta_\xi = (L/1000)$

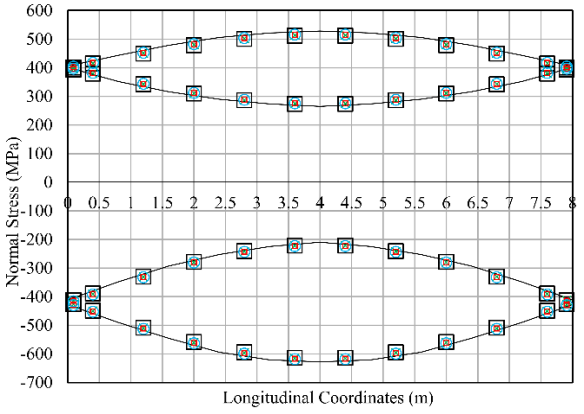

(a)

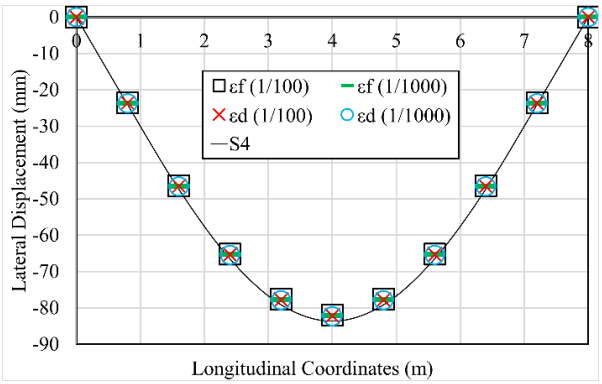

(b)

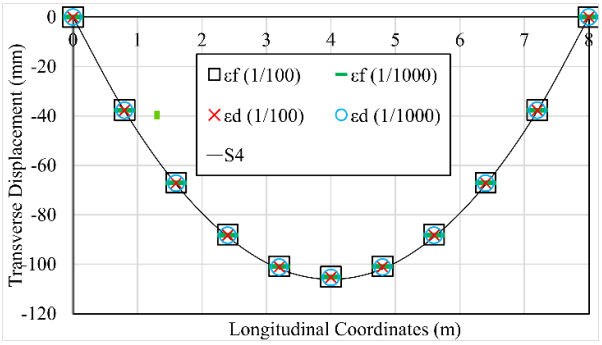

(c)

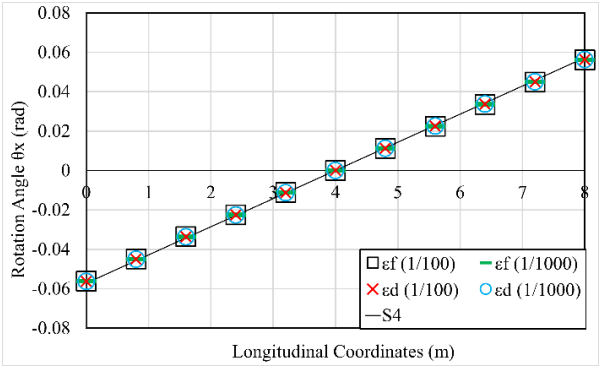

(d)

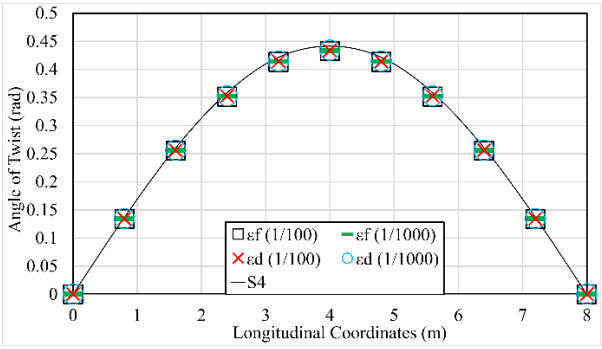

(e)

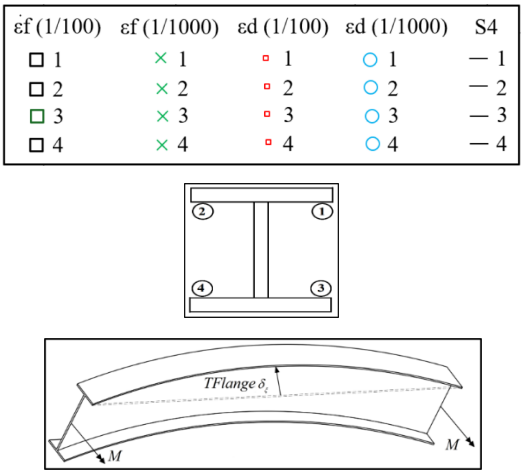

(f)

Fig. C.7 (a). Pinned Roller Beam with $\delta_\xi = (L/1000)$ of torsional IOS pure twist (a) Normal Stress. (b) Lateral displacement ξ. (c) Transverse displacement η. (d) Rotation angle θ_y. (e) Angle of twist. (f) Legend of stress and IOS and loading type.

C.5.8 W250x45 Twist IOS with Top Flange $\delta_\xi = (L/1000)$

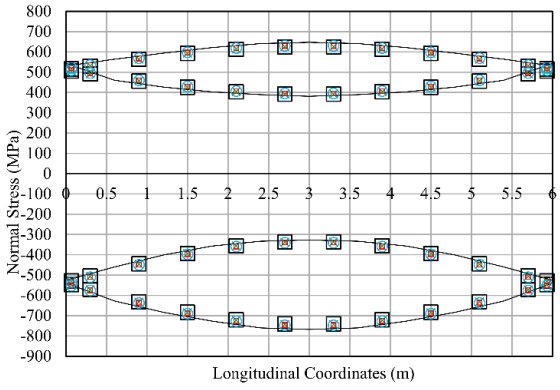

(a)

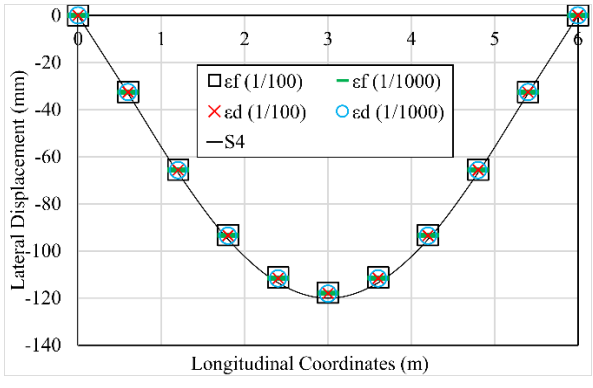

(b)

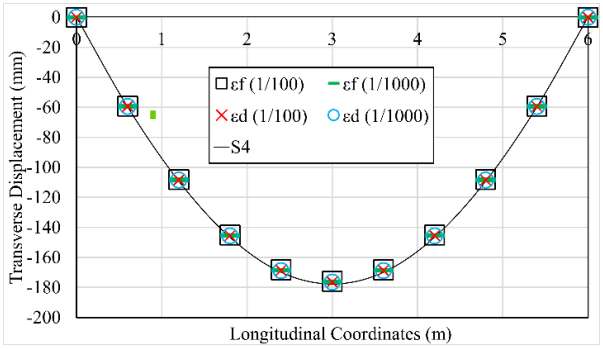

(c)

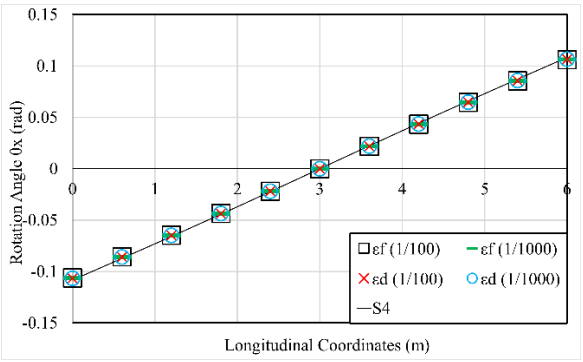

(d)

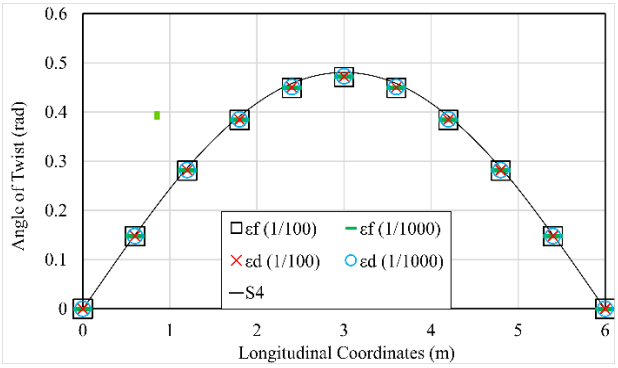

(e)

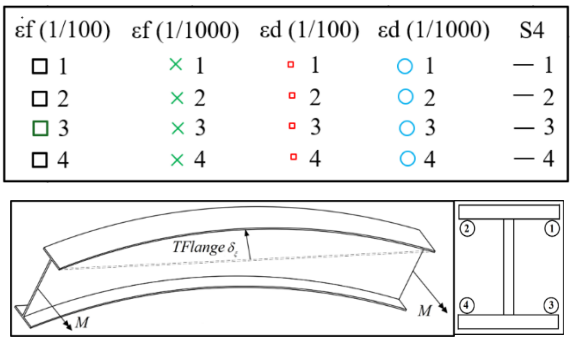

(f)

Fig. C.8 (a). Pinned Roller Beam with $\delta_\xi = (L/1000)$ of torsional IOS pure twist (a) Normal Stress. (b) Lateral displacement ξ. (c) Transverse displacement η. (d) Rotation angle θ_y. (e) Angle of twist. (f) Legend of stress and IOS and loading type.

C.5.9 W310x67 Twist IOS with Top Flange $\delta_\xi = (L/1000)$

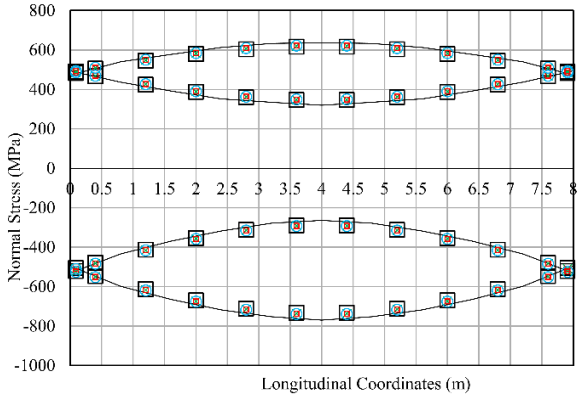

(a)

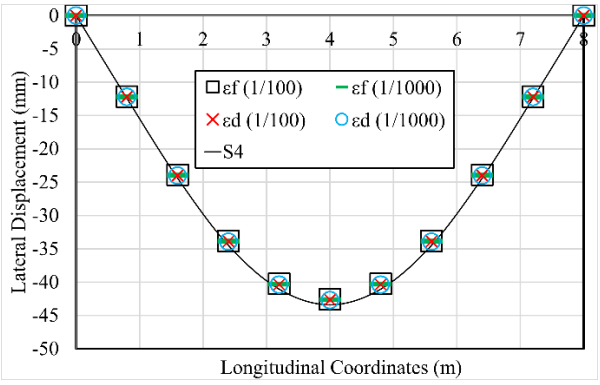

(b)

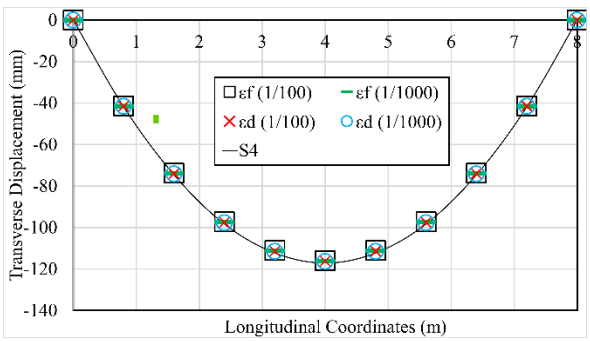

(c)

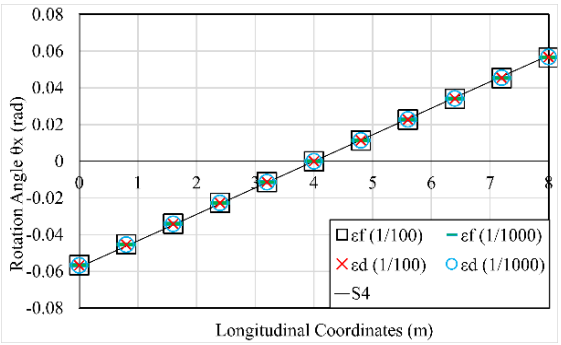

(d)

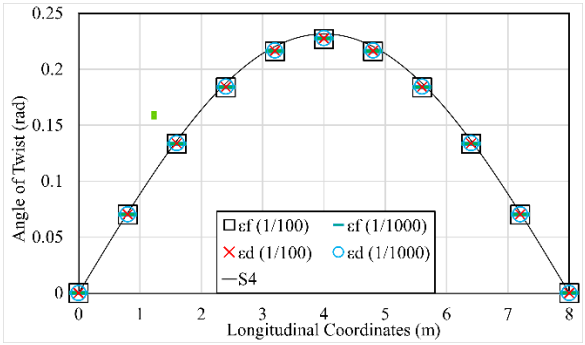

(e)

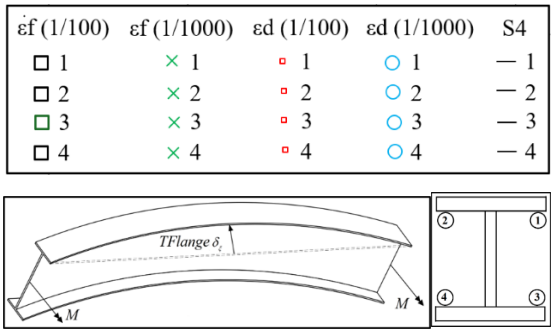

(f)

Fig. C.9 (a). Pinned Roller Beam with $\delta_{\xi} = (L/1000)$ of torsional IOS pure twist (a) Normal Stress. (b) Lateral displacement . (c) Transverse displacement η . (d) Rotation angle θ_y (e) Angle of twist (f) Legend of stress, IOS, and loading type.

Appendix D: Verification for Straight Doubly Symmetric Beams

D.1 General

This section examines the validity of the geometrically nonlinear finite element formulation developed in Chapter 2 for straight doubly symmetric beams by comparing its predictions against those of the ABAQUS thin-walled beam element B31OS and the shell element S4. Towards this objective, seven numerical examples were analyzed:

(1) Cantilever under combined transverse and axial loading acting at the tip.

(2) Cantilever beam under pure torque loading.

(3) Member with pinned roller supports under midspan transverse and axial loads

(4) Beam fixed at both ends under midspan point load.

(5) Beam fixed at both ends under midspan loading,

(6) Beam pinned roller under midspan loading.

D.2 Reference Cross-Section

In all examples, the reference cross-section adopted is doubly symmetric steel section with a flange width of 100 mm, a web height of 20 mm measured from the flange inner surfaces, and flange and web thicknesses of 10 mm. The corresponding cross-sectional properties are $A = 4100\,mm^2$, I_{xx}=2.98×10^7 mm^4, $I_{yy} = 1.68\times10^6$ mm^4, $J = 1.37\times10^5$ mm^4, and $I_\omega = 1.84\times10^{10}$ mm^6. The material is steel with a Young's modulus $E = 200\,GPa$ and a shear modulus $G = 77\,GPa$.

D.3 Mesh Study

D.3.1 Problem Description

A 4m span cantilever with the reference cross-section is considered. The member is subjected to two loading cases (1) a transverse load V_c at the beam tip acting at the shear center, and (2) an external moment M_c acting at the free end (Fig. D.1a-b). To specify an appropriate load level target in both cases, a buckling eigenvalue was first calculated for each case and yielded $V_c = 20.7\,kN$ and bending moment $M_c = 27.9\,kNm$. The targeted load in the present nonlinear analysis was applied incrementally in 10 steps, requiring 3 to 5 iterations at each step to achieve convergence.

D.3.2 Present Model

The integration scheme consisted of three Gaussian quadrature points along the longitudinal direction and nine Simpson integration points along the flange width and web height. For computational efficiency, two Gaussian quadrature points were taken across the thickness during the iterative procedure. However, when extracting the stress after convergence had been achieved, five Simpson integration points were taken across the thickness to accurately capture the stresses at the extreme fiber. Each loading case was analyzed using three uniform meshes with 16, 20, and 24 elements, respectively. Table D.1 shows that the predicted transverse displacement and the peak stresses remain essentially unchanged for the 20 and 24-element meshes. Therefore, convergence is deemed to have been achieved with 20 elements.

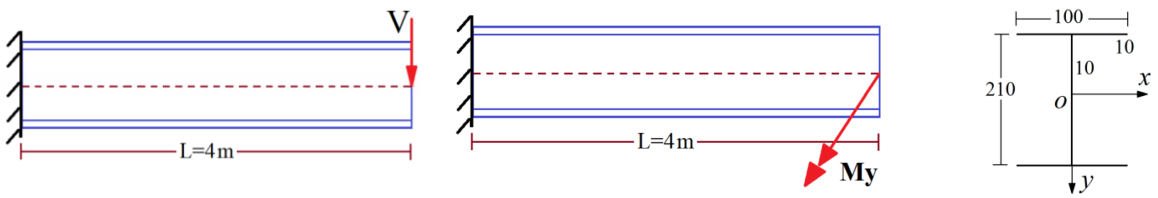

(a) (b) (c)

Fig. D.1 Cantilever beam under (a) Transverse load (b) Bending moment (c) Reference cross-section dimensions

Table D.1 Mesh study for the present model

Number of Elements	Transverse load		Bending moment	
	Transverse Displacement (1) (mm)	Normal stress (2) (MPa)	Transverse displacement (1) (mm)	Normal stress (2) (MPa)
16	75.5	303.8	38.1	107
20	75.2	301.6	38.0	105
24	75.2	301.7	38.0	105

(1) At the cantilever tip
(2) Peak normal stress at the extreme fibre at the cantilever root

D.3.3 B31OS Model

The B31OS element is an open-section, thin-walled beam element designed for three-dimensional analysis. The element has two nodes, each with seven degrees of freedom: three translations, three rotations, and a warping degree of freedom. All seven degrees of freedom were restrained at the cantilever root. The generalized cross-section profile option allows users to define custom cross-sectional properties for the B31OS element, rather than relying on predefined shapes such as circular or rectangular cross-sections pre-defined in Abaqus. Instead of specifying geometric dimensions like outer and inner diameters, users can directly input the cross-sectional area A, moment of inertia I_{xx}, I_{yy}, torsional inertia J, and warping inertia I_{ω}. The problem was solved using 16, 20, and 24 elements. Table D.2 indicates that 20 elements are enough for stresses and displacements to converge.

Table D.2 Mesh sensitivity analysis of B31OS beam element

Number of Elements	Transverse load		Bending moment	
	Transverse displacement(1) (mm)	Normal stress(2) (MPa)	Transverse displacement(1) (mm)	Normal stress(2) (MPa)
16	76.6	307	40.12	110
20	75.4	302	38.1	105
24	75.4	302	38.1	105

(1) At the cantilever tip
(2) Peak normal stress at the extreme fibre at the cantilever root

D.3.4 S4 Model

The S4 is a general-purpose shell (S) element with four (4) nodes and full integration. Each node has six degrees of freedom: three translations and three rotations. The cantilever beams were modelled with fully constrained boundary conditions, which restricted all degrees of freedom at one end. The problem was analyzed using n_l elements along the span, n_f elements along the flange width and n_w along the web. Three meshes were investigated with $(n_l, n_f, n_w) = (60,6,8)$, $(80,6,8)$ and $(84,6,8)$. Table D.3 shows that the transverse displacement and normal stresses converge for the medium mesh $(n_l, n_f, n_w) = (80,6,8)$.

A mesh convergence study was conducted for the reference cross-section using the S4 shell element in Abaqus. The study found that a minimum of 80 elements were required along the length of the beams, 6 elements across the flange and 8 elements along the web thicknesses, to achieve accurate predictions of stress and displacement (Table D.3).

Table D.3 Mesh sensitivity analysis of S4 shell element

# of elements along Span	# of Elements along Flange width	# of Elements along web height	Total # of elements	Transverse load		Bending moment	
				Transverse displacement (1) (mm)	Normal stress (2) (MPa)	Transverse displacement (1) (mm)	Normal stress(2) (MPa)
60	6	8	2880	76.9	310	40.7	110
80	6	8	3840	75.5	303	38.5	106
84	6	8	4032	75.5	303	38.5	106

(1) At the cantilever tip
(2) Peak normal stress at the extreme fiber at the cantilever root

D.4 Cantilever Under Transverse and Axial Loads

A 4m span cantilever with the reference section defined in D.2 is subjected to combined transverse and axial loading applied at its tip. The transverse load V is half of the buckling load V_c as determined through an eigenvalue buckling analysis (i.e., $V = V_c/2 = 11kN$),; and the axial

load P is taken has half of the critical buckling load $P_{cr} = \pi^2 EI_x / 4L^2$ i.e., $P = P_{cr}/2 = 450\,kN$, with. The loading was applied incrementally in 10 steps. Ten elements were adopted within the present formulation. The transverse displacement based on a first-order (linear) analysis is $v_{1st} = VL^3/3EI_x = 39.4\,mm$. By including second-order effects, the transverse displacement is governed by the equilibrium condition

$$EI_{xx} v'''' + Pv'' = 0 \tag{D.1}$$

in which $k^2 = P/EI_{xx}$. By imposing the boundary conditions $v(0) = v'(0) = v''(L) = 0$, and $EI_{xx} v'''(L) + Pv'(L) = V$, one obtains $v(z) = \left(V/k^3 EI_{xx}\right)\left[-\tan kL\left(\cos kz - 1\right) + \left(\sin kz - kz\right)\right]$. Also, the corresponding normal stress is given by $\sigma(y,z) = (P/A) + V\left(\tan kL \cos kz - \sin kz\right) y/\left(I_{xx} k\right)$, which yields $\sigma(y = 50mm, z = 0,) = 391\,MPa$ and $\sigma(y = 50, z = 4000) = 110\,MPa$. Linear (L) and nonlinear (N) analyses were conducted within the present formulation, and comparisons were made with the B31OS and S4 element models. Fig. D.2 and Table D.4 show that the transverse displacement predictions of the present model are in close agreement with the B31OS and S4 model predictions, with less than 2% differences. Similarly, the rotations about the strong axis predicted by the present model, the B31OS and S4 models were found in close agreement with results (Fig. D.2b). Additionally, the normal stresses at the top fiber of the flange edges were analyzed as in Fig. D.2c. At the beam tip, the stresses obtained from the present model align closely with the expected theoretical value $\sigma = P/A = 110\,MPa$.

The above results show the ability of the present model to capture second-order effects. As shown in Fig. D.3, the prediction of the present model of the transverse displacement at the cantilever tip agrees with the theoretical second order based on Eq. (D.1) and is in close agreement with the

B31OS and S4 models. Finally, Table D.4 shows that the longitudinal stresses predicted by the present study agree with those of the B31OS and S4 elements within 2%. The results also agree well with the theoretical solution based on Eq. (D.1).

Table D.4 Nonlinear analysis results for cantilever I-beam under transverse and axial loading

Variable	Present [1]	B31OS [2]	S4 [3]	%Difference ([3]-[1])/ [3]	%Difference ([2]-[1])/ [2]
$v_{max}\,(mm)$	77.5	78.6	78.5	1.33	1.49
$\theta_{max}\,(10^{-3}\,rad)$	29.6	30.1	29.9	1.01	1.46
$\sigma_{max}\,(MPa)$	394	397	396	0.404	0.780

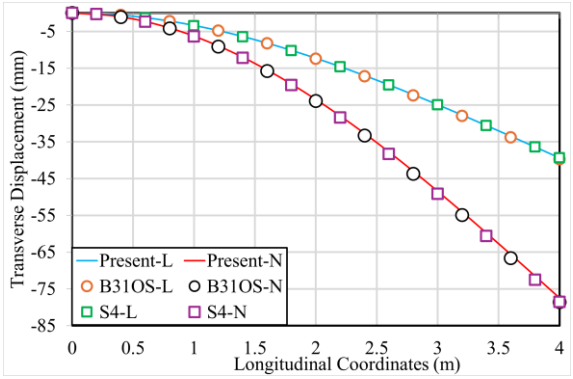

(a)

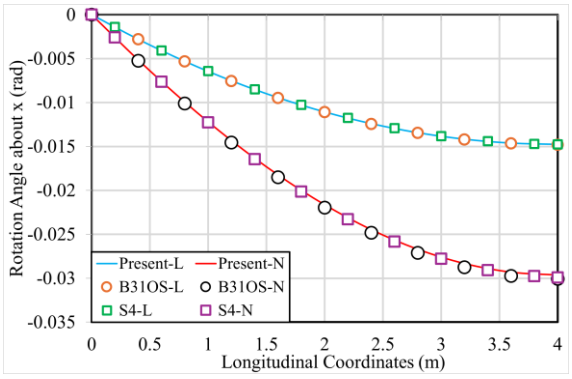

(b)

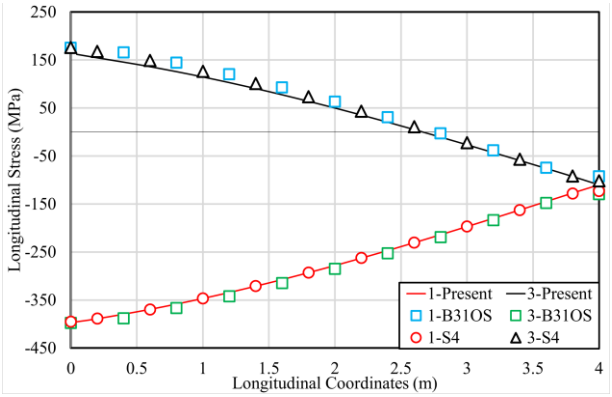

(c)

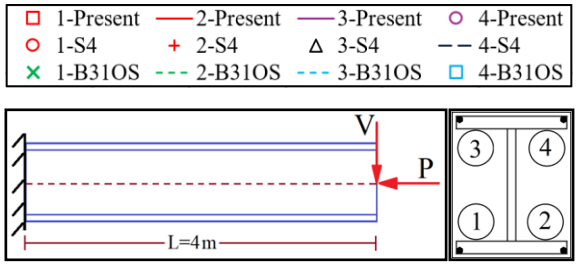

(d)

Fig. D.2 Comparison of results for a cantilever subjected to combined loading (a) Transverse displacement. (b) Rotation angle θ_y. (c) Longitudinal stress. (d) Stress legend and the load application

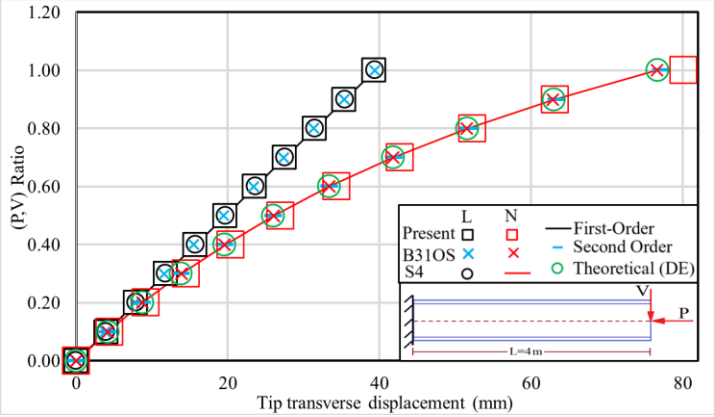

Fig. D.3 Tip transverse displacement for a cantilever - linear versus nonlinear analysis

D.5 Cantilever Beam Under End Torque

A cantilever beam spanning four meters is subjected to torque T applied at the tip. Cross-section dimensions are identical to those in section D.2 . The angle of twist is governed by the fourth-order differential equation

$$\theta^{iv} - \left(GJ/EC_w\right)\theta'' = 0 \tag{D.2}$$

which has the solution $\theta(z) = A_4 \cosh kz + A_3 \sinh kz + A_2 kz + A_1$. By imposing the boundary conditions $\theta(0) = 0, \theta'(0) = 0, \theta''(L) = 0$ and $GJ\theta'(L) - EI_{\omega\omega}\theta'''(L) = T$, the angle of twist can be expressed as

$$\theta(z) = \left(-T/kGJ\right)\left[\tanh kL\left(1-\cosh kz\right) + \left(\sinh kz - kz\right)\right] \tag{D.3}$$

in which $k = \sqrt{GJ/EI_{\omega\omega}}$. A torque is applied at the free end to induce an angle of twist $\theta(L) =$ 0.2 rad at the free end. Using Eq.(D.3) one obtains $T = 0.62\ kNm$. The twist angle at the cantilever

tip obtained from the present model is found to be 0.201 radians, in close agreement to the theoretical solution. The B31OS prediction is 0.207 radians while the S4 prediction is 0.204 radians. The difference between all four solutions remain within 2%. Additionally, the longitudinal stresses at the corners of cantilever root predicted by all three models are in close agreement: The present model predicts a maximum stress of 75.2 MPa, which compares to 77.6 MPa as predicted by the B31OS model and 76.6 MPa for S4 model (Fig. D.4b).

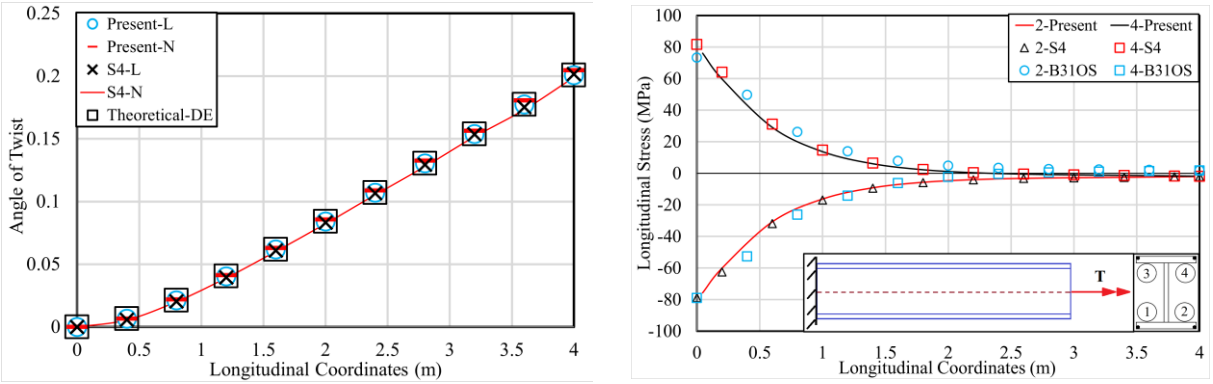

(a) (b)

Fig. D.4 Comparison of results for a cantilever beam subjected to pure torque loading: (a) Angle of twist and (b) Longitudinal stress

D.6 Simply Supported Member Under Transverse and Axial Loads

A simply supported member with 6m span is subjected to a midspan transverse load V and an axial load applied P at the member end. Member cross-sectional dimensions are identical to those described under section D.2 . Member ends were restrained transversely, laterally, and relative to twist, and the longitudinal displacement is restrained at one end.

The transverse load V is taken as half of the load that would induce lateral torsional buckling load V_c as determined by an eigenvalue analysis (i.e., $V = V_c/2 = 15\,kN$). The axial load P equal to half of the buckling load $P_c = \pi^2 EI_x/L^2$ (i.e., $P = P_c/2 = 820\,kN$) . The loading is applied

incrementally in 20 steps. A mesh study showed that convergence is achieved with 20 elements along the beam span.

As illustrated in Fig. D.5 Comparison of results for beam column a-b and summarized in Table D.5, the present model predictions of the transverse and longitudinal displacements are in agreement with those of the B31OS and S4 models within 1%. Also, the strong-axis rotation predictions of the present model and the B31OS and S4 models are in close agreement (Fig. D.5 Comparison of results for beam column c) with less than 1% differences. As shown in Fig. D.5 Comparison of results for beam column , the normal stresses at the end of the top fiber of the flange are in agreement with the theoretical stress value $\sigma = P/A = 200\,MPa$.

By conducting a linearly elastic analysis based on the present model, the predicted transverse displacement at beam midspan is found to be in close agreement with the classical first-order analysis $v_{1st} = VL^3/48EI_x = 11.3\,mm$ (Fig. C.5e).The results also agree with the B31OS and S4 predictions. Also, the prediction of the geometrically nonlinear analysis based on the present model is observed to be in close agreement with geometrically nonlinear analyses based on the B31OS and S4 models.

Table D.5 Nonlinear analysis results for pinned-roller I-beam under transverse load and axial loading

Variable	Present [1]	B31OS [2]	S4 [3]	Differences ([3]-[1])/ [3]	Differences ([2]-[1])/ [2]
$v_{max}\,(mm)$	22.6	22.8	22.7	0.484	0.964
$\theta_{max}\,(10^{-3}\,rad)$	11.6	11.6	11.6	1	1
$\sigma_{max}\,(MPa)$	335	340	342	1.93	1.30

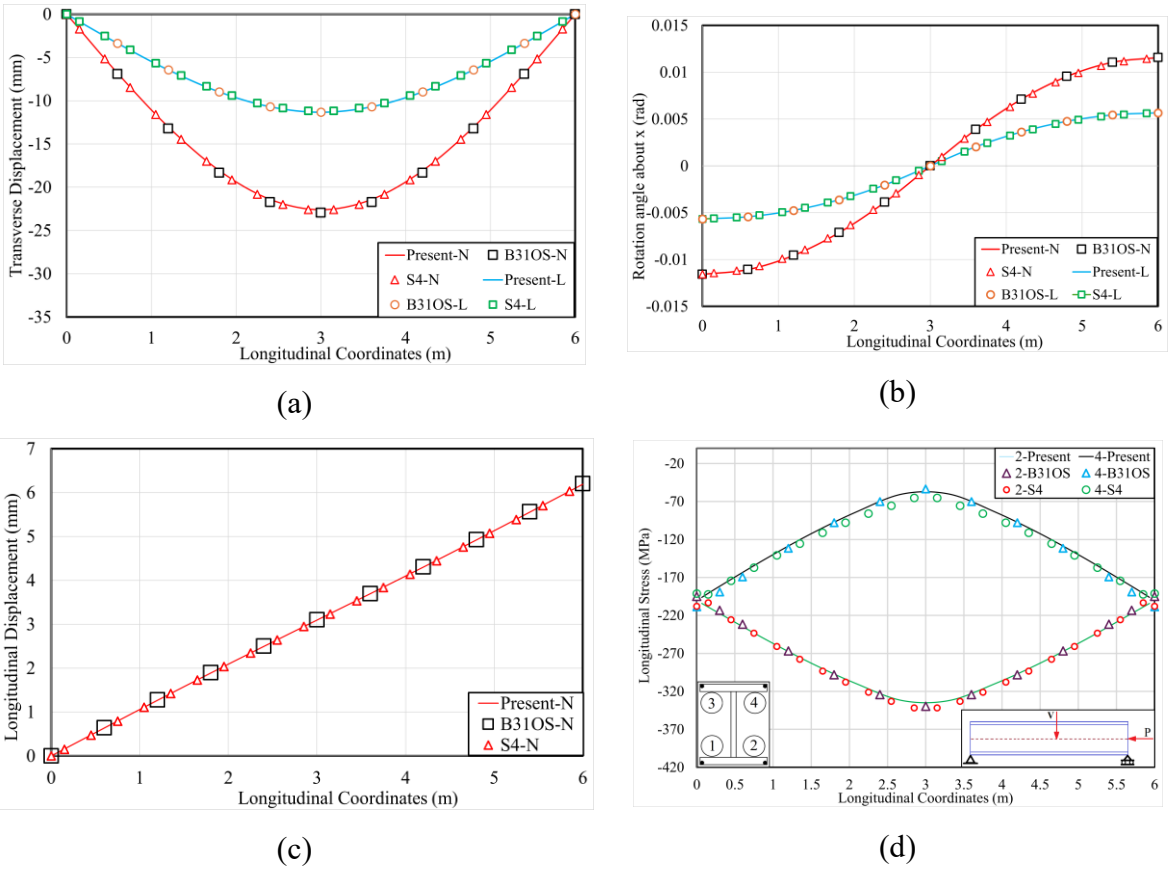

Fig. D.5 Comparison of results for beam column (a) Transverse displacement, (b) Longitudinal displacement, (c) Rotation angle θ_y and (d) Longitudinal stress

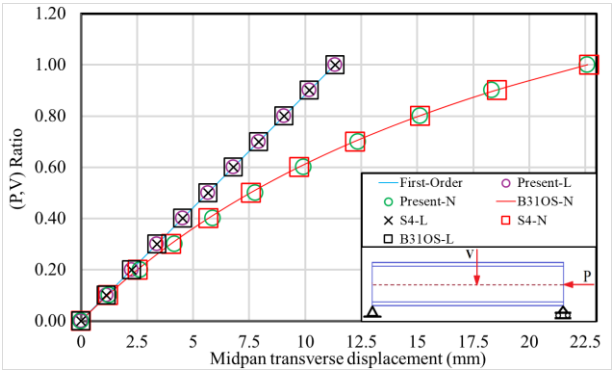

Fig. D.6 Comparison of midspan transverse displacement based on linear and nonlinear analyses

D.7 Beams with Various End Support Conditions

A 6m long beam is subjected to a midspan transverse point load V acting at the shear center. For each case, two values of a transverse point load V are investigated (1) $V = 1.5V_{cr} = 50\,kN$ and (2)

$V = 6V_{cr} = 200\,kN$ in which V_{cr} is the critical load associated with lateral torsional buckling of a simply supported beam, as determined from an eigenvalue analysis. Linear (L) and nonlinear (N) analyses are performed using the present formulation, the Abaqus B31OS beam model, and the 4S shell model. A convergence study indicated that 20 elements are sufficient to achieve convergence. Three types of boundary conditions are investigated as described in the following sub-sections.

D.7.1 Beam Fixed at Both Ends Under Midspan Point Load

Fixed end conditions were modelled in the present, B31OS, and S4 models by restraining all degrees of freedom at both ends. Fig. D.7a-c illustrates the transverse and axial displacements and strong-axis rotation distributions along the longitudinal coordinate of the beam. The predictions from the present formulation show good agreement with those from the B31OS and S4 models, underscoring the accuracy of the proposed formulation in capturing structural response. Additionally, Fig. D.7d shows that the predicted normal stresses are in agreement with the B31OS and 4S model predictions.

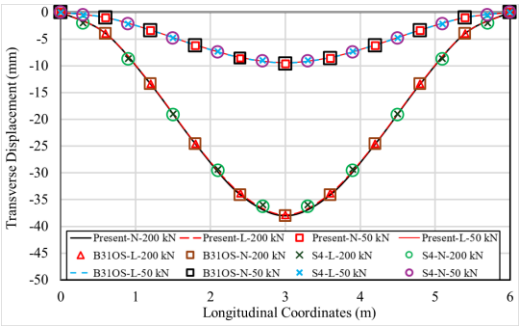

(a)

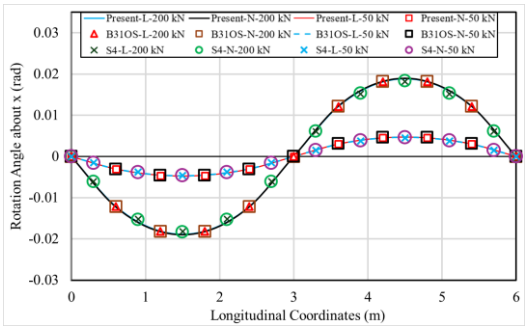

(b)

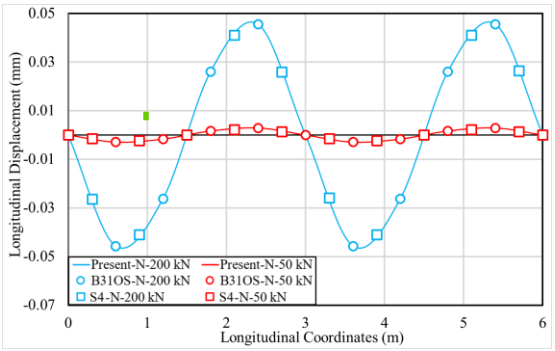

(c)

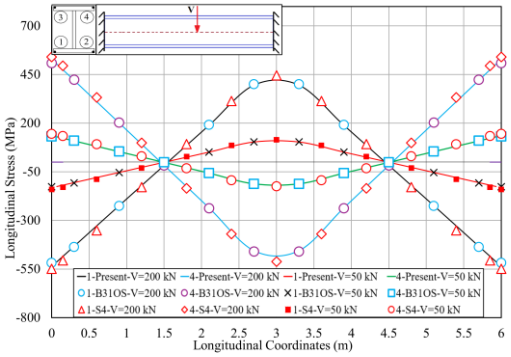

(d)

Fig. D.7 Comparison of Results for a beam clamped at both ends (a) Transverse displacement. (b) Rotation angle about x. (c) Longitudinal displacement. (d) Longitudinal stress.

D.7.2 Beam Pinned at Both Ends Under Midspan Point Load

In this section, beam ends is restrained relative to transverse, longitudinal, and lateral displacements and angle of twist. Fig. D.8a-c show close agreement between the predictions of the present, B31OS model, and S4 models of the transverse displacement, axial displacement, and strong-axis rotation. Also Fig. D.8d shows close agreement between predictions of all three models of the normal stresses.

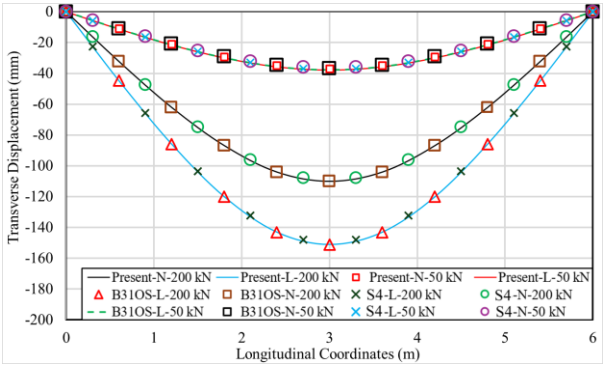

(a)

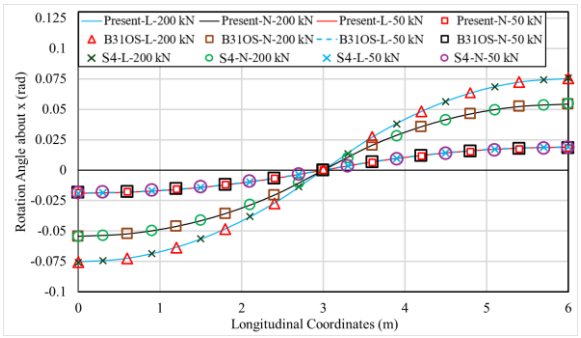

(b)

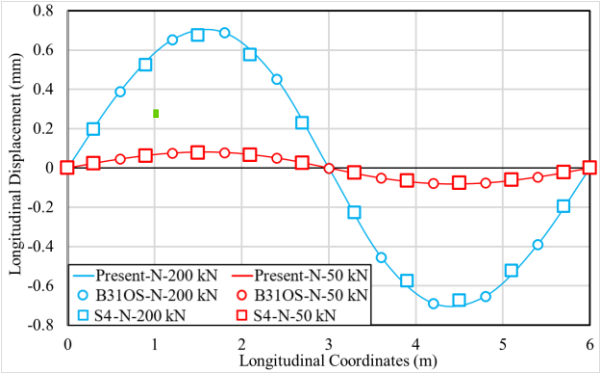

(c)

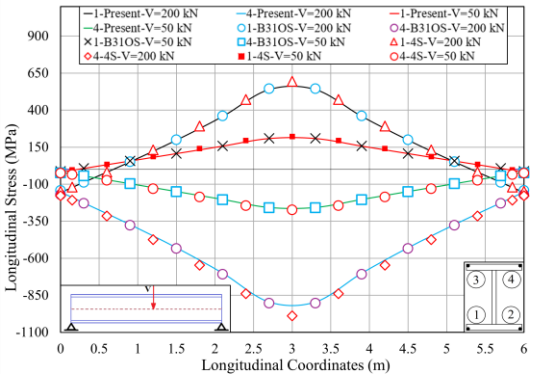

(d)

Fig. D.8 Beam response field distributions along the longitudinal coordinate for pinned-pinned beam: (a) Transverse displacement. (b) Rotation angle about x axis (c) Longitudinal displacement (d) Longitudinal stress.

D.7.3 Pin-Roller Beam Under Midspan Point Load

In this section, both ends of the beam are restrained relative to the transverse and lateral displacements and angle of twist while only the left end is longitudinally restrained. Fig. D.9a-c shows that the predictions of the present model closely match those of the B31OS beam model. Additionally, close agreement is observed between the longitudinal stress predictions of all three models (Fig. D.9d). Compared to the pin-pin case in Fig. D.8d, the longitudinal stress magnitudes for the present pin-roller case Fig. D.9d are notably larger. This is attributed to the catenary action occurring only in the pin-pin case, which induces additional tensile stresses.

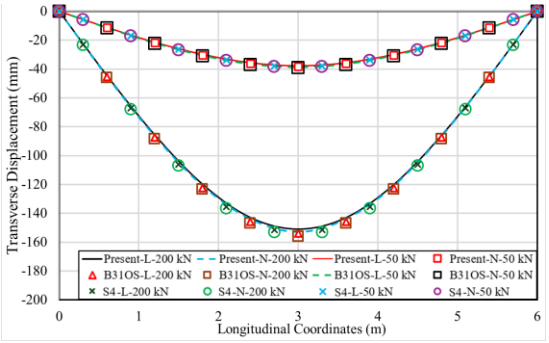

(a)

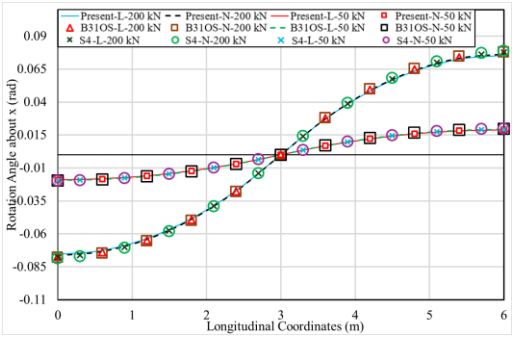

(b)

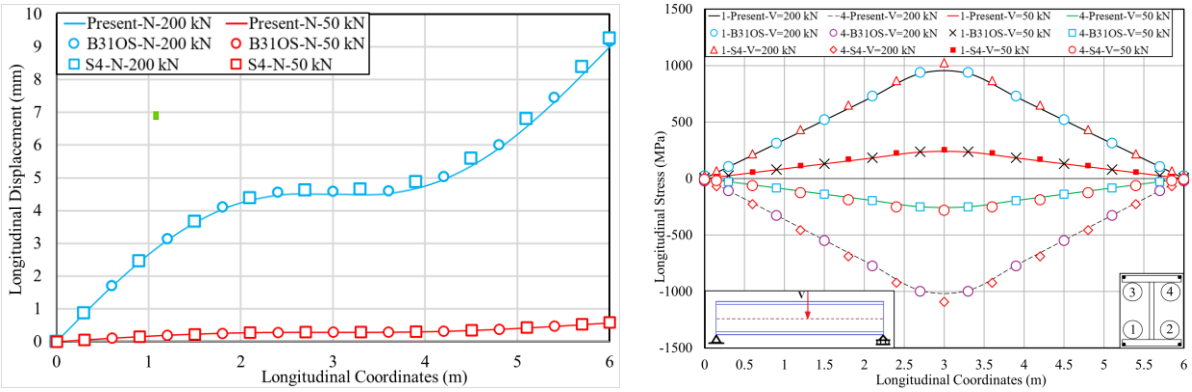

(c) (d)

Fig. D.9 Beam response field distributions along the longitudinal coordinate for pinned-roller beam: (a) Transverse displacement. (b) Rotation angle about x. (c) Longitudinal displacement. (d) Longitudinal stress.

D.8 Conclusion

The preceding findings show that the present model provides accurate and reliable predictions for the displacements and stresses for straight beams, under various loads, load combinations and boundary conditions.

Appendix E: Additional Verification for Beams with IOS

This appendix presents supplemental verification studies performed in Chapter 2 to assess the accuracy of the present finite element formulation for beams with various forms of Initial Out-of-Straightness (IOS). Comparisons are made against ABAQUS B31OS and S4 models to validate the geometric nonlinear response under different IOS patterns and loading conditions.

E.1 Reference Member

A reference member has a span $L = 5\ m$ and an I-shaped cross-section, with a flange width of 100 mm and thickness of 10 mm, and a web height of 200 mm and thickness of 10 mm. Cross-sectional properties are $A = 4100\,mm^2$, I_x=$2.98\times10^7\ mm^4$, $I_y = 1.68\times10^6\ mm^4$, 0 $J = 1.37\times10^5\ mm^4$, and $I_\omega = 1.84\times10^{10}\ mm^6$. Material is steel with $E = 200\,GPa$ and $G = 77\,GPa$. Member ends are restrained against twist, transverse and lateral displacements at both ends, and one end is longitudinally restrained i.e., $\zeta(0) = \xi(0) = \eta(0) = \theta(0)$ and $\xi(L) = \eta(L) = \theta(L) = 0$. The member has a Lateral Initial Out-of-Straightness (L-IOS) $\xi_0(z) = \gamma_\xi \sin(\pi z/L)$, a Camber Initial Out-of-Straightness (C-IOS) $\eta_0(z) = \gamma_\eta \sin(\pi z/L)$, and a Twist Initial Out-of-Straightness (T-IOS) $\theta_0(z) = \gamma_\theta \sin(\pi z/L)$. Under loading, the member is assumed to undergo displacements $\left[\xi(z), \eta(z), \theta(z)\right]$ from its initially crooked position, such that the total out-of-straightness is $\left[\hat{\xi}(z), \hat{\eta}(z), \hat{\theta}(z)\right] = \left[\xi_0(z), \eta_0(z), \theta_0(z)\right] + \left[\xi(z), \eta(z), \theta(z)\right]$. A geometric nonlinear analysis is performed under five combinations of loading and IOS $(\gamma_\xi, \gamma_\eta, \gamma_\theta)$. Results are compared to the predictions of a S4 shell element model and B31OS thin-walled beam model in Abaqus. The

analysis is based on the generalized cross-section option of the B31OS model, which enables the user to directly enter cross-sectional properties.

A mesh sensitivity analysis showed that the model based on the present formulation and the B31OS model converged with 20 elements, whereas the S4 shell model converged with 200 elements along the span, 8 along the web height, and 6 along the flange width. Both the present and B31OS models have 147 DOFs, while the S4 model has 76,000 DOFs.

E.2 Example 1: Column with Lateral IOS

The reference member is assumed to have a L-IOS $\xi_0(z) = \gamma_\xi \sin(\pi z/L)$, with no initial camber nor twist, i.e., $\gamma_\eta = \gamma_\theta = 0$. Two L-IOS amplitudes are considered: $\gamma_\xi = L/1000$ and $\gamma_\xi = L/400$. An axial compressive load P is applied at $z = L$. The load is incrementally increased from 0 to $1.5P_{cry}$ in which $P_{cry} = \pi^2 EI_y / L^2 = 132\,kN$ is the minor axis flexural buckling load of an initially straight member, i.e., the peak load targeted is $P = 1.5P_{cry} = 198\,kN$. An analytical estimate for the total Lateral Out-of-Straightness (LOS) - defined as the sum of the initial lateral out-of-straightness and the additional lateral displacement - is given by $\hat{\xi}(L/2) = \gamma_\xi / \left[1 - \left(P/P_{cry}\right)\right]$ and is provided for comparison.

Close agreement is observed between the predictions of all three models (Fig. E.1 and Fig. E.2). For example, at $P/P_{cry} = 1.5$ for a L-IOS of $\gamma_\xi = L/400$, the present solution predicts a midspan total LOS within 1.2% of the B31OS model prediction and within 1.4% of the S4 model prediction (Fig. 3). Initially, close agreement is observed between the analytical solution and the present model predictions. Yet, when the load ratio P/P_{cry} exceeds 90%, the total LOS predicted by the analytical solution deviates significantly from that based on the present model. This is attributed

to the fact that the analytical model does not account for moderate rotation effects, which are captured in the present model.

For a L-IOS of $\gamma_\xi = L/1000$, Fig. E.1 shows that the load versus total LOS follows a nearly bilinear response characterized by an initially steep slope followed by a milder one. When the L-IOS increases to $\gamma_\xi = L/400$, a somewhat different response is observed as characterized by an initially steep slope, followed by a milder one, which becomes steep again.

Fig. E.2a shows a significant increase in the lateral displacements when L-IOS amplitudes increase from $\gamma_\xi = L/1000$ to $\gamma_\xi = L/400$ for both axial load ratios considered. At $P/P_{cry} = 1.5$, Fig. E.2b shows that for a L-IOS amplitude of $\gamma_\xi = L/1000$, the peak tensile stress is $309\,MPa$. This value increases significantly to $608\,MPa$ when the L-IOS amplitude increases to $\gamma_\xi = L/400$, i.e., in this case, increasing the L-IOS by 150% is observed to increase the peak tensile stress by 96%. For a L-IOS amplitude of $\gamma_\xi = L/400$, the peak compressive normal stress at edge 2, located on the concave side, reaches $657\,MPa$, while edge 1 on the convex side attains a peak tensile stress of $608\,MPa$. It can be verified that the mean normal stress in the cross-section is equal to the stress induced by the compressive axial force $\sigma = P/A = 48MPa$, as expected. As a general rule, all displacement and stress values reported in the present and following results are based on the present model predictions.

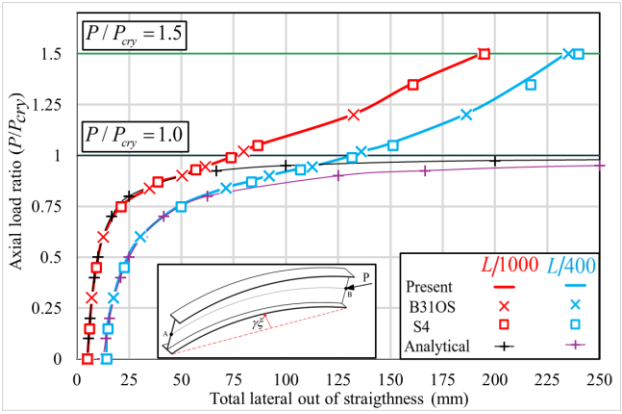

Fig. E.1 Load versus total LOS at midspan of a column with L-IOS

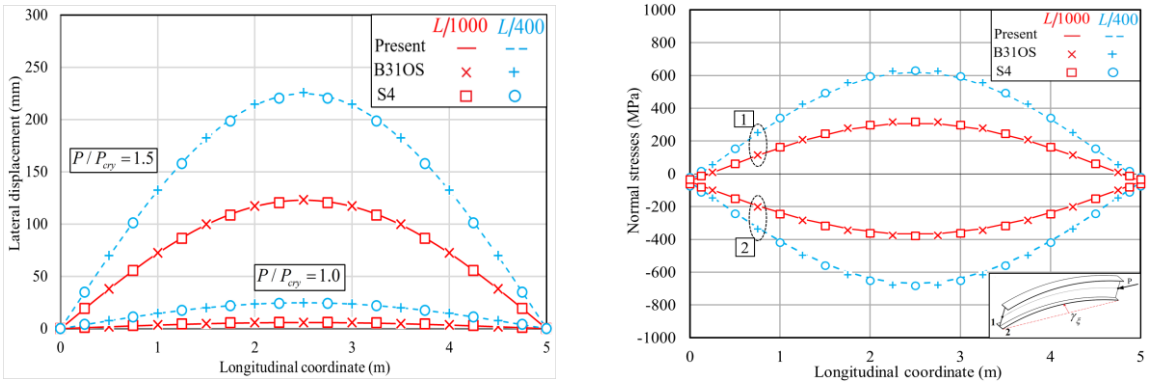

(a) (b)

Fig. E.2 Response of a column with L-IOS: (a) Lateral displacement and (b) Normal stresses for $P/P_{cry}=1.5$

E.3 Example 2: Beam with Lateral IOS

The reference member is assumed to have an IOS identical to that of Example 1. A midspan transverse point load V is applied at the shear center. The load is incrementally increased from 0 to $1.5V_{cr}$, V_{cr} being the load corresponding to the elastic critical moment of an initially straight member as determined from $M_u=\left(C_b\pi/L\right)\sqrt{EI_yGJ+\left(\pi E/L\right)^2 I_yI_\omega}=56.0\,kNm$, which corresponds to a critical load $V_{cr}=4M_u/L\simeq 45.0\,kN$. The nonlinear response of the member is sought by increasing the load from 0 to $1.5V_{cr}=67.5\,kN$.

As a general observation, the predictions of all three models are in close agreement. For example, at $M/M_u = 1.5$, the midspan total LOS for the member with $\gamma_\xi = L/400$, as predicted by the present model, is observed to be within 2.2% of the predictions of the B31OS model and within 3.4% of those of the S4 model (Fig. E.3a). Also, the midspan transverse displacement predicted by the present model is within 1.8 % of the predictions of the B31OS model and 2.1% of those of the S4 model (Fig. E.3b).

The slope of the moment ratio M/M_u versus midspan total LOS (Fig. E.3a) is initially steep, becomes milder in the neighborhood of M/M_u =1, and then exhibits a stiffening behavior characterized by a steeper slope. Comparatively, the slope of moment ratio M/M_u versus midspan transverse displacement (Fig. E.3b) exhibits a nearly bilinear response, characterized by an initially steep slope up to $M/M_u = 0.75$, and followed by a milder slope. The transverse displacement response is observed to be insensitive to the magnitude of L-IOS.

At $M/M_u = 1.5$, the midspan total LOS (Fig. E.3a) is $186\,mm$ at $\gamma_\xi = L/1000$. This value moderately increases to $193\,mm$ when the L-IOS increases to $\gamma_\xi = L/400$. Similarly, Fig. E.4 shows a moderate increase in lateral and transverse displacement as the L-IOS increases from $\gamma_\xi = L/1000$ to $\gamma_\xi = L/400$. Fig. E.5 shows that, at a moment ratio of $M/M_u = 1.14$, the midspan peak stress attains $357\,MPa$ for a L-IOS amplitude of $\gamma_\xi = L/1000$. At the same load level, the stress increases to $402\,MPa$ as the L-IOS amplitude increases to $\gamma_\xi = L/400$. In this case, increasing the L-IOS amplitude by 150 % led to a moderate increase in the maximum compressive stress by 14%. The maximum compressive stress of $402\,MPa$ takes place on the concave side of the top flange (Edge 4 of Fig. E.5b). This compares to a compressive stress of $307\,MPa$ on the

convex side (Edge 3). Conversely, the bottom flange experiences tensile stresses reaching 338 *MPa* on the concave side (Edge 2) and 252 *MPa* on the convex side (Edge 1).

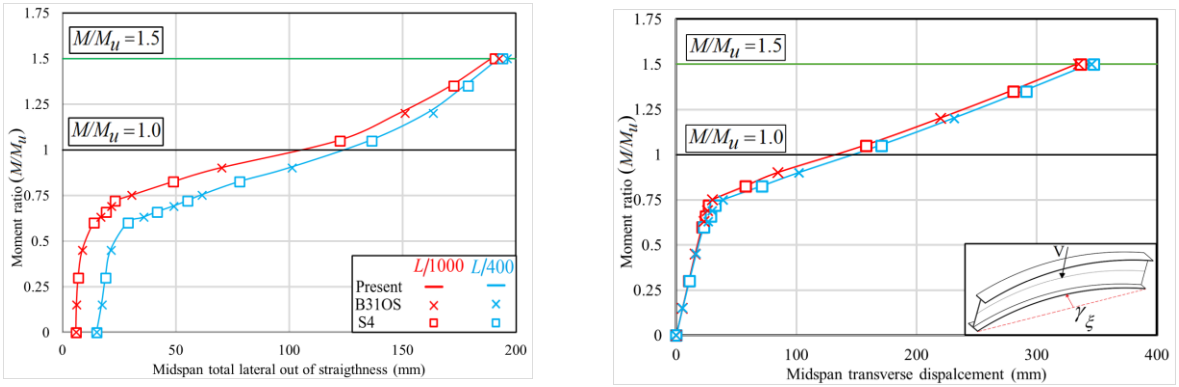

(a) (b)

Fig. E.3 Load deformation curves for a member with L-IOS. (a) Moment versus midspan total LOS and (b) Moment versus midspan transverse displacement

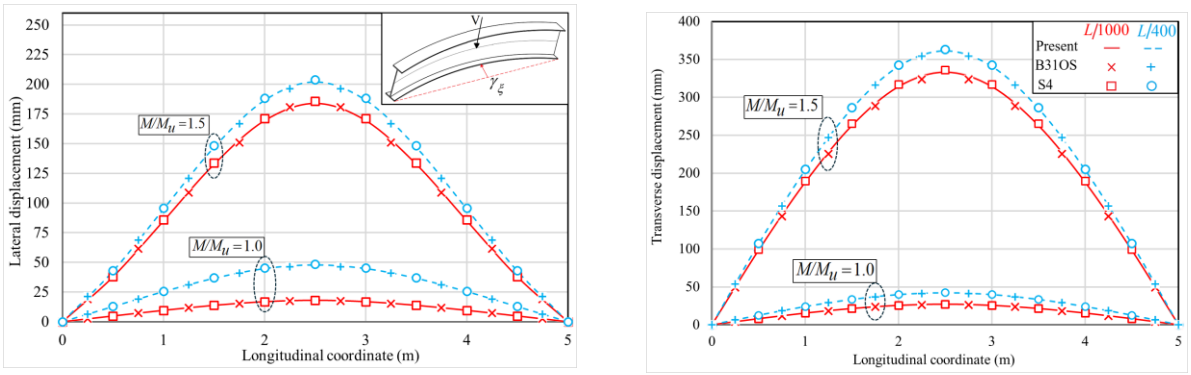

(a) (b)

Fig. E.4 Deformation of a beam with L-IOS (a) Lateral displacement and (b) Transverse displacement

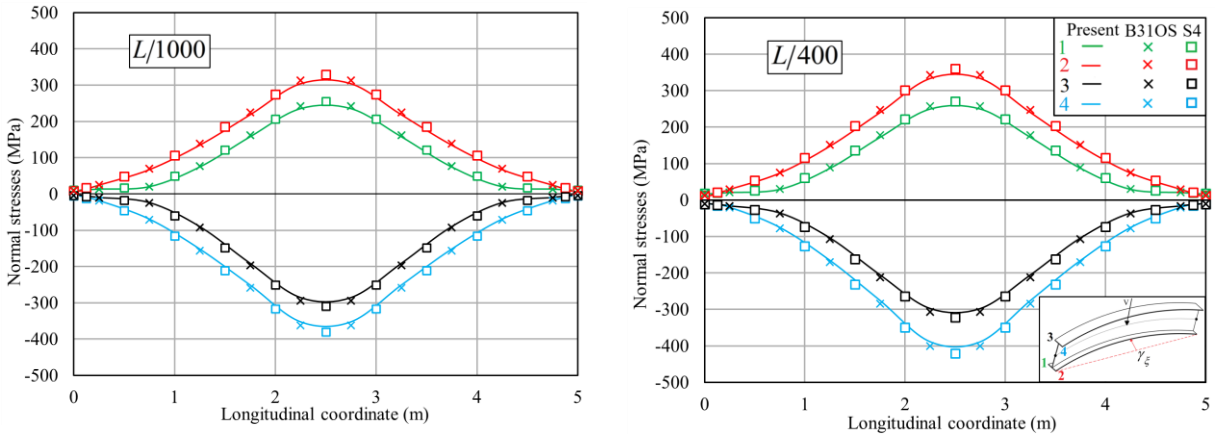

Fig. E.5 Normal stresses for a beam with L-IOS amplitude of (a) $\gamma_\xi = L/1000$ **and (b)** $\gamma_\xi = L/400$ **, at moment ratio** $M/M_u = 1.14$

E.4 Example 3: Beam with Camber IOS

The reference member is assumed to have a C-IOS $\eta_0(z) = \gamma_\eta \sin(\pi z/L)$. No initial lateral displacement nor twist are considered, i.e., $\gamma_\xi = \gamma_\theta = 0$. Two camber amplitudes are considered: $\gamma_\eta = L/1000$ and $\gamma_\eta = L/400$. The member is subjected to a midspan transverse force $V = 1.5V_{cr} = 67.5\ kN$ acting at the shear center, in which V_{cr} is the load corresponding the critical moment M_u for a perfectly straight member (as discussed in Example 2). Fig. E.6 shows that the midspan total Camber Out-of-straightness (COS) increases linearly with the applied load up to the peak moment ratio considered. Also, the plots for $\gamma_\eta = L/1000$ and $L/400$ are observed to have nearly identical slopes.

In general, the predictions of all three models are in close agreement. For example, at $M/M_u = 1.5$, the midspan total COS for a C-IOS amplitude of $\gamma_\eta = L/400$ predicted by the present formulation is within 1.4% of the B31OS prediction and within 2.8% of the S4 shell model prediction (Fig.

E.6). Also, the midspan peak tensile stress predicted by the present model is within 2.6% of the B31OS prediction and within 3.8% of the S4 shell model prediction (Fig. E.7b).

Fig. E.7a shows that, at $M/M_u = 1.5$, the difference between the total COS for $\gamma_\eta = L/1000$ and $\gamma_\eta = L/400$ is equal to the difference between C-IOS assumed in both cases, i.e., transverse displacement in both cases is equal, i.e., insensitive to the level of initial camber. For a C-IOS amplitude of $\gamma_\eta = L/400$, Fig. E.7b shows that the peak tensile stress at the midspan of the bottom edge attains $341 MPa$, while the peak compressive stress at the midspan of the top edge attains $339 MPa$. Stresses corresponding to $\gamma_\eta = L/1000$ (not shown for clarity) were found to be essentially identical.

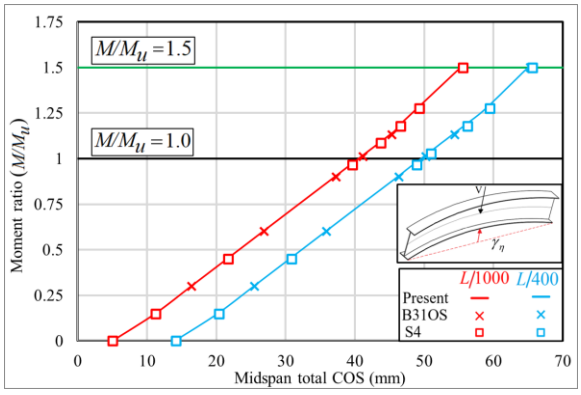

Fig. E.6 Moment ratio versus total COS at midspan for beam with C-IOS.

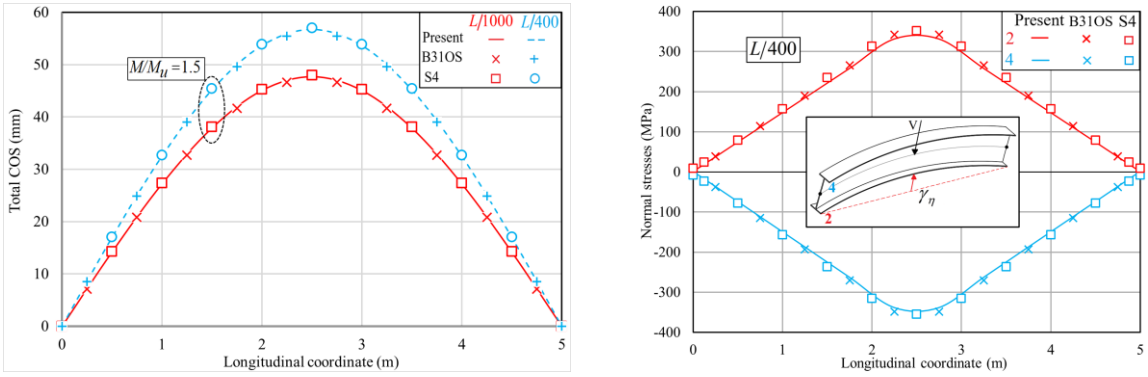

(a) (b)

Fig. E.7 Response of beam with T-IOS (a) Total camber out-of-straightness and (b) Normal stress distribution at $M/M_u = 1.5$ for $\gamma_\eta = L/400$

E.5 Example 4: Beam with Twist IOS

The reference member is assumed to have a T-IOS $\theta_0(z) = \gamma_\theta \sin(\pi z/L)$, with no L-IOS nor C-IOS, i.e., $\gamma_\xi = \gamma_\eta = 0$. For a section with a depth d between the flange centroids, an initial angle of twist $\theta_0(z)$ corresponds to a L-IOS $u_{0T}(z) = \gamma_\theta (d/2)\sin(\pi z/L)$ at the top flange, and $u_{0B}(z) = -\gamma_\theta (d/2)\sin(\pi z/L)$ at the bottom flange. Two amplitudes for the T-IOS are considered by setting the L-IOS of both flanges to $L/1000$ and $L/400$, which respectively correspond to peak T-IOS amplitudes of $\gamma_\theta = L/(500d)$ and $\gamma_\theta = L/(200d)$. It is noted that the T-IOS feature is not supported in the B31OS element implementation in Abaqus. As such, result comparisons in this example were made only against the S4 shell model. As discussed in Example 2, the member was subjected to a midspan transverse force $V = 1.5V_{cr} = 67.5\ kN$.

Fig. E.8 and Fig. E.9 show that predictions of the present model are in close agreement with those of the S4 shell model. For instance, at $M/M_u = 1.5$, the midspan twist angle predicted by the present model is within 2.3% of the S4 prediction for a T-IOS amplitude of $\gamma_\theta = L/(200d)$. Fig. E.8(a) shows that the angle of twist rapidly increases as the load level increases from $M/M_u = 1.0$ to 1.5. At $M/M_u = 1.5$, the midspan angle of twist is $0.33\,rad$ for a T-IOS amplitude of $\gamma_\theta = L/(500d)$. This value mildly increases to $0.38\,rad$ for a T-IOS $\gamma_\theta = L/(200d)$. Also, at $M/M_u = 1.5$, Fig. E.8(b) shows that the peak lateral displacement increases from $108\,mm$ at

$\gamma_\theta = L/(500d)$ to $122\,mm$ at $\gamma_\theta = L/(200d)$. A Similar trend is observed in Fig. E.8(c) for the transverse displacement.

For an amplitude of $\gamma_\theta = L/(500d)$, the peak stress at midspan attains $350\,MPa$ at a moment ratio $M/M_u = 0.96$ (Fig. E.9a). In comparison, for the larger T-IOS amplitude of $\gamma_\theta = L/(200d)$, the peak stress rises considerably to $468\,MPa$ at the same load level (Fig. E.9b), indicating that the stresses are sensitive to the magnitude of T-IOS amplitude. For an amplitude of $\gamma_\theta = L/(200d)$, Fig. E.9b shows that the highest compressive stress at midspan is $468\,MPa$, which occurs on the concave side of the top flange (Edge 4). On the convex side of the top flange (Edge 3), the compressive stress is significantly lower at $177\,MPa$. The bottom flange is subjected to tensile stresses, peaking at $365\,MPa$ on the convex side (Edge 1), and dropping to $224\,MPa$ on the concave side (Edge 2).

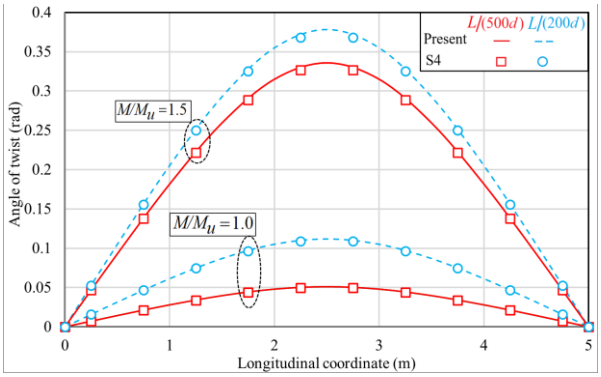

(a)

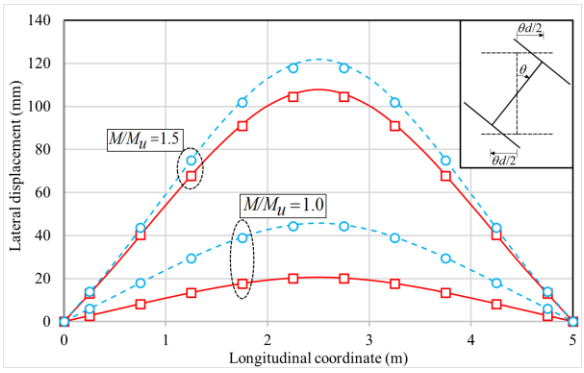

(b)

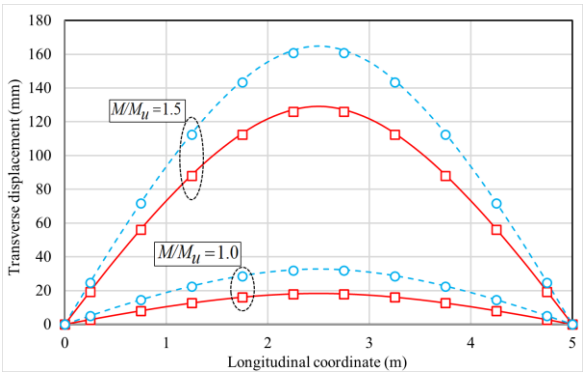

(c)

Fig. E.8 Response of a beam with T-IOS (a) Angle of twist (b) Lateral displacement, and (c) Transverse displacement

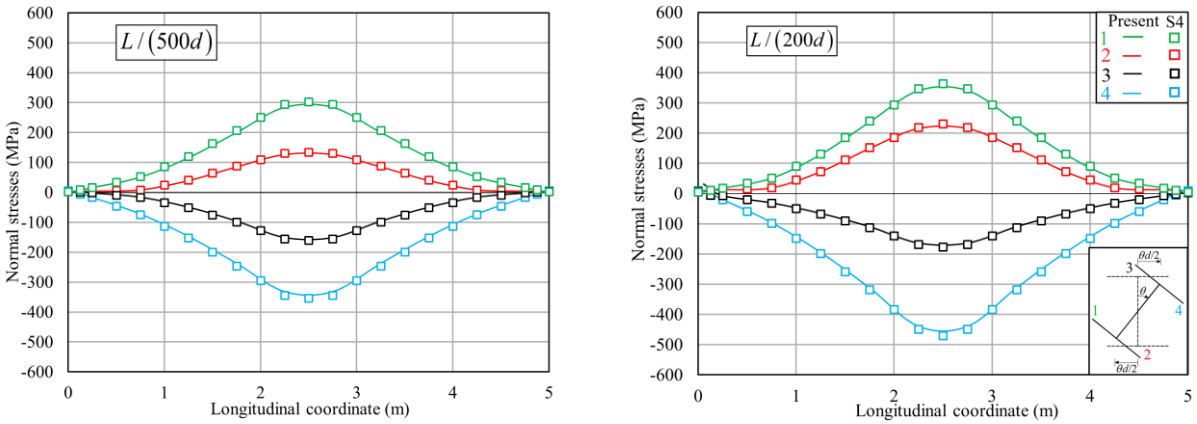

(a) (b)

Fig. E.9 Normal stress distribution for a beam with T-IOS: (a) $\gamma_\theta = L/(500d)$ and (b) $\gamma_\theta = L/(200d)$, at moment ratio $M/M_u = 0.96$

Appendix F: Lateral Torsional Buckling Resistance of Doubly Symmetric Members in Eurocode 3 and AS4100

This appendix provides the step-by-step calculations of the lateral-torsional buckling resistance, as per Eurocode 3 [2.4] and the Australian standards [2.5] in Chapters 2 and 3. The procedure covers section classification, characteristic bending resistance, elastic critical moment evaluation, slenderness determination, reduction factors, and final design moment capacity.

F.1 Problem Definition

A simply supported beam with a flange width of $b = 204\,mm$, and a thickness of $t = 12.8\,mm$, a web height of $d = 276.8\,mm$, and a thickness of $w = 8.5\,mm$ The member has a $8\,m$ span and is subjected to three loading cases: a uniform moment (UM), a uniformly distributed load (UD) and a midspan point load (PL). Steel Young's modulus is $E = 2\times10^5\ MPa$, and the shear modulus is $G = 7.7\times10^4\ MPa$, and the yield strength is F_y=$350\,MPa$. Sectional Properties are $I_x = 1.28\times10^8\,mm^4$, $I_y = 1.81\times10^7\,mm^4$, $C_\omega = 3.88\times10^{11}\,mm^6$, $J = 3.43\times10^5\,mm^4$, $S_x = 836\times10^3\,mm^3, Z_x = 933\times10^3\,mm^3$ $S_y = 178\times10^3\,mm^3$. It is required to determine the flexural resistance of the member in accordance with Eurocode 3 [2.4] and the Australian standards [2.5].

F.2 Eurocode 3 Solution

F.2.1 Classification

Material parameter (Cl. 5.2.5(2)) $\varepsilon = \sqrt{235/F_y} = \sqrt{235/350} = 0.819$

Web: Class 2 requirement for the web (Tables 7.3) $d/w \le 83\varepsilon$

$d / w = (306 - 12.8)/8.5 = 34.5 \le 83\varepsilon = 83\sqrt{235/350} = 68.0$

Thus, web meets the class 2 requirement

Flange: Class 2 classification requirement for the flange (Table 7.4) $b/t \le 10\varepsilon$

$$b/t = (204 - 8.5)/(2 \times 12.8) = 7.64 \le 10\sqrt{235/350} = 8.2$$

Section: Thus, the Section meets Class 2 requirements.

F.2.2 Characteristic Bending Resistance

The characteristic bending resistance (Cl. 8.2.26), for a class 2 section, is

$$M_P = Z_x F_y = 933 \times 10^3 \times 350 \times 10^{-6} = 326.6\,kNm \qquad \text{(F.1)}$$

F.2.3 Elastic Critical Moment for Lateral Torsional Buckling

The technical report prCEN/TR 1993-1-103 that was mentioned [2.4] provides the following expression for the elastic critical moment

$$M_{cr} = \frac{C\pi^2 EI_y}{L^2}\sqrt{\frac{C_w}{I_y} + \frac{L^2 GJ}{\pi^2 EI_y}} \qquad \text{(F.2)}$$

The technical report prCEN/TR 1993-1-103 gives the moment gradient factors $C = 1$ for uniform moment (UM), $C = 1.127$ for uniformly distributed load (UD), and $C = 1.348$ for the midspan point load (PL). However, in critical moment calculations, the values $C = 1$ for UM, $C = 1.13$ for UD, and $C = 1.35$ For PL, a thin-walled beam finite element analysis will be used instead.

$$M_{cr} = \frac{1.35 \times \pi^2 \times 2 \times 10^5 \times 1.81 \times 10^7}{8000^2}\sqrt{\frac{3.88 \times 10^{11}}{1.81 \times 10^7} + \frac{8000^2 \times 7.70 \times 10^4 \times 3.43 \times 10^5}{\pi^2 \times 2 \times 10^5 \times 1.81 \times 10^7}} \times 10^{-6} = 197.6\,kNm$$

F.2.4 Slenderness Parameter for Lateral Torsional Buckling

According to Clause 8.3.2.2 of [2.4], the slenderness parameter of LTB is given by

$$\lambda_{LT} = \sqrt{M_P / M_{cr}} = \sqrt{326.6/197.6} = 1.29 \tag{F.3}$$

F.2.5 Calculate ϕ_{LT} Factor

Clause 8.3.2.3 of [2.4] gives

$$\phi_{LT} = 0.5\left[1 + f_M\left(\left(\bar{\lambda}_{LT}/\bar{\lambda}_y\right)^2 \alpha_{LT}\left(\bar{\lambda}_y - 0.2\right) + \bar{\lambda}_{LT}{}^2\right)\right] \tag{F.4}$$

in which the relative slenderness for weak axis flexural buckling slenderness $\bar{\lambda}_y$ is defined in Clause 8.3.1.2 of [2.4] as $\bar{\lambda}_y = \sqrt{N_{Rk}/N_{cry}}$ in which $h/b > 1.2$. N_{Rk} is characteristic axial resistance as given by $N_{Rk} = AF_y$ (Cl. 8.2.2.6), and $N_{cry} = \pi^2 EI_y / L^2$ is the elastic flexural buckling about the minor axis

$$N_{Rk} = AF_y = 7.70\times10^3 \times 350\times10^{-3} = 2695\,kN \tag{F.5}$$

$$N_{cry} = \left[\left(\pi^2 \times 2\times10^5 \times 1.81\times10^7\right)/8000^2\right]\times10^{-3} = 558\,kN \tag{F.6}$$

$$\bar{\lambda}_y = \sqrt{(2695)/(558)} = 2.20 \tag{F.7}$$

For rolled sections with $t_f \le 40\,mm$, Table 8.5 gives the initial out-of-straightness factor $\alpha_{LT} = 0.12\sqrt{S_x/S_y} \le 0.34$, which depends on the elastic section modulus S_x, S_y. For the present cross-section, the initial out-of-straightness factor is computed as

$$\alpha_{LT} = 0.12\sqrt{S_x / S_y} = 0.12\sqrt{\left(836\times10^3\right)/\left(178\times10^3\right)} = 0.26 \quad \text{(F.8)}$$

Also, for the uniform moment case, Table 8.6 gives a factor that accounts for the effect of the bending moment distribution between discrete lateral restraints.

$$f_M = 1.10 \quad \text{(F.9)}$$

From Eqs. (F.3), (F.7) , (F.8), (F.9), by substituting into Eq. (F.4), one obtains

$$\phi_{LT} = 0.5\left\{1+1.10\left[\left(1.29/2.20\right)^2\times0.26\times\left(2.20-0.2\right)+1.29^2\right]\right\} = 1.51 \quad \text{(F.10)}$$

F.2.6 Reduction Factor

Clause 8.3.2.3 of [2.4] gives

$$\chi_{LT} = f_M \Big/ \left(\phi_{LT} + \sqrt{\phi_{LT}{}^2 - f_M \bar{\lambda}_{LT}{}^2}\right) \le 1.0$$

(F.11)(J.1)

From Eqs. (F.9), (F.10), (F.3), by substituting into Eq.(F.11) one obtains

$$\chi_{LT} = 1\Big/\left(1.51+\sqrt{1.51^2-1.10\times1.29^2}\right) = 0.46 \quad \text{(F.12)}$$

F.2.7 Design Lateral Torsional Buckling Resistance

According to Clause 8.3.2.1 of [2.4] is

$$M_r = \chi_{LT}\frac{M_P}{\gamma_{M1}} \quad \text{(F.13)}$$

The nominal flexural resistance is obtained by setting the partial safety factor $\gamma_{M1} = 1.0$. From Eqs. (F.1) and (F.11), the lateral torsional buckling resistance is obtained as

$$M_r = 0.46 \times \frac{326.6}{1} = 150\, kNm$$

which corresponds to a moment ratio of

$$\frac{M_r}{M_{cr}} = \frac{150}{197.6} = 0.76 \tag{F.14}$$

F.3 Australian Standard AS 4100:2020

F.3.1 Cross-Section Slenderness Parameters

Flange:

Flange slenderness (Clause 5.2.2 of [2.5])

$$\lambda_{e,f} = \left(\frac{b}{t}\right)\sqrt{\left(\frac{F_y}{250}\right)} = \frac{204}{2 \times 12.8}\sqrt{\frac{350}{250}} = 9.43$$

The yield classification limit for flanges of rolled section is $\lambda_{ey,f} = 16.0$ (Table 5.2).

The plastic classification limit for flanges of rolled section is $\lambda_{ep,f} = 9.0$ (Table 5.2).

$$\frac{\lambda_{e,f}}{\lambda_{ey,f}} = \frac{9.43}{16.0} = 0.59$$

Web:

Web slenderness (Clause 5.2.2)

$$\lambda_{e,w} = \left(\frac{d}{w}\right)\sqrt{\left(\frac{F_y}{250}\right)} = \frac{(306 - 2\times 12.8)}{8.5}\sqrt{\left(\frac{350}{250}\right)} = 39.0$$

The yield classification limit for the web of a rolled section is $\lambda_{ey,w} = 115$ (Table 5.2)

The plastic classification limit for the web of a rolled section is $\lambda_{ep,w} = 82$ (Table 5.2)

$$\frac{\lambda_{e,w}}{\lambda_{ey,w}} = \frac{39.0}{115} = 0.34$$

F.3.2 Section Classification:

Section plasticity slenderness limit λ_{sp} and yield slenderness limit λ_{sy} are those of the element with the larger λ_e/λ_{ey} (i.e., flange in this case). Thus,

Section plasticity slenderness limit $\lambda_{sp} = \lambda_{ep,w} = 9.0$

Section yield slenderness limit $\lambda_{sy} = \lambda_{e,w} = 16.0$

The limits λ_{sp} and λ_{sy} will be used to determine the effective section modulus Z_e for the section.

F.3.3 Effective Section Modulus Z_e

The effective section modulus Z_e for compact sections (Cl. 5.2.3 of [2.5]), non-compact sections (Cl. 5.2.4) and slender sections (Cl. 5.2.5) are summarized as

$$Z_e = S_x + \begin{cases} \min\left(Z_x, 1.5S_x\right) & \lambda_s \le \lambda_{sp} \quad \text{compact} \\ \left\{\dfrac{\left(\lambda_{sy} - \lambda_s\right)}{\left(\lambda_{sy} - \lambda_{sp}\right)}\left[\min\left(Z_x, 1.5S_x\right) - S_x\right]\right\} & \lambda_{sp} < \lambda_s \le \lambda_{sy} \quad \text{non-compact} \\ S_x\left(\lambda_{sy}/\lambda_e\right)^2 & \lambda_{sy} < \lambda_s \quad \text{slenderness} \end{cases} \tag{F.15}$$

For the present section, we have $\lambda_{sp} < \lambda_s \le \lambda_{sy} \Rightarrow 9.0 < 9.43 \le 16$. Thus, the section is non-compact, and its effective section modulus is

$$Z_e = 836\times10^3 + \left\{\frac{(16.0-9.43)}{(16.0-9.0)}\left[933\times10^3 - 836\times10^3\right]\right\} = 927\times10^3\ mm^3$$

in which $\min\left(933\times10^3\ mm^3, 1.5\times836\times10^3\ mm^3\right) = 933\times10^3\ mm^3$

F.3.4 Nominal Section Moment Capacity

The nominal section moment capacity (Cl. 5.2.1 of [2.5]) is given by

$$M_s = Z_e F_y = 927\times10^3\times350\times10^{-6} = 324.5\,kNm \tag{F.16}$$

F.3.5 Reference Buckling Moment

The reference buckling moment M_0 (Cl. 5.6.1.1(3)) is

$$M_0 = \sqrt{\left(\pi^2 EI_y/L_e^{\,2}\right)\left[GJ + \left(\pi^2 EC_\omega/L_e^{\,2}\right)\right]} \tag{F.17}$$

$$M_0 = \sqrt{\left(\pi^2\times2\times10^5\times1.81\times10^7/8000^2\right)\left[7.70\times10^4\times3.43\times10^5 + \left(\pi^2\times2\times10^5\times3.88\times10^{11}/8000^2\right)\right]}\times10^{-6}$$
$$= 146.4\,kNm$$

In Eq. (F.17) L_e is the member's effective length given by $L_e = k_t k_l k_r L = L$ and k_t is a twist restraint

factor, k_l is a load height factor and k_r is a lateral rotation restraint factor. For the present problem, Table 5.6.3 gives $k_t = k_l = k_r = 1$.

F.3.6 Moment Modification Factor

The moment modification factor (Cl. 5.6.1.1(1)) is

$$C = \frac{1.7M_{\max}}{\sqrt{\left[\left(M_a\right)^2 + \left(M_b\right)^2 + \left(M_c\right)^2\right]}} \qquad \leq 2.5 \tag{F.18}$$

Equation (F.18)**Error! Reference source not found.** yields $C = 1$ for UM, $C = 1.166$ for UD, and 1.388 for PL. However, in critical moment calculations, the values $C = 1$ for UM, $C = 1.13$ for UD, and $C = 1.35$ for PL based on thin-walled beam finite element analysis will be used instead.

F.3.7 Elastic Critical Moment

For the case of midspan point load, the elastic critical moment is given by

$$M_{cr} = CM_0 = 1.35 \times 146.4 = 197.6kNm \tag{F.19}$$

F.3.8 Slenderness Reduction Factor

The slenderness reduction factor α_s (Cl. 5.6.1.1(2)) is

$$\alpha_s = 0.6\left[\sqrt{\left(M_s/M_0\right)^2 + 3} - \left(M_s/M_0\right)\right] \tag{F.20}$$

From Eqs. (F.17) and (F.16), by substituting into Eq. (F.20), one obtain

$$\alpha_s = 0.6\left[\sqrt{\left(324.5/146.4\right)^2 + 3} - \left(324.5/146.4\right)\right] = 0.36$$

F.3.9 Nominal Member Moment Capacity

The nominal member moment capacity (Cl. 5.6.1.1(1)) is

$$M_r = C\,\alpha_s\,M_s \le M_P \tag{F.21}$$

From Eqs. (F.18), (F.16), (F.20), by substituting into Eq. (F.21) one obtains the nominal member moment capacity

$$M_r = 1.35 \times 0.36 \times 324.5 = 157.7\,kNm \le 324.5\,kNm$$

which corresponds to a moment ratio

$$\frac{M_r}{M_{cr}} = \frac{157.7}{197.6} = 0.80$$

Appendix G: Tables of Results for Parametric Analyses Related to Cross-Section Geometry

This appendix presents a numerical database generated in Chapter 3 for a beam with a different IOS pattern and amplitude. Table G.1 presents the geometric parameters. Each beam is characterized by its span L, web depth *d*, flange width *b*, flange thickness *t*, and web thickness (*w*). The relevant nondimensional ratios are *L/d*, *b/d*, *b/t*, and *d/w*. These geometric parameters were selected to represent a broad range of rolled and welded I-sections and are intended to characterize the way geometric variations affect the lateral-torsional buckling (LTB) strength of members with IOS.

Table G.2 to

Table G.25 present the finite element (FE) results for beams with various initial out-of-straightness (IOS) patterns, amplitudes, and loading conditions. For each case, the table lists the critical moment M_{cr}, the corresponding reduced moment capacity as predicted by the present FE model (M with IOS), and the nominal resistances based on the Eurocode 3 [3.3] and the Australian standard [3.4] provisions. The final three columns provide the ratios of the present model, the Eurocode, and Australian standards to the critical moments.

Table G.1 The beam's cross-section geometric parameters

Section #	Span (m)	d (mm)	b (mm)	t (mm)	w (mm)	L/d	b/d	b/t	d/w
R	8.000	306	204	14.600	8.500	26.144	0.667	13.973	36
1	7.344	306	204	14.600	8.500	24.000	0.667	13.973	36
2	8.262	306	204	14.600	8.500	27.000	0.667	13.973	36
3	9.180	306	204	14.600	8.500	30.000	0.667	13.973	36
4	10.098	306	204	14.600	8.500	33.000	0.667	13.973	36

5	11.016	306	204	14.600	8.500	36.000	0.667	13.973	36
6	8.000	306	153	10.950	8.500	26.144	0.500	13.973	36
7	8.000	306	183.6	13.140	8.500	26.144	0.600	13.973	36
8	8.000	306	214.2	15.330	8.500	26.144	0.700	13.973	36
9	8.000	306	244.8	17.520	8.500	26.144	0.800	13.973	36
10	8.000	306	275.4	19.710	8.500	26.144	0.900	13.973	36
11	8.000	306	204	20.400	8.500	26.144	0.667	10.000	36
12	8.000	306	204	17.000	8.500	26.144	0.667	12.000	36
13	8.000	306	204	14.571	8.500	26.144	0.667	14.000	36
14	8.000	306	204	12.750	8.500	26.144	0.667	16.000	36
15	8.000	306	204	11.333	8.500	26.144	0.667	18.000	36
16	8.000	306	204	14.600	20.400	26.144	0.667	13.973	15
17	8.000	306	204	14.600	12.240	26.144	0.667	13.973	25
18	8.000	306	204	14.600	8.743	26.144	0.667	13.973	35
19	8.000	306	204	14.600	6.800	26.144	0.667	13.973	45
20	8.000	306	204	14.600	5.564	26.144	0.667	13.973	55

Table G.2 Comparison of present FE with design standards of beams with LT-IOS of L/1000 subjected to UM

Sec. #	Load Type	IOS Pattern	Amplitude	Mcr Present FE (kNm)	M (with IOS) (kNm)	M (Eurocode3) (kNm)	M (AS4100) (kNm)	(2/1)	(3/1)	(4/1)
				1	2	3	4			
1	UM	LT	1000	200.73	156.20	164.96	151.25	0.78	0.82	0.75
2		LT	1000	172.68	137.76	146.54	135.20	0.80	0.85	0.78
3		LT	1000	151.61	123.60	131.65	122.00	0.82	0.87	0.80
4		LT	1000	135.21	111.80	119.45	111.02	0.83	0.88	0.82
5		LT	1000	122.4	103.54	109.59	101.78	0.85	0.90	0.83
6		LT	1000	62.54	53.94	56.82	53.53	0.86	0.91	0.86
7		LT	1000	120.98	99.85	105.49	98.42	0.83	0.87	0.81
8		LT	1000	216.65	168.01	178.66	163.38	0.78	0.82	0.75

9		LT	1000	362.91	255.85	277.12	248.25	0.71	0.76	0.68
10		LT	1000	575.01	363.28	396.57	351.38	0.63	0.69	0.61
11		LT	1000	315.28	228.32	252.85	223.76	0.72	0.80	0.71
12		LT	1000	230.41	179.58	190.48	172.63	0.78	0.83	0.75
13		LT	1000	179.28	145.73	150.95	139.08	0.81	0.84	0.78
14		LT	1000	146.04	120.90	124.49	115.98	0.83	0.85	0.79
15		LT	1000	123.15	103.63	105.91	99.42	0.84	0.86	0.81
16		LT	1000	265.66	205.70	223.26	195.49	0.77	0.84	0.74
17		LT	1000	195.49	153.04	165.54	150.99	0.78	0.85	0.77
18		LT	1000	180.56	142.19	152.09	140.04	0.79	0.84	0.78
19		LT	1000	175.79	136.84	147.27	136.01	0.78	0.84	0.77
20		LT	1000	173.83	134.74	144.99	134.07	0.78	0.83	0.77

Table G.3 Comparison of present FE with design standards of beams with T-IOS of L/1000 subjected to UM

Sec. #	Load Type	IOS Pattern	Amplitude	Mcr Present FE (kNm)	M (with IOS) (kNm)	M (Eurocode3) (kNm)	M (AS4100) (kNm)	(2/1)	(3/1)	(4/1)
				1	2	3	4			
1	UM	T	1000	200.73	146.71	164.96	151.25	0.73	0.82	0.75
2		T	1000	172.68	128.13	146.54	135.20	0.74	0.85	0.78
3		T	1000	151.61	115.90	131.65	122.00	0.76	0.87	0.80
4		T	1000	135.21	104.53	119.45	111.02	0.77	0.88	0.82
5		T	1000	122.40	95.26	109.59	101.78	0.78	0.90	0.83
6		T	1000	62.54	50.94	56.82	53.53	0.81	0.91	0.86
7		T	1000	120.98	92.86	105.49	98.42	0.77	0.87	0.81
8		T	1000	216.65	155.61	178.66	163.38	0.72	0.82	0.75
9		T	1000	362.91	234.23	277.12	248.25	0.65	0.76	0.68
10		T	1000	575.01	331.86	396.57	351.38	0.58	0.69	0.61
11		T	1000	315.28	213.91	252.85	223.76	0.68	0.80	0.71

12		T	1000	230.41	167.41	190.48	172.63	0.73	0.83	0.75
13		T	1000	179.28	135.55	150.95	139.08	0.76	0.84	0.78
14		T	1000	146.04	112.94	124.49	115.98	0.77	0.85	0.79
15		T	1000	123.15	97.89	105.91	99.42	0.79	0.86	0.81
16		T	1000	265.66	185.79	223.26	195.49	0.70	0.84	0.74
17		T	1000	195.49	142.49	165.54	150.99	0.73	0.85	0.77
18		T	1000	180.56	132.29	152.09	140.04	0.73	0.84	0.78
19		T	1000	175.79	127.73	147.27	136.01	0.73	0.84	0.77
20		T	1000	173.83	126.49	144.99	134.07	0.73	0.83	0.77

Table G.4 Comparison of present FE with design standards of beams with L-IOS of L/1000 subjected to UM

Sec. #	Load Type	IOS Pattern	Amplitude	Mcr Present FE (kNm)	M (with IOS) (kNm)	M (Eurocode3) (kNm)	M (AS4100) (kNm)	(2/1)	(3/1)	(4/1)
				1	2	3	4			
1		L	1000	200.73	167.59	164.96	151.25	0.83	0.82	0.75
2		L	1000	172.68	146.62	146.54	135.20	0.85	0.85	0.78
3		L	1000	151.61	132.33	131.65	122.00	0.87	0.87	0.80
4		L	1000	135.21	120.23	119.45	111.02	0.89	0.88	0.82
5		L	1000	122.4	109.12	109.59	101.78	0.89	0.90	0.83
6		L	1000	62.54	58.53	56.82	53.53	0.94	0.91	0.86
7	UM	L	1000	120.98	106.86	105.49	98.42	0.88	0.87	0.81
8		L	1000	216.65	175.87	178.66	163.38	0.81	0.82	0.75
9		L	1000	362.91	265.67	277.12	248.25	0.73	0.76	0.68
10		L	1000	575.01	378.07	396.57	351.38	0.66	0.69	0.61
11		L	1000	315.28	244.21	252.85	223.76	0.77	0.80	0.71
12		L	1000	230.41	190.53	190.48	172.63	0.83	0.83	0.75
13		L	1000	179.28	154.42	150.95	139.08	0.86	0.84	0.78

14		L	1000	146.04	129.25	124.49	115.98	0.89	0.85	0.79
15		L	1000	123.15	111.52	105.91	99.42	0.91	0.86	0.81
16		L	1000	265.66	212.09	223.26	195.49	0.80	0.84	0.74
17		L	1000	195.49	161.83	165.54	150.99	0.83	0.85	0.77
18		L	1000	180.56	151.01	152.09	140.04	0.84	0.84	0.78
19		L	1000	175.79	145.52	147.27	136.01	0.83	0.84	0.77
20		L	1000	173.83	142.81	144.99	134.07	0.82	0.83	0.77

Table G.5 Comparison of present FE with design standards of beams with LT-IOS of L/2000 subjected to UM

Sec. #	Load Type	IOS Pattern	Amplitude	Mcr Present FE (kNm)	M (with IOS) (kNm)	M (Eurocode3) (kNm)	M (AS4100) (kNm)	(2/1)	(3/1)	(4/1)
				1	2	3	4			
1	UM	LT	2000	200.73	169.62	164.96	151.25	0.84	0.82	0.75
2		LT	2000	172.68	150.14	146.54	135.20	0.87	0.85	0.78
3		LT	2000	151.61	132.40	131.65	122.00	0.87	0.87	0.80
4		LT	2000	135.21	120.87	119.45	111.02	0.89	0.88	0.82
5		LT	2000	122.4	111.96	109.59	101.78	0.91	0.90	0.83
6		LT	2000	62.54	59.04	56.82	53.53	0.94	0.91	0.86
7		LT	2000	120.98	107.90	105.49	98.42	0.89	0.87	0.81
8		LT	2000	216.65	180.29	178.66	163.38	0.83	0.82	0.75
9		LT	2000	362.91	271.13	277.12	248.25	0.75	0.76	0.68
10		LT	2000	575.01	384.71	396.57	351.38	0.67	0.69	0.61
11		LT	2000	315.28	247.27	252.85	223.76	0.78	0.80	0.71
12		LT	2000	230.41	194.09	190.48	172.63	0.84	0.83	0.75
13		LT	2000	179.28	156.28	150.95	139.08	0.87	0.84	0.78
14		LT	2000	146.04	130.18	124.49	115.98	0.89	0.85	0.79
15		LT	2000	123.15	112.82	105.91	99.42	0.92	0.86	0.81
16		LT	2000	265.66	217.76	223.26	195.49	0.82	0.84	0.74

17		LT	2000	195.49	165.54	165.54	150.99	0.85	0.85	0.77
18		LT	2000	180.56	152.81	152.09	140.04	0.85	0.84	0.78
19		LT	2000	175.79	148.73	147.27	136.01	0.85	0.84	0.77
20		LT	2000	173.83	145.28	144.99	134.07	0.84	0.83	0.77

Table G.6 Comparison of present FE with design standards of beams with T-IOS of L/2000 subjected to UM

Sec. #	Load Type	IOS Pattern	Amplitude	Mcr Present FE (kNm)	M (with IOS) (kNm)	M (Eurocode3) (kNm)	M (AS4100) (kNm)	(2/1)	(3/1)	(4/1)
				1	2	3	4			
1	UM	T	2000	200.73	162.91	164.96	151.25	0.81	0.82	0.75
2		T	2000	172.68	142.66	146.54	135.20	0.83	0.85	0.78
3		T	2000	151.61	128.60	131.65	122.00	0.85	0.87	0.80
4		T	2000	135.21	115.49	119.45	111.02	0.85	0.88	0.82
5		T	2000	122.4	107.71	109.59	101.78	0.88	0.90	0.83
6		T	2000	62.54	55.52	56.82	53.53	0.89	0.91	0.86
7		T	2000	120.98	103.81	105.49	98.42	0.86	0.87	0.81
8		T	2000	216.65	172.50	178.66	163.38	0.80	0.82	0.75
9		T	2000	362.91	259.82	277.12	248.25	0.72	0.76	0.68
10		T	2000	575.01	369.77	396.57	351.38	0.64	0.69	0.61
11		T	2000	315.28	237.48	252.85	223.76	0.75	0.80	0.71
12		T	2000	230.41	186.09	190.48	172.63	0.81	0.83	0.75
13		T	2000	179.28	152.62	150.95	139.08	0.85	0.84	0.78
14		T	2000	146.04	124.92	124.49	115.98	0.86	0.85	0.79
15		T	2000	123.15	104.96	105.91	99.42	0.85	0.86	0.81
16		T	2000	265.66	207.80	223.26	195.49	0.78	0.84	0.74
17		T	2000	195.49	157.40	165.54	150.99	0.81	0.85	0.77
18		T	2000	180.56	146.29	152.09	140.04	0.81	0.84	0.78

19		T	2000	175.79	141.42	147.27	136.01	0.80	0.84	0.77
20		T	2000	173.83	139.70	144.99	134.07	0.80	0.83	0.77

Table G.7 Comparison of present FE with design standards of beams with L-IOS of L/2000 subjected to UM

Sec. #	Load Type	IOS Pattern	Amplitude	Mcr Present FE (kNm)	M (with IOS) (kNm)	M (Eurocode3) (kNm)	M (AS4100) (kNm)	(2/1)	(3/1)	(4/1)
				1	2	3	4			
1	UM	L	2000	200.73	177.19	164.96	151.25	0.88	0.82	0.75
2		L	2000	172.68	156.13	146.54	135.20	0.90	0.85	0.78
3		L	2000	151.61	139.64	131.65	122.00	0.92	0.87	0.80
4		L	2000	135.21	126.53	119.45	111.02	0.94	0.88	0.82
5		L	2000	122.4	116.78	109.59	101.78	0.95	0.90	0.83
6		L	2000	62.54	61.50	56.82	53.53	0.98	0.91	0.86
7		L	2000	120.98	112.95	105.49	98.42	0.93	0.87	0.81
8		L	2000	216.65	187.68	178.66	163.38	0.87	0.82	0.75
9		L	2000	362.91	284.35	277.12	248.25	0.78	0.76	0.68
10		L	2000	575.01	403.04	396.57	351.38	0.70	0.69	0.61
11		L	2000	315.28	259.90	252.85	223.76	0.82	0.80	0.71
12		L	2000	230.41	204.54	190.48	172.63	0.89	0.83	0.75
13		L	2000	179.28	164.84	150.95	139.08	0.92	0.84	0.78
14		L	2000	146.04	136.98	124.49	115.98	0.94	0.85	0.79
15		L	2000	123.15	117.06	105.91	99.42	0.95	0.86	0.81
16		L	2000	265.66	228.13	223.26	195.49	0.86	0.84	0.74
17		L	2000	195.49	174.34	165.54	150.99	0.89	0.85	0.77
18		L	2000	180.56	161.07	152.09	140.04	0.89	0.84	0.78
19		L	2000	175.79	155.43	147.27	136.01	0.88	0.84	0.77
20		L	2000	173.83	153.13	144.99	134.07	0.88	0.83	0.77

Table G.8 Comparison of present FE with design standards of beams with T-IOS of L/1500 subjected to UM

Sec. #	Load Type	IOS Pattern	Amplitude	Mcr Present FE (kNm)	M (with IOS) (kNm)	M (Eurocode3) (kNm)	M (AS4100) (kNm)	(2/1)	(3/1)	(4/1)
				1	2	3	4			
1	UM	T	1500	200.73	153.02	164.96	151.25	0.76	0.82	0.75
2		T	1500	172.68	134.45	146.54	135.20	0.78	0.85	0.78
3		T	1500	151.61	121.10	131.65	122.00	0.80	0.87	0.80
4		T	1500	135.21	109.25	119.45	111.02	0.81	0.88	0.82
5		T	1500	122.4	100.08	109.59	101.78	0.82	0.90	0.83
6		T	1500	62.54	53.02	56.82	53.53	0.85	0.91	0.86
7		T	1500	120.98	97.80	105.49	98.42	0.81	0.87	0.81
8		T	1500	216.65	162.73	178.66	163.38	0.75	0.82	0.75
9		T	1500	362.91	244.86	277.12	248.25	0.67	0.76	0.68
10		T	1500	575.01	347.19	396.57	351.38	0.60	0.69	0.61
11		T	1500	315.28	223.73	252.85	223.76	0.71	0.80	0.71
12		T	1500	230.41	175.23	190.48	172.63	0.76	0.83	0.75
13		T	1500	179.28	142.04	150.95	139.08	0.79	0.84	0.78
14		T	1500	146.04	117.91	124.49	115.98	0.81	0.85	0.79
15		T	1500	123.15	101.47	105.91	99.42	0.82	0.86	0.81
16		T	1500	265.66	193.48	223.26	195.49	0.73	0.84	0.74
17		T	1500	195.49	149.65	165.54	150.99	0.77	0.85	0.77
18		T	1500	180.56	138.31	152.09	140.04	0.77	0.84	0.78
19		T	1500	175.79	133.98	147.27	136.01	0.76	0.84	0.77
20		T	1500	173.83	131.52	144.99	134.07	0.76	0.83	0.77

Table G.9 Comparison of present FE with design standards of beams with T-IOS of L/3000 subjected to UM

Sec. #	Load Type	IOS Pattern	Amplitude	Mcr Present FE (kNm)	M (with IOS) (kNm)	M (Eurocode3) (kNm)	M (AS4100) (kNm)	(2/1)	(3/1)	(4/1)
				1	2	3	4			
1	UM	T	3000	200.73	175.95	164.96	151.25	0.88	0.82	0.75
2		T	3000	172.68	155.09	146.54	135.20	0.90	0.85	0.78
3		T	3000	151.61	137.90	131.65	122.00	0.91	0.87	0.80
4		T	3000	135.21	125.50	119.45	111.02	0.93	0.88	0.82
5		T	3000	122.4	115.47	109.59	101.78	0.94	0.90	0.83
6		T	3000	62.54	61.11	56.82	53.53	0.98	0.91	0.86
7		T	3000	120.98	112.08	105.49	98.42	0.93	0.87	0.81
8		T	3000	216.65	186.60	178.66	163.38	0.86	0.82	0.75
9		T	3000	362.91	280.85	277.12	248.25	0.77	0.76	0.68
10		T	3000	575.01	398.73	396.57	351.38	0.69	0.69	0.61
11		T	3000	315.28	259.63	252.85	223.76	0.82	0.80	0.71
12		T	3000	230.41	203.45	190.48	172.63	0.88	0.83	0.75
13		T	3000	179.28	161.75	150.95	139.08	0.90	0.84	0.78
14		T	3000	146.04	134.94	124.49	115.98	0.92	0.85	0.79
15		T	3000	123.15	116.47	105.91	99.42	0.95	0.86	0.81
16		T	3000	265.66	222.34	223.26	195.49	0.84	0.84	0.74
17		T	3000	195.49	171.65	165.54	150.99	0.88	0.85	0.77
18		T	3000	180.56	158.63	152.09	140.04	0.88	0.84	0.78
19		T	3000	175.79	154.14	147.27	136.01	0.88	0.84	0.77
20		T	3000	173.83	150.62	144.99	134.07	0.87	0.83	0.77

Table G.10 Comparison of present FE with design standards of beams with LT-IOS of L/1000 subjected to PL

Sec. #	Load Type	IOS Pattern	Amplitude	Mcr Present FE	M	M (Eurocode3) (kNm)	M (AS4100) (kNm)	(2/1)	(3/1)	(4/1)

				(kNm)	(with IOS) (kNm)					
				1	2	3	4			
1	PL	LT	1000	270.98	186.93	215.48	204.19	0.69	0.80	0.75
2		LT	1000	233.12	166.40	193.22	182.52	0.71	0.83	0.78
3		LT	1000	204.67	149.70	174.64	164.70	0.73	0.85	0.80
4		LT	1000	182.53	138.12	159.10	149.87	0.76	0.87	0.82
5		LT	1000	164.82	128.21	146.01	137.40	0.78	0.89	0.83
6		LT	1000	84.43	66.37	76.18	72.27	0.79	0.90	0.86
7		LT	1000	163.32	120.53	140.19	132.86	0.74	0.86	0.81
8		LT	1000	292.48	201.67	233.47	220.56	0.69	0.80	0.75
9		LT	1000	489.93	304.13	352.51	335.13	0.62	0.72	0.68
10		LT	1000	776.26	420.44	488.35	474.36	0.54	0.63	0.61
11		LT	1000	425.62	282.00	325.32	302.08	0.66	0.76	0.71
12		LT	1000	311.06	216.58	248.63	233.05	0.70	0.80	0.75
13		LT	1000	242.03	171.80	198.62	187.76	0.71	0.82	0.78
14		LT	1000	197.16	144.55	164.59	156.58	0.73	0.83	0.79
15		LT	1000	166.25	124.28	140.46	134.22	0.75	0.84	0.81
16		LT	1000	358.63	252.98	290.62	263.92	0.71	0.81	0.74
17		LT	1000	263.91	186.15	217.73	203.84	0.71	0.82	0.77
18		LT	1000	243.76	173.50	200.10	189.05	0.71	0.82	0.78
19		LT	1000	237.31	167.47	193.60	183.61	0.71	0.82	0.77
20		LT	1000	234.67	164.73	190.44	180.99	0.70	0.81	0.77

Table G.11 Comparison of present FE with design standards of beams with T-IOS of L/1000 subjected to PL

Sec. #	Load Type	IOS Pattern	Amplitude	Mcr Present FE (kNm)	M (with IOS) (kNm)	M (Eurocode3) (kNm)	M (AS4100) (kNm)	(2/1)	(3/1)	(4/1)

				1	2	3	4			
1	PL	T	1000	270.98	172.19	215.48	204.19	0.64	0.80	0.75
2		T	1000	233.12	152.06	193.22	182.52	0.65	0.83	0.78
3		T	1000	204.67	138.37	174.64	164.70	0.68	0.85	0.80
4		T	1000	182.53	127.82	159.10	149.87	0.70	0.87	0.82
5		T	1000	164.82	119.80	146.01	137.40	0.73	0.89	0.83
6		T	1000	84.43	61.77	76.18	72.27	0.73	0.90	0.86
7		T	1000	163.32	110.49	140.19	132.86	0.68	0.86	0.81
8		T	1000	292.48	184.99	233.47	220.56	0.63	0.80	0.75
9		T	1000	489.93	278.77	352.51	335.13	0.57	0.72	0.68
10		T	1000	776.26	384.56	488.35	474.36	0.50	0.63	0.61
11		T	1000	425.62	258.56	325.32	302.08	0.61	0.76	0.71
12		T	1000	311.06	197.00	248.63	233.05	0.63	0.80	0.75
13		T	1000	242.03	158.64	198.62	187.76	0.66	0.82	0.78
14		T	1000	197.16	130.41	164.59	156.58	0.66	0.83	0.79
15		T	1000	166.25	112.91	140.46	134.22	0.68	0.84	0.81
16		T	1000	358.63	231.86	290.62	263.92	0.65	0.81	0.74
17		T	1000	263.91	172.12	217.73	203.84	0.65	0.82	0.77
18		T	1000	243.76	157.16	200.10	189.05	0.64	0.82	0.78
19		T	1000	237.31	153.00	193.60	183.61	0.64	0.82	0.77
20		T	1000	234.67	151.35	190.44	180.99	0.64	0.81	0.77

Table G.12 Comparison of present FE with design standards of beams with L-IOS of L/1000 subjected to PL

Sec. #	Load Type	IOS Pattern	Amplitude	Mcr Present FE (kNm)	M (with IOS) (kNm)	M (Eurocode3) (kNm)	M (AS4100) (kNm)	(2/1)	(3/1)	(4/1)
				1	2	3	4			
1	PL	L	1000	270.98	202.41	215.48	204.19	0.75	0.80	0.75

2		L	1000	233.12	178.44	193.22	182.52	0.77	0.83	0.78
3		L	1000	204.67	160.23	174.64	164.70	0.78	0.85	0.80
4		L	1000	182.53	147.29	159.10	149.87	0.81	0.87	0.82
5		L	1000	164.82	137.05	146.01	137.40	0.83	0.89	0.83
6		L	1000	84.43	71.16	76.18	72.27	0.84	0.90	0.86
7		L	1000	163.32	132.59	140.19	132.86	0.81	0.86	0.81
8		L	1000	292.48	217.37	233.47	220.56	0.74	0.80	0.75
9		L	1000	489.93	331.42	352.51	335.13	0.68	0.72	0.68
10		L	1000	776.26	455.16	488.35	474.36	0.59	0.63	0.61
11		L	1000	425.62	302.60	325.32	302.08	0.71	0.76	0.71
12		L	1000	311.06	230.93	248.63	233.05	0.74	0.80	0.75
13		L	1000	242.03	183.88	198.62	187.76	0.76	0.82	0.78
14		L	1000	197.16	154.67	164.59	156.58	0.78	0.83	0.79
15		L	1000	166.25	131.59	140.46	134.22	0.79	0.84	0.81
16		L	1000	358.63	269.60	290.62	263.92	0.75	0.81	0.74
17		L	1000	263.91	201.83	217.73	203.84	0.76	0.82	0.77
18		L	1000	243.76	186.46	200.10	189.05	0.76	0.82	0.78
19		L	1000	237.31	180.59	193.60	183.61	0.76	0.82	0.77
20		L	1000	234.67	176.97	190.44	180.99	0.75	0.81	0.77

Table G.13 Comparison of present FE with design standards of beams with LT-IOS of L/2000 subjected to PL

Sec. #	Load Type	IOS Pattern	Amplitude	Mcr Present FE (kNm)	M (with IOS) (kNm)	M (Eurocode3) (kNm)	M (AS4100) (kNm)	(2/1)	(3/1)	(4/1)
				1	2	3	4			
1	PL	LT	2000	270.98	203.80	215.48	204.19	0.75	0.80	0.75
2		LT	2000	233.12	185.09	193.22	182.52	0.79	0.83	0.78
3		LT	2000	204.67	164.66	174.64	164.70	0.80	0.85	0.80

4		LT	2000	182.53	150.68	159.10	149.87	0.83	0.87	0.82
5		LT	2000	164.82	141.03	146.01	137.40	0.86	0.89	0.83
6		LT	2000	84.43	73.30	76.18	72.27	0.87	0.90	0.86
7		LT	2000	163.32	132.76	140.19	132.86	0.81	0.86	0.81
8		LT	2000	292.48	223.68	233.47	220.56	0.76	0.80	0.75
9		LT	2000	489.93	334.98	352.51	335.13	0.68	0.72	0.68
10		LT	2000	776.26	464.47	488.35	474.36	0.60	0.63	0.61
11		LT	2000	425.62	309.30	325.32	302.08	0.73	0.76	0.71
12		LT	2000	311.06	239.10	248.63	233.05	0.77	0.80	0.75
13		LT	2000	242.03	187.59	198.62	187.76	0.78	0.82	0.78
14		LT	2000	197.16	157.02	164.59	156.58	0.80	0.83	0.79
15		LT	2000	166.25	136.70	140.46	134.22	0.82	0.84	0.81
16		LT	2000	358.63	276.29	290.62	263.92	0.77	0.81	0.74
17		LT	2000	263.91	204.77	217.73	203.84	0.78	0.82	0.77
18		LT	2000	243.76	189.17	200.10	189.05	0.78	0.82	0.78
19		LT	2000	237.31	184.21	193.60	183.61	0.78	0.82	0.77
20		LT	2000	234.67	181.20	190.44	180.99	0.77	0.81	0.77

Table G.14 Comparison of present FE with design standards of beams with T-IOS of L/2000 subjected to PL

Sec. #	Load Type	IOS Pattern	Amplitude	Mcr Present FE (kNm)	M (with IOS) (kNm)	M (Eurocode3) (kNm)	M (AS4100) (kNm)	(2/1)	(3/1)	(4/1)
				1	2	3	4			
1		T	2000	270.98	195.36	215.48	204.19	0.72	0.80	0.75
2		T	2000	233.12	174.03	193.22	182.52	0.75	0.83	0.78
3	PL	T	2000	204.67	156.50	174.64	164.70	0.76	0.85	0.80
4		T	2000	182.53	145.31	159.10	149.87	0.80	0.87	0.82
5		T	2000	164.82	138.23	146.01	137.40	0.84	0.89	0.83

6		T	2000	84.43	68.67	76.18	72.27	0.81	0.90	0.86
7		T	2000	163.32	122.97	140.19	132.86	0.75	0.86	0.81
8		T	2000	292.48	209.22	233.47	220.56	0.72	0.80	0.75
9		T	2000	489.93	313.31	352.51	335.13	0.64	0.72	0.68
10		T	2000	776.26	434.94	488.35	474.36	0.56	0.63	0.61
11		T	2000	425.62	293.80	325.32	302.08	0.69	0.76	0.71
12		T	2000	311.06	224.25	248.63	233.05	0.72	0.80	0.75
13		T	2000	242.03	181.08	198.62	187.76	0.75	0.82	0.78
14		T	2000	197.16	148.08	164.59	156.58	0.75	0.83	0.79
15		T	2000	166.25	127.70	140.46	134.22	0.77	0.84	0.81
16		T	2000	358.63	260.25	290.62	263.92	0.73	0.81	0.74
17		T	2000	263.91	192.68	217.73	203.84	0.73	0.82	0.77
18		T	2000	243.76	177.05	200.10	189.05	0.73	0.82	0.78
19		T	2000	237.31	172.53	193.60	183.61	0.73	0.82	0.77
20		T	2000	234.67	170.78	190.44	180.99	0.73	0.81	0.77

Table G.15 Comparison of present FE with design standards of beams with L-IOS of L/2000 subjected to PL

Sec. #	Load Type	IOS Pattern	Amplitude	Mcr Present FE (kNm)	M (with IOS) (kNm)	M (Eurocode3) (kNm)	M (AS4100) (kNm)	(2/1)	(3/1)	(4/1)
				1	2	3	4			
1	PL	L	2000	270.98	216.23	215.48	204.19	0.80	0.80	0.75
2		L	2000	233.12	194.54	193.22	182.52	0.83	0.83	0.78
3		L	2000	204.67	174.64	174.64	164.70	0.85	0.85	0.80
4		L	2000	182.53	157.02	159.10	149.87	0.86	0.87	0.82
5		L	2000	164.82	144.79	146.01	137.40	0.88	0.89	0.83
6		L	2000	84.43	76.18	76.18	72.27	0.90	0.90	0.86
7		L	2000	163.32	140.63	140.19	132.86	0.86	0.86	0.81

8		L	2000	292.48	234.32	233.47	220.56	0.80	0.80	0.75
9		L	2000	489.93	354.36	352.51	335.13	0.72	0.72	0.68
10		L	2000	776.26	492.32	488.35	474.36	0.63	0.63	0.61
11		L	2000	425.62	326.69	325.32	302.08	0.77	0.76	0.71
12		L	2000	311.06	248.94	248.63	233.05	0.80	0.80	0.75
13		L	2000	242.03	200.16	198.62	187.76	0.83	0.82	0.78
14		L	2000	197.16	166.00	164.59	156.58	0.84	0.83	0.79
15		L	2000	166.25	143.83	140.46	134.22	0.87	0.84	0.81
16		L	2000	358.63	294.05	290.62	263.92	0.82	0.81	0.74
17		L	2000	263.91	218.33	217.73	203.84	0.83	0.82	0.77
18		L	2000	243.76	201.44	200.10	189.05	0.83	0.82	0.78
19		L	2000	237.31	195.94	193.60	183.61	0.83	0.82	0.77
20		L	2000	234.67	192.90	190.44	180.99	0.82	0.81	0.77

Table G.16 Comparison of present FE with design standards of beams with T-IOS of L/1500 subjected to PL

Sec. #	Load Type	IOS Pattern	Amplitude	Mcr Present FE (kNm)	M (with IOS) (kNm)	M (Eurocode3) (kNm)	M (AS4100) (kNm)	(2/1)	(3/1)	(4/1)
				1	2	3	4			
1		T	1500	270.98	181.65	215.48	204.19	0.67	0.80	0.75
2		T	1500	233.12	160.21	193.22	182.52	0.69	0.83	0.78
3		T	1500	204.67	145.47	174.64	164.70	0.71	0.85	0.80
4		T	1500	182.53	135.05	159.10	149.87	0.74	0.87	0.82
5	PL	T	1500	164.82	126.07	146.01	137.40	0.76	0.89	0.83
6		T	1500	84.43	64.99	76.18	72.27	0.77	0.90	0.86
7		T	1500	163.32	117.01	140.19	132.86	0.72	0.86	0.81
8		T	1500	292.48	195.51	233.47	220.56	0.67	0.80	0.75
9		T	1500	489.93	294.96	352.51	335.13	0.60	0.72	0.68

10		T	1500	776.26	405.94	488.35	474.36	0.52	0.63	0.61
11		T	1500	425.62	273.78	325.32	302.08	0.64	0.76	0.71
12		T	1500	311.06	208.45	248.63	233.05	0.67	0.80	0.75
13		T	1500	242.03	166.88	198.62	187.76	0.69	0.82	0.78
14		T	1500	197.16	139.01	164.59	156.58	0.71	0.83	0.79
15		T	1500	166.25	120.18	140.46	134.22	0.72	0.84	0.81
16		T	1500	358.63	245.64	290.62	263.92	0.68	0.81	0.74
17		T	1500	263.91	179.14	217.73	203.84	0.68	0.82	0.77
18		T	1500	243.76	167.98	200.10	189.05	0.69	0.82	0.78
19		T	1500	237.31	162.23	193.60	183.61	0.68	0.82	0.77
20		T	1500	234.67	160.22	190.44	180.99	0.68	0.81	0.77

Table G.17 Comparison of present FE with design standards of beams with T-IOS of L/3000 subjected to PL

Sec. #	Load Type	IOS Pattern	Amplitude	Mcr Present FE (kNm)	M (with IOS) (kNm)	M (Eurocode3) (kNm)	M (AS4100) (kNm)	(2/1)	(3/1)	(4/1)
				1	2	3	4			
1	PL	T	3000	270.98	210.93	215.48	204.19	0.78	0.80	0.75
2		T	3000	233.12	192.19	193.22	182.52	0.82	0.83	0.78
3		T	3000	204.67	171.11	174.64	164.70	0.84	0.85	0.80
4		T	3000	182.53	155.96	159.10	149.87	0.85	0.87	0.82
5		T	3000	164.82	146.79	146.01	137.40	0.89	0.89	0.83
6		T	3000	84.43	75.47	76.18	72.27	0.89	0.90	0.86
7		T	3000	163.32	138.00	140.19	132.86	0.84	0.86	0.81
8		T	3000	292.48	231.15	233.47	220.56	0.79	0.80	0.75
9		T	3000	489.93	347.47	352.51	335.13	0.71	0.72	0.68
10		T	3000	776.26	481.52	488.35	474.36	0.62	0.63	0.61
11		T	3000	425.62	320.72	325.32	302.08	0.75	0.76	0.71

12		T	3000	311.06	246.97	248.63	233.05	0.79	0.80	0.75
13		T	3000	242.03	194.16	198.62	187.76	0.80	0.82	0.78
14		T	3000	197.16	163.04	164.59	156.58	0.83	0.83	0.79
15		T	3000	166.25	139.31	140.46	134.22	0.84	0.84	0.81
16		T	3000	358.63	285.56	290.62	263.92	0.80	0.81	0.74
17		T	3000	263.91	211.93	217.73	203.84	0.80	0.82	0.77
18		T	3000	243.76	196.51	200.10	189.05	0.81	0.82	0.78
19		T	3000	237.31	191.45	193.60	183.61	0.81	0.82	0.77
20		T	3000	234.67	187.03	190.44	180.99	0.80	0.81	0.77

Table G.18 Comparison of present FE with design standards of beams with LT-IOS of L/1000 subjected to UD

Sec. #	Load Type	IOS Pattern	Amplitude	Mcr Present FE (kNm)	M (with IOS) (kNm)	M (Eurocode3) (kNm)	M (AS4100) (kNm)	(2/1)	(3/1)	(4/1)
				1	2	3	4			
1		LT	1000	226.82	172.57	184.49	170.91	0.76	0.81	0.75
2		LT	1000	195.13	152.81	164.37	152.78	0.78	0.84	0.78
3		LT	1000	171.32	136.30	147.94	137.86	0.80	0.86	0.80
4		LT	1000	152.79	123.59	134.41	125.45	0.81	0.88	0.82
5		LT	1000	138.31	114.16	123.11	115.01	0.83	0.89	0.83
6		LT	1000	70.67	60.27	64.06	60.49	0.85	0.91	0.86
7	UD	LT	1000	136.71	110.83	118.61	111.21	0.81	0.87	0.81
8		LT	1000	244.81	183.15	199.84	184.62	0.75	0.82	0.75
9		LT	1000	410.09	283.22	307.34	280.52	0.69	0.75	0.68
10		LT	1000	649.76	401.18	435.00	397.06	0.62	0.67	0.61
11		LT	1000	356.27	252.41	281.47	252.85	0.71	0.79	0.71
12		LT	1000	260.36	197.48	212.99	195.07	0.76	0.82	0.75
13		LT	1000	202.59	160.00	169.21	157.16	0.79	0.84	0.78

14		LT	1000	165.03	133.59	139.75	131.06	0.81	0.85	0.79
15		LT	1000	139.16	114.20	119.01	112.35	0.82	0.86	0.81
16		LT	1000	300.20	226.03	249.46	220.91	0.75	0.83	0.74
17		LT	1000	220.90	168.83	185.54	170.62	0.76	0.84	0.77
18		LT	1000	204.03	156.68	170.48	158.24	0.77	0.84	0.78
19		LT	1000	198.64	152.92	165.03	153.69	0.77	0.83	0.77
20		LT	1000	196.43	153.23	162.43	151.49	0.78	0.83	0.77

Table G.19 Comparison of present FE with design standards of beams with T-IOS of L/1000 subjected to UD

Sec. #	Load Type	IOS Pattern	Amplitude	Mcr Present FE (kNm)	M (with IOS) (kNm)	M (Eurocode3) (kNm)	M (AS4100) (kNm)	(2/1)	(3/1)	(4/1)
				1	2	3	4			
1	UD	T	1000	226.82	161.73	184.49	170.91	0.71	0.81	0.75
2		T	1000	195.13	142.36	164.37	152.78	0.73	0.84	0.78
3		T	1000	171.32	127.45	147.94	137.86	0.74	0.86	0.80
4		T	1000	152.79	114.83	134.41	125.45	0.75	0.88	0.82
5		T	1000	138.31	106.22	123.11	115.01	0.77	0.89	0.83
6		T	1000	70.67	56.51	64.06	60.49	0.80	0.91	0.86
7		T	1000	136.71	101.87	118.61	111.21	0.75	0.87	0.81
8		T	1000	244.81	171.09	199.84	184.62	0.70	0.82	0.75
9		T	1000	410.09	258.19	307.34	280.52	0.63	0.75	0.68
10		T	1000	649.76	363.39	435.00	397.06	0.56	0.67	0.61
11		T	1000	356.27	234.73	281.47	252.85	0.66	0.79	0.71
12		T	1000	260.36	184.91	212.99	195.07	0.71	0.82	0.75
13		T	1000	202.59	149.05	169.21	157.16	0.74	0.84	0.78
14		T	1000	165.03	123.92	139.75	131.06	0.75	0.85	0.79
15		T	1000	139.16	106.47	119.01	112.35	0.77	0.86	0.81

16		T	1000	300.20	204.44	249.46	220.91	0.68	0.83	0.74
17		T	1000	220.90	152.81	185.54	170.62	0.69	0.84	0.77
18		T	1000	204.03	143.63	170.48	158.24	0.70	0.84	0.78
19		T	1000	198.64	141.00	165.03	153.69	0.71	0.83	0.77
20		T	1000	196.43	139.65	162.43	151.49	0.71	0.83	0.77

Table G.20 Comparison of present FE with design standards of beams with L-IOS of L/1000 subjected to UD

Sec. #	Load Type	IOS Pattern	Amplitude	Mcr Present FE (kNm)	M (with IOS) (kNm)	M (Eurocode3) (kNm)	M (AS4100) (kNm)	(2/1)	(3/1)	(4/1)
				1	2	3	4			
1		L	1000	226.82	184.57	184.49	170.91	0.81	0.81	0.75
2		L	1000	195.13	161.10	164.37	152.78	0.83	0.84	0.78
3		L	1000	171.32	144.83	147.94	137.86	0.85	0.86	0.80
4		L	1000	152.79	131.65	134.41	125.45	0.86	0.88	0.82
5		L	1000	138.31	121.36	123.11	115.01	0.88	0.89	0.83
6		L	1000	70.67	64.04	64.06	60.49	0.91	0.91	0.86
7		L	1000	136.71	119.47	118.61	111.21	0.87	0.87	0.81
8		L	1000	244.81	195.36	199.84	184.62	0.80	0.82	0.75
9	UD	L	1000	410.09	294.99	307.34	280.52	0.72	0.75	0.68
10		L	1000	649.76	410.49	435.00	397.06	0.63	0.67	0.61
11		L	1000	356.27	272.58	281.47	252.85	0.77	0.79	0.71
12		L	1000	260.36	213.06	212.99	195.07	0.82	0.82	0.75
13		L	1000	202.59	172.54	169.21	157.16	0.85	0.84	0.78
14		L	1000	165.03	141.97	139.75	131.06	0.86	0.85	0.79
15		L	1000	139.16	121.48	119.01	112.35	0.87	0.86	0.81
16		L	1000	300.20	236.38	249.46	220.91	0.79	0.83	0.74
17		L	1000	220.90	178.16	185.54	170.62	0.81	0.84	0.77

18		L	1000	204.03	165.31	170.48	158.24	0.81	0.84	0.78
19		L	1000	198.64	161.52	165.03	153.69	0.81	0.83	0.77
20		L	1000	196.43	160.09	162.43	151.49	0.82	0.83	0.77

Table G.21 Comparison of present FE with design standards of beams with LT-IOS of L/2000 subjected to UD

Sec. #	Load Type	IOS Pattern	Amplitude	Mcr Present FE (kNm)	M (with IOS) (kNm)	M (Eurocode3) (kNm)	M (AS4100) (kNm)	(2/1)	(3/1)	(4/1)
				1	2	3	4			
1		LT	2000	226.82	189.30	184.49	170.91	0.83	0.81	0.75
2		LT	2000	195.13	165.27	164.37	152.78	0.85	0.84	0.78
3		LT	2000	171.32	148.02	147.94	137.86	0.86	0.86	0.80
4		LT	2000	152.79	134.62	134.41	125.45	0.88	0.88	0.82
5		LT	2000	138.31	125.71	123.11	115.01	0.91	0.89	0.83
6		LT	2000	70.67	66.06	64.06	60.49	0.93	0.91	0.86
7		LT	2000	136.71	120.36	118.61	111.21	0.88	0.87	0.81
8		LT	2000	244.81	201.94	199.84	184.62	0.82	0.82	0.75
9		LT	2000	410.09	301.35	307.34	280.52	0.73	0.75	0.68
10	UD	LT	2000	649.76	413.95	435.00	397.06	0.64	0.67	0.61
11		LT	2000	356.27	274.32	281.47	252.85	0.77	0.79	0.71
12		LT	2000	260.36	215.94	212.99	195.07	0.83	0.82	0.75
13		LT	2000	202.59	174.08	169.21	157.16	0.86	0.84	0.78
14		LT	2000	165.03	143.33	139.75	131.06	0.87	0.85	0.79
15		LT	2000	139.16	123.36	119.01	112.35	0.89	0.86	0.81
16		LT	2000	300.20	237.64	249.46	220.91	0.79	0.83	0.74
17		LT	2000	220.90	183.61	185.54	170.62	0.83	0.84	0.77
18		LT	2000	204.03	170.71	170.48	158.24	0.84	0.84	0.78
19		LT	2000	198.64	166.70	165.03	153.69	0.84	0.83	0.77

20		LT	2000	196.43	165.31	162.43	151.49	0.84	0.83	0.77

Table G.22 Comparison of present FE with design standards of beams with T-IOS of L/2000 subjected to UD

Sec. #	Load Type	IOS Pattern	Amplitude	Mcr Present FE (kNm)	M (with IOS) (kNm)	M (Eurocode3) (kNm)	M (AS4100) (kNm)	(2/1)	(3/1)	(4/1)
				1	2	3	4			
1	UD	T	2000	226.82	182.75	184.49	170.91	0.81	0.81	0.75
2		T	2000	195.13	158.78	164.37	152.78	0.81	0.84	0.78
3		T	2000	171.32	142.67	147.94	137.86	0.83	0.86	0.80
4		T	2000	152.79	128.96	134.41	125.45	0.84	0.88	0.82
5		T	2000	138.31	118.95	123.11	115.01	0.86	0.89	0.83
6		T	2000	70.67	61.49	64.06	60.49	0.87	0.91	0.86
7		T	2000	136.71	114.36	118.61	111.21	0.84	0.87	0.81
8		T	2000	244.81	190.79	199.84	184.62	0.78	0.82	0.75
9		T	2000	410.09	290.29	307.34	280.52	0.71	0.75	0.68
10		T	2000	649.76	412.38	435.00	397.06	0.63	0.67	0.61
11		T	2000	356.27	262.02	281.47	252.85	0.74	0.79	0.71
12		T	2000	260.36	203.30	212.99	195.07	0.78	0.82	0.75
13		T	2000	202.59	167.06	169.21	157.16	0.82	0.84	0.78
14		T	2000	165.03	138.75	139.75	131.06	0.84	0.85	0.79
15		T	2000	139.16	119.31	119.01	112.35	0.86	0.86	0.81
16		T	2000	300.20	232.87	249.46	220.91	0.78	0.83	0.74
17		T	2000	220.90	173.06	185.54	170.62	0.78	0.84	0.77
18		T	2000	204.03	160.83	170.48	158.24	0.79	0.84	0.78
19		T	2000	198.64	156.97	165.03	153.69	0.79	0.83	0.77
20		T	2000	196.43	157.51	162.43	151.49	0.80	0.83	0.77

Table G.23 Comparison of present FE with design standards of beams with L-IOS of L/2000 subjected to UD

Sec. #	Load Type	IOS Pattern	Amplitude	Mcr Present FE (kNm)	M (with IOS) (kNm)	M (Eurocode3) (kNm)	M (AS4100) (kNm)	(2/1)	(3/1)	(4/1)
				1	2	3	4			
1	UD	L	2000	226.82	197.13	184.49	170.91	0.87	0.81	0.75
2		L	2000	195.13	172.92	164.37	152.78	0.89	0.84	0.78
3		L	2000	171.32	156.40	147.94	137.86	0.91	0.86	0.80
4		L	2000	152.79	141.14	134.41	125.45	0.92	0.88	0.82
5		L	2000	138.31	130.43	123.11	115.01	0.94	0.89	0.83
6		L	2000	70.67	68.61	64.06	60.49	0.97	0.91	0.86
7		L	2000	136.71	125.97	118.61	111.21	0.92	0.87	0.81
8		L	2000	244.81	207.94	199.84	184.62	0.85	0.82	0.75
9		L	2000	410.09	315.94	307.34	280.52	0.77	0.75	0.68
10		L	2000	649.76	446.77	435.00	397.06	0.69	0.67	0.61
11		L	2000	356.27	291.90	281.47	252.85	0.82	0.79	0.71
12		L	2000	260.36	227.72	212.99	195.07	0.87	0.82	0.75
13		L	2000	202.59	184.90	169.21	157.16	0.91	0.84	0.78
14		L	2000	165.03	152.48	139.75	131.06	0.92	0.85	0.79
15		L	2000	139.16	129.73	119.01	112.35	0.93	0.86	0.81
16		L	2000	300.20	253.88	249.46	220.91	0.85	0.83	0.74
17		L	2000	220.90	194.15	185.54	170.62	0.88	0.84	0.77
18		L	2000	204.03	179.75	170.48	158.24	0.88	0.84	0.78
19		L	2000	198.64	175.55	165.03	153.69	0.88	0.83	0.77
20		L	2000	196.43	174.25	162.43	151.49	0.89	0.83	0.77

Table G.24 Comparison of present FE with design standards of beams with T-IOS of L/1500 subjected to UD

Sec. #	Load Type	IOS Pattern	Amplitude	Mcr Present FE	M	M (Eurocode3) (kNm)	M (AS4100) (kNm)	(2/1)	(3/1)	(4/1)

				(kNm)	(with IOS) (kNm)					
				1	2	3	4			
1	UD	T	1500	226.82	169.00	184.49	170.91	0.75	0.81	0.75
2		T	1500	195.13	147.69	164.37	152.78	0.76	0.84	0.78
3		T	1500	171.32	133.53	147.94	137.86	0.78	0.86	0.80
4		T	1500	152.79	120.68	134.41	125.45	0.79	0.88	0.82
5		T	1500	138.31	110.59	123.11	115.01	0.80	0.89	0.83
6		T	1500	70.67	59.17	64.06	60.49	0.84	0.91	0.86
7		T	1500	136.71	108.87	118.61	111.21	0.80	0.87	0.81
8		T	1500	244.81	180.54	199.84	184.62	0.74	0.82	0.75
9		T	1500	410.09	270.68	307.34	280.52	0.66	0.75	0.68
10		T	1500	649.76	379.14	435.00	397.06	0.58	0.67	0.61
11		T	1500	356.27	249.57	281.47	252.85	0.70	0.79	0.71
12		T	1500	260.36	193.73	212.99	195.07	0.74	0.82	0.75
13		T	1500	202.59	156.07	169.21	157.16	0.77	0.84	0.78
14		T	1500	165.03	128.48	139.75	131.06	0.78	0.85	0.79
15		T	1500	139.16	109.74	119.01	112.35	0.79	0.86	0.81
16		T	1500	300.20	215.19	249.46	220.91	0.72	0.83	0.74
17		T	1500	220.90	164.02	185.54	170.62	0.74	0.84	0.77
18		T	1500	204.03	153.37	170.48	158.24	0.75	0.84	0.78
19		T	1500	198.64	150.31	165.03	153.69	0.76	0.83	0.77
20		T	1500	196.43	149.45	162.43	151.49	0.76	0.83	0.77

Table G.25 Comparison of present FE with design standards of beams with T-IOS of L/3000 subjected to UD

Sec. #	Load Type	IOS Pattern	Amplitude	Mcr Present FE (kNm)	M (with IOS) (kNm)	M (Eurocode3) (kNm)	M (AS4100) (kNm)	(2/1)	(3/1)	(4/1)

				1	2	3	4			
1	UD	T	3000	226.82	194.63	184.49	170.91	0.86	0.81	0.75
2		T	3000	195.13	171.52	164.37	152.78	0.88	0.84	0.78
3		T	3000	171.32	154.67	147.94	137.86	0.90	0.86	0.80
4		T	3000	152.79	139.66	134.41	125.45	0.91	0.88	0.82
5		T	3000	138.31	129.68	123.11	115.01	0.94	0.89	0.83
6		T	3000	70.67	68.46	64.06	60.49	0.97	0.91	0.86
7		T	3000	136.71	123.44	118.61	111.21	0.90	0.87	0.81
8		T	3000	244.81	207.69	199.84	184.62	0.85	0.82	0.75
9		T	3000	410.09	312.20	307.34	280.52	0.76	0.75	0.68
10		T	3000	649.76	446.60	435.00	397.06	0.69	0.67	0.61
11		T	3000	356.27	289.00	281.47	252.85	0.81	0.79	0.71
12		T	3000	260.36	224.69	212.99	195.07	0.86	0.82	0.75
13		T	3000	202.59	180.17	169.21	157.16	0.89	0.84	0.78
14		T	3000	165.03	149.78	139.75	131.06	0.91	0.85	0.79
15		T	3000	139.16	128.47	119.01	112.35	0.92	0.86	0.81
16		T	3000	300.20	247.71	249.46	220.91	0.83	0.83	0.74
17		T	3000	220.90	189.13	185.54	170.62	0.86	0.84	0.77
18		T	3000	204.03	175.88	170.48	158.24	0.86	0.84	0.78
19		T	3000	198.64	172.32	165.03	153.69	0.87	0.83	0.77
20		T	3000	196.43	171.21	162.43	151.49	0.87	0.83	0.77

Appendix H: Sectional Properties for Monosymmetric I Section

This appendix derives expressions for the location of the centroid and shear centre coordinate for a monosymmetric I-section, which is used in Chapter 4.

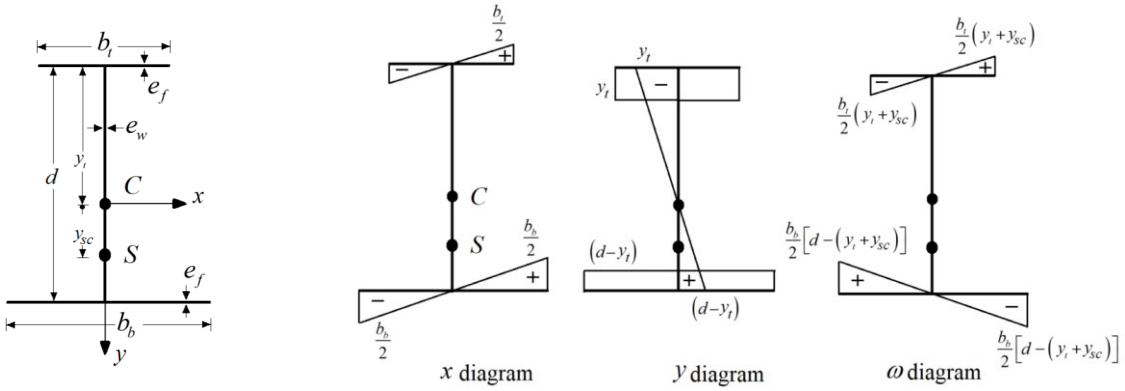

(a) (b)

Fig. H.1 Monosymmetric section (a) Dimensions and notation (b) Sectorial coordinate

A monosymmetric I section has top flange dimensions $b_t \times e_f$, bottom flange dimensions $b_b \times e_f$, a depth d between flange centroids, and web thickness e_w (Fig. H.1a). The centroidal height measured from the top flange is denoted y_t and the shear centre is located at a distance y_{sc} below the centroid. The centroidal distance y_t is obtained by satisfying the condition $S_y = \int_A y dA = 0$, which yields

$$S_y = b_t e_f \left(-y_t\right) + b_b e_f \left(d - y_t\right) + \frac{1}{2} d e_w \left[-y_t + \left(d - y_t\right)\right] = 0 \qquad \text{(H.1)}$$

$$y_t = \frac{b_b e_f d + 0.5 e_w d^2}{b_t e_f + b_b e_f + d e_w} \tag{H.2}$$

The shear centre coordinate y_{sc} relative to the centroid is given by setting

$$I_{x\omega} = \int_A \omega x dA = 0 \qquad \begin{aligned} I_{x\omega} &= 2\left(I_{x\omega,b} + I_{x\omega,t}\right) = 0 \\ I_{x\omega,t} &= \frac{1}{3}\left(\frac{b_t}{2}\right)^2 \left(y_t + y_{sc}\right)\frac{b_t}{2} e_f = \frac{1}{24} b_t^3 \left(y_t + y_{sc}\right) e_f \\ I_{x\omega,b} &= \frac{1}{3}\left(\frac{b_b}{2}\right)^2 \left(-b_b\left[d - \left(y_t + y_{sc}\right)\right]\right)\frac{b_b}{2} e_f = -\frac{1}{24} b_b^3 \left[d - \left(y_t + y_{sc}\right)\right] e_f \end{aligned} \tag{H.3}$$

which yields

$$y_{sc} = \frac{+b_b^3 \left(d - y_t\right) - b_t^3 y_t}{b_b^3 + b_t^3} \tag{H.4}$$

Appendix I: Verification for Straight Monosymmetric Beams

I.1 General

This section examines the validity of the geometrically nonlinear finite element formulation developed in Chapter 4 for straight beams with monosymmetric cross-section through comparisons against those of S4 shell models in the ABAQUS. Towards this objective, six numerical examples are analyzed:

(1) Cantilever under combined transverse and axial loading acting at the tip.

(2) Cantilever under pure torque.

(3) Pin-roller member under midspan transverse and axial loads

(4) Beam fixed at both ends under mid-span point load.

(5) Beam pinned at both ends under midspan point load.

(6) pinned roller Beam under midspan point load.

I.2 Reference Cross-Section

In all examples, the reference cross-section adopted consists of a monosymmetric steel section with a top flange width of 300 mm, a bottom flange width of 150 mm, and a web height of 400 mm which is measured from the inner flange surfaces, and flange thicknesses of 12 mm, and web thickness of 8 mm. The corresponding cross-sectional properties are $A = 8600\,mm^2$, I_{xx}=2.40×10^8 mm^4, $I_{yy} = 3.04\times10^7$ mm^4, $J = 3.27\times10^5$ mm^4, and $I_\omega = 4.81\times10^{11}$ mm^6. The material is steel with a Young's modulus $E = 200\,GPa$ and a shear modulus $G = 77\,GPa$

I.3 Mesh Study

I.3.1 Problem Description

A 5-meter cantilever with a reference monosymmetric cross-section is considered. The member is subjected to two loading cases (1) a transverse load V_c at the beam tip acting at the shear center and (2) an external moment M_c acting at the free end Fig. I.1(a-c). To specify an appropriate load level target in both cases, a lateral torsional buckling eigenvalue was first conducted, which cases and yielded $V_c = 132\,kN$ for Case 1 and $M_c = 190\,kNm$ for case 2. The target load in the present nonlinear analysis was applied in 10 increments, and required 3 to 5 iterations per increment to achieve convergence.

I.3.2 Present Model

The integration scheme utilized three Gaussian quadrature points along the longitudinal direction and nine Simpson integration points across both the flange width and web height. For computational efficiency, two Gaussian quadrature points were employed through the thickness during the iterative process. However, once convergence was achieved, five Simpson integration points were used through the thickness to accurately determine stresses at the extreme fibers. Three uniform meshes consisting of 10, 20, and 24 elements were analyzed for each loading case. As shown in Table I.1, the transverse displacements and peak stresses displayed minimal variation between the meshes with 20 and 24 elements, indicating that mesh convergence was reached with the 20 elements mesh.

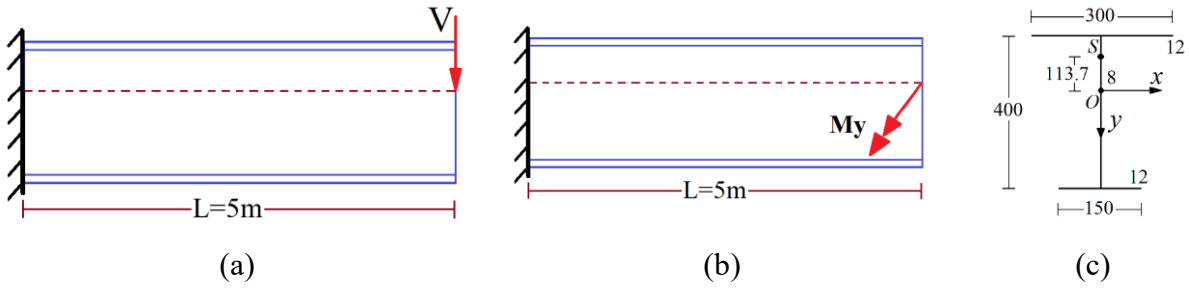

Fig. I.1 Cantilever beams for mesh density study under (a) Transverse load, (b) Bending moment, (c) The reference cross-section dimensions

Table I.1 Mesh study for the present model

Number of Elements	Transverse load		Bending moment	
	Transverse displacement (1) (mm)	Normal stress (2) (MPa)	Transverse displacement (1) (mm)	Normal stress (2) (MPa)
10	106.2	654.7	50.7	214.2
20	106.1	653.2	50.8	212.3
24	106.1	652.7	50.8	212.1

(3) At the cantilever tip

(4) Peak normal stress at the extreme fiber at the cantilever root

I.3.3 S4 Model

The S4 shell element is a general-purpose element characterized by four nodes and full integration. Each node has six degrees of freedom, which include three translational and three rotational components. The analysis utilized a discretization scheme with n_l elements along the beam's span, n_f elements across the flange width, and n_w elements along the web thickness. Three mesh configurations were examined: $(n_l, n_f, n_w) =$ (150, 6, 8), (200, 6, 8), and (250, 6, 8). As shown in Table I.2, both transverse displacement and normal stress values attain convergence for the medium mesh configuration (200, 6, 8).

Table I.2 Mesh sensitivity analysis of S4 shell element

# of elements along Span	# of Elements along Flange width	# of Elements along web height	Total # of elements	Transverse load		Bending moment	
				Transverse displacement (1) (mm)	Normal stress (2) (MPa)	Transverse displacement (1) (mm)	Normal stress (2) (MPa)

150	6	8	7200	107.2	674	51.8	219.1
200	6	8	9600	106.7	668	51.2	218.5
250	6	8	12000	106.2	664	50.9	218.2

(3) At cantilever tip
(4) Peak normal stress at extreme fiber at cantilever root

I.4 Cantilever Under Transverse and Axial Loads

A 5m span cantilever with the reference section defined in section I.2 is subjected to combined transverse and axial loads acting at the tip. The transverse load V is half of the buckling load V_c as determined through a lateral torsional buckling eigenvalue analysis (i.e., $V = V_c/2 = 66\,kN$), and the axial load P is taken has half of the critical buckling load, i.e., $P = P_{crx}/2 = 2400\,kN$, with $P_{crx} = \pi^2 EI_x/4L^2$. The loading is applied incrementally in 10 steps. Twenty elements are used to model the problem. The transverse displacement based on a first order (linear) analysis is $v_{1st} = VL^3/3EI_x = 57.8\,mm$ The transverse displacement, including second-order effects, is governed by the equilibrium condition

$$EI_{xx}v'''' + Pv'' = 0 \tag{I.1}$$

in which $k^2 = P/EI_{xx}$. By imposing the boundary conditions $v(0) = v'(0) = v''(L) = 0$, and $EI_{xx}v'''(L) + Pv'(L) = V$, one obtains $v(z) = \left(V/k^3 EI_{xx}\right)\left[-\tan kL\left(\cos kz - 1\right) + \left(\sin kz - kz\right)\right]$. Also, the stress is given by $\sigma(y,z) = (P/A) + V\left(\tan kL \cos kz - \sin kz\right) y/\left(I_{xx}k\right)$, which yields $\sigma(z = 0, y = 241.9mm) = 563\,MPa$ and $\sigma(z = 5000, y) = 279\,MPa$.

Both linear (L) and nonlinear (N) analyses are performed within the present solution, and the results are compared with those based on the S4 shell model. As illustrated in Fig. I.2(a) and summarized in Table I.3, the transverse displacement predictions of the present model are in close agreement with those of the S4 models, with differences less than 2%. Furthermore, the normal

stresses at the top fiber of the flange edges were evaluated, as shown in Fig. I.2(b), at the beam tip, the stresses derived from the present model closely align with the theoretically expected value, given by $\sigma = P/A = 279\,kNm$.

Table I.3 Nonlinear analysis results for cantilever I-beam under transverse and axial loading

Variable	Present [1]	S4 [2]	%Difference ([2]-[1])/ [2]
$v_{max}\,(mm)$	93.0	93.5	0.52
$\theta_{max}\,(10^{-3}\,rad)$	93.1	93.7	0.64
$\sigma_{max}\,(MPa)$	578	582	0.68

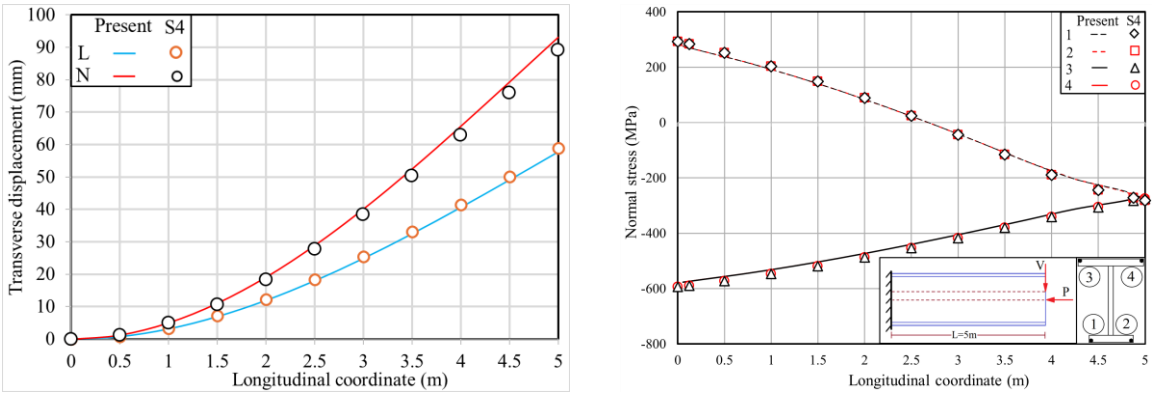

(a) (b)

Fig. I.2 Comparison of results for cantilever under transverse and axial forces (a) Transverse displacement and (b) Longitudinal stresses

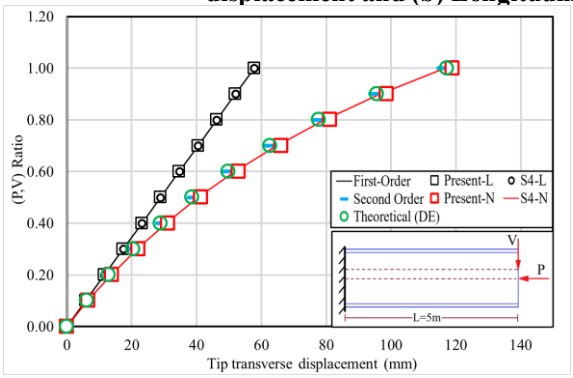

Fig. I.3 Comparison of first and second order displacement predictions for cantilever under transverse and axial forces

I.5 Cantilever Under End Torque

A cantilever of span $L =$ 5m is subjected to a twisting moment T applied at its free end. Cross-sectional dimensions are identical to those of Section I.2 . The angle of twist as given in Appendix D is

$$\theta(z) = (-T/kGJ)\left[\tanh kL\,(1-\cosh kz) + (\sinh kz - kz)\right] \tag{I.2}$$

in which $k = \sqrt{GJ/EI_{\omega\omega}}$. The twisting moment T , as determined by from Eq.(I.2), corresponding to an angle a twist angle of 0.2 radians at the cantilever tip is $T = 1.64\ kNm$. Figure I.4 shows that the tip angle of twist predicted by the present model is 0.201 radians and that based on the S4 model is 0.204 radians, i.e., the prediction of the present is within 2% from that of the S4 model. The peak normal stress at the corners of the flanges of the root as predicted by the present model is 138 MPa. This value compares to 148 MPa as predicted by the S4 element, a 7% difference.

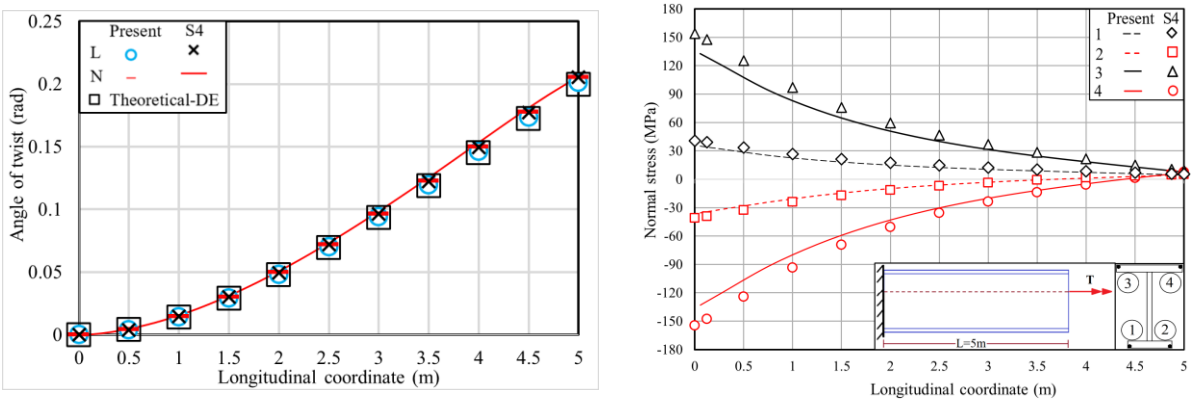

(a) (b)

Fig. I.4 Comparison for results for a cantilever under end twisting moment (a) Angle of twist and (b) Normal stress

I.6 Pin-Roller Member Under Midspan Transverse And Axial Loads

A 6m span simply supported beam is subjected to a combined midspan transverse load V and axial load P applied at its pin support. Cross-sectional dimensions are identical to those given in section

I.2 . Beam ends is restrained transversely and laterally and relative to twist at both ends, and the longitudinal displacement is restricted at one end. The transverse load V is taken as half of the critical load V_c (i.e., $V = V_c/2 = 133\,kN$), where V_c was determined through a lateral torsional bucking eigenvalue analysis, and the axial load P equal is taken as half of the critical load P_c (i.e., $P = P_{crx}/2 = 6540\,kN$), with $P_{crx} = \pi^2 EI_x/L^2$. The loading is applied incrementally in 20 steps. A mesh study showed that convergence was achieved with 20 elements along the beam span.

As illustrated in Fig. I.5(a) and summarized in Table I.4, the present model's transverse displacement predictions are in close agreement with those of the S4 model, with discrepancies of less than 3%. Also, the normal stresses in Fig. I.5(b) at the flange edges agrees with the theoretical stress value $\sigma = P/A = 760\,MPa$.

Fig. I.6 shows that the prediction of the present model of the midspan transverse displacement is in close agreement with the first order (linear) analysis prediction $v_{1st} = VL^3/48EI_x = 12.5\,mm$, as well as the S4 prediction. Furthermore, the nonlinear response prediction of the present model is in close agreement with that of the S4 model.

Table I.4 Nonlinear analysis results for pinned roller beam under transverse and axial load

Variable	Present [1]	S4 [2]	Differences ([2]-[1])/ [2]
$v_{max}\,(mm)$	41.3	42.1	1.9
$\theta_{max}\,(10^{-3}\,rad)$	22.8	22.9	0.44
$\sigma_{max}\,(MPa)$	1307	1346	2.9

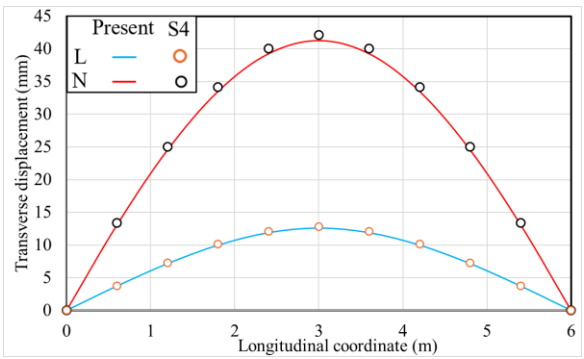

(a)

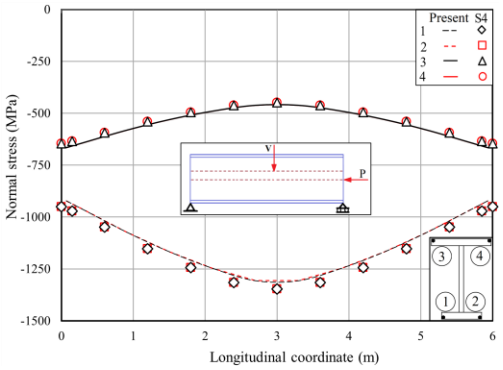

(b)

Fig. I.5 Comparison of results for pin-roller beam subjected to transverse and axial loads (a) Transverse displacement and (b) Normal stresses

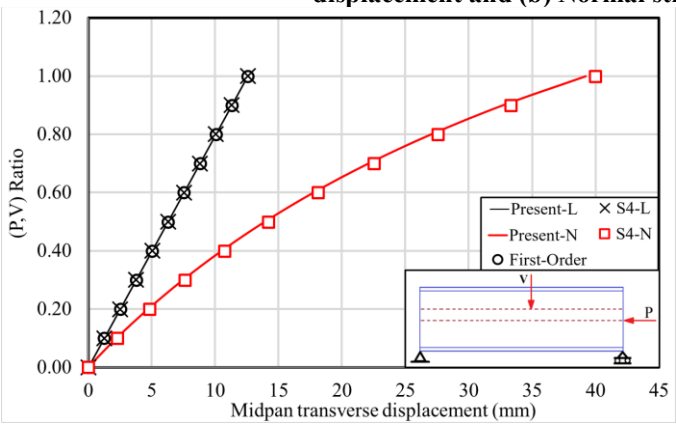

Fig. I.6 Comparison of first and second order midspan displacement predictions for pinned-roller beam cantilever under transverse and axial forces

I.7 Beams with Various End Support Conditions

A 6m span beam is subjected to a midspan transverse point load V acting at the shear center. The member is subjected to a transverse point load V. Two load levels are investigated (1) $V_1 = 100\,kN$ and (2) $V_2 = 500\,kN$. Linear (L) and nonlinear (N) analyses are performed using the present formulation and the S4 shell model. A convergence study indicated that 20 elements are sufficient to achieve convergence. Three types of boundary conditions are investigated as described in the following sub-sections.

I.7.1 Beam Fixed at Both Ends Under Midspan Point Load

Fixed end conditions were modelled in the present and S4 model by restraining all degrees of freedom at both ends Fig. I.7a illustrates the transverse distributions along the longitudinal coordinate of the beam. The present formulation predictions show close agreement with those from S4 model, underscoring the accuracy of the proposed formulation in capturing structural response. Additionally, Fig. I.7b shows that the predicted normal stresses agree with the 4S model predictions.

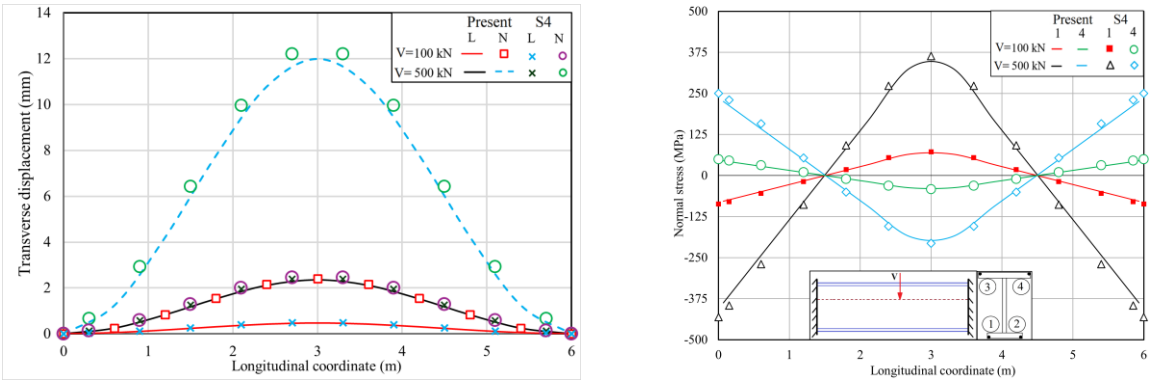

(a) (b)

Fig. I.7 Comparison of results for a beam clamped at both ends: (a) Transverse displacement. and (b) Normal stress.

I.7.2 Beam Pinned at Both Ends Under Midspan Load

In this section, beam ends are restrained relative to transverse, longitudinal, and lateral displacements and angle of twist. Fig. I.8(a) shows close agreement between the predictions of the present and S4 models of the transverse displacement. Additionally, Fig. I.8(b) shows close agreement between predictions of the present and S4 models of the normal stresses.

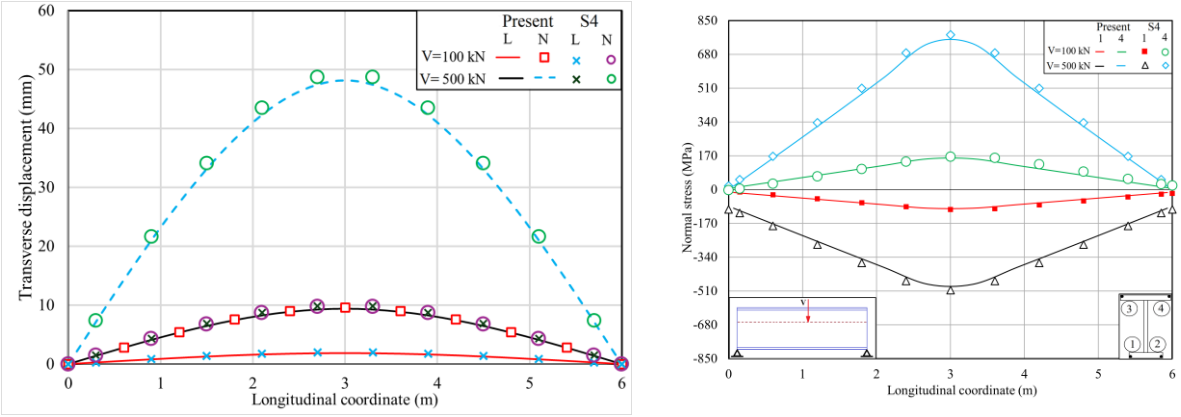

(a) (b)

Fig. I.8 Beam response field distributions along the longitudinal coordinate for pinned-pinned beam: (a) Transverse displacement. and (b) Normal stress.

I.7.3 Pin-Roller Beam Pinned Under Midspan Load

In this section, both ends of the beam are restrained relative to the transverse and lateral displacements and angle of twist, while only the left end is longitudinally restrained. Fig. I.9(a) shows that the predictions of the present model closely match those of the S4 model. Additionally, close agreement is observed between the longitudinal stress predictions of both models Fig. I.9b. Compared to the pin-pin case in Fig. I.8b, the longitudinal stress magnitudes for the present pin-roller case Fig. D.9d are notably larger. This is attributed to the catenary action occurring only in the pin-pin case, which induces additional tensile stress.

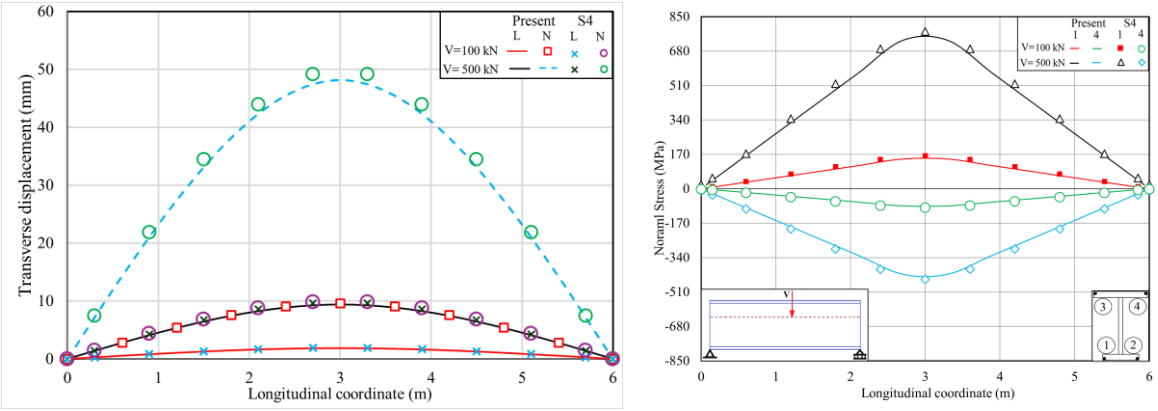

(a) (b)

Fig. I.9 Beam response field distributions along the longitudinal coordinate for pinned-roller beam: (a) Transverse displacement. and (b) Normal stress.

I.8 Conclusion

The previous verification problems have shown that the present model is capable of predicting the response of perfectly straight monosymmetric members under various loading conditions, load combinations, and boundary conditions. In most situations, the model predicted results within 2% compared to shell models and theoretical solutions. An exception was observed for the case of warping stresses induced by a torque acting at the tip of a cantilever. In this case, the present model predictions were within 7% of the shell model predictions.

Appendix J: Residual Stress Distribution in Monosymmetric I-Sections

Past studies have reported residual stresses in both flanges of rolled monosymmetric I section but did not report the residual stress distributions on the web. In this context, this appendix adopts the self-balancing characteristic of residual stresses $\int_A \sigma_r dA = \int_A y\sigma_r dA = 0$ (Fig. J.1) to approximate the residual stress distribution along the web height. The resulting stress pattern forms the basis of the parametric runs conducted in Chapter 4. The residual stresses at the top and bottom junctions of the web are taken to match those of the flanges at the same location and a bilinear residual stress pattern is assumed to occur in between the junctions, leading to two unknowns; (a) the peak compressive residual stress mF_y in the web (Fig. J.2) and it's the height$(d - y_t) - y_g$. The resulting residual stress patterns are subsequently input as initial stresses in the present finite element model and the S4 shell model used for verification in Chapter 4.

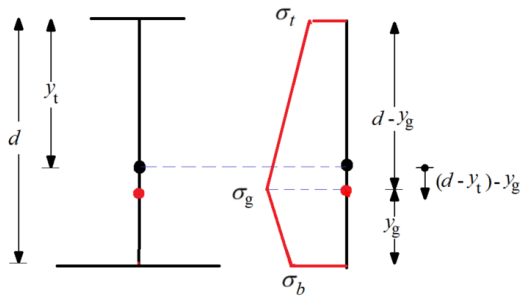

Fig. J.1 Assumed initial residual stresses distribution in monosymmetric section web

J.1 First Self-Balancing Condition

$$\int_A \sigma_r dA = 0 = \int_{A_w} \sigma_r dA = e_w \int_{s_w} \sigma_r ds \qquad \text{(J.1)}$$

$$\frac{1}{2}\left(\sigma_b+\sigma_g\right)y_g+\frac{1}{2}\left(\sigma_t+\sigma_g\right)\left(d-y_g\right)=0$$
$$\sigma_g=-\left[\sigma_b\frac{y_g}{d}+\sigma_t\left(1-\frac{y_g}{d}\right)\right] \tag{J.2}$$

J.2 Second Self-Balancing Condition

$$\int_A\sigma_r y dA=0=\int_{A_w}\sigma_r y dA=e_w\int_{s_w}\sigma_r s ds$$
$$\sigma_t\left(d-y_g\right)\left[\frac{1}{2}\left(d-y_g\right)-\left(d-y_t\right)-y_g\right]+\frac{1}{2}\left(\sigma_g-\sigma_t\right)\left(d-y_g\right)\left[\frac{1}{3}\left(d-y_g\right)-\left(d-y_t\right)-y_g\right] \tag{J.3}$$
$$-\sigma_b y_g\left(\frac{1}{2}y_g+\left(d-y_t\right)-y_g\right)-\frac{1}{2}\left(\sigma_g-\sigma_b\right)y_g\left(\frac{1}{3}y_g+\left(d-y_t\right)-y_g\right)$$

For the reference section, we have $\left(b_b,b_t,e_f,d,e_w\right)=\left(300,150,16.0,400,10.0\right)mm$ and $y_t=242.9mm$, $F_y=350MPa$, $\sigma_b=0.3F_y$, $\sigma_a=0.15F_y$. Solving Eq. (J.2) and Eq. (J.3) one obtains $\sigma_g=-70.0\,MPa$ and $y_g=133.3\,mm$. The residual stress pattern is depicted in Fig. J.2.

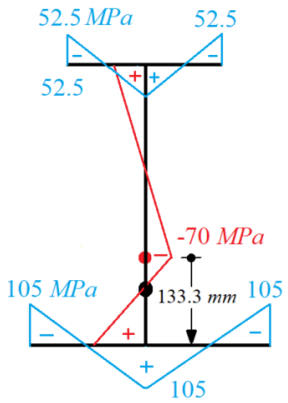

Fig. J.2 The residual stress distribution in monosymmetric section

Appendix K: Threshold Span for Monosymmetric I-Beam

This appendix determines the threshold span used in Chapter 4, to delineate the elastic LTB region from the inelastic LTB region. The procedure incorporates the effects of section monosymmetric and residual stresses, and compares results with those obtained from the Canadian standards [4.1] and the American specifications [4.2]. Fig. K.1 depicts the geometric parameters and sign conventions of the reference monosymmetric section in Chapter 4.

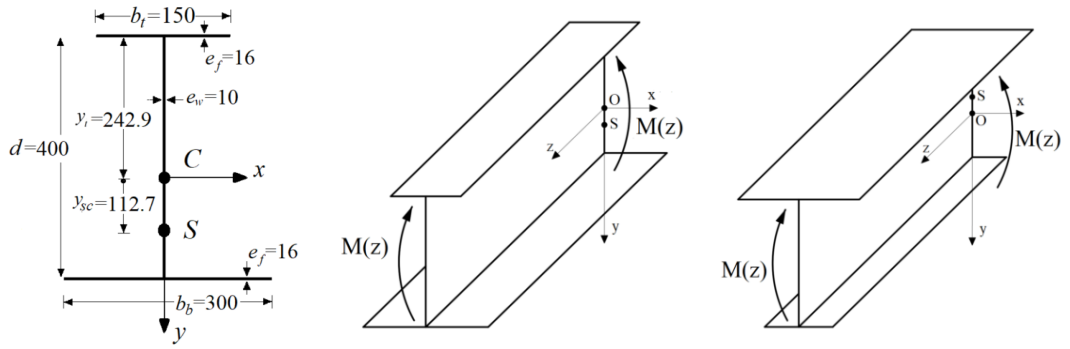

(a) (b) (c)

Fig. K.1 Monosymmetric section (a) Dimensions and notation (b) Smaller flange in compression and sign convention for axes and moments, (c) Larger flange in compression.

The member ends are restrained against twist, transverse and lateral displacements at both ends, and a longitudinal restraint is provided at one end is i.e., $\zeta(0)=\xi(0)=\eta(0)=\theta(0)$ and $\xi(L)=\eta(L)=\theta(L)=0$. Top flange dimensions are $b_t \times e_f = 150\times 16.0mm$ and bottom flange dimensions are $b_b \times e_f = 300\times 16.0mm$. The distance between flange centroids is $d = 400\,mm$ and the web thickness is $e_w = 10.0\,mm$. The distance from the top flange to the section centroid is $y_t = 242.9\,mm$. The coordinate of the shear center relative to the s centroid is $y_{sc} = 112.7mm$. Sectional properties are $I_x = 3.21\times 10^8\,mm^4$, $I_y = 4.06\times 10^7\,mm^4$, $C_\omega = 6.42\times 10^{11}\,mm^6$,

$J = 7.48\times10^5\,mm^4$, $Z_x = 1.76\times10^6\,mm^3$. The monosymmetric parameter β_x for an I-section with unequal flanges is given by

$$\begin{aligned}\beta_x &= \int_A y\left(x^2+y^2\right)dA/I_x - 2y_{sc}\\ &= \frac{1}{I_x}\left[\left(d-y_t\right)\left(\frac{b_b^3 e_f}{12}+be_f\left(d-y_t\right)^2+\frac{e_w}{4}\left(d-y_t\right)^3\right)-y_t\left(\frac{b_t^3 e_f}{12}+b_t e_f y_t^{\,2}+\frac{e_w}{4}y_t^{\,3}\right)\right]-2y_{sc}\end{aligned} \tag{K.1}$$

When the small flange is on top, the positive moments shown in Fig. K1.c induce compression in it and β_x takes the value

$$\begin{aligned}\beta_x = \frac{1}{3.21\times10^8}\Bigg[&157.1\times\left(\frac{300^3\times16}{12}+300\times16\times157.1^2+\frac{10}{4}\times157.1^3\right)\\ &-242.9\times\left(\frac{150^3\times16}{12}+150\times16\times242.9^2+\frac{10}{4}\times242.9^3\right)\Bigg]-2\times112.6=-282mm\end{aligned}$$

When the large flange is on top, the positive moments shown in Fig. K1.b induce compression in it and β_x takes the value

$$\begin{aligned}\beta_x = \frac{1}{3.21\times10^8}\Bigg[&242.9\times\left(\frac{150^3\times16}{12}+150\times16\times242.9^2+\frac{10}{4}\times242.9^3\right)\\ &-157.1\times\left(\frac{300^3\times16}{12}+300\times16\times157.1^2+\frac{10}{4}\times157.1^3\right)\Bigg]-2\times\left(-112.6\right)=282mm\end{aligned}$$

Steel properties are taken as $E = 200\,GPa$ and $G = 77.0\,GPa$. The section is assumed to have the residual stress profile shown in Fig. K.2, i.e., the compressive residual stresses at the tips of the top flange are $\alpha_1 F_y$ while those at the tips of the bottom flange are $\alpha_2 F_y$. The residual stress pattern is taken to conform to that reported in [4.24], with a peak compressive stress of $\alpha_1 = 0.3$ and

$\alpha_2 = 0.3 b_s / b_l$ which corresponds to $\alpha_2 = 0.15$ for the given cross-section. A bilinear residual stress distribution is assumed to take place on the web, i.e., the peak stress in the web is $-\alpha_3 F_y$ and is located at a distance y_3 from the bottom flange, in which α_3, y_3 are determined from the self-equilibrating conditions $\int_A \sigma_r dA = \int_A y\sigma_r dA = 0$ as detailed in Appendix J, which yields the values $\alpha_3 = 0.2, y_3 = 133.3\,mm$

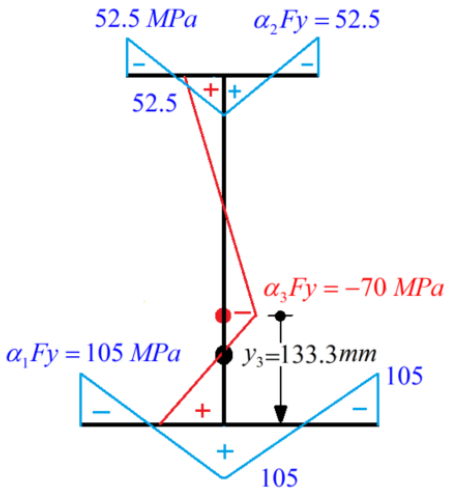

Fig. K.2 Residual stress assumed in the present study

The elastic section moduli S_{x1} , S_{x2} related to the small and large flanges, respectively, are

$$S_{x1} = I_x / y_t = 3.21\times10^8 / 242.9 = 1.32\times10^6\,mm^3$$
$$S_{x2} = I_x / (d - y_t) = 3.21\times10^8 / 157.1 = 2.04\times10^6\,mm^3 \quad \text{(K.2)}$$

When the loads are applied at cross-section mid-height, the elastic critical moment for a monosymmetric beam under Canadian standards [4.1] is given by

$$M_{cr} = C_b \frac{\pi^2 EI_y}{2L^2}\left[\beta_x + \sqrt{\beta_x^2 + 4\left(\frac{GJL^2}{\pi^2 EI_y} + \frac{C_\omega}{I_y}\right)}\right] \quad \text{(K.3)}$$

K.1 Threshold Span

The threshold span L_{tc} at which the elastic critical moment causes the top flange to attain the first yield in compression is obtained by equating the elastic lateral buckling M_{cr} to $S_{x1}F_y\left(1-\alpha_1\right)$ when the smaller flange is on top and equating M_{cr} to $S_{x2}F_y\left(1-\alpha_2\right)$

For the case where the small flange is on top, one has

$$\frac{C_b\pi^2 EI_y}{2L_{tc}^{\ 2}}\left[\beta_x+\sqrt{\beta_x^{\ 2}+4\left(\frac{GJL_{tc}^{\ 2}}{\pi^2 EI_y}+\frac{C_\omega}{I_y}\right)}\right]=S_{x1}F_y\left(1-\alpha_1\right) \tag{K.4}$$

Equation (K.4)**Error! Reference source not found.** can be expressed as

$$\begin{aligned}\sqrt{\beta_x^{\ 2}+4\left(\frac{GJL_{tc}^{\ 2}}{\pi^2 EI_y}+\frac{C_\omega}{I_y}\right)}&=\frac{2S_{x1}F_y\left(1-\alpha_1\right)}{C_b\pi^2 EI_y}L_{tc}^{\ 2}-\beta_x\\ \beta_x^{\ 2}+4\left(\frac{GJL_{tc}^{\ 2}}{\pi^2 EI_y}+\frac{C_\omega}{I_y}\right)&=\left(\frac{2S_{x1}F_y\left(1-\alpha_1\right)}{C_b\pi^2 EI_y}L_{tc}^{\ 2}-\beta_x\right)^2\end{aligned} \tag{K.5}$$

or

$$\left(\beta_x^{\ 2}+4\frac{C_\omega}{I_y}\right)+4\left(\frac{GJ}{\pi^2 EI_y}\right)L_{tc}^{\ 2}=\left[\frac{2S_{x1}F_y\left(1-\alpha_1\right)}{C_b\pi^2 EI_y}\right]^2 L_{tc}^{\ 4}-4\frac{S_{x1}F_y\left(1-\alpha_1\right)\beta_x}{C_b\pi^2 EI_y}L_{tc}^{\ 2}+\beta_x^{\ 2} \tag{K.6}$$ (O.1)

which yields

$$\left[\frac{2S_{x1}F_y\left(1-\alpha_1\right)}{C_b\pi^2 EI_y}\right]^2 L_{tc}^{\ 4}-\left(\frac{4S_{x1}F_y\left(1-\alpha_1\right)}{C_b\pi^2 EI_y}\beta_x+\frac{4GJ}{\pi^2 EI_y}\right)L_{tc}^{\ 2}-4\frac{C_\omega}{I_y}=0 \tag{K.7}$$

or

$$P^2 L_{tc}^{\ 4} - \left(2P\beta_x + Q\right) L_{tc}^{\ 2} - R = 0 \tag{K.8}$$

in which

$$P = \frac{2S_{x1}F_y\left(1-\alpha_1\right)}{C_b\pi^2 EI_y}, Q = \frac{4GJ}{\pi^2 EI_y}, R = 4\frac{C_\omega}{I_y} \tag{K.9)a-c}$$

By solving for the threshold span, one obtains

$$L_{tc} = \frac{\sqrt{2P\beta_x + Q + \sqrt{\left(2P\beta_x + Q\right)^2 + 4P^2 R}}}{\sqrt{2}P} \tag{K.10}$$

When the larger flange is on top, Eq. (K.10) a remains valid after modifying Eq. (K.9) to

$$P = \frac{2S_{x2}F_y\left(1-\alpha_2\right)}{C_b\pi^2 EI_y}$$

In the above equations, the moment gradient factors are $C_b = 1.00, C_b = 1.13$ and $C_b = 1.35$ for UM, UD and PL under the Canadian Standard. In contrast, under the American Specifications, the moment gradient factor C_b is taken as unity for all loading cases when computing the threshold span L_t. The threshold spans can be determined using Eq. (K.10) for the following cases:

1- Case 1: Small flange on top (Fig. K.1b) $\beta_x = -282mm$, $\alpha_2 = 0.15$ and $S_{x2} = 2.04\times10^6 mm^3$

Standards	AISC L_t	CSA-16 L_{tc}		
		UM	UD	PL
Span threshold	4.10	4.10	4.50	5.30

*All spans in the table are in meters

2- Case 2: Large flange on top (Fig. K.1c) $\beta_x = 282mm$, $\alpha_1 = 0.30$ and $S_{x1} = 1.32\times10^6 mm^3$

Standards	ASIC L_t	CSA-16 L_{tc}		
		UM	UD	PL
Span threshold	10.90	10.90	11.50	13.30

*All spans in the table are in meters

Appendix L: Lateral Torsional Buckling Resistance for Monosymmetric Beams in Eurocode 3 and AS4100

This appendix provides the steps for calculating of the lateral-torsional buckling (LTB) resistance for a monosymmetric beam, in accordance with Eurocode 3 [4.3] and Australian standards [4.4]. The procedure covers classification, evaluation of the elastic critical moment, determination of slenderness and reduction factors, and the determination of the moment resistance.

L.1 Problem Definition

A simply supported beam with a large flange width and thickness of $b_2 = 300\,mm$ and $t_2 = 16.0\,mm$, small flange width and thickness of $b_1 = 150\,mm$ and $t_1 = 16.0\,mm$, a web height of $h = 400\,mm$, and a thickness of $t_w = 10.0\,mm$ as presented in Fig. L.1a. The member has a $9\,m$ span and is subjected to a uniform moment (UM) acting at the section centroid. Steel Young's modulus is $E = 2\times10^5\ MPa$, and the shear modulus is $G = 7.7\times10^4\ MPa$, and the yield strength is F_y=350 MPa. Sectional Properties are $I_x = 3.26\times10^8\,mm^4$, $I_y = 4.06\times10^7\,mm^4$, $C_\omega = 6.42\times10^{11}\,mm^6$, $J = 7.48\times10^5\,mm^4$, $Z_x = 1.76\times10^6\,mm^3$. It is required to determine the flexural resistance of the member in accordance with Eurocode 3 [4.3] and the Australian standards [4.4]. The elastic section moduli S_{x1} , S_{x2} related to the top and bottom flanges, respectively, are

$$\begin{aligned} S_{x1} &= I_x / y_1 = 3.26\times10^8 / 242.9 = 1.34\times10^6\,mm^3 \\ S_{x2} &= I_x / y_2 = 3.26\times10^8 / 157.1 = 2.08\times10^6\,mm^3 \end{aligned} \tag{L.1}$$

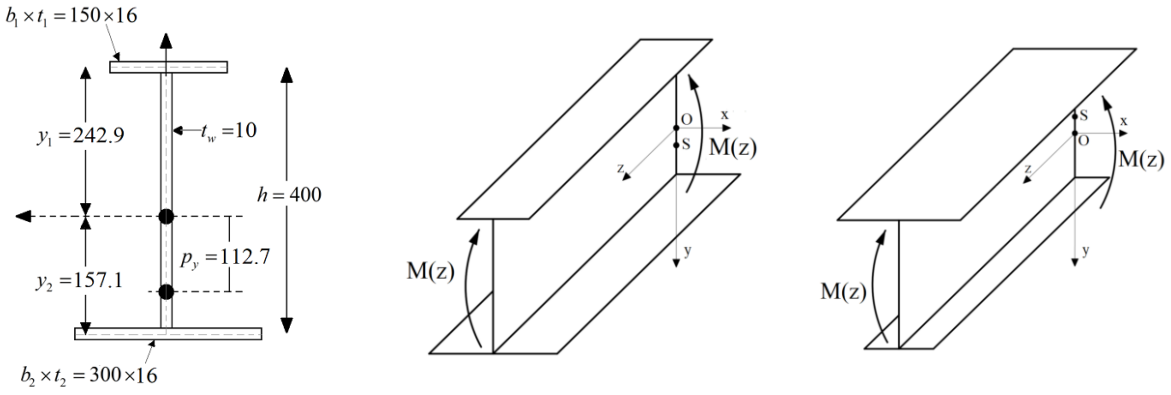

(a) (b) (c)

Fig. L.1 Monosymmetric section (a) Dimensions and notation (b) Sign convention for axes and moments - smaller flange in compression, (c) Larger flange in compression.

The monosymmetric parameter β_x for an I-section with unequal flanges is given by

$$\begin{aligned}\beta_x &= \int_A y\left(x^2+y^2\right)dA/I_x - 2p_y \\ &= \frac{1}{I_x}\left[y_2\left(\frac{b_2^3 t_2}{12} + b_2 t_2 {y_2}^2 + \frac{t_w}{4}{y_2}^3\right) - y_1\left(\frac{b_1^3 t_1}{12} + b_1 t_1 {y_1}^2 + \frac{t_w}{4}{y_1}^3\right)\right] - 2p_y\end{aligned} \tag{L.2}$$

By substituting for the section dimensions, one obtains

1- Case 1: For a small flange on top $\beta_x(-)$

$$\beta_x = \frac{1}{3.26\times10^8}\left[157.1\times\left(\frac{300^3\times16}{12} + 300\times16\times157.1^2 + \frac{10}{4}\times157.1^3\right)\right.$$
$$\left. -242.9\times\left(\frac{150^3\times16}{12} + 150\times16\times242.9^2 + \frac{10}{4}\times242.9^3\right)\right] - 2\times112.7 = -282\,mm$$

2- Case 2: For a large flange on top $\beta_x(+)$

$$\beta_x = \frac{1}{3.26\times10^8}\left[242.9\times\left(\frac{150^3\times16}{12} + 150\times16\times242.9^2 + \frac{10}{4}\times242.9^3\right)\right.$$
$$\left. -157.1\times\left(\frac{300^3\times16}{12} + 300\times16\times157.1^2 + \frac{10}{4}\times157.1^3\right)\right] - 2\times(-112.7) = 282\,mm$$

L.2 Eurocode 3 Procedure for LTB Resistance

1- Classification

Material parameter (Cl. 5.2.5(2)) $\varepsilon = \sqrt{235/F_y} = \sqrt{235/350} = 0.819$

Web: Class 2 requirement for the web (Tables 7.3) $d/w \le 83\varepsilon$

$d / w = \left(416 - 16.0\right)/10.0 = 40.0 \le 83\varepsilon = 83\sqrt{235/350} = 68.0$

Thus, web meets the class 2 requirement

Flange: Class 3 classification requirement for the flange (Table 7.4) $b/t \le 14\varepsilon$

$b / t = \left(300 - 10.0\right)/\left(2 \times 16.0\right) = 9.1 \le 14\sqrt{235/350} = 11.5$

$b / t = \left(150 - 10.0\right)/\left(2 \times 16.0\right) = 4.4 \le 14\sqrt{235/350} = 11.5$

Large and small flanges meet Class 3 requirements

Section: Thus, the Section meets Class 3 requirements.

L.2.1 Eurocode 3 Procedure for LTB Resistance - Small Flange on Top

2- Characteristic Bending Resistance

The characteristic bending resistance (Cl. 8.2.26), for a class 3 section, is

$$M_y = S_{x1} F_y = 1.34 \times 10^6 \times 350 \times 10^{-6} = 469\, kNm \qquad \text{(L.3)}$$

3- Elastic critical moment for lateral torsional buckling

NCCI (2005) does not provide an expression for the elastic critical moment of monosymmetric sections; therefore, finite element analysis was performed to obtain the M_{cr}. Using the BG program developed by [4.31] for the beam span of 9m, case 1, Fig. L.1b, the elastic critical moment $M_{cr} = 163.7\,kNm$.

4- Slenderness parameter for lateral torsional buckling

According to Clause 8.3.2.2 of [4.3], the slenderness parameter for LTB is given by

$$\lambda_{LT} = \sqrt{M_y / M_{cr}} = \sqrt{469/163.7} = 1.70 \qquad \text{(L.4)}$$

5- Calculate ϕ_{LT} factor

Clause 8.3.2.3 of EN-1993-1-1-22 gives

$$\phi_{LT} = 0.5\left[1 + \alpha_{LT}\left(\bar{\lambda}_{LT} - 0.2\right) + \bar{\lambda}_{LT}{}^2\right] \qquad \text{(L.5)}$$

The imperfection factor α_{LT} for a monosymmetric is obtained from Table 8.4. For $h/b_{\min} > 2.0$ use lateral torsional buckling curve (b)

$$\alpha_{LT} = 0.34, \qquad \text{(L.6)}$$

From Eqs. (L.4) and (L.6), by substituting into Eq. (L.5), one obtains

$$\phi_{LT} = 0.5\left[1 + 0.34\left(1.70 - 0.20\right) + \left(1.70\right)^2\right] = 2.20 \qquad \text{(L.7)}$$

6- Reduction factor

Clause 8.3.2.3 of EN-1993-1-1-22 gives

$$\chi = 1\Big/\left(\phi_{LT} + \sqrt{\phi_{LT}{}^2 - \bar{\lambda}_{LT}{}^2}\right) \le 1.0 \qquad \text{(L.8)}$$

From Eqs. (L.7) and (L.4), by substituting into Eq.(L.8) one obtains

$$\chi = 1.0 \Big/ \left(2.20 + \sqrt{2.20^2 - \left(1.70\right)^2} \right) = 0.28 \qquad \text{(L.9)}$$

7- Nominal lateral torsional buckling resistance

According to Clause 8.3.2.1 of [4.3] is

$$M_r = \chi \frac{M_y}{\gamma_{M1}} \qquad \text{(L.10)}$$

The nominal flexural resistance is obtained by setting the partial safety factor to $\gamma_{M1} = 1.0$. From Eqs. (L.3) and (L.8), the lateral torsional buckling resistance is

$$M_r = 0.28 \times \frac{469}{1} = 131.3\, kNm$$

which corresponds to the moment ratio

$$\frac{M_r}{M_{cr}} = \frac{131.3}{163.7} = 0.80 \qquad \text{(L.11)}$$

L.2.2 Eurocode 3 Procedure for LTB Resistance - Large Flange on Top

1- Characteristic Bending Resistance

The characteristic bending resistance (Cl. 8.2.26), for a class 3 section is

$$M_y = S_{x1} F_y = 1.34 \times 10^6 \times 350 \times 10^{-6} = 469\, kNm \qquad \text{(L.12)}$$

2- Elastic critical moment for lateral torsional buckling

Using the BG program developed by [4.31] for the beam span of 9m, case 2, Fig. L.1c the elastic critical moment $M_{cr} = 442.2\,kNm$.

3- Slenderness parameter for lateral torsional buckling

According to Clause 8.3.2.2 of [4.3], the slenderness parameter of LTB is given by

$$\lambda_{LT} = \sqrt{M_y / M_{cr}} = \sqrt{469/442.2} = 1.03 \tag{L.13}$$

4- Calculate ϕ_{LT} factor

Clause 8.3.2.3 [4.3] gives

$$\phi_{LT} = 0.5\left[1 + 0.34\left(1.03 - 0.20\right) + \left(1.03\right)^2\right] = 1.17 \tag{L.14}$$

5- Reduction factor

Clause 8.3.2.3 of EN-1993-1-1-22 gives

$$\chi = 1.0 \Big/ \left(1.17 + \sqrt{1.17^2 - \left(1.03\right)^2}\right) = 0.58 \tag{L.15}$$

6- Design lateral torsional buckling resistance

According to Clause 8.3.2.1 of [4.3] is

$$M_r = 0.58 \times \frac{469}{1} = 272\,kNm$$

which corresponds to the moment ratio

$$\frac{M_r}{M_{cr}} = \frac{272}{442.8} = 0.61 \tag{L.16}$$

L.2.3 Proposed Modification for Eurocode 3 LTB Resistance Large Flange on Top

1- Characteristic Bending Resistance

The characteristic bending resistance (Cl. 8.2.26), for a class 3 section, is

$$M_y = S_{x2} F_y = 2.08 \times 10^6 \times 350 \times 10^{-6} = 728\, kNm \tag{L.17}$$

2- Elastic critical moment for lateral torsional buckling

Using the BG program developed by [4.31] for the beam span of 9m, case 2 Fig. L.1c the elastic critical moment $M_{cr} = 442.2\, kNm$.

3- Slenderness parameter for lateral torsional buckling

According to Clause 8.3.2.2 of [4.3], the slenderness parameter of LTB is given by

$$\lambda_{LT} = \sqrt{M_y / M_{cr}} = \sqrt{728/442.2} = 1.28 \tag{L.18}$$

4- Calculate ϕ_{LT} factor

Clause 8.3.2.3 (EN-1993-1-1-22) gives

$$\phi_{LT} = 0.5\left[1 + 0.34\left(1.28 - 0.20\right) + \left(1.28\right)^2\right] = 1.50 \tag{L.19}$$

5- Reduction factor

Clause 8.3.2.3 of [4.3] gives

$$\chi = 1.0 \Big/ \left(1.50 + \sqrt{1.50^2 - \left(1.28\right)^2}\right) = 0.44 \tag{L.20}$$

6- Design lateral torsional buckling resistance

According to Clause 8.3.2.1 of [4.3] is

$$M_r = 0.44 \times \frac{728}{1} = 320.32\, kNm$$

which corresponds to the moment ratio

$$\frac{M_r}{M_{cr}} = \frac{320.32}{442.2} = 0.72 \qquad \text{(L.21)}$$

L.3 Australian Standard AS 4100:2020

L.3.1 Australian Standard - Small Flange on Top

1- Section slenderness

Flange:

Flange slenderness [4.4] (Clause 5.2.2):

$$\lambda_{e,f} = \left(\frac{b}{t}\right)\sqrt{\left(\frac{F_y}{250}\right)} = \frac{300.10}{2 \times 16}\sqrt{\frac{350}{250}} = 10.7 \quad \text{Large flange}$$

$$\lambda_{e,f} = \left(\frac{b_1}{t}\right)\sqrt{\left(\frac{F_y}{250}\right)} = \frac{150 - 10}{2 \times 16}\sqrt{\frac{350}{250}} = 5.18 \quad \text{Small flange}$$

Yield classification limit for flanges of rolled section is $\lambda_{ey,f} = 16.0$ (Table 5.2).

Plastic classification limit for flanges of rolled section is $\lambda_{ep,f} = 9.0$ (Table 5.2).

$$\frac{\lambda_{e,f}}{\lambda_{ey,f}} = \frac{10.7}{16.0} = 0.67 \quad \text{Large flange}$$

$$\frac{\lambda_{e,f}}{\lambda_{ey,f}} = \frac{5.18}{16.0} = 0.32 \quad \text{Small flange}$$

Web:

Web slenderness [4.4] (Clause 5.2.2)

$$\lambda_{e,w} = \left(\frac{d}{w}\right)\sqrt{\left(\frac{F_y}{250}\right)} = \frac{(416 - 2\times 16.0)}{10}\sqrt{\left(\frac{350}{250}\right)} = 45.4$$

Yield classification limit for the web of rolled section is $\lambda_{ey,w} = 115$ (Table 5.2)

Plastic classification limit for the web of rolled section is $\lambda_{ep,w} = 82$ (Table 5.2)

$$\frac{\lambda_{e,w}}{\lambda_{ey,w}} = \frac{45.4}{115} = 0.40$$

Section:

Section plasticity slenderness limit λ_{sp} and yield slenderness limit λ_{sy} are those of the element

with the larger λ_e / λ_{ey} (i.e., flange in this case). Thus,

Section plasticity slenderness limit $\lambda_{sp} = \lambda_{ep,w} = 9.0$

Section yields slenderness limit $\lambda_{sy} = \lambda_{e,w} = 16.0$

The limits λ_{sp} and λ_{sy} will be used to determine the effective section modulus Z_e for the section.

2- Effective section modulus Z_e

The effective section modulus Z_e for compact sections [4.4] (Cl. 5.2.3), non-compact sections (Cl. 5.2.4) and slender sections (Cl. 5.2.5) are summarized as

$$Z_e = S_x + \begin{cases} \dfrac{(\lambda_{sy} - \lambda_s)}{(\lambda_{sy} - \lambda_{sp})}\left[\min(Z_x, 1.5S_x) - S_x\right] \end{cases} \quad \begin{matrix} \min(Z_x, 1.5S_x) & \lambda_s \le \lambda_{sp} & \text{compact} \\ & \lambda_{sp} < \lambda_s \le \lambda_{sy} & \text{non-compact} \\ S_x(\lambda_{sy}/\lambda_e)^2 & \lambda_{sy} < \lambda_s & \text{slenderness} \end{matrix} \tag{L.22}$$

For the present section, we have $\lambda_{sp} < \lambda_s \le \lambda_{sy} \Rightarrow 9.0 < 14.8 \le 16$

Thus, section is non-compact, and its effective section modulus is

$$Z_e = 1.34\times10^6 + \left\{\frac{(16.0-10.7)}{(16.0-9.0)}\left[1.76\times10^6 - 1.34\times10^6\right]\right\} = 1.66\times10^6\ mm^3$$

in which $\left[\min(Z_x, 1.5S_x)\right] = \left[\min(1.76\times10^6, 1.5\times1.34\times10^6)\right] = 1.76\times10^6\ mm^3$

3- Nominal section moment capacity

The nominal section moment capacity [4.4] (Cl. 5.2.1) is given by

$$M_s = Z_e F_y = 1.66\times10^6 \times 350\times10^{-6} = 581\,kNm \tag{L.23}$$

4- Reference Buckling Moment

The reference buckling moment M_0 [4.4] (Cl. 5.6.1.1(3)) is

$$M_0 = \frac{\pi^2 EI_y}{L^2}\left[\frac{\beta_x}{2} + \sqrt{\left(\frac{\beta_x}{2}\right)^2 + \left(\frac{GJL^2}{\pi^2 EI_y} + \frac{C_\omega}{I_y}\right)}\right] \tag{L.24}$$

$$M_0 = \frac{\pi^2\times200\times10^3\times4.06\times10^7}{9000^2}\left[\frac{-282}{2} + \sqrt{\left(\frac{-282}{2}\right)^2 + \left(\frac{77\times10^3\times7.48\times10^5\times9000^2}{\pi^2\times200\times10^3\times4.06\times10^7} + \frac{6.42\times10^{11}}{4.06\times10^7}\right)}\right]$$

$$M_0 = 163.7\,kNm$$

5- Elastic critical moment

For the case of uniform moment, the elastic critical moment is given by

$$M_{cr} = CM_0 = 1.00 \times 163.7 = 163.7\,kNm \tag{L.25}$$

6- Slenderness reduction factor

The slenderness reduction factor α_s [4.4] (Cl. 5.6.1.1(2)) is

$$\alpha_s = 0.6\left[\sqrt{\left(M_s/M_0\right)^2 + 3} - \left(M_s/M_0\right)\right] \tag{L.26}$$

From Eqs.(L.23) and (L.24), by substituting into Eq. (L.26), one obtains

$$\alpha_s = 0.6\left[\sqrt{\left(581/163.7\right)^2 + 3} - \left(581/163.7\right)\right] = 0.24$$

7- Nominal member moment capacity

The nominal member moment capacity [4.4] (Cl. 5.6.1.1(1)) is

$$M_r = C\,\alpha_s\,M_s \le M_P \tag{L.27}$$

From Eqs. (L.23) and (L.26), by substituting into Eq. (L.27) one obtains the nominal member moment capacity

$$M_r = 1.0 \times 0.24 \times 581 = 139.4\,kNm \le 581\,kNm$$

which corresponds to a moment ratio

$$\frac{M_r}{M_{cr}} = \frac{139.4}{163.7} = 0.85$$

L.3.2 Australian Standard AS 4100:2020 - Large Flange on Top

1- Effective section modulus Z_e

The effective section modulus Z_e for compact sections [4.4] (Cl. 5.2.3), non-compact sections (Cl. 5.2.4) and slender sections (Cl. 5.2.5) are summarized as

$$Z_e = S_x + \begin{cases} \dfrac{\left(\lambda_{sy}-\lambda_s\right)}{\left(\lambda_{sy}-\lambda_{sp}\right)}\left[\min\left(Z_x, 1.5S_x\right) - S_x\right] \end{cases} \quad \begin{matrix} \min\left(Z_x, 1.5S_x\right) & \lambda_s \le \lambda_{sp} & \text{compact} \\ & \lambda_{sp} < \lambda_s \le \lambda_{sy} & \text{non-compact} \\ S_x\left(\lambda_{sy}/\lambda_e\right)^2 & \lambda_{sy} < \lambda_s & \text{slenderness} \end{matrix} \tag{L.28}$$

For the present section, we have $\lambda_{sp} < \lambda_s \le \lambda_{sy} \Rightarrow 9.0 < 14.8 \le 16$

Thus, the section is non-compact, and its effective section modulus is

$$Z_e = 1.34\times10^6 + \left\{\frac{(16.0-10.7)}{(16.0-9.0)}\left[1.76\times10^6 - 1.34\times10^6\right]\right\} = 1.66\times10^6\ mm^3$$

in which

$$\left[\min\left(Z_x, 1.5S_x\right)\right] = \left[\min\left(1.76\times10^6, 1.5\times1.34\times10^6\right)\right] = 1.76\times10^6\ mm^3$$

2- Nominal section moment capacity

The nominal section moment capacity [4.4] (Cl. 5.2.1) is given by

$$M_s = Z_e F_y = 1.66\times10^6 \times 350\times10^{-6} = 581 kNm \tag{L.29}$$

3- Reference Buckling Moment

$$M_0 = \frac{\pi^2 \times 200 \times 10^3 \times 4.06 \times 10^7}{9000^2}\left[\frac{282}{2} + \sqrt{\left(\frac{282}{2}\right)^2 + \left(\frac{77 \times 10^3 \times 7.48 \times 10^5 \times 9000^2}{\pi^2 \times 200 \times 10^3 \times 4.06 \times 10^7} + \frac{6.42 \times 10^{11}}{4.06 \times 10^7}\right)}\right]$$

$$M_0 = 442.2\,kNm$$

4- Elastic critical moment

For the case of uniform moment, the elastic critical moment is given by

$$M_{cr} = CM_0 = 1.00 \times 442.2 = 442.2\,kNm \qquad \text{(L.30)}$$

5- Slenderness reduction factor

The slenderness reduction factor α_s (Cl. 5.6.1.1(2)) is

$$\alpha_s = 0.6\left[\sqrt{(581/442.2)^2 + 3} - (581/442.2)\right] = 0.52$$

6- Nominal member moment capacity

The nominal member moment capacity [4.4] (Cl. 5.6.1.1(1)) is

$$M_r = 1.0 \times 0.52 \times 481 = 250\,kNm \le 581\,kNm$$

which corresponds to a moment ratio

$$\frac{M_r}{M_{cr}} = \frac{250}{442.2} = 0.57$$

L.3.3 Proposed Modification for AS 4100 LTB Resistance - Large Flange on Top

1- Effective section modulus Z_e

The effective section modulus Z_e for compact sections (Cl. 5.2.3), non-compact sections (Cl. 5.2.4) and slender sections (Cl. 5.2.5) are summarized as

$$Z_e = S_x + \begin{cases} \min\left(Z_x, 1.5S_x\right) & \lambda_s \le \lambda_{sp} \quad \text{compact} \\ \dfrac{\left(\lambda_{sy} - \lambda_s\right)}{\left(\lambda_{sy} - \lambda_{sp}\right)}\left[\min\left(Z_x, 1.5S_x\right) - S_x\right] & \lambda_{sp} < \lambda_s \le \lambda_{sy} \quad \text{non-compact} \\ S_x\left(\lambda_{sy}/\lambda_e\right)^2 & \lambda_{sy} < \lambda_s \quad \text{slenderness} \end{cases} \qquad \text{(L.31)}$$

For the present section, we have $\lambda_{sp} < \lambda_s \le \lambda_{sy} \Rightarrow 9.0 < 14.8 \le 16$

Thus, the section is non-compact, and its effective section modulus is

$$Z_e = 2.08\times10^6 + \left\{\frac{(16.0-10.7)}{(16.0-9.0)}\left[1.76\times10^6 - 2.08\times10^6\right]\right\} = 1.84\times10^6\ mm^3$$

in which $\left[\min\left(Z_x, 1.5S_x\right)\right] = \left[\min\left(1.76\times10^6, 1.5\times2.08\times10^6\right)\right] = 1.76\times10^6\ mm^3$

$Z_e \ge Z_x$ therefore $Z_e = Z_x = 1.76\times10^6\ mm^3$

2- Nominal section moment capacity

The nominal section moment capacity [4.4] (Cl. 5.2.1) is given by

$$M_s = Z_e F_y = 1.76\times10^6 \times 350\times10^{-6} = 616\,kNm \qquad \text{(L.32)}$$

3- Reference Buckling Moment

$$M_0 = \frac{\pi^2\times200\times10^3\times4.06\times10^7}{9000^2}\left[\frac{282}{2} + \sqrt{\left(\frac{282}{2}\right)^2 + \left(\frac{77\times10^3\times7.48\times10^5\times9000^2}{\pi^2\times200\times10^3\times4.06\times10^7} + \frac{6.42\times10^{11}}{4.06\times10^7}\right)}\right]$$

$M_0 = 442.2\,kNm$

4- Elastic critical moment

For the case of uniform moment, the elastic critical moment is given by

$$M_{cr} = CM_0 = 1.00 \times 442.2 = 442.2\,kNm \tag{L.33}$$

5- Slenderness reduction factor

The slenderness reduction factor α_s [4.4] (Cl. 5.6.1.1(2)) is

$$\alpha_s = 0.6\left[\sqrt{\left(616/442.2\right)^2 + 3} - \left(616/442.2\right)\right] = 0.50 \tag{L.34}$$

6- Nominal member moment capacity

The nominal member moment capacity (Cl. 5.6.1.1(1)) is

$$M_r = 1.0 \times 0.50 \times 616 = 308\,kNm \le 616\,kNm$$

which corresponds to a moment ratio

$$\frac{M_r}{M_{cr}} = \frac{308}{442.2} = 0.70$$